A Numerical Eigenmode Analysis of the Progressive Buckling of Thin-Walled Tubes

Timothy Mark Fuggle

Department of Mechanical Engineering
University of Cape Town
South Africa

September 2005

Thesis submitted in partial fulfillment of the requirements for a Masters in Engineering

ACKNOWLEGDEMENTS

I would like to appreciate and acknowledge the assistance received from my supervisor Professor G N Nurick and the CERECAM staff, especially Mr. V Balden. I would also like to thank Professor A Zingoni his special interest and his encouragement and for some of his valuable comments for this thesis.

I especially wish to thank my mother, Joan, for her support.

DECLARATION

I, Timothy Mark Fuggle, declare that this thesis is essentially my own work and has not been submitted in this or any other form for a degree at any other university.

SYNOPSIS

Progressive buckling of thin-walled tubes has already been used very successfully to absorb the kinetic energy during the impact between motor vehicles, trains, etc. This field is of particular interest for the crash-worthiness design of aeroplanes, motor cars, buses, trains, ships and marine structures, where the survivability of passengers is at risk.

This thesis describes a numerical eigenmode analysis of the progressive buckling of thin-walled steel tubes by means of the numerically modelling of 300 mm long by 50 mm wide thin-walled square tubes having a wall thickness of 1.2 mm. A theoretical analysis of buckling problems shows that they are eigenvalue problems, governed by the following equation:

$$([k] + \lambda[k_G]) \{U\} = 0$$

where $[k_G]$ is the geometric stiffness matrix, λ is the eigenvalue related to the buckling load and $\{U\}$ is the associated vector of nodal displacements describing the mode shape or eigenmode.

One of the objectives of this thesis is to determine the first ten eigenmodes and the associated eigenvalues of various shaped thin-walled tubes, namely square tubes, triangular, hexagonal and circular shaped tubes. Another objective is to use the eigenmodes as initial imperfection factors to perturb the model in order to produce a more accurate model.

Since experimental work did not form part of this thesis, it was necessary first to verify the results of the initial models with almost identical models to the models undertaken by Nannucci [42], who in turn verified his models from experimental work. Prior to performing the detailed analysis of the square tube models, a mini investigation had to be undertaken beforehand to determine a small enough time sampling interval in ABAQUS. In order for the output results to be recorded correctly, such as the initial peak reaction force, it was found that a time sampling period of less than 1 microsecond was required. Next a suitable mass scaling factor had to be determined in order to reduce

the ABAQUS analysis duration. Once a suitable mass scaling factor of 225 was determined it reduced the analysis time to 15.7 hours per analysis.
The first part of the detailed analysis of this thesis involved research to determine the first ten eigenmodes and the associated eigenvalues of various shaped thin-walled tubes. The eigenmodes for each of the square tubes were then introduced into the respective square tube models and used as the imperfection factors to perturb (or seed) the mesh in the crushing analysis of the model. The purpose of perturbing the model i.e. introducing and using the eigenmodes of the tube as imperfection factors from eigenmode buckling analysis is that it provides greater accuracy than using arbitrary imperfection factors, such as those used by Nannucci [42]. The eigenmodes also provide an alternative means of determining the initial collapse mode of the tubes.
Prior to introducing the arbitrary imperfection factors into his model, Nannucci had to determine the collapse modes for his tube models given by Jone's [47] theoretical method for square tubes. Due to the fact, according to the literature and as far as the author is currently aware, that no theoretical method exists yet for predicting the collapse modes of other shaped tubes such as for triangular and hexagonal shaped tubes, etc. This factor then becomes a problem when modelling these shapes of tubes because one needs to know the collapse modes of these tubes first, if using arbitrary imperfection factors, prior to performing the crushing analysis. Besides improving the accuracy of the model, perturbing the model with the introduction of the eigenmodes as the initial imperfection factors overcomes this limitation.

The effects of initial imperfection factors under different loading conditions as well as subject to various end boundary conditions were then studied in detail for the square tubes. Although most tube models were studied using single eigenmodes as imperfection factors, the models using multiple eigenmodes as imperfection factors are the most accurate, because for a long thin-walled tube all of the eigenmodes are involved. The first eigenmode being the dominant one has the greatest effect and the subsequent eigenmodes being correspondingly progressively of less significance with their increasing higher order.

The initial buckling load of a tube can be determined by multiplying the 1st eigenvalue by the applied load used in the eigenmode analysis. When imperfection factors are not used or applied correctly, this can result in errors. Both the loading conditions and the end boundary conditions have a significant effect on the results of a tube analysis. When a tube model undergoes crushing the deformed profile of a tube is much more non-uniform and random-like and incorrect when using a specific mass and initial velocity loading, than when using a constant velocity loading. End boundary conditions have a significant effect on the deformed profile of the crushed tube, particularly when it begins to buckle, as well as on the final deformed profile.

Another significant benefit of performing an eigenmode buckling analysis of a tube model is for the energy absorption of an impact in order to absorb the energy uniformly over the impact time period. The eigenmodes have a practical use in the sense that a tube that is to be utilized as a shock absorber can be manufactured to the same profile as its natural eigenmodes. This will reduce the initial peak reaction force (the ultimate buckling force) to a similar size as the 2nd and 3rd, etc. peak reaction forces and lead to the impact energy being absorbed more uniformly over time causing less harm or injury to passengers in vehicles.

TABLE OF CONTENTS

LIST OF ILLUSTRATIONS

Figure: **Page**

LIST OF TABLES

LIST OF SYMBOLS

E	Young's modulus
σ	stress
C	mean width of square tube
H	mean wall thickness of square tube
P_m	mean static crushing load
P'_m or P_m^d	mean dynamic crushing load
M_0	plastic collapse moment
l	distance between plastic hinges
$\dot{\varepsilon}$	uniaxial plastic strain rate
D	Cowper-Symonds constant
q	Cowper-Symonds constant
σ_o	static yield stress
σ'_o	dynamic yield stress
V_0	velocity
P_{ult}	ultimate buckling load
A	cross sectional area
k_G	geometric stiffness matrix
λ	associated eigenvalue
U	associated vector of nodal displacements
w	transverse displacement
f(x)	transverse load
P	compressive load
P_n	critical load
u_1	translational motion in the x direction
u_2	translational motion in the y direction
u_3	translational motion in the z direction
Φ_1	rotation in the x plain
Φ_2	rotation in the y plain
Φ_3	rotation in the z plain
n	positive normal

S4R	4 noded general shell element
t	point in time
Δt	time increment
i	time increment number in a step
M	diagonal lumped mass matrix
F	the applied load vector
I	internal force vector
ω_{max}	highest frequency of system
ε_{max}	fraction of critical damping in highest frequency mode
L_{min}	smallest element dimension in the mesh
c_d	dialational wave speed of the material
$\hat{\mu}$	Lame's constant
$\hat{\lambda}$	Lame's constant
ρ	material density
v	Poisson's ratio
σ_{true}	true stress
σ_{nom}	nominal stress
ε_{nom}	nominal strain
ε_{ln}^{pl}	logarithmic plastic strain
$\dot{\varepsilon}_0$	material constant for mild steel
T	material temperature
σ_{y0}	static yield stress at the reference temperature of the tensile test
L^e	characteristic element length

1. INTRODUCTION

1.1 BACKGROUND

Structural impact is concerned with the behaviour of structures subject to static and dynamic loads which produce inelastic deformations. This field is of particular interest for the crash-worthiness design of aeroplanes, motor cars, buses, trains, ships and marine structures, where the survivability of passengers is at risk, as well as for the energy absorbing characteristics of various other components such as the petrochemical industry for safety devices. Progressive buckling of thin-walled tubes has already been used very successfully to absorb the kinetic energy during impact between motor vehicles, trains, etc.

A great deal of research has been performed in the field of energy absorption devices and in particular for thin-walled square and cylindrical tubes being axially crushed. Many rigorous and time-consuming experimental models have been carried out in order to gain a better understanding of the different collapse modes of thin-walled square and cylindrical tubes. The ability of numerical models to predict the failure modes and forces associated with the collapse of the tubes accurately has meant that extensive time and expense required for experimental methods can be eliminated.

The finite element method is one particular numerical procedure used to analyse structures over a particular time duration. Many physical problems have become too complicated to be solved analytically and because of this, finite element analysis has become an extremely important due to its accuracy and efficiency in modern day design and problem solving. Finite element analysis can also eliminate, to an extent, expensive and time consuming prototyping of initial designs in many fields such as crash-worthiness design, extrusion and moulding problems, structural testing and so forth.

ABAQUS version 6.3, the finite element package used in this numerical analysis is a 3-dimensional finite element package which can be used to analyse the behaviour of a range of structural and other problems, under a variety of different conditions.

1.2 OBJECTIVES OF THIS THESIS

1. To find a method of predicting the collapse mode of thin-walled tubes, other than square tubes which can already be theoretically predicted, such as triangular, hexagonal and circular, etc. shaped tubes.

2. To determine the eigenmodes of thin-walled tubes. Due to the fact that a mathematical formulation would be very complex, a numerical method had to be found first with the aid of finite element analysis using ABAQUS.

3. To determine the reaction forces over the crushed distance of the crushed tubes as well as the associated stresses and strains.

4. To determine a sufficiently small time sampling interval in ABAQUS in order to detect the correct initial peak reaction force.

5. To investigate the effects of using mass scaling, i.e. when it can be used, the degree it can be used, the corresponding accuracy and the speedup factor it produces.

6. To determine the eigenmodes and their associated eigenvalues for tubes of various shapes having a specific length and thickness. To determine which eigenmodes are the dominant eigenmodes as these eigenmodes affect the collapse mode and buckling load of a tube. To show an alternative method of determining the initial buckling load of a tube from its first eigenvalue.

7. To investigate the use of eigenmodes for their introduction as imperfection factors as well as the advantages of using eigenmodes as imperfection factors. To determine how to apply the imperfection factors correctly and the errors which result when the imperfection factors are not applied correctly. To determine how to use the eigenmodes as imperfection factors for tubes as a means of reducing the initial first peak reaction force to a similar magnitude to the second, third, etc peak reaction forces in order to absorb the energy of an impact uniformly over time to minimise shock and injury to passengers of vehicles, etc.

8. To investigate the effects of initial imperfection factors under different loading conditions.

9. To investigate the effects of eigenmode imperfections subject to various end boundary conditions under a specific mass and initial velocity loading.

10. To investigate the effects of eigenmode imperfection factors subject to various end boundary conditions under a constant velocity loading.

11. To draw conclusions and give recommendations based on the models.

1.3 SCOPE OF THIS THESIS

The scope of this thesis involves a numerical eigenmode analysis of the progressive buckling of thin-walled steel tubes by means of the numerically modelling of 300 mm long by 50 mm wide thin-walled square tubes having a wall thickness of 1.2 mm. Triangular, hexagonal and circular thin-walled tubes of equivalent dimensions were also modelled in order to determine their eigenmodes and associated eigenvalues. The tubes were crushed quasi-statically using either a constant velocity loading or a specific mass and initial velocity loading under various end boundary conditions. Since experimental work did not form part of this thesis, it was necessary first to verify the results of the initial models with almost identical models to the models undertaken by Nannucci [42] earlier, who in turn verified his models from experimental work. The comparison with Nannucci's [42] models was done mainly by comparing the reaction force versus displacement graphs with the ones obtained by Nannucci [42] and by specifically the peak reaction forces from the graphs as well as by comparing the amount of energies that the tubes in both models absorbed. Prior to performing the crushing analysis of the square tube models an eigenmode buckling analysis for the square tubes as well as for other shaped tubes such as triangular, hexagonal and circular shaped tubes to determine both the first ten eigenmodes and the associated eigenvalues for these tubes. The eigenmodes for the square tube models were then introduced into the model and used as the imperfection factors to perturb (or seed) the mesh in the crushing analysis of the square tube models. Suitable scaling factors then had to be determined for the imperfection factors to produce reliable results.

In order for output results to be recorded correctly, such as the initial peak reaction force, a mini investigation had to be undertaken beforehand to determine a small enough time sampling interval in ABAQUS. Next a suitable mass scaling factor had to be determined in order to reduce the ABAQUS analysis duration which took 4 days 8 hours per model, of which there were approximately 80 models, as the use of symmetry would be insufficient as it can only reduce the analysis time duration by half. The mass scaling factor had to be within acceptable limits as a too large mass scaling factor can lead to errors in the model.

The following three effects of imperfection factors and specifically eigenmodes introduced as initial imperfection factors were then studied in detail for the square tubes:

i) The effects of initial eigenmode imperfection factors under different loading conditions

ii) The effects of initial eigenmode imperfection factors subject to various end boundary conditions under a specific mass and initial velocity loading

iii) The effects of initial eigenmode imperfection factors subject to various end boundary conditions under a constant velocity loading.

1.4 PLAN OF DEVELOPMENT

This thesis has the following plan of development:

- *Literature Review* - This section outlines the literature on axial buckling of thin-walled tubes and the energy that these tubes absorb. In particular it concentrates on the quasi-static crushing of thin-walled square and cylindrical tubes and is divided into three sections, namely experimental, theoretical and numerical studies.
- *Tube Buckling Theory* - When thin-walled square and cylindrical tubes are crushed axially, they fail in a number of buckling modes, namely Euler buckling, Progressive buckling and Plastic buckling and these modes are discussed. When thin-walled square and cylindrical tubes undergo progressive buckling they can buckle forming a number of distinct collapse modes and these collapse modes are discussed in detail. An introduction and explanation of eigenmode buckling analysis theory is also discussed.
- *The Finite Element Model* - This section describes how the numerical models were set up and the various boundary conditions that were applied to the various tube models.
- *Results and Discussion* - The results and observations of the range of models are presented and discussed.
- *Conclusions* - Conclusions are drawn for this study on the eigenmode buckling analysis of thin-walled tubes from the numerical models and their results and from the literature review.

- *Recommendations* - Aspects of modelling that should be considered and further investigations to this study are discussed.

2. LITERATURE REVIEW

This literature review concentrates on the references relating to the subject of axial localized buckling of thin-walled tubes and the energy that these structures absorb. In particular, it concentrates on the quasi-static crushing of thin-walled square and cylindrical tubes. For ease of articulation it was decided to categorize this literature review into three main sections i.e. Experimental studies, Analytical studies and Computational / Numerical studies. For each section, the references have been grouped in chronological order. Although there is often some overlap of the references in each of the three study groupings, the references are grouped to the main purpose of each study, accordingly.

2.1 EXPERIMENTAL STUDIES

Mamalis and Johnson [1] investigated thin-walled circular cylinders and frustra (truncated circular cones) of an aluminium alloy subjected to axial static loading. The initial length and the outside diameter of the cylinders and frustra (the larger top end) were kept constant whilst the wall thickness was varied. They observed that the relatively thick tubes fail by collapsing into circumferential axisymmetric rings by folding progressively into diamond-shaped lobes after assuming an initially axisymmetric ring mode of deformation. In the latter case the initial axisymmetric rings developed into non-symmetric diamond patterns (elliptic, triangular and square, etc.) as loading progressed. Also initially non-symmetric diamond buckle patterns were observed to be characteristic modes of frustrum collapse.

Mamalis, Johnson and Viegelahn [2] also investigated the crumpling of steel thin-walled tubes and frustra under axial compression at elevated strain-rates. Initial axisymmetric rings ('ring', 'bellows' or 'concertina' buckling) developed into non-symmetric 'diamond' patterns (elliptic, triangular and square, etc.) as loading progressed and initially non-symmetric diamond buckle patterns were observed to characterize the modes of frustrum collapse.

Ren, Mingbao, Zhuping and Quingchun [3] conducted an experimental study on the dynamic axial plastic buckling of cylindrical shells. They found that when the impact velocity is less than a certain critical velocity V_{c1} the shell will exhibit only uniform plastic deformation in both the axial and radial directions and does not produce sinusoidal waves. Alternatively, when the impact velocity exceeds another critical value V_{c2} the shell will change from the axisymmetric mode into a non-uniform type of large deformation, the number of waves decreases slightly and the shell begins to lose its load carrying capacity.

The crush behaviour of glass fibre reinforced plastic sections was studied by Thornton [4] with particular reference to the effects of the geometry of the crush trigger initiator. It was found that the propagation of delamination cracks contributed little to the energy absorption capacity, most of the crush resistance being derived from the development of kink bands in the fibre structure. The crush resistance of square tubes with thinner walls was largely provided by the corners. As the wall thickness increased, the planar portions contributed more to the crush resistance. The trigger geometry alters the energy absorption capacity by the extent to which it generates deformation flaws which can then propagate within the cell structure. Softer crush anvils reduce the effectiveness of the trigger crush initiator and can lead to global failure of the section, rather than to stable, progressive crush.

Thornton and Jeryan [5] examined FRP (Fibre Reinforced Plastic) composite materials with particular reference to their use in the automotive environment. Although simple tube structures made of FRP composites have exhibited energy absorption greater than similar metal structures, the crush process in many cases is accompanied by fracture rather than plastic deformation.

Hull [6] gave a detailed account of the two main modes of progressive crushing, splaying and fragmentation which occur in tubes made from fibre-reinforced composite materials. Transitions between splaying and fragmentation modes were identified and found to be related to the force-displacement response.

Hamada, Coppola and Hull [7] studied the effect of surface treatment on crushing behaviour of glass cloth / epoxy composite tubes. The fracture mode of amino-silane treated tubes was by splaying, whereas in acryl-treated tubes the fragmentation mode of crushing was observed.

Hamada, Coppola, Hull, Mackawa and Sato [8] carried out a comparison of the energy absorption of carbon / epoxy and carbon / PEEK composite tubes. The carbon fibre / PEEK tubes had a specific energy absorption of 180 $kJ.kg^{-1}$, and was the highest value recorded for any material type.

Marshall [9] studied the effect of a number of different mechanical indenters to invoke side dents on the tubes prior to them being buckled progressively. Side dents were made with cylindrical indenters with a radius ranging from 1mm to 25mm.

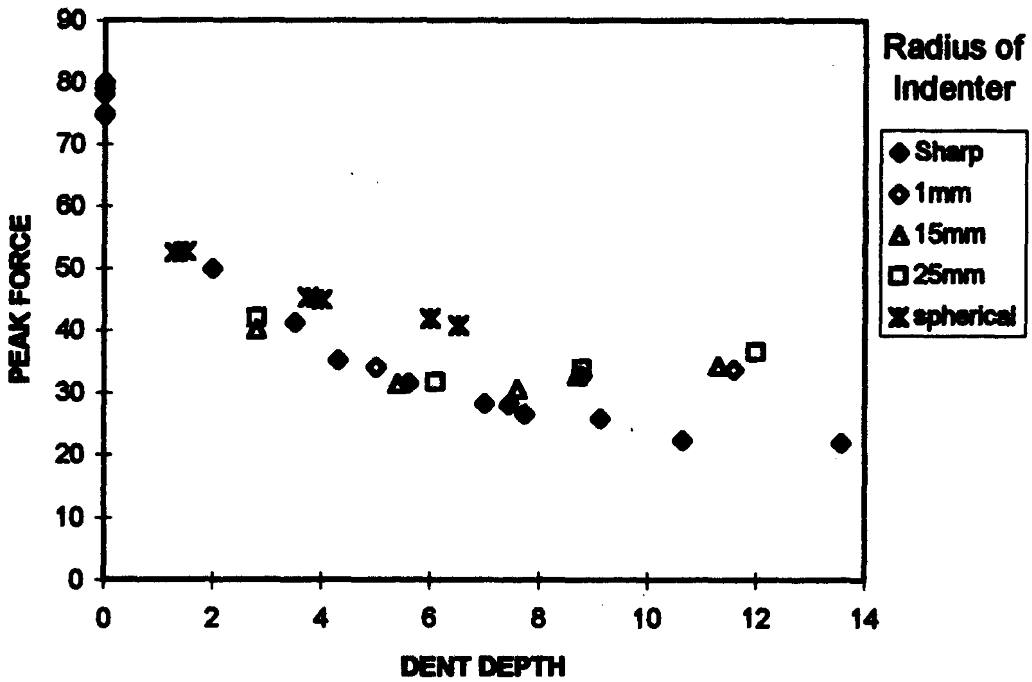

Figure 2.1: The effect of the depth of the corner dent on the ultimate buckling load. The tubes had a width of 50mm and a wall thickness of 1.2mm. [9]

Figure 2.1 shows the effect that the cylindrical side dents have on the buckling loads. The mean crushing load was unaffected by the depth and size of the indent. The dents affected the shape of the first lobe formed. If the dent was sufficiently large, the opposite sides of the tubes touched and tended to create a very large first lobe which, in the case of the largest pre-dents, caused the tubes to bend over and progressive buckling did not continue. In the case of spherical indents there was a similar trend in the results. The inclusion of the dent reduced the ultimate force, but did not affect the subsequent peak forces or the mean force. Again with the larger dents the opposite sides of the tubes touched and caused overall buckling of the structure.

Marshall [9] also performed a number of experiments in which spherical dents in the tubes were added together with the centrally drilled holes. This decreased the ultimate load further than just having holes alone. There was also no change to the mean buckling load. The addition of dents reduced the ultimate load by between 15% and 35% of the load with only holes present in the square tubes. The addition of the dents considerably changed the formation of the first lobe. A comparison of tubes with different hole diameters and the same dent depth shows that the larger the hole diameter, the smaller the size of the first lobe. This means that a tube with a large hole diameter and spherical side dent deforms the most like a perfect tube, although the initial peak force can be altered to be the same as the subsequent peak forces.

Marshall and Nurick [9, 10] performed experiments on square thin-walled tubes with a number of different mechanical imperfections. Two holes were drilled into the opposite faces of a square tube with a width of 50 mm and a wall thickness of 1.2 mm. The diameter of the holes were varied from 16 mm to 38 mm and compared to a tube without a hole. The tubes were crushed quasi-statically. The inclusion of round holes in two opposite faces of the square tubes decreases the ultimate buckling load of the specimen. The effect of including holes in the square tubes on the critical buckling loads can be seen in the Figure 2.2.

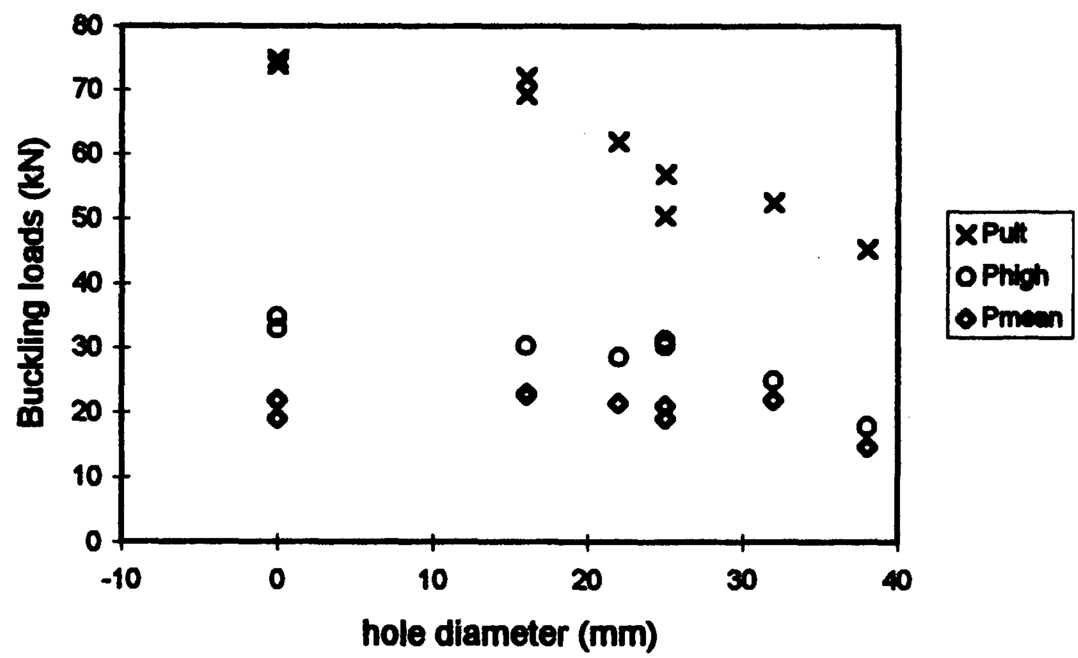

Figure 2.2: The effect of holes on the critical buckling loads of thin-walled square tubes. [9]

The mean and subsequent peak forces did not differ from that for a tube without a hole, for tubes with a hole diameter of less than 32mm. The specimens with holes of greater than 32mm tore rather than buckle progressively. The oscillating characteristic of the load displacement curve thus disappeared. The size of the first lobe formed was also affected by the introduction of holes. This tended to cause an instability in the tube as one lobe would fold upwards and the other one downwards.

Knebel and Schweizerhof [11] studied the buckling of cylindrical shells containing granular solids. They observed that thin-walled structures are likely to buckle under axial loading way below the classical value. In the presence of granular solids (e.g. sand) in cylindrical shells the stiffness of the contents has a positive influence on the buckling load, similar to internal pressure. In practical silo design this effect is not considered. It was observed that the presence of a granular solid can increase the buckling load remarkably and also that small modifications in the interaction assumptions have a major influence on the buckling loads.

Grzebieta [12] conducted research into failure mechanisms of some thin-walled circular tubes. His research was as a result of a real life example which clearly illustrated the need to be able to design for the residual load of a collapsed structure which occurred in the Hyogoken-Nabu earthquake in Japan, where a large number of bridges underwent considerable vertical and shear movement. These bridges were supported using steel frames made from thin-walled tube sections and round stocky tubes. In some cases the primary bridge structure remained intact but with slight settlement as a result of the supporting frame having distorted at localized points. Figure 2.3 (a) and (b) shows a support column where a ductile bulge occurred in the middle of the column during the earthquake. This bulge is similar to that observed in the laboratory when stocky round tubes are subjected to an axial crush load and an extensional elephants foot mode of collapse occurs as illustrated in Figure 2.3 (c) and (d). Such localized deformations are essentially plastic mechanisms capable of dissipating substantial amounts of kinetic energy. The residual load resisted by the bulge mechanism was sufficient to withstand the dead load of the bridge once the earthquake had ceased.

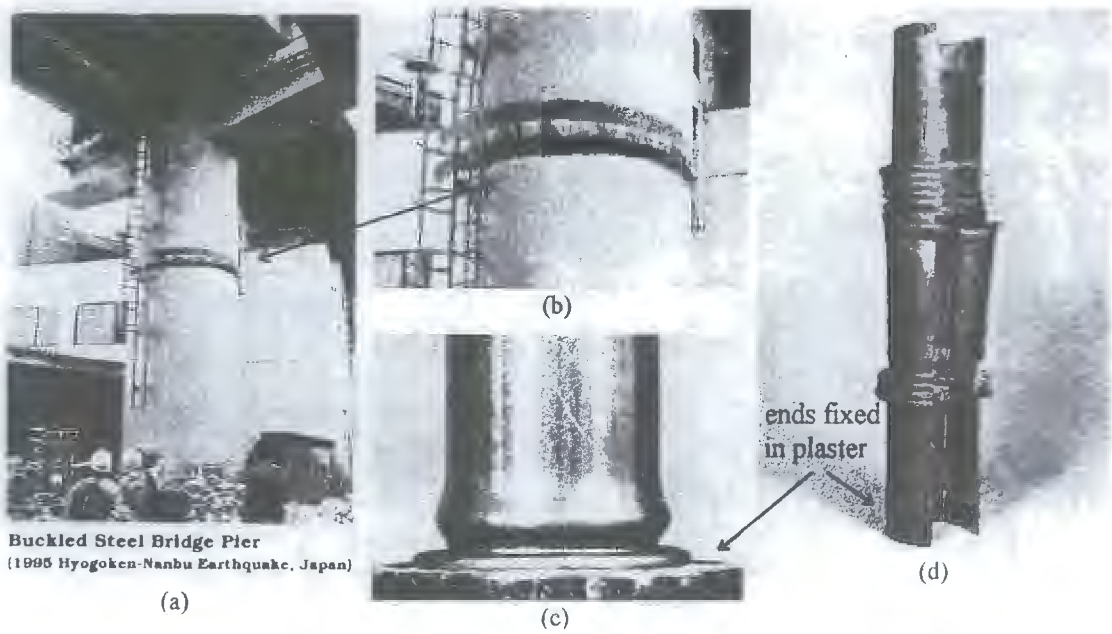

Figure 2.3: The plastic collapse mechanism of a thick-walled cylindrical bridge column in an earthquake (a) and (b) is similar to a round stocky tube (R / t = 15.4) axially crushed in a laboratory. [12]

Figure 2.4 shows a thin-walled round tube with a R / t = 81 (R= tube radius, t = wall thickness) being progressively crushed. These thinner structures deform into a diamond type pattern at one end when subjected to either a slow quasi-static or medium strain-rate impact load. This is in contrast to the elephants foot bulging fold which commonly occurs in the thicker or stockier tubes (R / t < 25) in Figure 2.3.

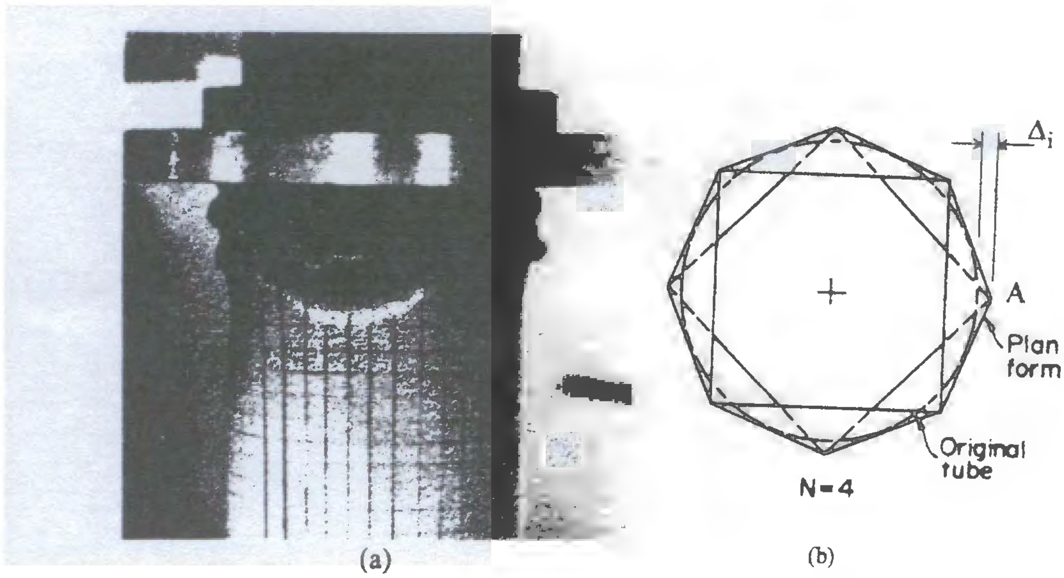

Figure 2.4: Thin-walled tube subjected to an axial crush load and deforming in a diamond collapse mode (R / t = 81). [12]

Karbhari and Haller [13] investigated the crushing rate on energy absorption of braided composite tubes. They reported that conventional energy absorption mechanisms based on progressive crush loading in automotive and rotorcraft structures are often compared on the basis of the load ratio of the peak to the mean crush load, with efficiency being considered as optimum when the ratio is 1 and decreasing as it increases above 1. They cautioned that although useful as a measure of relative efficiency, results on the basis of load comparison of different specimens on the basis of load ratio alone should be treated with caution since it is possible for a specimen to have an extremely good load ratio at very low overall load levels and hence at low corresponding levels of energy absorption.

Lancaster, Calladine and Palmer [14] investigated the buckling behaviour of a thin shell with introduced imperfections under axial compression subject to different boundary conditions. Their tests either with or without deliberate imperfections showed very little imperfection sensitivity and even gross imperfections in the form of large stable dimples at zero load, reduced the peak load on average by only about 12%. They attributed this unexpected behaviour to their use of frictional rather than fixed boundary conditions at the two ends of the shell.

Seitzberger, Rammerstorfer, Gradinger, Degischer, Blaimschein and Walch [15] performed experimental studies on the quasi-static axial crushing of steel columns filled with aluminium foam. Their test results confirmed that considerable mass efficiency improvements with respect to energy absorption may be obtained, even with reduced stroke lengths, by the presence of foam.

Guillow, Lu and Grzebieta [16] performed experimental investigations into quasi-static axial compression of thin-walled circular aluminium tubes. They established a non-dimensional empirical formula for the average crush force as $F_{AV} / M_p = 72.3\ (D / t)^{0.32}$. Comprehensive comparisons were made between existing theories and their test results for F_{AV} which revealed some shortcomings suggesting further theoretical work was required. It was found that the ratio F_{MAX} / F_{AV} increased substantially with an increase in the D / t ratio. The effect of filling aluminium tubes with different density polyurethane foam was also examined because foam-filling of thin-walled tubes had previously been observed to affect the mode of collapse. The collapse mode of an empty aluminium tube was non-symmetric and the same applied to an identical tube filled with foam of density 35 kg/m^3. However, filling with polyurethane foam of 60 kg/m^3 forced the aluminium tube to collapse in a mixed mode and foam of density 140 kg/m^3 produced axisymmetric mode collapse.

Gupta, Sekon and Gupta [17] carried out an experimental study of fold formation in the axisymmetric axial collapse of round tubes. They showed that the load compression curve is dependent on the amount of internal folding, while the mean collapse load and the folding length are independent of it. Also, the relative extent of internal and external folding depended upon the diameter to thickness ratio of a given tube.

2.2 ANALYTICAL STUDIES

In 1960 Pugsley and Macaulay [18] examined the static crushing of thin-walled cylindrical shells when compressed between two plates. In particular the mode, which resulted in diamond shaped deformations of the tube, was examined. A theoretical approximation was derived for static buckling of the tube collapsing with this diamond shape mode.

The same year, Alexander [19] examined the axisymmetric mode of crushing under an axial load and the amount of work required for a simple mode of collapse. Alexander also determined the mean load required to collapse the tube experimentally and theoretically by equating into the work done multiplied by the distance through which the load acts. Since these early experimental and theoretical results were obtained there has been much work undertaken in the field of axial crushing of thin-walled cylindrical and square tubes.

Alexander [19] was the first to present a mathematical formulation of the crushing problem of tubular members. He developed an approximate procedure for calculating the mean crushing force of tubes collapsing in an axisymmetric or concertina mode. The Alexander solution fails in the determination of the crushing distance and the final shape of the deformed tube. His model with stationary plastic hinges assumes that a section of the tube of the original length 2H, fully collapses into a flat disc of thickness negligible compared to 2H (Figure 2.5).

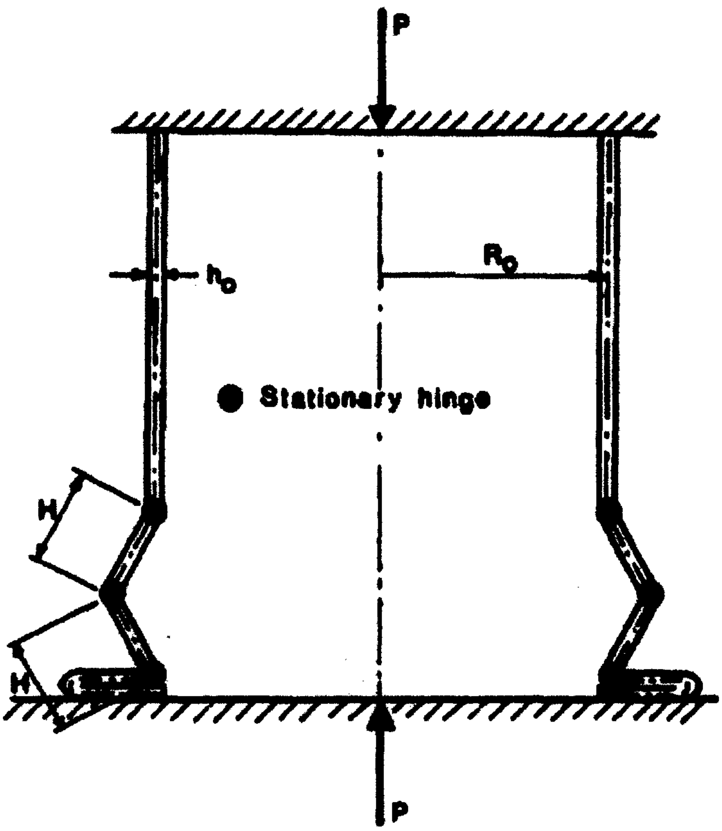

Figure 2.5: Alexander's model for axisymmetric axial crushing of circular tube. [19]

This is a very unrealistic assumption which leads to the underestimation of the mean crushing force. The mean crushing force is given by

$$P_m = 8.4630\ \sigma_0\ h_0^{1.5}\ R_0^{0.5}$$

(σ_0 = uniaxial yield stress, h_0 = tube thickness, R_0 = tube radius)

It was suggested as early as 1972 by Shaw [20] that thin-walled tubes could be used as energy absorber devices for absorbing the kinetic energy in vehicle crashes. Shaw proposed design concepts for the implementation of this theory for motor vehicle bumpers.

Ho [21] investigated buckling loads of non-linear systems with multiple eigenvalues and found that for structural systems the influence of imperfections on the buckling of the systems depends to a very large extent upon the distribution of the imperfections. Moreover, the system may buckle either at a limit point or at a bifurcation point before this limit point is reached.

Wierbicki and Bhat [22] reconsidered the Alexander problem of an axisymmetric crushing of circular tubes with the objective of giving a more adequate description of the kinematics of the plastic collapse process. It was assumed that a single fold is formed by a suitably chosen set of extending and contracting hinge circles. The hinge moves with respect to the shell material leaving behind a smooth double curvature surface. Closed form solutions were obtained for the instantaneous and mean crushing force, the effective crush distance and the length of the local folding wave. The mean crushing force is given by

$$P_m = 12.4516\, \sigma_0\, h_0^{1.5}\, R_0^{0.5}$$ (σ_0 = uniaxial yield stress, h_0 = tube thickness, R_0 = tube radius)

The difference between this equation and the previous equation is the larger constant in this equation giving better accuracy.

Grzebieta [23] developed an alternative theoretical method for determining the behaviour of round stocky tubes subjected to an axial crush load which were compared to experimental investigations. The results indicated that the effects of axial and hoop stresses, imperfection sensitivity, strain-hardening and hinge curvature should be considered in the analysis if the tube behaviour is to be predicted accurately.

Wierzbicki, Bhat, Abromwicz and Brodkin [26] revisited Alexander's model and developed a new model of the progressive crushing of circular tubes in which an active zone of plastic deformations contains two folds or buckles. The model captured with great realism several features of the crushing process which were unaccounted for in all previous computational and theoretical models of progressive buckling. These included: finite values of the load peaks, alternating heights of the peaks, unequal distance between peaks, reduced crush distance, realistic final shape of crushed tubes and a longer distance between the two first peaks. Closed form solutions derived for the length of the plastic folding wave and the mean crushing force showed very good agreement with the experimental results. The history of the crushing force was shown to depend on the eccentricity parameter i.e. on the way the tube material folds with respect to the original tube radius. However, the mean crushing force was found to be independent of the eccentricity parameter.

Showkati and Ansorian [27] studied the influence of primary boundary conditions on the buckling of shallow cylindrical shells. Slender cylinders of intermediate length subjected to internal pressure normally buckle into sinusoidal waves in the circumferential and meridional directions, the wave numbers are a function of the edge restraints, aspect ratio (L / R) and wall slenderness (R / t). The influence of edge restraints diminishes with increasing L / R and disappears in very long cylinders. All instability formulae purporting to evaluate the lowest eigenvalue require minimisation with respect to the circumferential wave number (n), any exact formulation requires the priori evaluation of n. Therefore, in any investigation of the effect of boundary conditions on the buckling pressure (q_{cr}), the evaluation of n is critical. It was found that, as the restraint of the cylinder edges increases, the meridional wavelength decreases, and the wave number increases. The meridional wavenumber is not necessarily an integer value and therefore the concept of an effective length similar to that of columns is appropriate. Cook [refer to 27] had shown previously experimentally that a thin cylinder buckles into a greater number of lobes than a thicker one of the same L and R. Showkati and Ansorian formulated equations for the wave number and the buckling pressure (q_{cr}), which are dependent on the boundary conditions of the shallow circular shell.

The boundary conditions are classified as follows; A: axial restraint, C: full rotational restraint and translational restraint, F: free, R: rotational restraint about the tangent and S: radial restraint.

Binary mode case (n = 2):

Three sets of boundary conditions, namely F-F, A-A and S-F, always produce the buckling mode characterised by n=2, in the range $0.5 \leq L / R \leq 5$ and $300 \leq R / t \leq 3000$. The mode is therefore independent of the geometry in the range considered. It was also found from this study that rotational edge restraint alone (in the absence of radial restraint) does not affect either q_{cr} or n, which remains equal to 2.

Other modes (n > 2):

The eight remaining cases are all a function of geometry and include the classical case S-S (Figure 2.6)

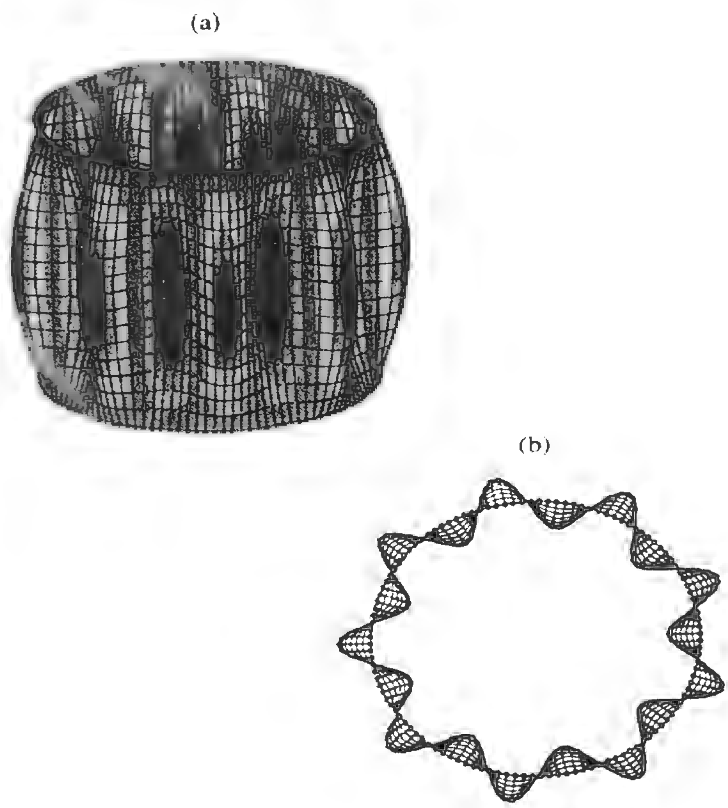

Figure 2.6: Classical boundary conditions S-S. L / R = 1.5, R / t = 1500. (a) Oblique view (b) plan view. [27]

The equation for n, applicable to all cases for which n>2, was found to be

$$n = 1.2 - 0.55k + 2.58\sqrt{\frac{R}{kL}\sqrt{\frac{R}{t}}}$$

For each of 10 sets of boundary conditions, a least squares approximation to the computed buckling pressures was derived. The general expression, valid in the range $0.5 \le L/R \le 5$ and $300 \le R/t \le 3000$ is given by

$$q_{cr} = \gamma E\left(\frac{R}{L}\right)^{\alpha}\left(\frac{t}{R}\right)^{\beta}$$

where the coefficients α, β and γ are listed in Table 2.1.

Table 2.1: Buckling Pressure Coefficients.

Boundary Conditions	**α**	**β**	**γ**
F-F	0.000	3.000	0.363
S-F	0.280	3.000	0.554
S-A	0.997	2.499	0.469
SA-F	0.991	2.496	0.536
SA-R	1.055	2.503	0.580
SA-A	0.967	2.484	0.599
S-S	1.020	2.510	1.033
SA-S	0.987	2.494	1.096
SA-SA	0.951	2.476	1.098
C-C	0.982	2.491	1.269

Gupta and Velmurugan [28] carried out a detailed theoretical study to understand the effect of internal folding on the fold length, mean collapse load and the post collapse load-compression curve. In this analysis the bending moment for a perfectly plastic material was used in calculating the fold length and the mean collapse and the reduced bending moment was used to find the post collapse load compression curve. The actual variation of hoop strain along the profile was considered in calculating the hoop strain. When the reduced bending moment capacity is used to compute the fold length and the mean load, the values come out to be less than those calculated with the perfectly plastic bending moment. The lengthy equations to determine the mean load are given in reference [28].

Abramowicz and Jones [29] presented some elementary theoretical considerations on the initiation of the collapse process for tubes having square cross sections and on the transition from global bending to progressive buckling induced by the local plastic collapse for both circular and square tubes. The global bending of a column that collapses in a Euler-type mode continues up to the point where a side face(s) collapse(s) locally. At this point, depending on the length, geometry of the cross section and the material properties, a column may continue to bend globally, or, alternatively, can switch to the progressive collapse mode. Abramowicz and Jones developed empirical formulae to predict the transition from global buckling to progressive buckling for both quasi-static load cases and dynamic load cases as follows:

Quasi-static load case:

Circular columns
$$\left(\frac{L}{2R}\right)_{cr} = 2.996\exp\left(0.02\frac{2R}{t}\right)$$

Dynamic load case:

Circular columns
$$\left(\frac{L}{2R}\right)_{cr} = 3.355\exp\left(0.03\frac{2R}{t}\right)$$

Square columns $$\left(\frac{L}{C}\right)_{cr} = 3.423\exp\left(0.04\frac{C}{t}\right)$$

They observed that the initiation of the collapse process for the dynamic crushing of columns is similar to that for a quasi-static loading. However, columns that buckled locally, collapsed progressively under higher dynamic crushing forces. This increase in the crushing force is due likely to the influence of material strain rate effects.

Karagiozova and Jones [30] studied dynamic elastic-plastic buckling of circular cylindrical shells under axial impact. Particular attention was paid to the influence of stress wave propagation on the initiation of buckling. It was found that the development of the buckling shape depends strongly on the inertia properties of the striker and on the geometry of the shell. The theoretical method was used to clarify some experimental data and good agreement was obtained with results on aluminium alloy tubes. It was found that the dynamic buckling process is governed by stress wave propagation effects and, in general, the entire length of the shell is involved in the deformation process for a high velocity impact. This phenomenon is known as dynamic plastic buckling. However, the final plastic shape depends strongly on the inertia properties of the striker and the geometry of the shell. Larger mass-lower initial velocity impacts tend to cause large bending deformations near the impacted end which leads to progressive folding.

Karagiozova and Jones [31] also studied the influence of stress waves on the dynamic progressive and dynamic plastic buckling of cylindrical shells. The phenomena of dynamic plastic buckling (when the entire length of the shell wrinkles before the development of large radial displacements) and dynamic progressive buckling (when the shell folds forms sequentially) were analysed from the viewpoint of stress wave propagation resulting from axial impact. The conditions for the plastic buckling were obtained. An analysis of the buckling phenomena revealed that the material properties together with the geometrical characteristics of the shell determine the particular type of response for high velocity impacts. It was shown that the initiation of buckling for a high velocity impact is sensitive to the material properties, particularly to the strain hardening modulus. The combination of the plastic wave speed, which is determined by the hardening modulus and inertia properties of a shell, leads either to dynamic plastic buckling or to dynamic progressive buckling. The material approximation can change the predicted pattern for the initial instability and the final buckling shape of a shell. A regular buckling shape can occur for strain rate insensitive materials when buckling develops within a sustained axial plastic flow, while the localisation of strain leads to progressive buckling in shells made of materials having a low strain hardening behaviour or strain rate sensitive properties. Shells made of strain rate sensitive materials always buckle progressively. Buckling starts either from the impacted end due to the relaxation properties of the material causing strain localisation near this particular end, or from the distal end due to the increased strains caused by the reflected stress wave. It was also shown that the prediction for the peak load, which can develop in a shell for a high velocity impact, depends on the particular yield criterion used in the analysis.

2.3 COMPUTATIONAL / NUMERICAL STUDIES

Remseth, Holthe, Bergan and Holand [32] were one of the first to model the collapse of a tube using finite element analysis to simulate oil pipelines in deep waters subjected to extreme conditions of bending and external pressure, resulting in the tube developing deep transverse and longitudinal buckles. The model was capable of accounting for very large displacements and gross yielding and was able to simulate non-linear behaviour, instabilities and complete collapse mechanisms of the steel tube.

When a tube structure collapses completely, a single surface may buckle enough that it comes into contact with itself. Benson and Hallquist [24] presented a contact algorithm that requires only a single surface definition for its input because the traditional approach of defining master and slave contact surfaces does not work because we do not know a priori how to partition the surface of the structure.

Hunt and Neto [25] investigated localized buckling in long axially-loaded cylindrical shells. They found that a double scale perturbation analysis of a long elastic cylindrical shell under axial compression revealed a second-order non-linear differential equation for the buckle pattern amplitude. Numerical solution then suggests that the most easily triggered failure mode is localized along the length.

Miyazaki, Hagihara and Munakata [33] used the finite element analysis method to study bifurcation creep buckling of circular cylindrical shells under compression. In previously conducted experiments axially compressive cylindrical shells with a large ratio of radius to thickness were observed to buckle with circumferential waves. The number of circumferential waves obtained from the numerical analysis agreed well with their experimental results. This implied that the circumferential waves observed in the creep buckling experiments were due to bifurcation.

Sasaki, Takeshi, Kurokawa and Tomoaki [34] studied the axisymmetric collapse of a circular tube due to impact and its use as a shock absorber. The impact behaviour of axisymmetric plastic buckling of the circular tube was investigated numerically and experimentally. In order to estimate the performance as an energy absorber, numerical parametric studies by Finite Element Method analyses were carried out. Tube impact experiments using aluminium circular tubes were performed for impact velocity ranges of 30 to approximately 70 m/s and were compared with numerical results. Good agreements were exhibited between the numerical and the experiments results. During the formation of one buckle, the axial load-time history showed two load peaks, each of them corresponding to the collision of the outer surfaces and the collision of the inner surfaces. The first peak load was observed to increase with increasing impact velocity and showed a very high value for a high impact velocity, however it decayed with wave propagation and after some distance propagation, it exhibited no more remarkable high amplitude and tended to approach a constant value. The mean axial crumpling load during the collapsing process after the second peak was approximately 10% higher than the static one. The axial length of one buckle showed a tendency to increase linearly with the ratio of thickness to radius of the tube. It was also showed that the crumpling mode transition from progressive buckling mode to dynamic plastic mode is affected by the stress-strain curve. The higher the work hardening modulus of the tube material, the more probably the tube will be wrinkled over the entire length.

Otubushin [35] gave a detailed validation of a non-linear finite element code simulating the dynamic axial crushing of a square tube. An isotropic elastic, linear strain-hardening material model was used in the Finite Element analysis and the strain-rate sensitive nature of mild steel was modelled using the Cowper-Symonds constitutive equation with coefficients suggested by Abramowicz and Jones [29], $D = 6844\ s^{-1}$, $q = 3.91$). The uniform symmetric collapse mode was displayed by both specimens in the analysis although the size of the layers of folds was less regular in the model with greater strain-hardening. The increase in hardening modulus also resulted in one layer of folds less in the collapsed specimen. Both FE models predicted the energy absorbed by, and the average strain, in a basic collapse element to within 5% of the previously available estimate. Two force versus time history graphs for the finite element analyses are given in Figure 2.7.

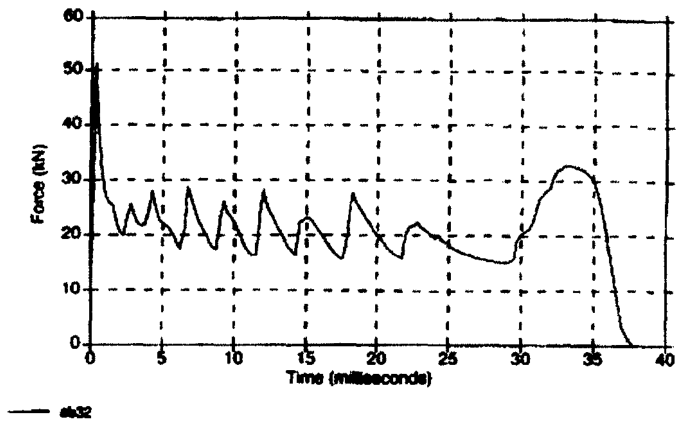

(a)

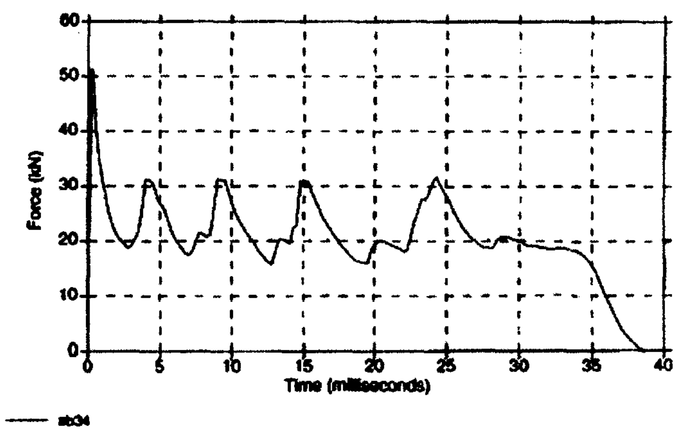

(b)

Figure 2.7: Force histories for the FE analyses: (a) E_t = 1000 N.mm^{-2} (b) E_t = 1400 N.mm^{-2} . [35]

Choong and Ramm [36] simulated the buckling process of shells by using the finite element method. From their computational work they noted that it is better to include damping in a non-linear dynamic analysis if one is to simulate a buckling process realistically. Although it is important to include damping in a non-linear Finite Element analysis of the buckling of tubes, one does not have to be too concerned with this if one is using ABAQUS, since ABAQUS automatically takes damping into account by including a damping factor. The study by Choong and Ramm revealed that they needed to carry out further investigations into a number of important points such as:

1. sensitivity of the final outcome of simulation against initial imperfections in structural shape and initial condition (type, magnitude, etc.).
2. the effects of a more refined finite element model and different loading conditions on the outcome of simulation.
3. a possible way to speed up the process of non-linear dynamic analysis.

Bathe, Walczak, Guillermin, Bouzinov and Chen [37] presented some advances in the capabilities of finite element packages such as ADINA, for the crush analysis of structures which require advanced analysis procedures. In their analyses they found that if an incremental static analysis is carried out, the solution indicates bifurcation points that in an explicit dynamic solution are not detected, because no stiffness matrix is calculated and the artificial effects mask these physical instabilities. They also listed further improvements which can be made in both static and dynamic analyses, namely increasing the efficiency of the contact algorithm, using higher-order shell elements and by making more effective use of parallel processing.

Bardi, Yun and Kyriakides [38] developed a finite element model of the axisymmetric progressive crushing of circular tubes and the results from the simulations were directly compared with experiments. The model was found to reproduce the crushing response to a significant degree of accuracy. The mean crushing load was essentially the same as in the experiments, the calculated wavelength of the folds were within a few percent from measured values as were other geometric variables considered. Thus the crushing energy per unit length was predicted to a very good degree of accuracy. In addition, the model was used to demonstrate that changes in the loading cycles which take place as the number of folds increases, are due to small differences between the inner and outer folds which in turn affect the self contact of the fold walls. The transition from axisymmetric to non-axisymmetric collapse and crushing was found to depend on the tube R / t and on the hardening characteristics of the material.

Three simpler models taken from the literature in which steady-state folding is modelled by kinematically admissible collapse mechanisms were critically reviewed by comparing predictions of key variables to measured variables. The three simpler models considered were mainly aimed at predicting the mean crushing load and the period of folding. The mean half wavelength ($\bar{w}$) of the fold and the mean load of the steady-state cycles ($\bar{P}$) are given below:

(a) Alexander (1960)

$$\frac{\bar{w}}{R} = 1.347\sqrt{\frac{t}{R}}$$

$$\bar{P} = \bar{\sigma}_0\, t^2\left[8.462\sqrt{\frac{R}{t}} + 1.814\right]$$

$\bar{\sigma}_0$ is the mean level of stress under the uniaxial stress-strain response (from the yield point up to failure)

(b) Singace (1995)

$$\frac{\bar{w}}{R} = 1.253\sqrt{\frac{t}{R}}$$

$$\bar{P} = \bar{\sigma}_0\, t^2\left[7.874\sqrt{\frac{R}{t}} + 1.408\right]$$

(c) Wierzbicki (1992)

$$\frac{\bar{w}}{R} = 1.853\sqrt{\frac{t}{R}}$$

$$\bar{P} = 11.22\,\bar{\sigma}_0\, t^2 \sqrt{\frac{R}{t}}$$

The models of Alexander and Singace under predicted the mean crushing load significantly while the model of Wierzbicki yielded values of engineering accuracy due to the more realistic folding mechanism assumed. The prediction of the period of folding was less successful for all three models.

Webb, Webster and Kormi [39] performed a finite element simulation of energy absorption devices under axial static compression and impact loading. Their study examined the response of thin square section columns to axial impact loading so that fracture propagated along the corner edges as the tube inverted. The results from quasi-static and dynamic axial loading cases were compared with reported experimental results by others.

Karagiozova, Alves and Jones [40] studied the inertia effects in axisymmetrically deformed cylindrical shells under axial impact. The final buckling shapes of a shell when subjected to equal impact energies, but resulting from different combinations of the striking mass and the initial velocities are shown in Figure 2.8. For a given impact energy the crushing distance increases with decreasing velocity.

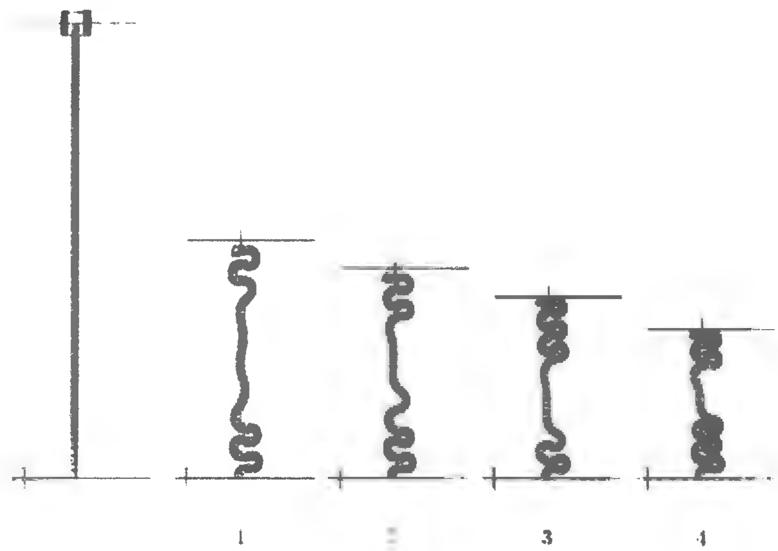

Figure 2.8: Final buckling shapes of a shell for an impact energy of 2.1 kJ and different combinations of the striking mass and the impact velocity: (1) G = 0.2485 kg, V_0 = 130 m/s (2) G = 2.625 kg, V_0 = 40 m/s (3) G = 42 kg, V_0 = 10 m/s (4) G = 262.5 kg, V_0 = 4m/s. [40]

The variation of the mean crushing force with a striking mass is shown in Figure 2.9.

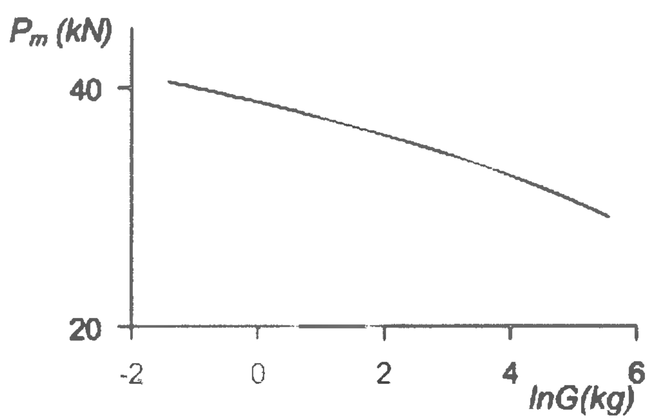

Figure 2.9: Variation of the mean crushing force with a striking mass. [40]

The above study revealed that the dynamic behaviour of cylindrical shells subjected to axial impact are both velocity and mass sensitive. A larger kinetic energy could be absorbed for higher-velocity impacts when decreasing the striking mass, because larger strains and stresses are accumulated in the shell during the initial compression phase. The compression of the shell develops intermittently throughout the entire response for a low velocity impact which causes a significant shortening of the shell. The shortening of the shell due to compression for a high velocity impact develops mainly during the initial phase of deformation before buckling commences. Thicker shells made of materials exhibiting large strain hardening characteristics tend to buckle in a dynamic plastic buckling pattern in contrast to the thinner shells, or shells made of materials with a smaller strain hardening, which buckle progressively, even for high velocity impacts.

Nannucci [41] performed a numerical analysis of the progressive buckling of thin-walled tubes under a dynamic axial impact load. Both thin-walled cylindrical and square tubes were examined under these conditions. Thick cylindrical tubes with a radius to thickness ratio of less than 40 – 45, approximately, deformed in the axisymmetric (or concertina) mode. In the case of square tubes, with an average width to thickness ratio of greater than 40.8, they deformed in the symmetric mode. The collapse modes predicted by the numerical analyses were the same as those predicted by theory and the results for the distance that the tube crushed under certain impact masses and initial velocities correlated well with theory in both the cylindrical and square tubes. The amount of energy that all of the tubes absorbed were also consistent with theory.

Nannucci, Marshall and Nurick [42] performed a computational investigation of the progressive buckling of square tubes with geometric imperfections. A numerical study of the effect of various triggers on the quasi-static progressive buckling of thin-walled square tubes was undertaken. Triggers considered were holes, indents and a combination of both. The model was successfully verified by comparison with existing experimental results. The boundary conditions were approximated by a fully built in condition, which was not strictly accurate. However, the deformation shapes reproduce by the numerical analyses were very similar to the experimental shapes. The buckling loads were 5%-10% lower the numerical analyses than were experimentally measured. However the trends observed were similar. Holes decreased the buckling load after some critical diameter was exceeded. The decrease in the load was linear with respect to the increasing hole diameter. Dents in the opposite sides of the tube reduced the initial peak by up to 40%. The drop was most marked for dents up to 2 mm, The numerical analyses showed a more rapid approach to a buckling load of 40 kN than was observed experimentally. In general triggers reduced the buckling load. While the holes decreased the wavelength of the first lobe, spherical indents increased the wavelength. A combination of triggers allowed control of the size of the wavelength.

Karagiozova and Jones [43] examined the crushing behaviour of aluminium and steel when subjected to an axial impact, using a numerical simulation. The influence of the material properties, shell geometry, boundary conditions and loading techniques on the energy absorbed and the buckling shape was explored. Various shell response characteristics, such as the peak load, fold lengths, axial compression and energy absorption were studied. The simulation of an axial impact of shells having various geometrical parameters showed that response of steel exhibited larger dynamic effects in comparison with aluminium ones due to the influence of material strain-rate sensitivity. The slenderness ratios h / L and h / R, together with the material properties, play an important role during the shell deformation. It was found that the fold length increases with increase of the shell thickness when keeping the cross-sectional area of the shell constant, whereas it is defined as a function of the product of h, R in the available analytical predictions. The lengths of fully developed folds were related to a particular shell geometry, but were virtually independent of the impact velocity. It was shown that the axial compression of the shell could reduce significantly the shell length available for folding. This compression depended on the shell geometry, but was only slightly affected by the impact velocity. An analysis of the shell response caused by different loading techniques and boundary conditions revealed differences in the response predictions when replacing an actual moving object striking a rigid wall by a stationary object struck by a mass, as found in laboratory conditions. An interpretation of data obtained usually in dynamic tests showed that an estimate of the energy absorbed from a filtered load –displacement history could lead to significantly lower values, particularly for high velocity impacts.

Wang and Lu [44] carried out both experimental and finite element simulations into the mushrooming of circular tubes under dynamic axial loading. When a tube is subjected to a severe dynamic axial load, the response would be a dynamic buckling one which may become quite different from a progressive one. Wrinkling will occur if the loading is severe enough. Both the experiments and the axisymmetric finite element model confirmed the effect of mushrooming in the axial dynamic crushing process of tubes with a relatively thick wall. It showed that various modes of deformation will emerge and they can be significantly different from those under a static or a low speed loading condition. Generally, three patterns of deformation may be expected: dynamic progressive folding for relatively thin tubes under a low impact speed, end mushrooming with folds formed at a distance from the striking end for all tubes at medium speeds, and mushrooming and wrinkling for thick tubes. For thick-walled tubes under high speed axial impact, Taylor's model [refer to 44] was found to be more appropriate as the dominant mode is lateral deformation at the striking end. The difference in the response between a thick-walled tube and a solid rod was the extensive fractures and splitting associated with a thick-walled tube. Direct correlation between the test results and simulations was difficult, mainly because the Finite Element code could not model the dynamic fracture failures. The lack of such modelling capacity in commercial finite element codes raised the question of their validity when used for simulations in the higher velocity domain. However, for low speed impact up to the range of 200-300 mm/s where cracks are not commonly present, the numerical analyses provided valid information.

2.4 DISCUSSION

Of the numerous papers mentioned in this literature review, only two papers refer to and mention eigenvalues of tubes, which is the main topic of discussion in this thesis, as this topic is relatively new and has not been widely researched. Nonetheless, the numerous papers researched by the author of this thesis provided him with a comprehensive knowledge of the theoretical behaviour of thin-walled tubes. This in turn enabled him with sufficient background and theoretical knowledge to progress on to newer and more complex aspects of thin-walled tube research, namely eigenmode analyses for the progressive buckling of thin-walled tubes.

3. TUBE BUCKLING AND EIGENMODE ANALYSIS THEORY

Sections 3.1 to 3.4 of this chapter cover the literature as given by Nannucci [42] on the theory of the buckling of thin-walled tubes. It provides a comprehensive summary with most of the information originally coming from Jones [47]. Section 3.5 of this chapter describes eigenmode buckling analysis theory which is the essence of this thesis. It gives a description of eigenmode buckling analysis theory in general, shows the first four buckling modes of flat square plates subject to in-plane loads, gives an example of an eigenmode buckling analysis to determine the exact shape and the critical load of a column and describes how the eigenvalues may be used to determine the corresponding buckling loads of tubes.

3.1 MODES OF BUCKLING

When thin-walled square and cylindrical tubes are crushed axially, they fail in a number of distinct buckling modes. These modes can be categorised into Euler buckling, Progressive buckling and Plastic buckling. In particular, these modes of buckling are influenced by tube length, diameter and wall thickness. These buckling modes are discussed in the following sections.

3.1.1 EULER BUCKLING

In Euler buckling, the tube bends in the same manner as a strut would under axial loading. As the tube begins to collapse, a plastic mechanism develops at a point in the tube which causes the tube to buckle in such a way that it folds over on itself. The longitudinal axes on each side of the hinge are thus no longer parallel with each other. Examples of Euler buckling can be seen in Figure 3.1.

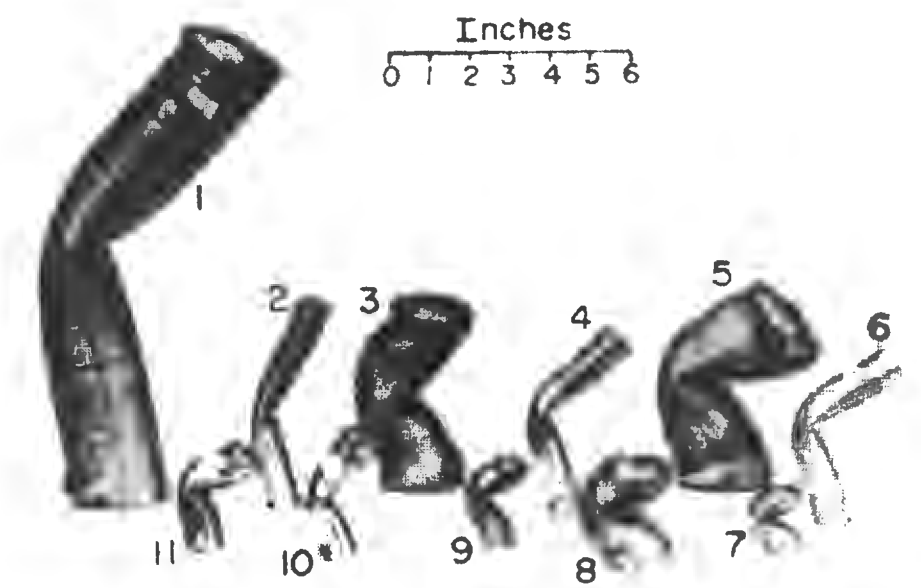

Figure 3.1: Typical examples of the Euler collapse mode. [45]

In Figure 3.2 , a typical load - displacement curve can be seen for a cylindrical tube which has failed due to Euler buckling. In this particular example, the aluminium cylindrical tube has a length of 38.1mm (1.5”), an internal diameter of 57.15mm (2.25”) and a wall thickness of 3.18mm (0.125”). These figures equate to a length / internal diameter ratio of 6.67 and a thickness / internal diameter ratio of 0.0556. The distance through which the tube absorbs a significant amount of energy is very small in comparison with the total length of the tube.

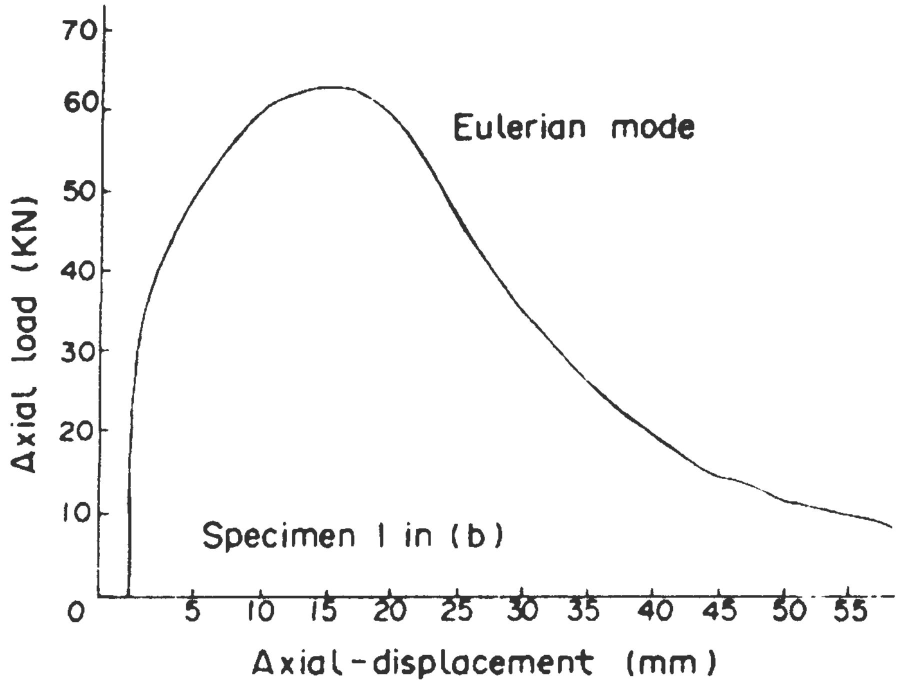

Figure 3.2: The load displacement curve for Euler Buckling of a thin-walled cylindrical tube. [45]

Andrews, England and Ghani [45] investigated the axial collapse of cylindrical tubes under quasi-static loading and found that Euler buckling occurs in tubes with large length to internal diameter and thickness to internal diameter ratios. This can be seen in Figure 3.3.

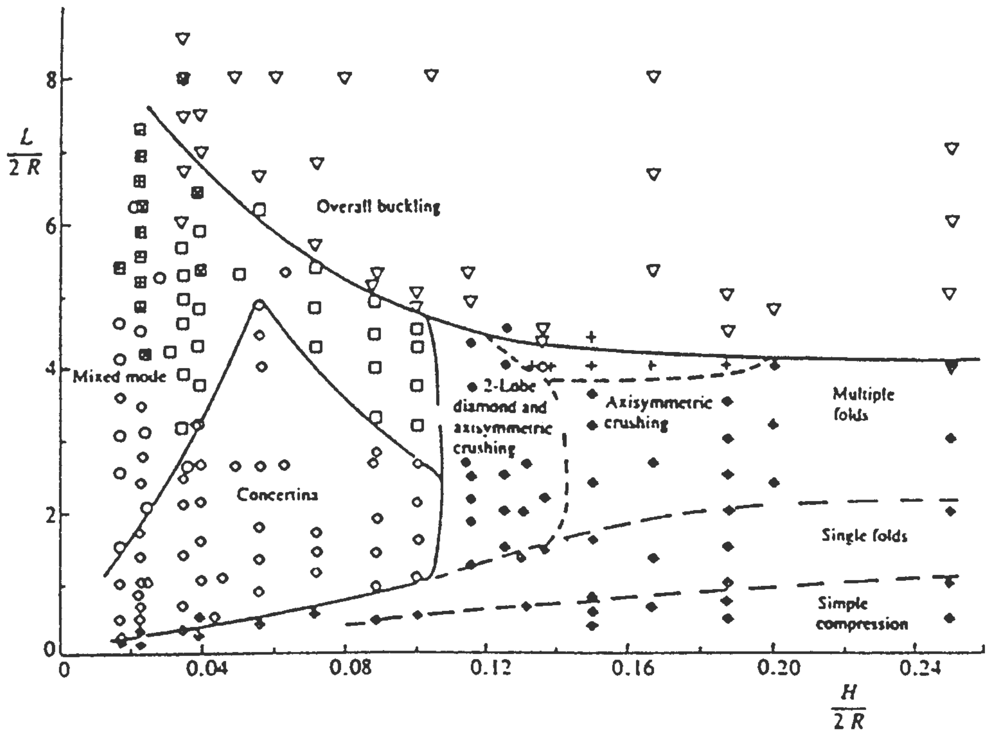

Experimental results: ▽: overall buckling. ◇: concertina. □: concertina + 2-lobe diamond. ○: concertina + 3-lobe diamond. ⊞: concertina + 2-lobe and 3-lobe diamond. ⊠: 3-lobe diamond. ⊕: concertina (axisymmetric) crushing. ◈: 2-lobe diamond crushing. +: crushing and tilting of tube axis.

Figure 3.3: Classification chart for the collapse modes of thin-walled aluminium alloy circular tubes subjected to static axial loads. [45]

Korneck [46] found, in his experimental work, that Euler buckling also occurs in thin-walled square tubes with large length to width ratios. This can be seen in Figure 3.4.

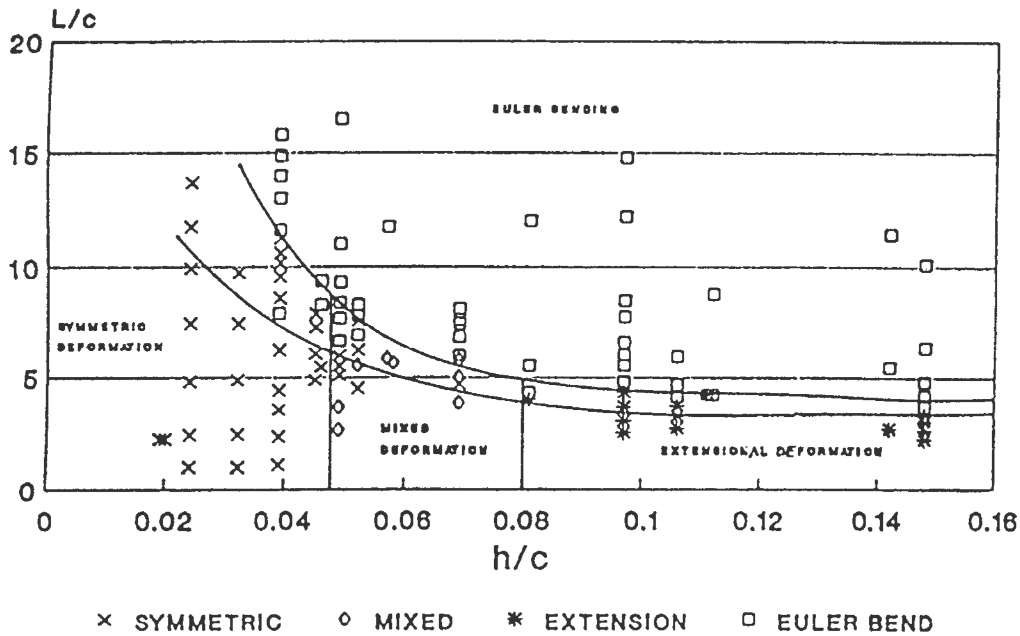

Figure 3.4: Classification chart for the collapse modes of thin-walled mild steel square tubes subjected to static axial loads. [46]

Jones and Abramowicz [29] performed a similar experimental study of the transition from global bending to progressive buckling of tubes, with both static and dynamic loading conditions. Square and cylindrical thin-walled mild steel columns were used with a variety of cross sections and lengths in order to encompass both progressive buckling and overall bending. The deformation maps for the square and cylindrical tubes crushed statically and dynamically can be seen in Figures 3.5 and 3.6. The transition points from bending to progressive buckling can also be seen in these figures.

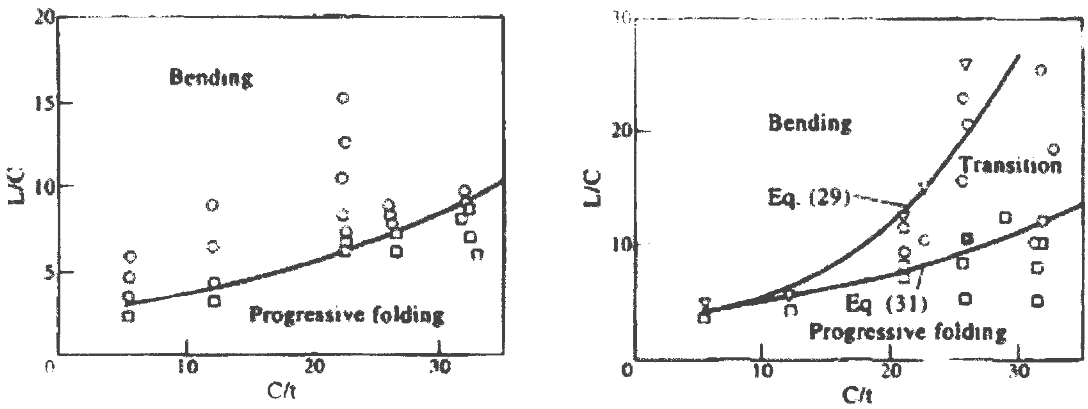

Figure 3.5: The deformation map for square columns (a) Quasi-static (b) Dynamic axial loading. [29]

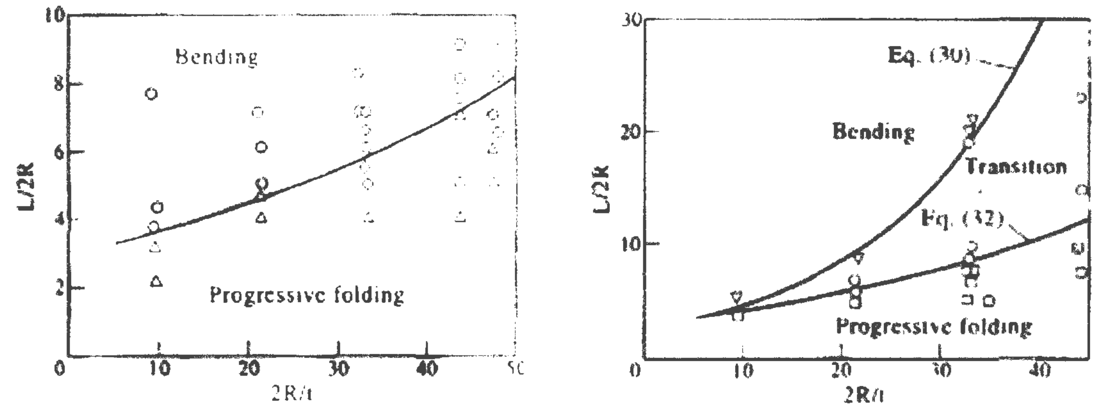

Figure 3.6: The deformation map for circular columns (a) Quasi-static (b) Dynamic axial loading. [29]

Euler buckling is not an efficient buckling mode for energy absorption as the energy absorption occurs in a small local position relative to the total length of the structure, and the effective stroke is very short. The construction of energy absorbers from thin-walled tubes should, therefore, be such that Euler buckling is avoided.

3.1.2 PROGRESSIVE BUCKLING

Local buckling in a tube, as opposed to global Euler buckling, is more likely to occur in a tube than in other structural members such as a strut due to its high torsional rigidity and to a much lesser degree due to its orthogonal stiffness as in the case of a structural I-beam member. When the load is a dynamic load we generally refer to the localised buckling as progressive buckling.

When a thin-walled tube, whether square or cylindrical, is subjected to an axial compressive load which exceeds the yield strength of the material, the tube starts to buckle.

A typical load deflection curve for the progressive buckling of a thin-walled square tube can be seen in Figure 3.7.

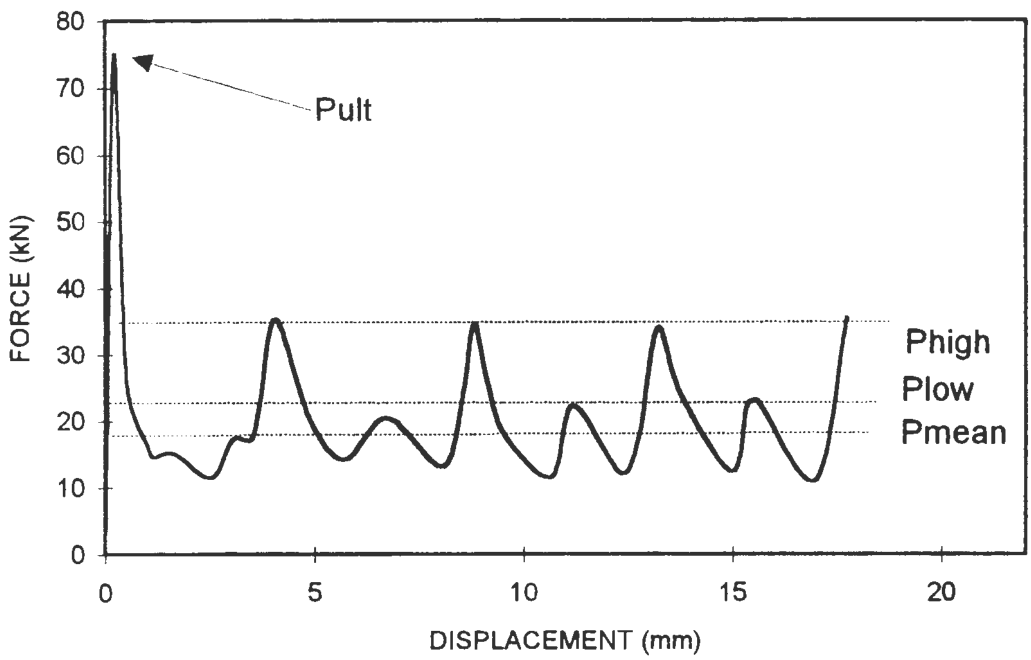

Figure 3.7: A typical load displacement curve for progressive buckling of a thin-walled square tube. [9]

After reaching the first peak load, it is evident that the tube exhibits a repetitive behaviour. The load carrying ability of the tube decreases to a minimum and then it increases again, and oscillates around a mean buckling force thereafter. It is evident from Figure 3.7 that the force displacement curve follows a repetitive pattern. Each pair of peaks can be associated with the formation of a complete buckle or lobe. Usually the development of these buckles or lobes starts at one end of the tube, and then progress sequentially along the length of the tube. This phenomenon is thus known as progressive buckling. This form of buckling has been described extensively by Jones and others [47, 48, 49].

When a tube collapses due to progressive buckling, a significant amount of energy is absorbed after the initial collapse of the tube (unlike Euler buckling), thus making progressive buckling of thin-walled tubes suitable for energy absorption.

3.1.2.1 DESCRIPTION OF THE VARIOUS MODES OF PROGRESSIVE BUCKING

When thin-walled cylindrical and square tubes buckle due to progressive buckling, they can buckle forming a number of different lobe shapes or deformation modes. These different buckling modes all have the same oscillatory force displacement curves, but their respective mean loads differ from mode to mode. Cylindrical and square thin-walled tubes have different deformation modes, so they will be dealt with separately. A more detailed analysis will follow later.

Deformation modes in Cylindrical Tubes

In the work of Abramowicz and Jones [49], two modes of deformation were distinguished for thin-walled cylindrical tubes. The progressive buckling results in either axisymmetric (concertina) deformation or non-axisymmetric (diamond) deformation. These modes can be seen in Figure 3.8.

i. Concertina mode - In this mode there are three stationary circumferential plastic hinges during the formation of one lobe. These plastic hinges form at the top, middle and bottom of the lobe and relate to the inner and outer extremes of the lobe once formed. The tube deforms to form ring shaped lobes along the length of the tube. (Figure 3.8 left)

ii. Diamond mode - In this mode the tube buckles progressively in such a way that a number of diamond shaped sections are formed around the circumference of the tube, which fold inwards in half over each other. This was first seen by Pugsley and Macaulay [18] (Figure 3.8 centre and right)

The effect of the initial tube geometry on the buckling modes can be seen in the classification chart for the collapse modes of thin-walled circular tubes (Figure 3.3).

Figure 3.8: Progressive buckling in thin-walled cylindrical tubes. The Axisymmetric mode is shown on the left and the non-axisymmetric mode is shown on the centre and right. [47]

Deformation modes in Square Tubes

Abramowicz and Jones [48] identified four distinct progressive buckling modes of failure for thin-walled square tubes, namely symmetric, asymmetric mixed collapse modes A and B, and the extensional collapse mode of failure.

i. Symmetric modes - This mode describes three different modes of deformation. All three modes, however, have identical crushing loads and energy absorption characteristics. The first case is where all four individual lobes in one layer move inwards. This is reminiscent of the axisymmetric mode of behaviour associated with the axial crushing of cylindrical tubes. The term symmetric is also used to describe the cases where in one layer two opposite lobes move inwards and two outwards, as well as the case where three lobes move inwards and one outwards.

ii. Asymmetric mixed collapse mode A - The first layer of lobes which forms is symmetric and then an asymmetric layer forms next. This sequence of lobe formation is repeated with the same pattern for further deformations. The second asymmetric layer consists of three lobes deforming outwards and one deforming inwards.

iii. Asymmetric mixed collapse mode B - This mode is similar to the asymmetric mixed collapse mode A, except that the asymmetric layer consists of two adjacent lobes deforming inwards and the other two deforming outwards.

iv. Extensional mode - In this mode of collapse all four lobes deform outwards. This collapse mode was not, however, observed by Abramowicz and Jones in their tests.

The effect of the initial tube geometry on the buckling modes can be seen in the classification chart for the collapse modes thin-walled square tubes (Figure 3.4). The different buckling modes can be seen in Figure 3.9.

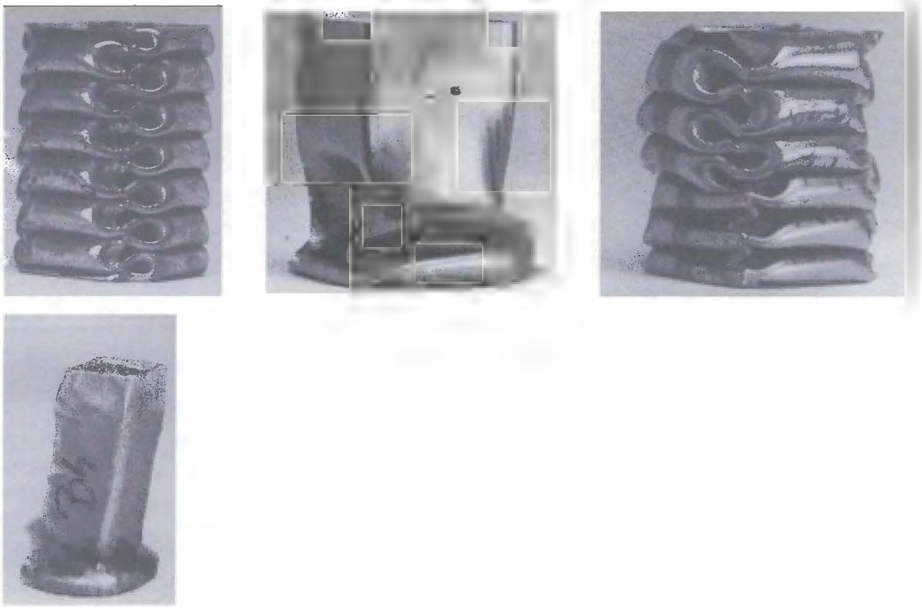

Figure 3.9: Progressive buckling in thin-walled tubes. These modes shown are symmetric, asymmetric mixed collapse modes A and B, and the extensional mode. [47]

3.1.3 DYNAMIC PLASTIC BUCKLING

In the case of dynamic progressive buckling of thin-walled tubes subjected to axial loads (as in the previous section), the impact loads were applied sufficiently slowly so that the inertia effects, both axial and lateral, of the tube did not have a significant effect on the buckling process. The duration of the impact loading was much longer than the time it took for an elastic stress wave to propagate along the length of the tube. This means that the tube was unable to support a mean dynamic axial load greater than the static value (ignoring the effects of strain rate sensitivity). The deformed profile of the tube is similar for both static and dynamic progressive buckling and these correspond well with experimental results [47].

When a thin-walled tube is subjected to a severe dynamic axial load, the structural inertia effects produce the phenomenon of dynamic plastic buckling.

The deformed shape of the tube is quite different from the dynamic progressive buckling as can be seen in Figure 3.10 for an axially loaded thin-walled cylindrical tube. The tube is wrinkled over the entire length of the tube when buckled dynamically compared with the dynamic progressive buckling where the buckling is confined to one end of the tube.

Figure 3.10: Dynamic plastic buckling. The permanent profile of an aluminium cylindrical tube subjected to an axial load. [47]

Generally, the influence of lateral inertia forces on the dynamic plastic buckling of structures favours lateral displacement of the structure with high mode numbers.

Dynamic plastic buckling is of great importance in industries such as the aerospace industry where for example dynamic buckling may arise from the sudden thrust of a rocket engine ignition. It is also relevant in the nuclear and petrochemical industries for safety devices.

The impact velocities associated with motor vehicle impact are much lower, and in these cases tubes would buckle due to dynamic progressive buckling.

3.2 PROGRESSIVE BUCKLING OF CYLINDRICAL TUBES

When a thin-walled cylindrical tube of mean radius R and thickness H is subjected to an axial force, it may deform either axisymmetrically or non-axisymmetrically. This is dependent on the ratio of the mean radius to the wall thickness. Various theoretical methods predict that thick tubes with a ratio of $R / H < 40 - 45$ deform axisymmetrically. Thinner tubes with larger values of R / H buckle in a non-axisymmetric mode [49]. Some tubes can develop both axisymmetric and non-axisymmetric (or diamond) buckles by switching during the crushing process.

A detailed analysis of the modes of buckling as well as the mean buckling load for thin-walled cylindrical tubes when crushed axially can be found in Jones [47] (pp 388 - 400). This analysis has not been included as the focus of this project was on the progressive buckling of thin-walled square tubes with various mechanical defects.

3.3 PROGRESSIVE BUCKLING OF SQUARE TUBES

The crushing behaviour of square tubes, because of the geometry, is more complicated than in the case of cylindrical tubes. The details of the analysis are more complex, as anticipated from pictures showing the axial crushing of square tubes in Figure 3.9. Wierzbicki and Abramowicz [50] identified and developed two basic collapse elements, known as type I and type II, as shown in Figure 3.11.

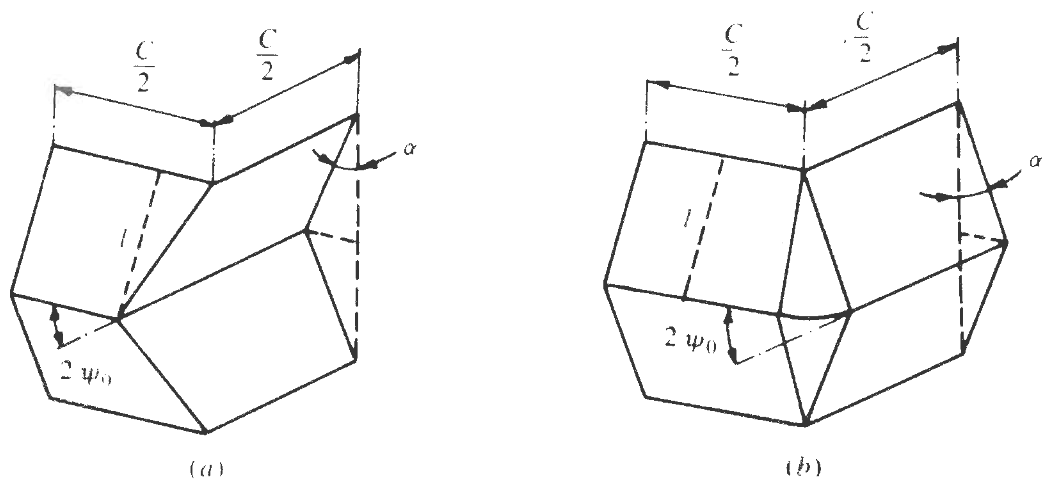

Figure 3.11: Basic collapse elements (a) Type I (b) Type II. [47]

These basic collapse elements have been used to examine the static progressive buckling of thin-walled square tubes with a mean width C and mean wall thickness H. These elements have also been used to study the dynamic progressive buckling of square tubes. From these two basic collapse elements, the four different progressive buckling collapse modes, as described in section 3.1.2.1, can be constructed. The various modes were created from these basic elements by either having one layer with four of these elements, or two layers with eight elements in the analysis. The symmetric mode of crushing, as can be seen in Figure 3.9, is idealised with four of the basic collapse elements, as shown in Figure 3.11 (a), for each layer of lobes. This crushing mode is predicted to form in thin-walled square tubes with a ratio of mean width to mean wall thickness greater than 40.8, approximately [11]. In the extensional mode of crushing, each layer of lobes is idealised with four of the type II collapse elements in Figure 3.11 (b). This type of progressive buckling is shown in Figure 3.11, and is predicted to form in thick square tubes with C / H < 7.5, approximately [51]. The asymmetric mixed collapse mode B type of progressive buckling is idealised as two layers of lobes having seven of the type I elements and one of the type II elements.

This type of crushing takes place within the range $7.5 \leq C / H \leq 40.8$ [51]. The difference between the theoretical buckling forces of the symmetric and asymmetric B modes is small, which means that either mode may develop in a tube with slight imperfections. The other mode of deformation is the extensional crushing mode, which has a slightly higher collapse force than the other three modes, but this mode was nonetheless observed by Abramowicz and Jones [48].

3.3.1 STATIC CRUSHING

The mean axial crushing force is important in the buckling of tubes from the aspect of being an energy absorber. The mean crushing force is used to approximate the total energy that a particular tube is able to absorb if it were crushed completely.

The effective crushing distance, found by Abramowicz [52], is used to predict the distance over which the crushing of the tube will occur. In order to predict the mean crushing force P_m, the internal energy consumed by four of the basic collapse elements in forming one complete layer of lobes is equated to the external work done by the mean axial crushing force. Abramowicz and Jones [48] found the mean crushing load P_m by minimising this expression. Abramowicz and Jones [53] thereafter developed the following expressions for the mean static crushing load using the type II collapse element:

3.3.1.1 SYMMETRIC MODE

$$\frac{P_m}{M_0} = 38.12\left(\frac{C}{H}\right)^{\frac{1}{3}} \qquad (3.1)$$

with $$\frac{l}{H} = 0.99\left(\frac{C}{H}\right)^{\frac{2}{3}} \tag{3.2}$$

where $$M_0 = \frac{\sigma_0 H^2}{4} \tag{3.3}$$

As can be seen in Figure 3.9, the lobes do not flatten completely during crushing, as was idealised in the theoretical analysis leading up to equation 3.1. It was shown in [48] that the effective crushing distance for the symmetric crushing of a square tube is

$$\frac{\delta_e}{2l} = 0.73 \tag{3.4}$$

which allows equation 3.1 to be re-written

$$\frac{P_m}{M_0} = 52.22\left(\frac{C}{H}\right)^{\frac{1}{3}} \tag{3.5}$$

3.3.1.2 ASYMMETRIC MIXED COLLAPSE MODE A

$$\frac{P_m}{M_0} = 42.92\left(\frac{C}{H}\right)^{\frac{1}{3}} + 3.17\left(\frac{C}{H}\right)^{\frac{2}{3}} + 2.04 \tag{3.6}$$

and $$\frac{l}{H} = 0.78\left(\frac{C}{H}\right)^{\frac{2}{3}} \tag{3.7}$$

3.3.1.3 ASYMMETRIC MIXED COLLAPSE MODE B

$$\frac{P_m}{M_0} = 45.90\left(\frac{C}{H}\right)^{\frac{1}{3}} + 3.17\left(\frac{C}{H}\right)^{\frac{2}{3}} + 1.02 \tag{3.8}$$

$$\frac{l}{H} = 0.78\left(\frac{C}{H}\right)^{\frac{2}{3}} \tag{3.9}$$

3.3.1.4 EXTENSIONAL MODE

$$\frac{P_m}{M_0} = 32.64\left(\frac{C}{H}\right)^{\frac{1}{2}} + 8.16 \tag{3.10}$$

and

$$\frac{l}{H} = \left(\frac{C}{H}\right)^{\frac{1}{2}} \tag{3.11}$$

3.3.2 DYNAMIC CRUSHING

The dynamic progressive buckling of square tubes is idealised as a quasi-static response. This means that the equations listed in the previous section predict the dynamic axial crushing force of a thin-walled square tube made from strain rate independent material.

The strain rate characteristics of materials play an important role in the dynamic plastic behaviour of structures. Experimental tests have been performed under axial and bending conditions in order to calculate the effect that strain rate has on the flow stress. Cowper and Symonds [47] suggested the constitutive equation

$$\dot{\varepsilon} = D\left(\frac{\sigma_0'}{\sigma_0} - 1\right)^q \text{, where } \quad \sigma_0' \geq \sigma_0$$

Where σ_0' is the dynamic flow stress at a uniaxial plastic strain rate $\dot{\varepsilon}$, σ_o is the associated static flow stress and D and q are constants relating to a particular material. Equation 3.12 can be rearranged as

$$\frac{\sigma_0'}{\sigma_0} = 1 + \left(\frac{\dot{\varepsilon}}{D}\right)^{\frac{1}{q}}$$

where D = 40.4 s^{-1} and q = 5, which are the standard Symond's values for mild steel. It is interesting to note that $\sigma_0' = 2\,\sigma_0$ when $\dot{\varepsilon}$ = D, regardless of the value for q. This means that for mild steel the dynamic flow stress is doubled at a strain rate of 40.4 s^{-1}, while for aluminium a strain rate of 6500 s^{-1} is required to double the flow stress. This means that aluminium can be treated as a strain rate insensitive material in most cases.

The equations for static crushing of square tubes in section 3.3.1 need to be modified to take into account these strain rate effects for dynamic axial crushing.

Since σ = F / A, and the area of the tube is considered to be constant during progressive buckling, the mean dynamic crushing load can be found by relating it to the mean static crushing load by substituting into equation 3.13:

Thus $$\frac{P_m'}{P_m} = 1 + \left(\frac{\dot{\varepsilon}}{D}\right)^{\frac{1}{q}} \tag{3.14}$$

Equation 3.5 thus becomes

$$\frac{P_m^d}{M_0} = 52.22\left(\frac{C}{H}\right)^{\frac{1}{3}}\left\{1 + \left(\frac{\dot{\varepsilon}}{D}\right)^{\frac{1}{q}}\right\} \tag{3.15}$$

for the symmetric mode of progressive buckling. It is difficult to make an accurate estimate of the strain rate $\dot{\varepsilon}$ in a square tube due to the complex deformation patterns when the tubes undergo progressive buckling.

Abramowicz and Jones [48] estimated a relation for the mean strain rate in the corner sections of a square tube as it buckles:

$$\dot{\varepsilon} = 0.33\,\frac{V_0}{C} \tag{3.16}$$

Substituting equation 3.16 into 3.15, the equation becomes

$$\frac{p_m^d}{M_0} = 52.22\left(\frac{C}{H}\right)^{\frac{1}{3}}\left\{1+\left(\frac{0.33\,V_0}{CD}\right)^{\frac{1}{q}}\right\} \tag{3.17}$$

Figure 3.12 shows the effect that strain rate effects have on the different modes of collapse.

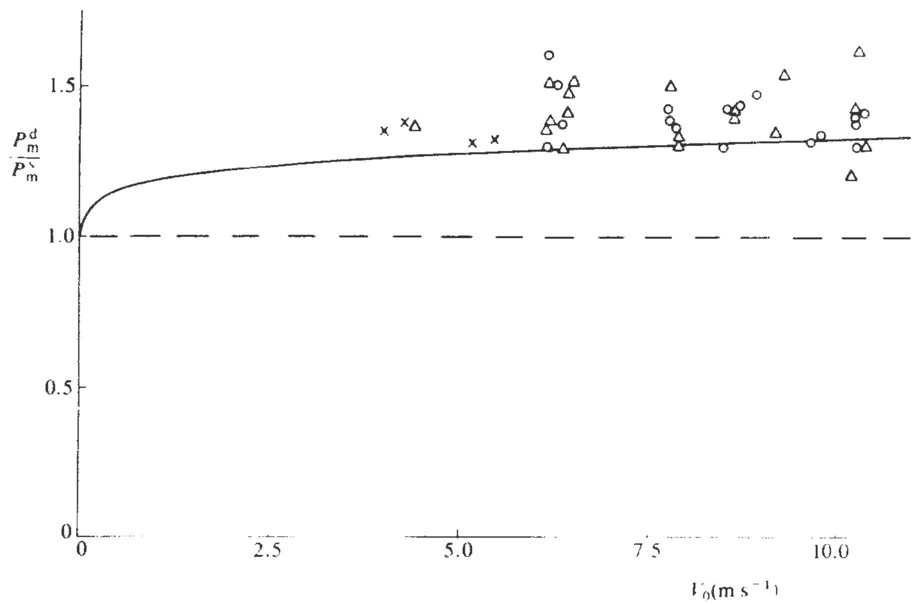

- - - - : Strain rate insensitive material

———: Equation 3.12 & 3.14 for a strain rate sensitive material with D = 6844 s^{-1} and q = 3.91.

Experimental results: O : Symmetric collapse mode. Δ : Asymmetric collapse mode. X : Wierzbicki et al

.

Figure 3.12: Variation of dynamic to static mean crushing force ratio with impact velocity for square tubes. C = 37.07 mm, H = 1.152 mm. [47]

As long as the strain rate effects are minimal, the difference between a static and dynamic test is related to the inertia forces set up at the instant of impact. This means that tests can be done statically and yet the same force displacement curve can be expected for the dynamic case as long as the strain rate effects are minimal.

3.3.3 ULTIMATE BUCKLING LOAD

The ultimate buckling load of a square tube, without any geometric imperfections, failing under static or dynamic progressive buckling is greater than the peak loads in the forming of subsequent lobes. This characteristic of tubes when buckling under progressive buckling can be seen in Figure 3.2. This ultimate buckling load can be approximated by

$$P_{ult} = \sigma_0 A \tag{3.18}$$

where σ_o is the plastic flow stress and A is the cross sectional area of the tube. Abramowicz and Wierzbicki found that the flow stress σ_o could be approximated by 92% of the ultimate tensile stress.

3.4 GEOMETRIC IMPERFECTIONS AND PERTURBING

As mentioned in the previous sections, when a perfect tube fails under progressive buckling, the initial peak force can be much greater than the subsequent peak forces. An ideal energy absorber is defined as one that absorbs energy at a constant rate. This means that it needs to deform at a constant force throughout the buckling process, which in turn means that it must cause uniform deceleration during the entire stroke. Attempts have thus been made to reduce this initial peak force by pre-denting the tube or including mechanical defects in the tube. Another important reason for wanting to introduce geometric imperfections into a thin-walled square or cylindrical tube is to force it to deform in a particular mode of failure. The best possibility would thus be a tube which deforms under progressive buckling with an initial peak force equal to the subsequent peak forces. This would result in an energy absorbing device which has an energy versus displacement curve which is almost linear.

It has been demonstrated that the inclusion of geometric imperfections affects the initial peak force. Langseth et al [54] performed a number of experiments on pre-dented thin-walled aluminium tubes. All the experiments were done on 80 mm square tubing with a wall thickness of 1.8 to 2.5 mm. It was found that the number of lobes formed in tubes with different material properties differed. Langseth attributed this to the fact that the effective crushing distance to form a complete lobe is a function of the hardening properties of the material. It was found that the thinner tubes deformed in a combination of symmetric and asymmetric modes, while the thicker ones (2.5 mm) deformed in the symmetric mode only. This is consistent with work done by Jones [47] as can be seen in Figure 3.4. Langseth also pre-dented a number of specimens statically. In Figures 3.13 and 3.14 the effect of pre-buckling on the dynamic force displacement curve is illustrated.

Figure 3.13: The effect of static pre-buckling. [54]

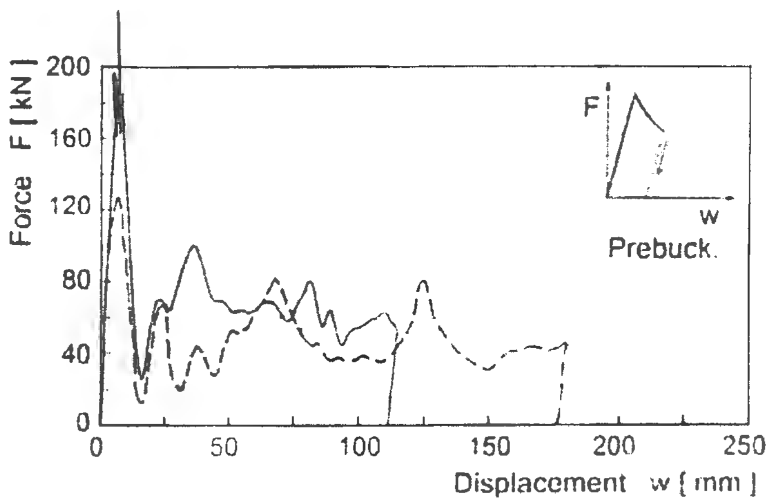

———————— : no pre-buckling, v_i = 17.33 m.s^{-1}

\- - - - - - - : with pre-buckling, v_i = 17.50 m.s^{-1}

Figure 3.14: The force displacement curve for an aluminium square tube. [54]

The peak load is reduced with the introduction of the static pre-buckling prior to the dynamic test. The total axial deformation is also increased compared to an initially straight tube. It was also found, that the magnitude of the first peak load could be controlled by varying the amount of static pre-buckling that was induced on the tube. In many actual situations where tubes are used as energy absorbers, the force may not be applied exactly axially to the tube. The tube may then buckle in the Euler mode rather than in the progressive mode. It has been found that by including a pre-dent or geometric imperfection in the tube the tubes are forced to follow the shape of the imperfection when buckling. By including geometric imperfections in the structure, one can force the tube to deform in a particular mode of failure, even if the tube's geometric ratios would normally cause it to deform in another mode of failure. In this way it may be possible to force a tube which normally deforms under Euler buckling to deform progressively, and at the same time the initial peak load can be decreased to the same level as subsequent peak forces.

3.5 EIGENMODE BUCKLING ANALYSIS THEORY

Since this thesis mainly concerns investigating the buckling of tubes, it was felt that it was necessary to give a brief overview of the theory of eigenmode buckling analysis.

3.5.1 EIGENMODE BUCKLING ANALYSIS THEORY FOR BUCKLING PROBLEMS IN GENERAL

Buckling problems are concerned with the calculation of the critical loads to cause elastic instability of a structure. The most frequently encountered example is buckling of a strut, where an increasing axial load suddenly causes a critical failure. Other examples include the buckling of plates and externally pressurized cylinders.

A theoretical analysis of buckling problems shows that they are eigenvalue problems, governed by the following equation:

$$([k] + \lambda[k_G]) \ \{U\} = 0 \qquad (3.19)$$

Where k_G is the geometric stiffness matrix, previously encountered with stress stiffening problems, λ is the eigenvalue related to the buckling load, and $\{U\}$ is the associated vector of nodal displacements describing the mode shape. According to the theory, there will be a number of buckling loads and mode shapes. Figure 3.15 (a - d) shows the first four buckling modes of a flat square plate subjected to in-plane edge loads.

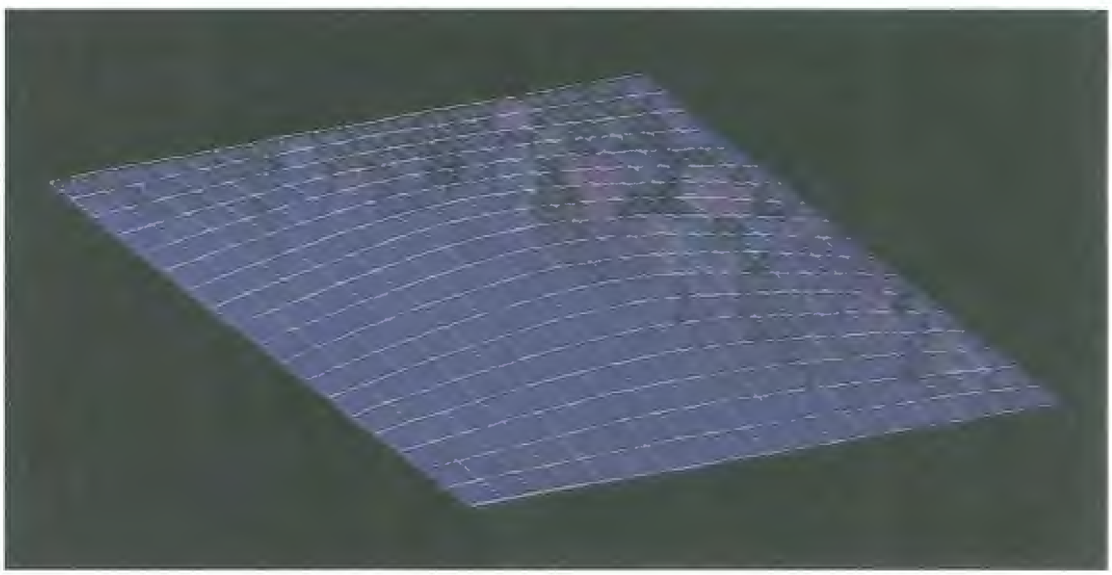

Figure 3.15 (a): The first buckling mode of a square plate simply supported on all four sides. [1]

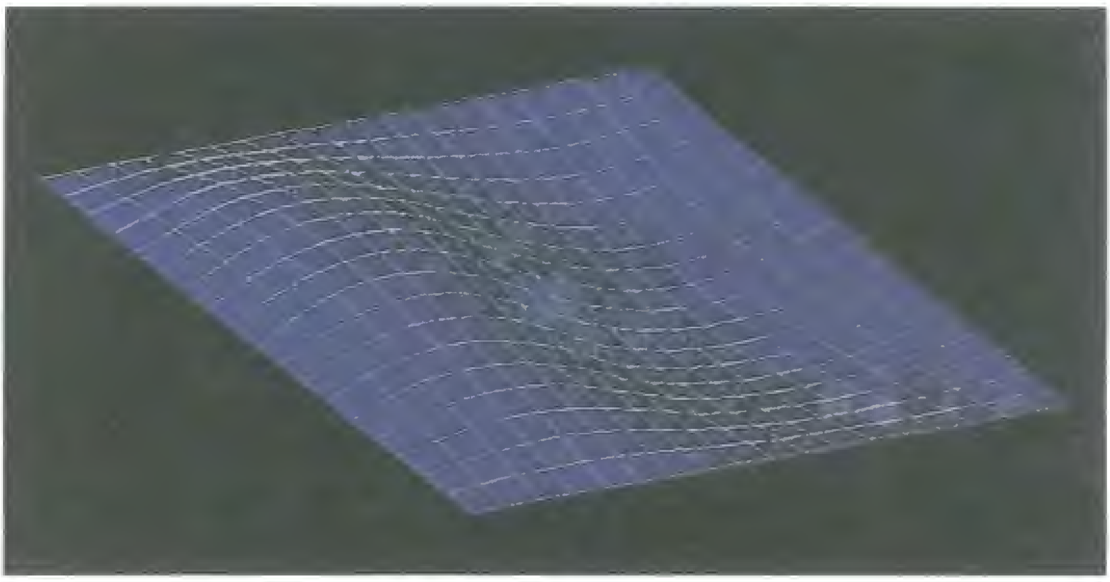

Figure 3.15 (b): The second buckling mode of a square plate simply supported on all four sides. [1]

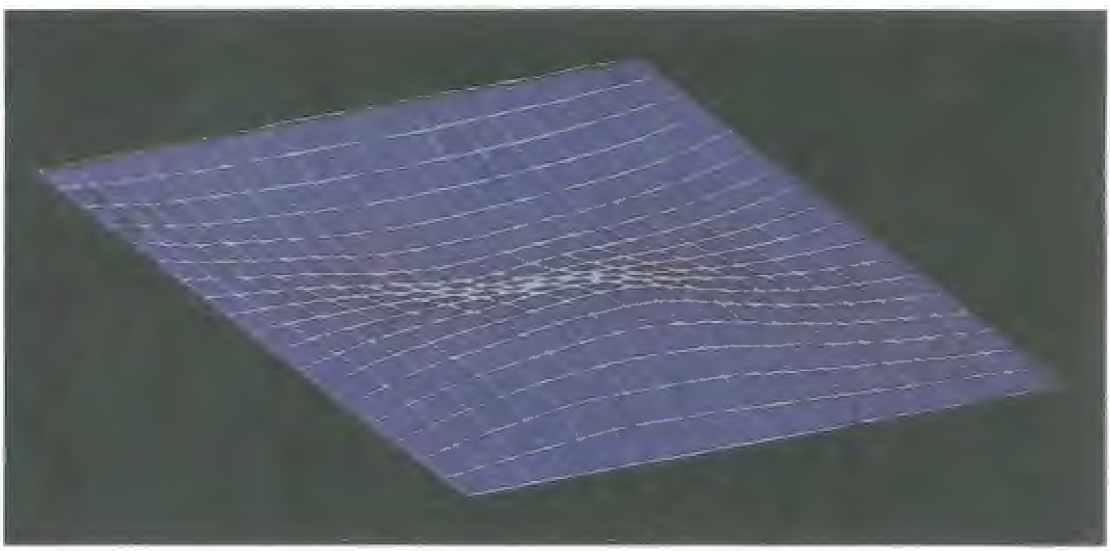

Figure 3.15 (c): The third buckling mode of a square plate simply supported on all four sides. [1]

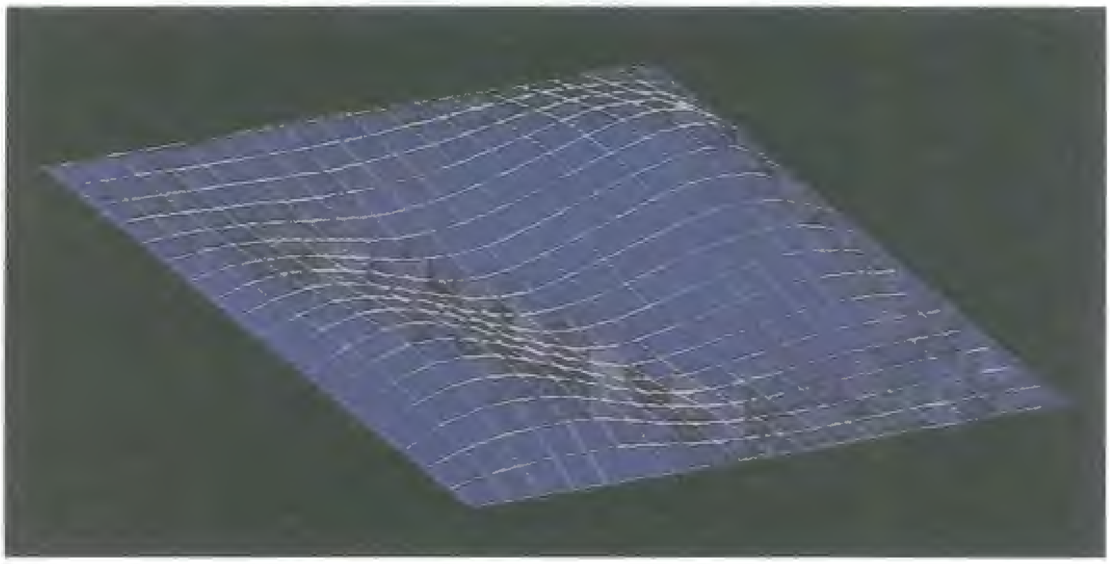

Figure 3.15 (d): The fourth buckling mode of a square plate simply supported on all four sides. [1]

Unfortunately, however, this method does not take account of any initial imperfections in the structure or component, and the results rarely agree with those determined in practice. For the square plate, the buckling loads will not be correct unless the plate is perfectly flat, and the loads are applied exactly in the plane of the plate. Therefore, instead of the load-deflection graph being similar to that illustrated in Figure 3.16 (a) it is more likely to be of the type shown in Figure 3.16 (b).

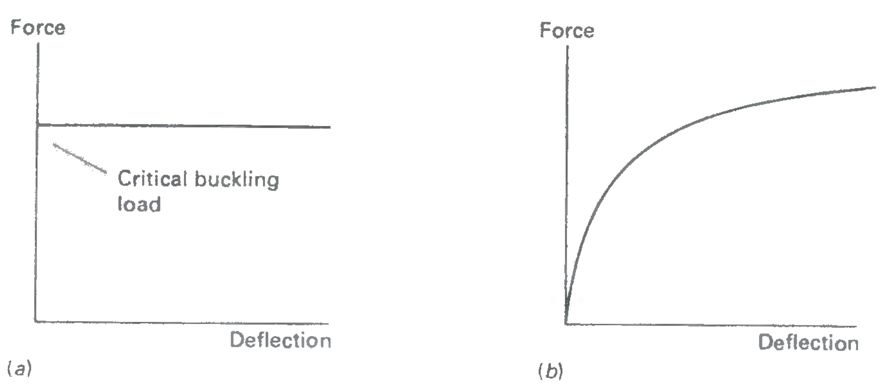

Figure 3.16: Load-deflection graphs defining buckling: (a) idealized behaviour (b) actual behaviour. [1]

Thus a sudden buckling is unlikely to occur. Instead of using equation 3.19 buckling problems should be solved by a large-displacement static analysis, possibly with stress stiffening. Using a large-displacement analysis, buckling can be detected by the change of displacement at any node. If the displacement change is increasing, the load is above critical and buckling is occurring. If the change is decreasing, the load is below the buckling load.

The eigenvalue method of solution of buckling is usually approximate and overestimates the buckling load, i.e. produces unsafe answers. It also gives no information about the post buckling behaviour. A large displacement analysis, on the other hand, is accurate and does give the complete behaviour of the complete component before and after buckling. Besides an eigenvalue method of solution (an eigenmode buckling analysis), a large displacement analysis is also undertaken in this thesis.

3.5.2 EIGENMODE BUCKLING ANALYSIS OF A COLUMN

An example is given on the next page of a 2-dimensional eigenmode buckling analysis of a column using Euler buckling theory. The example is given to illustrate eigenmode buckling analysis. Equations for a 3-dimensional eigenmode buckling analysis for a tube, such as the tubes in this thesis, could be theoretically derived, but this is beyond the scope of this thesis as the equations are both considerably complex and time consuming to derive. In practice, one would resort to numerical methods such as the Finite Element Method or the Boundary Element Method. For the purposes of this thesis, the Finite Element Method was used and in particular the ABAQUS Finite Element software package was used.

3.5.2.1 FORMULATION OF AN EIGENMODE BUCKLING ANALYSIS TO DETERMINE THE EXACT BUCKLING MODE SHAPE AND THE CRITICAL LOAD OF A COLUMN

The governing differential equation for an axially compressed column subject to an axial compressive load P and a transverse load f(x) is given by

$$\frac{d^2}{dx^2}\left[EI\frac{d^2w}{dx^2}\right]+P\left[\frac{d^2w}{dx^2}\right] = f(x) \tag{3.20}$$

To determine the critical load P_n , using equation (3.20) we set the transverse load equal to zero, f(x) = 0, to obtain

$$\frac{d^2}{dx^2}\left[EI\frac{d^2w}{dx^2}\right]+P\left[\frac{d^2w}{dx^2}\right] = 0 \tag{3.21}$$

The general solution of which is given by

$$w(x) = C_1 \sin (kx) + C_2 \cos (kx) + C_3\, x + C_4 \tag{3.22}$$

where

$$k^2 = \frac{P}{EI} \tag{3.23}$$

and the constants C, are determined from the boundary conditions.
For a simply supported column, the boundary conditions w(0) = 0; w(L) = 0 and BM(0) = 0 result in C2 = C3 = C4 = 0 and the condition BM(L) = 0 gives

$$C_1 \sin (kL) = 0 \tag{3.24}$$

For a non-trivial solution, (i.e. $C_1 \neq 0$) we have

$$\sin (kL) = 0 \tag{3.25}$$

which is the buckling equation for the column. The equation is satisfied for

$$kL = n\pi \qquad \text{for } n = 1, 2, 3, \ldots \tag{3.26}$$

Substituting back in to equation 3.23, we obtain the buckling loads

$$k^2 = \frac{P}{EI} \qquad \therefore \quad \left(\frac{n\pi}{L}\right)^2 = \frac{P}{EI} \qquad \text{for } n = 1, 2, 3, \ldots \tag{3.27}$$

$$P_n = \frac{n^2\pi^2 EI}{L^2} \qquad \text{for } n = 1, 2, 3, \ldots \tag{3.28}$$

The buckling mode shapes are

$$w(x) = C_1 \sin(kx) \tag{3.29}$$

$$= C_1 \sin\left(\frac{n\pi}{L}x\right) \qquad \text{for } n = 1, 2, 3, \ldots \tag{3.30}$$

The first three buckling modes and associated loads are shown in Figure 3.17.

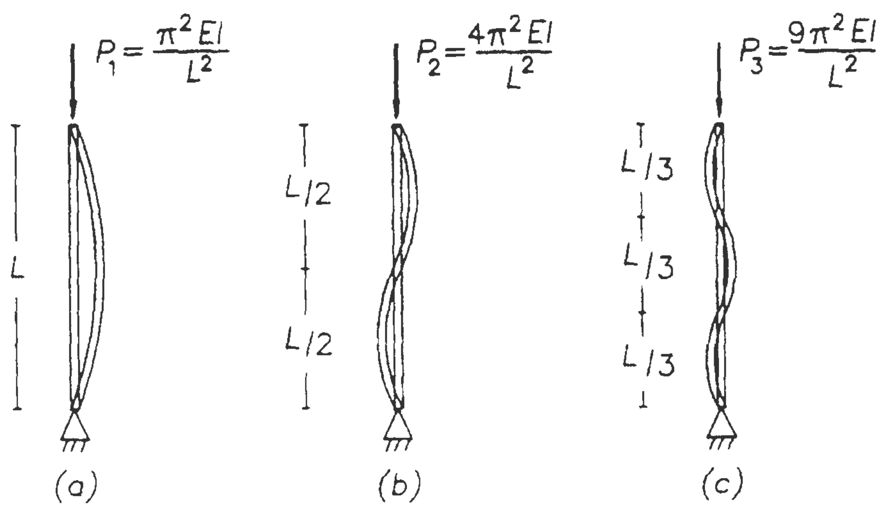

Figure 3.17: Buckling Loads and Mode Shapes: (a) First (b) Second (c) Third. [3]

3.5.3 USE OF EIGENVALUES TO DETERMINE THE CORRESPONDING BUCKLING LOADS OF TUBES

One of the many uses of an eigenmode buckling analysis is that the calculated eigenvalues can be used to determine the corresponding buckling loads of a structural member under a compressive loading and in particular the eigenvalues calculated for a tube can be used to determine the corresponding buckling load of the tube by the following general equation.

$$\text{Corresponding buckling load} = \lambda * \text{The applied load} \tag{3.31}$$

where

λ is the associated eigenvalue, related to the buckling load

Because this is a general equation it may be applied to all buckling analyses in general and therefore to tubes specifically. The application of this equation to tubes investigated in this thesis will be discussed in more detail later.

4. THE FINITE ELEMENT MODEL

4.1 INTRODUCTION

With a finite element program, such as ABAQUS, many problems which are otherwise too difficult to solve, are solved quite trivially. Numerical analyses should, however, always be confirmed by experimental analyses or other methods. The tube models in this thesis were first compared and confirmed with the models undertaken by Nannucci [42], who verified his models experimentally. Since the models in this thesis compared very well to Nannucci's [42] models, it was therefore unnecessary to perform further experimental tests. The very slight differences between the two models can be attributed to the material properties used in this model as they are more current and accurate than the ones used by Nannucci [42], because they include temperature effects. Due to the fact that the model was loaded quasi-statically under relatively low strain rates, adiabatic effects are therefore not relevant and were therefore not included in the model.

The initiation of buckling for a high velocity impact is sensitive to the material properties, particularly to the strain hardening modulus. The combination of the plastic wave speed, which is determined by the hardening modulus and inertia properties of a shell, leads either to dynamic plastic buckling (when the entire length of the tube participates in the buckling process) or to dynamic progressive buckling. Shells made of strain rate sensitive materials always buckle progressively. Buckling starts either from the impacted end due to the relaxation properties of the material causing strain localisation near this particular end, or from the distal end due to the increased strains caused by the reflected stress wave. This thesis is focussed only on the progressive buckling of tubes.

When a square tube, having a mean width (C) and a wall thickness (H), buckles progressively, depending on the mean width to wall thickness ratio, either the two opposite sides can fold outwards and the other two opposite sides can fold inwards (referred to by Jones [47] as a Type I collapse mode), or all four sides can fold outwards and then fold inward (referred to by Jones [47] as a Type II collapse mode). In order to predict the collapse mode (the type of folding i.e. whether the sides of the tube fold outward or inward relative to each other) of a square tube, Jones formulated an equation which states that the Type I collapse mode will occur in thin tubes when $C/H > 40.8$ and the Type II collapse mode will occur when $C/H < 7.5$. As far as it is known from the literature, no theoretical equations have been formulated for other types of polygon shaped tubes, such as triangular and hexagonal tubes, etc., to predict the collapse modes.

The investigation of the collapse modes of these triangular and hexagonal tubes, etc. fold outward became a major part of this thesis and the author decided to use a numerical method, namely ABAQUS to investigate this. The numerical investigation of the tubes using ABAQUS consisted of a two step process. Firstly, an eigenmode buckling analysis was performed using ABAQUS / Standard to determine the eigenmodes and the associated eigenvalues of the tube. Secondly, the eigenmodes calculated using ABAQUS / Standard were then used as imperfection factors to perturb the mesh in ABAQUS / Explicit for the tube crushing analysis.

In Nannucci's [42] tube models, he did not make use of an eigenmode buckling analysis to calculate the imperfection factors for perturbing, but used a more simplified approach by introducing arbitrary imperfection factors at the end of the tubes, in the form of an arbitrary curvature and with an approximate displacement. In order to determine the collapse mode of square tubes Nannucci [42] relied upon the two equations given by Jones [47] for square tubes to predict the collapse mode.

The use of arbitrary imperfection factors has two major disadvantages:

1. It can lead to errors in the model, particularly by the over or under estimation of the first peak reaction force and to a lesser extent to the subsequent peak reaction forces.

2. It does not predict the type of folding. One therefore has to rely on equations to predict the type of folding such as the one formulated by Jones for square tubes. If one does not use these equations to check the model, or in cases were there are no equations such as for triangular and hexagonal tubes, etc. then the ABAQUS analysis can proceed incorrectly with incorrect folding of the sides of the tubes. One can then resort to performing an eigenmode buckling analysis on the tube to determine the eigenmodes, or else one can resort to some other method such as experimental verification to check the type of folding so that the ABAQUS analysis can proceed correctly with the correct folding of the sides of the tubes.

For this thesis, three types of imperfection factors determined from the eigenmode buckling analysis in ABAQUS/Standard were used, namely:

- Multiple imperfection factors
- Single imperfection factors, and
- No imperfection factors, i.e. no perturbing

4.2 ABAQUS OVERVIEW

The ABAQUS / Explicit finite element code was used in all the numerical analysis for this thesis. Explicit integration is particularly well suited to dynamic problems where the process takes place in a small time interval, as in the case of progressive buckling of thin-walled tubes. This method of analysis also simplifies the treatment of contact, which, in this case takes place as the tube buckles and the lobes formed come into contact with one another.

The ABAQUS / Explicit analysis is based upon the implementation of an explicit integration rule together with the use of diagonal element mass matrices. The equations of motion for the body are integrated using the explicit central difference integration rule.

$$\dot{u}^{i+1/2} = \dot{u}^{i-1/2} + \frac{\Delta t^{i+1} + \Delta t^{i}}{2}\,\ddot{u}^{i} \tag{4.1}$$

$$u^{i+1} = u^{i} + \Delta t^{i+1}\,\dot{u}^{i+1/2} \tag{4.2}$$

The method is explicit in that the current state is calculated based solely on values from the previous increment and is computationally simple. The key to the computational efficiency of the explicit procedure is the use of the diagonal element mass matrices, because the accelerations at the beginning of each increment can be computed using the diagonal lumped mass matrix, the applied load vector and the internal force vector. Using these diagonal or 'lumped' mass matrices, the accelerations at the start of a new increment are computed by

$$\ddot{u}^{i} = M^{-1}\left(F^{i} - I^{i}\right) \tag{4.3}$$

where M is the diagonal lumped mass matrix, F is the applied load vector and I is the internal force vector. Thus the explicit procedure requires no iterations and thus no tangent stiffness matrix.

The explicit procedure integrates through time by using small time increments. The central difference method is conditionally stable and is governed by the size of the time steps in integration. This time limit is given in terms of the highest eigenvalue in the system as

$$\Delta t \le \frac{2}{\omega_{max}} \qquad \text{without damping} \tag{4.4}$$

$$\Delta t \le \frac{2}{\omega_{max}}\left(\sqrt{1+\varepsilon_{max}^{2}} - \varepsilon_{max}\right) \qquad \text{with damping} \tag{4.5}$$

where

ω_{max} = highest frequency of system

ε_{max} = fraction of critical damping in highest frequency mode

The size of the stable time increment can be estimated as the shortest time it would take a dilatational wave to travel across any element in the mesh by

$$\Delta t \approx \frac{L_{min}}{c_d} \qquad \text{where} \qquad c_d = \sqrt{\frac{\hat{\lambda} + 2\hat{\mu}}{\rho}} \qquad (4.6)$$

In equation 4.6, L_{min} is the smallest element dimension in the mesh and c_d is the dialational wave speed of the material given in terms of Lame constants $\hat{\mu}$ and $\hat{\lambda}$ and the material density ρ.

In many cases this estimate is not conservative (safe) and the actual stable time increment chosen by ABAQUS / Explicit will be less than the estimate by a factor between $\frac{1}{\sqrt{2}}$ and 1 in a two-dimensional model and between $\frac{1}{\sqrt{3}}$ and 1 in a three-dimensional model. Thus the performance of the code is very dependent on mesh design, as even a single element of smaller dimension than the next largest will lead to a considerable increase in solution time.

Convergence in ABAQUS / Explicit is not implemented after each time increment, thus the time stepping in the explicit scheme is very small to maintain accuracy. Thus the explicit scheme is suited for short duration and high-speed dynamic events.

4.3 DESCRIPTION OF THE TUBE GEOMETRIES

The model involved the progressive buckling of thin-walled tubes under quasi-static loading conditions. Geometric perturbations were included in the model in order to establish what effect these imperfections have on the forces when the tube buckles, however not all of the models had geometric perturbations included in them. The geometric perturbations consisted of sinusoidal-like indents along the length of the tube. The exact shapes for the geometric perturbations were calculated by performing an eigenmode buckling analysis using ABAQUS / Standard. Both the eigenmodes i.e. modal shapes (used for the perturbations) and the corresponding eigenvalues were calculated. For this thesis, only the first 10 eigenmodes and their corresponding eigenvalues were determined and studied, as 10 eigenmodes were felt to be of sufficient quantity.

For this thesis, square tubes, circular tubes, hexagonal tubes and triangular tubes were investigated, but square tubes were mainly focused on in the most detail. Although the tube geometries were varied, for comparative purposes the perimeter lengths of the different tube geometries were kept constant, namely 200 mm. The lengths of the tubes were all equal in length and were all 300 mm long. The tube dimensions were:

Square Tube

Mean width, C	50 mm x 50 mm
Wall thickness, H	1.2 mm
Tube length	300 mm

Circular Tube

Radius	31.8 mm
Wall thickness	1.2 mm
Tube length	300 mm

Hexagonal Tube

Side length	33.3 mm
Wall thickness	1.2 mm
Tube length	300 mm

Triangular Tube

Side length	66.7 mm
Wall thickness	1.2 mm
Tube length	300 mm

4.4 MATERIAL PROPERTIES

The material model of the tubes incorporates yield hardening, stain rate sensitivity and temperature dependence. The known material properties for the tubes can be seen in Table 4.1 Young's Modulus, Poisson's ratio and the uniaxial tensile yield strength of the steel were obtained from quasi-static uniaxial tensile tests and were also obtained, along with the density, at room temperature.

Table 4.1: General material properties for steel tubes.

Young's modulus, E	200 GPa
Yield Strength, σ_0	250 Mpa
Poisson's ratio, v	0.3
Density, p	7850 kg/m^3

4.4.1 YIELD HARDENING

The material model being used incorporates the von Mises yield criterion with isotropic hardening and can be used when rate-dependent effects are important. Isotropic hardening is the type of hardening selected as the steel displays significant yield hardening and therefore cannot be considered to be perfectly plastic.

The elastic region is described by Young's modulus. However, for the plastic region, true stress and logarithmic plastic strain data are required. For an isotropic material, nominal stress-strain data can be determined from uniaxial tests. This can then be converted to true stress and logarithmic plastic strain by the following equations:

$$\sigma_{true} = \sigma_{nom}(1+\varepsilon_{nom}) \qquad (4.7)$$

$$\varepsilon_{ln}^{pl} = \ln(1+\varepsilon_{nom}) - \frac{\sigma_{true}}{E} \tag{4.8}$$

where σ_{true} = true stress

σ_{nom} = nominal stress

ε_{nom} = nominal strain

ε_{ln}^{pl} = logarithmic plastic strain

E = Young's modulus

A graph of the true stress and logarithmic plastic strain for mild steel is shown in Figure 4.1.

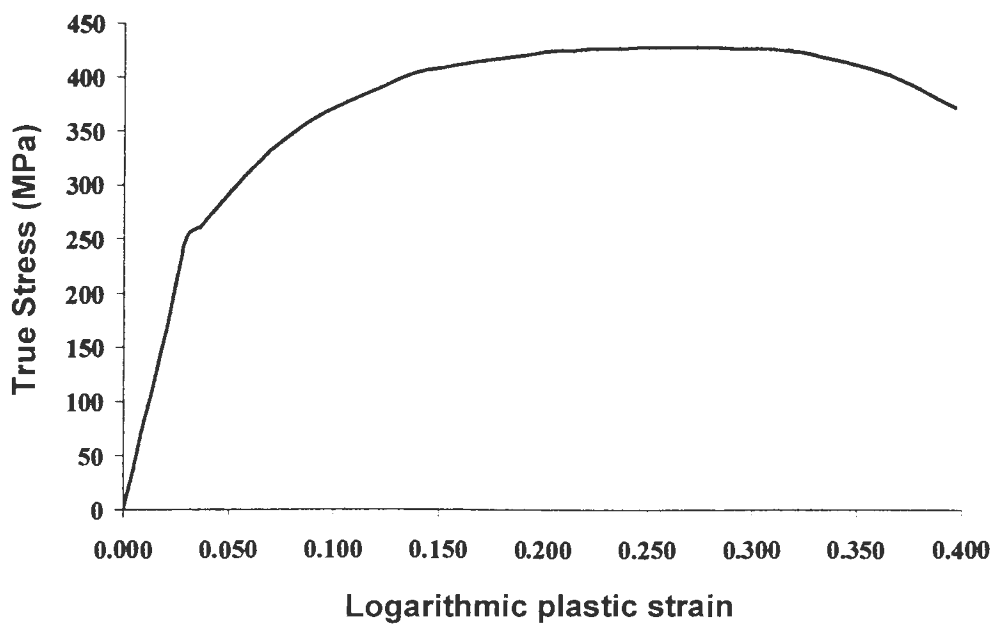

Figure 4.1: Graph of True Stress versus Logarithmic Strain.

4.4.2 STRAIN RATE

As strain rate increases most metals show an increase in yield stress. Mild steel typically exhibits linear elastic and isotropic strain hardening plastic behaviour with significance dependence on strain rate. Hardening as a result of the strain rate effect was modelled using the Cowper-Symonds relation shown in equation 4.9.

$$\frac{\sigma_0^1}{\sigma_0} = 1 + \left(\frac{\dot{\varepsilon}}{\dot{\varepsilon}_0}\right)^{\frac{1}{\eta}} \quad (4.9)$$

where σ_0^1 = Dynamic yield stress

σ_0 = Static yield stress

$\dot{\varepsilon}$ = Strain rate

$\dot{\varepsilon}_0 = 40.1\ s^{-1}$ (material constant for mild steel)

$\mu = 5$ (material constant for mild steel)

4.4.3 TEMPERATURE DEPENDENCE

Heat is generated from plastic work which causes the degradation of material properties. ABAQUS / Explicit allows adiabatic stress analysis to be performed where heat is generated by the plastic strain. In order to model the tubes as accurately as possible it was therefore decided to incorporate temperature dependent properties into the numerical model. This was not done however in earlier attempts to model tubes by Nannucci [41, 42], in his model. Masui, Nunokawa and Hiramatsu [55] reported the temperature dependence of Young's modulus and yield stress for mild steel, as shown in following equations.

$E = 207x10^9 - 58.34x10^6.T$ for $T \leq 600\ ^0C$ [4.10]

$E = 3.1x10^5 \cdot (T - 1100) + 97x10^9$ for $600\ ^0C < T \geq 1100\ ^0C$ [4.11]

$\sigma_0 = \sigma_{y0}$ for $T \leq 700\ ^0C$ [4.12]

$\sigma_0 = \sigma_{y0} \cdot [1 - 0.00178 \cdot (T - 200)]$ for $200\ ^0C < T < 700\ ^0C$ [4.13]

The static yield stress as a function of temperature is shown in Figure 4.3. In this case, the yield stress remains constant until the temperature reaches 200 ^{0}C, at which point it decays at a rate of 449 kPa / ^{0}C, (gradient of curve) until the temperature reaches 700 ^{0}C. From 700 ^{0}C to 1000 ^{0}C, the yield stress further decreases but at a slower rate of 100 kPa / ^{0}C, (gradient of curve).

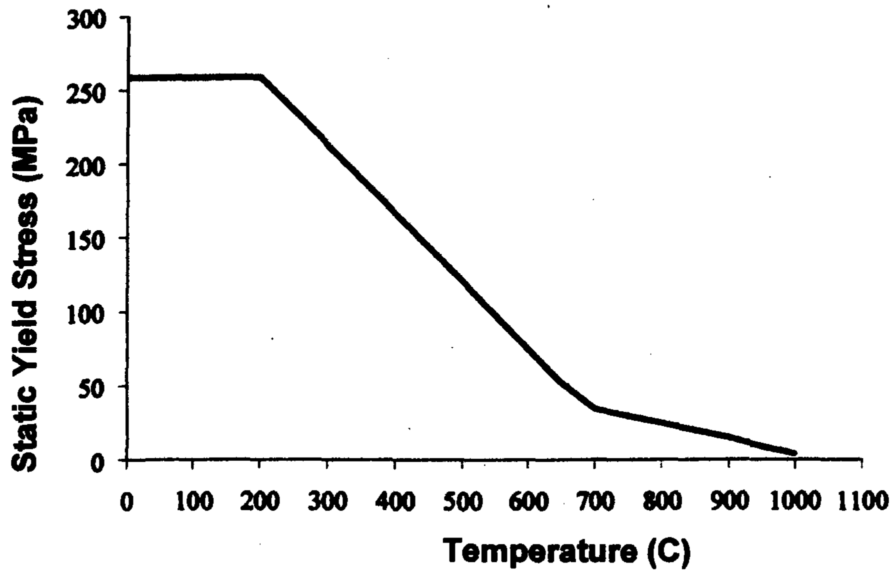

Figure 4.3: Graph of Yield Stress versus Temperature.

4.5 ELEMENTS USED AND MESH DETAILS

ABAQUS, like other finite element packages, models the real situation by dividing the model into numerous small elements, which contain information and assumptions about the properties of the model. Each model is made up of a grid of nodes upon which the element displacement is dependent.

An ideal model must have sufficient elements to accurately describe he model history and also be able to minimise these elements to reduce computational expense. Another constraint on the model is the aspect ratio, the ratio between the longer and shorter dimensions of an element. If the aspect ratio exceeds by a factor of four, the element is considered excessively distorted and the analysis will be terminated.

Quadrilateral shell elements were used to build up the models of the tubes for the numerical analysis. The element type S4R (a 4-noded element) is a general shell element which is intended for both thin and thick shell applications. It also accounts for finite membrane strain, allows thickness changes, permits transverse shear stress output and incorporates hourglass control. The S4R element can be seen in Figure 4.4, which shows the number of the element on the Cartesian plane as well as the definition of the outward facing positive normal according to the right hand rule.

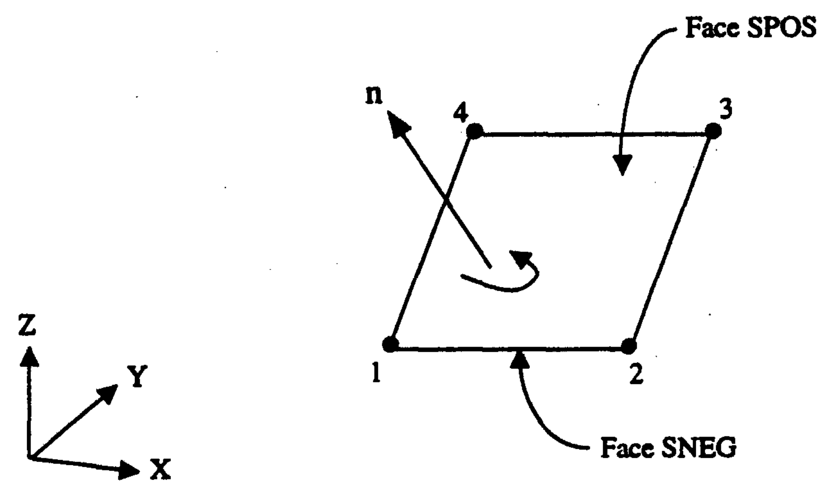

Figure 4.4: The S4R element on the Cartesian plane with its element numbering and positive normal.

The S4R element has six degrees of freedom at each node on the element. These degrees of freedom are:

u_1 - translational motion in the x direction
u_2 - translational motion in the y direction

u_3 - translational motion in the z direction

Φ_1 - rotation in the x plain

Φ_2 - rotation in the y plain

Φ_3 - rotation in the z plain

An initial investigation was carried out on models with different mesh sizes to determine the effect of mesh refinement on the results because the number of elements used in the finite element model is important as it affects the accuracy of the solution. The model was first tested with 10 mm square elements which gave a rough solution with minor errors. The model was then refined using 5mm square elements and this was then found to be the optimum and most efficient solution. The tube geometries were assumed to be perfectly square with no corner radii and these have very little effect on the results for the ultimate peak force and mean force as well as the deformation shape.

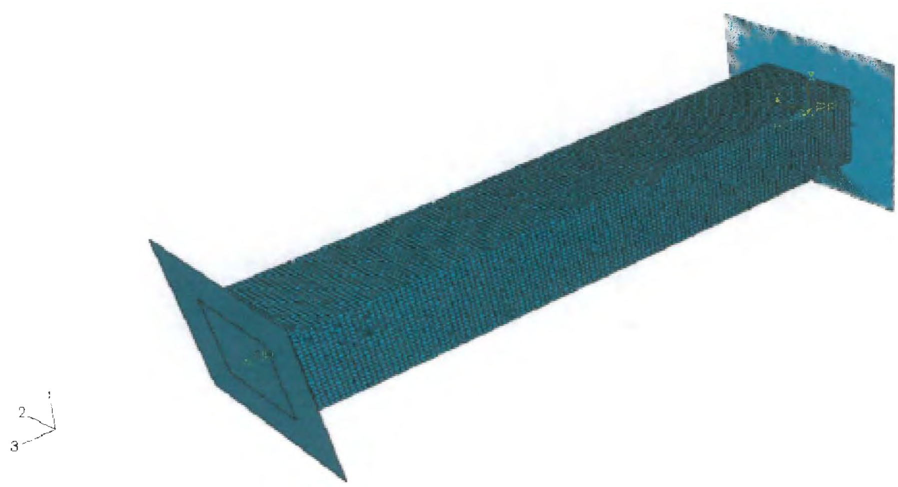

Figure 4.5: Mesh used for the undeformed square tube with the 5 mm sized elements.

4.6 PERTURBING WITH IMPERFECTION FACTORS FROM THE EIGENMODE BUCKLING ANALYSIS

Depending on the type of loading and boundary conditions applied, it is often necessary to use imperfection factors by perturbing (seeding) the mesh in ABAQUS before performing a tube crushing analysis, particularly in the case of when a tube is crushed with a dynamic mass loading at one end and the tube is only allowed to resist the applied crushing load in the opposite direction, i.e. the tube is only prevented from movement along the same axis as the applied load, i.e. the tube is not fully fixed or encastred at one end.

By either not perturbing the tube at all, or by not perturbing it sufficiently accurately enough, this can result in various adverse errors in the numerical model. The resultant type of numerical errors, and well as the magnitudes of their adverse effects, will be discussed in further detail in the next chapter. In cases where it is necessary to perturb the mesh first, this was done in a very rough manner by Nannucci (41, 42) and others, by arbitrary moving the nodes outward at the end of the tube. They then compared their numerical models to tubes that were crushed in the laboratory in order to determine a sufficiently accurate model from the rough perturbing (introduction of imperfection factors).

For this thesis, the imperfection factors were determined with a greater degree of accuracy, by first performing an eigenmode buckling analysis for each tube specimen to determine its eigenmodes and associated eigenvalues, which were then used as the imperfection factors for perturbing the mesh.

Where perturbing is required and / or used, and because the tube's deformation involves buckling, it is necessary to perturb the mesh with the lowest buckling modes of the tube (the imperfection factors) to obtain a smooth post-buckling response. Thus before performing the ABAQUS / Explicit crushing analysis an ABAQUS / Standard buckling analysis was performed to obtain the 10 lowest buckling modes and their associated eigenvalues, of the tube. The eigenvalues were calculated using the Lanczos eigen solver in ABAQUS / Standard. These buckling eigenmodes were then used to perturb the mesh.

When choosing perturbation magnitudes, the goal is to perturb the mesh with a deformation pattern that will allow the post-buckling deformation to proceed correctly. Typically, the magnitudes of the perturbations used for the different eigenmodes are a small percentage of the relevant structural dimension, such as shell thickness. Since the lowest eigenmodes are most pertinent to a crushing analysis, because they are the dominant eigenmodes, the magnitude of the perturbation associated with those modes should be greatest. Increasing the imperfection factors causes the crushing to proceed more smoothly. However, imperfections that are too large are unrealistic.

The post-buckling response of a structure with many closely spaced eigenvalues may be highly sensitive to the mesh imperfections that are imposed. In such cases slight changes to the mesh imperfections can cause significant changes in post-buckling behaviour, requiring a sensitivity study to determine realistic mesh imperfections. One method to establish the importance of the eigenmode is to examine the mass matrix in ABAQUS / Explicit. The larger the mass matrix, the more important is the eigenmode. Another more trivial way is to examine the eigenvalues. If the first eigenvalue is significantly lower than the rest, then the first eigenmode will dominate. In the tube crushing analysis of the model studied in this thesis, the first eigenvalue is significantly lower than the second, so the first eigenmode will therefore dominate. Only eigenmodes 2 and 3 have closely spaced eigenvalues, but these are far enough away from the lowest eigenvalue that they will not dominate the post-buckling response. A structure such as a short thin-walled cylinder may have several low eigenvalues that are nearly the same. The imperfections then have to be scaled with an imperfection factor. Since ABAQUS / Standard scales the eigenvalue output from the buckling analysis so that the maximum deformation in each eigenmode is 1.0 m, choosing an imperfection factor of 1 will perturb the mesh by exactly the displacement obtained as output from the buckling analysis. From a sensitivity study, it was found that imperfections that are a maximum of 2% of the shell thickness are the most appropriate to use giving the most accurate results. The scaling factors for the imperfections used from the first ten buckling modes, based on a tube thickness of 1mm, are shown in Table 4.2.

Table 4.2: Scaling factors used for the first 10 buckling modes.

Buckling mode number	Scaling factor
1	2.40×10^{-5}
2	9.60×10^{-6}
3	4.80×10^{-6}
4	2.16×10^{-6}
5	1.92×10^{-6}
6	1.20×10^{-6}
7	1.20×10^{-6}
8	9.60×10^{-7}
9	2.40×10^{-7}
10	2.40×10^{-7}

In the models where single imperfection factors were used, the maximum scaling factor of 2.4×10^{-5} was used.
The introduction and use of imperfection factors from an eigenmode buckling analysis has two main benefits:

1. It gives the exact eigenmode (imperfection factor) shape of the tube and thus the collapse mode of the tube and hence greater accuracy in modelling, than introducing arbitrary imperfection factors, particularly

where no experimental tests have been performed to undertake a sensitivity analysis.

2. It is the best method of introducing imperfections for the purpose of reducing the initial peak reaction force to the same magnitude as the subsequent 2nd and 3rd, etc peak reaction forces. One would want to utilise this typically for the energy absorption of an impact, in order to absorb the energy uniformly over the impact time period, in order to minimise shock to passengers of vehicles, etc.

For this thesis, three types of imperfection factors determined from the eigenmode buckling analysis in ABAQUS / Standard were used, namely:

- Multiple imperfection factors
- Single imperfection factors, and
- No imperfection factors, i.e. no perturbing

4.7 BOUNDARY CONDITIONS AND END RESTRAINTS

Boundary conditions applied to the model enable the numerical models to simulate the experimental model as closely as possible.

The tube was crushed between two perfectly rigid surfaces. The top rigid surface was used to apply the load and the bottom rigid surface was used to prevent the tube from rigid body movement. An end boundary condition was applied to the bottom node set, i.e. between the bottom end of the tube and the rigid surface. The boundary condition imposed was that there was no friction between the bottom end of the tube and the rigid surface, so that the only restraint (boundary condition) was in the opposite z-direction (in the tube length direction) to the applied force. The tube was therefore able to displace freely in the x-y plane.

The top surface of the tube was displaced by various loading types, one of which was at a constant velocity, by imposing a velocity boundary condition on the top node set of the tube. Other boundary conditions include the surface contact and loading conditions, which are described separately in more detail in the following conditions.

4.8 LOADING

The tubes were crushed using a dynamic axial loading applied to the top of the tubes. Two perfectly rigid surfaces were created and the tube was crushed between the two rigid surfaces. The top rigid surface was used to apply the load to the top end of the tube in the and the loading conditions were imposed on the rigid surface, which was only allowed to move in a single degree of freedom, i.e. in the negative z-direction.

For the investigation two main types of loading conditions were used to investigate what effect the different types of loading conditions would have.

4.8.1 SPECIFIC MASS AND INITIAL VELOCITY LOADING

The first type of loading condition used was a specific mass loading with an initial velocity which gradually reduces as the tube absorbs the impact energy. An example where this type of loading condition would be utilised, would be in the modelling of a vehicle energy absorber device for use in crash-worthiness design to absorb impact energy. The tubes were impacted with an initial Kinetic Energy of 9991.8 J as this was found to be a reasonable amount of energy for crushing a 300 mm tube of 1 mm thickness. A mass of 250 kg with an initial velocity of 8.94 $m.s^{-1}$ was used. Various other mass / initial velocity combinations were used, all of which having a total initial Kinetic Energy of 9991.8 J.

4.8.2 VELOCITY LOADING

The second type of loading condition used was a constant velocity loading. The constant loading condition was the loading condition used mostly in this investigation because it allows easier and more accurate comparisons of the results of the various eigenmode analyses investigations, because the tube's displacement over time can be controlled.

The top of the tube was displaced 200 mm, a two-thirds reduction of the length of the tube. By running the models to the point where the tubes are completely crushed would require much more processing time, as the processing becomes slower and slower as the complexity of the geometry increases.

A constant load velocity of 0.5 $m.s^{-1}$ was used and since this is a quasi-static loading condition and is relatively low, the strain rate effects as outlined by Cowper and Symonds (section 4.4.2) are minimal and can be ignored. This means that the results for the analysis will be identical for any chosen velocity, given that the velocity is low enough that the inertia effects do not influence the model. Nannucci [42] had previously undertaken experiments and found that the forces associated with the buckling process are independent of inertia effects up to 0.5 $m.s^{-1}$, so all models where a velocity load condition was used, were crushed at this velocity.

4.9 CONTACT

Contact surfaces need to be specified in ABAQUS on all surfaces which come into contact with one another. The coefficient of friction between the surfaces is also defined, which allows one to simulate the actual contact interaction between the surfaces with reasonable accuracy.

In this model, surface contact has been defined on the surfaces of the tube for the case when the lobes touch one another. This type of contact is known as self contact. The self contact has been defined on both the inside and outside of the tube and the contact conditions using the self-contact and double-sided contact features of the contact pair algorithm in ABAQUS / Explicit.
In cases where the tube was not fully fixed (encastred) at the end, contact also had to be specified between the end of the tube and the rigid plate.

A coefficient of friction of 0.3 was specified for both particular cases of contact, namely self contact of the tube onto itself and contact between the end of the tube and the rigid plate.

In the newer current versions of ABAQUS CAE, from versions 6.3 and upwards, ABAQUS / Explicit uses two main types of contact algorithms between regions and surfaces, namely General Contact and Contact Pairs.

4.9.1 GENERAL CONTACT

General contact interactions allow one to define contact between many or all regions of a model with a single interaction. The surfaces can span many disconnected regions in a model. For General Contact, ABAQUS / Explicit enforces contact constraints using a Penalty Contact method, as opposed to the Kinematic Contact method, which searches for node-into-face and edge-into-edge penetrations in the current configuration. The penalty stiffness that relates the contact force to the penetration distance is chosen automatically by ABAQUS. The General Contact algorithm uses a balanced master-slave weighting and uses a somewhat more sophisticated global/local tracking approach that does not require or allow much user control.

4.9.2 CONTACT PAIRS

The Contact Pairs algorithm has two subcategory algorithms, namely the Kinematic Contact method and the Penalty Contact method. For the Contact Pairs algorithm, ABAQUS will decide which type of weighting to use for a given contact pair, based on the nature of the two surfaces involved and the constraint enforcement method used.

4.9.2.1 KINEMATIC CONTACT

Kinematic Contact is the default algorithm for surface to surface contact that ABAQUS / Explicit uses to enforce contact constraints when using Contact Pairs. It does not affect the stable time increment as it is a predictor/corrector algorithm and because of it being a predictor / corrector algorithm, achieves precise compliance with the contact conditions.

4.9.2.2 PENALTY CONTACT

The Penalty Contact algorithm results in less stringent enforcement of contact constraints than the Kinematic Contact algorithm, but the Penalty Contact algorithm can model some types of contact that the Kinematic Contact algorithm cannot, such as contact between rigid surfaces (except when both surfaces are analytic rigid surfaces). The Penalty stiffness is chosen automatically by ABAQUS and is similar to that used by the General Contact algorithm. Since the Penalty Contact algorithm introduces additional stiffness behaviour into a model, this stiffness can influence the stable time increment.

The Penalty Contact algorithm searches for slave node penetrations in the current configuration. Penalty Contact and softened Kinematic Contact introduce numerical softening to the contact enforcement comparable to adding elastic springs to the contact interface, which means that these algorithms do not dissipate energy upon impact (the energy stored in the springs is recoverable).

For all of the tube models for this thesis, the Contact Pair algorithm was used and specifically the Penalty Control subset algorithm was used, as it allows more user control. Alternatively, the General Contact algorithm could equally well have been used, but since, as stated above, the General Contact algorithm employs Penalty stiffness, the difference in results between using the Penalty Contact algorithm as opposed to General Contact algorithm for the models, is negligible.

4.10 MASS SCALING

Mass scaling enables an analysis to be performed economically without artificially increasing the loading rate in order to reduce analysis time of the model. Mass scaling and the use of symmetry are the only two options for reducing the solution time in analyses involving a rate-dependent material or rate-dependent damping, such as dashpots. In such analyses, increasing the loading rate is not an option because material strain rates increase by the same factor as the loading rate. When the properties of the model change with the strain rate, artificially increasing the loading rate artificially changes the process. Mass scaling is also the preferred means of reducing the solution time if rate dependencies are included in the model because the normal time scale is preserved.

The following equations show how the stable time increment is related to the material density. As discussed in Section 4.2, "ABAQUS Overview", the stability limit for the model is the minimum stable time increment of all elements. It can be expressed as

$$\Delta t = \frac{L^e}{c_d} \qquad [4.15]$$

where L^e is the characteristic element length and c_d is the dilatational wave speed of the material. The dilatational wave speed for a linear elastic material with Poisson's ratio equal to zero is given by

$$c_d = \sqrt{\frac{E}{\rho}} \qquad [4.16]$$

where p is the material density.

According to the above equations, artificially increasing the material density, p, by a factor of f^2 decreases the wave speed by a factor of f and increases the stable time increment by a factor of f. When the global stability limit is increased, fewer increments are required to perform the same analysis, which is the goal of mass scaling. Scaling the mass, however, has exactly the same influence on inertial effects as artificially increasing the loading rate. Therefore, excessive mass scaling, just like excessive loading rates, can lead to erroneous solutions. The approach to determining an acceptable mass scaling factor, is similar to the approach to determining an acceptable loading rate scaling factor. The only difference to the approach is that the speedup associated with mass scaling is the square root of the mass scaling factor,

i.e. $\text{Speedup Factor due to Mass Scaling} = \sqrt{\text{Mass Scaling Factor}}$ [4.17]

whereas the speedup associated with loading rate scaling is proportional to the loading rate scaling factor. For example, a mass scaling factor of 100 corresponds exactly to a loading rate scaling factor of 10. The mass scaling definition and mass scaling factors can be changed from step to step in ABAQUS.

There are two options to perform mass scaling in ABAQUS / Explicit, namely "Fixed Mass Scaling" and "Variable Mass Scaling". These options can be applied separately or they can be applied together to define an overall mass scaling strategy. The options can also apply globally to the entire model or on an element set by element set basis.

4.10.1 FIXED MASS SCALING

Two basic approaches are available for fixed mass scaling: One can define a mass scaling factor directly, or the user can define a desired minimum stable time increment for which the mass scaling factors are determined by ABAQUS / Explicit. The determination of a minimum stable time increment is not easily determined, so the defining of a mass scaling factor is preferable because ABAQUS / Explicit will then determine the minimum stable time increment.

Fixed Mass Scaling provides a simple means to modify the mass properties of a quasi-static model at the beginning of an analysis or to modify the masses of a few small elements in a dynamic model so that they do not control the stable increment size. Since the scaling operation is performed only once at the beginning of the step for which the option is used, Fixed Mass Scaling is computationally efficient.

4.10.2 VARIABLE MASS SCALING

The Variable Mass Scaling option is used to scale the mass of elements periodically during a step. Variable mass scaling may scale the masses in addition to any fixed mass scaling that is specified. When using this option, the user defines a minimum stable time increment and the mass scaling factors are then calculated automatically and applied, as required, throughout the step.

Variable mass scaling is most useful when the stiffness properties that control the stable time increment change drastically during a step. This situation can occur in both quasi-static bulk forming and dynamic analysis in which elements are highly compressed or crushed.

4.10.3 DISCUSSION OF MASS SCALING

When one is using mass scaling in order to reduce the analysis time of a model, one has to ensure that not too excessive mass scaling is used, as this can lead to errors in the model. In order to check that the amount of mass scaling used is within acceptable limits. There are two methods to check this:

1. The output parameters of ABAQUS with and without mass scaling can be compared with one another and checked that the differences between them are within a reasonable tolerance factor. Typical output parameters that can be compared with one another are Equivalent Plastic Strains, forces such as Shear Forces and stresses such as Von Mises stresses.
2. An even more effective check is that the kinetic energy of the deforming model should not exceed a small fraction of the internal energy throughout most of the analysis. The ABAQUS / Explicit User's Manual recommends that the accumulated kinetic energy should be a maximum of 5 to 10 percent of the accumulated internal energy.

Another method which could have been employed to reduce the analysis time of the model, and which has been used extensively in the past, is the use of symmetry in ABAQUS. Mass scaling has two main advantages over the use of symmetry:

1. The reduction in analysis time is much larger.
2. It allows the whole model to be viewed throughout the analysis.

Due to these two major advantages of mass scaling over the use of symmetry, it was therefore decided to rather incorporate mass scaling into the model.

5. RESULTS AND DISCUSSION

This chapter shows the results for the thin-walled tube models crushed under a dynamic axial load.

- Section 5.1 examines the effect of time sampling in ABAQUS and its effect on the output results, such as the reaction forces versus displacement over time.
- Section 5.2 examines the use of Mass Scaling to determine if and where Mass Scaling can be utilised. It was then necessary to determine the optimum Mass Scaling to reduce the time taken for each analysis while maintaining and preserving the same degree of accuracy in the model.
- Section 5.3 determines and displays the shapes of the first 10 eigenmodes of square, hexagonal, circular and triangular thin-walled tubes.
- Section 5.4 examines the effects of initial imperfection factors under different loading conditions, namely a specific mass and initial velocity loading and a constant velocity loading.
- Section 5.5 examines the effects of eigenmode imperfection factors subject to various end boundary conditions under a specific mass and initial velocity loading in more detail.
- Section 5.6 examines the detailed effects of eigenmode imperfection factors subject to a frictionless end boundary condition under a constant velocity loading.

5.1 REACTION FORCES AND THE EFFECT OF TIME SAMPLING

A typical reaction force versus displacement graph for the crushing of a square tube with a constant velocity loading of 0.5 $m.s^{-1}$ is shown in Figure 5.1.

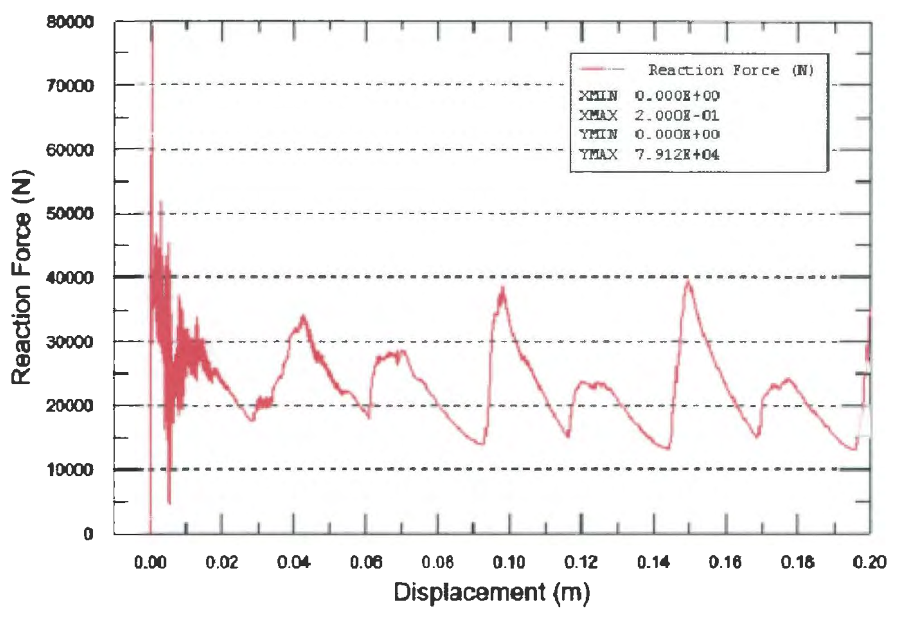

Figure 5.1: Reaction force versus displacement for a square tube subject to a constant velocity loading.

From Figure 5.1 it can be seen that there is an initial peak reaction force followed by a series of subsequent peak reaction forces and that the initial peak reaction force of 79.1 kN is approximately double the magnitude of the subsequent peak reaction forces of approximately 39.0 kN. This peak also occurs over a very short time interval, typically in the order of a few micro-seconds. Because of the extremely short time interval over which the initial peak reaction force occurs, the default time sampling interval of 1 millisecond that is used by ABAQUS / Explicit proved to be too large and often resulted in the initial peak force being undetected and a much shorter time sampling interval therefore had to be used. It then became necessary to find an appropriate time sampling interval small enough to detect the initial peaks but not exceedingly small so as to generate an enormous amount of data which becomes extremely difficult to process and to plot.

Figure 5.2 shows the reaction force versus the displacement graph for the crushing of a square tube using a time sampling interval of 0.1 microseconds. Note that the graph is only plotted for a displacement up to 0.05 m and not the full crushing distance of 0.2 m. This was because of the time sampling unit of 0.1 microseconds generating an enormous amount of data and also because the initial peak reaction force occurs well before a displacement of 0.05 m and typically occurs around 0.001 m.

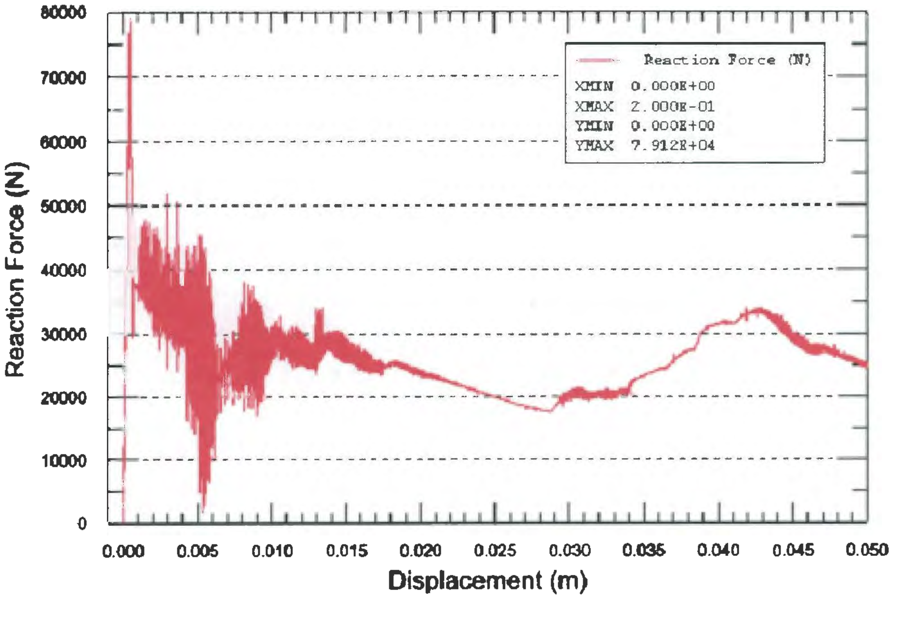

Figure 5.2: Reactions force versus displacement of a square tube using a time sampling interval of 0.1 microseconds.

From Figure 5.2 it can be seen that the initial peak reaction force of 79.1 kN is detectable when using a time sampling interval of 0.1 microseconds. It was then decided to try using a slightly larger time sampling interval of 1 microsecond and the reaction force versus displacement graph for this can be seen in Figure 5.3.

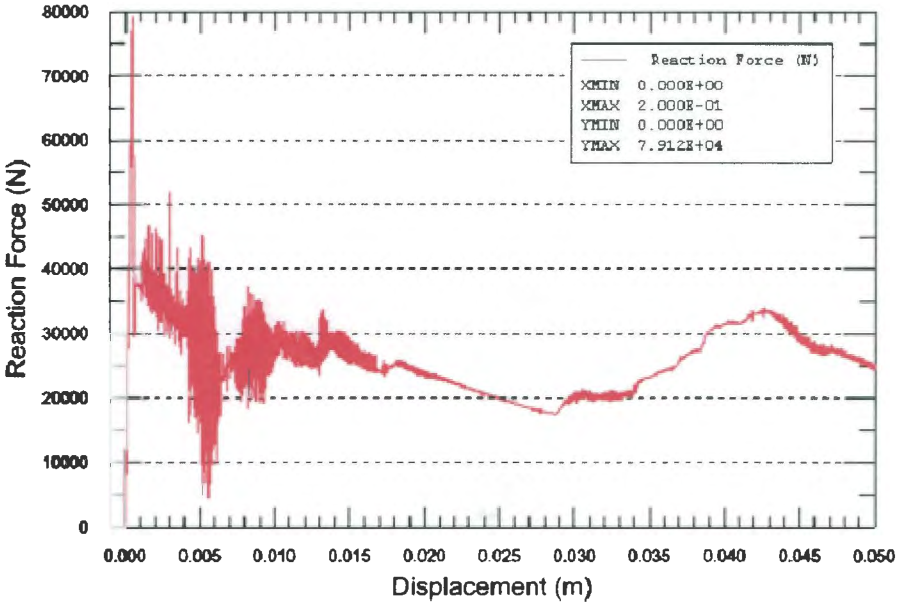

Figure 5.3: Reactions force versus displacement of a square tube using a time sampling interval of 1 microsecond.

From Figure 5.3 it can be seen that the initial peak reaction force of 79.1 kN is still detected and that the overall reaction forces versus displacements graph is virtually identical to the graph shown in Figure 5.2 with a time sampling interval of 0.1 microseconds. When using a time sampling interval greater than 1 microsecond it was found that the true initial peak reaction force was not detected correctly and usually resulted in a lesser incorrect initial peak reaction force being recorded. From these results it was therefore decided to use a maximum time sampling interval of 1 microsecond for the rest of all of the numerical models in this study.

5.2 MASS SCALING EFFECTS

Without the use of mass scaling it took 104.6 hours (4 days 8 hours 38 minutes) to run one tube crushing analysis in ABAQUS / Explicit, and this was excluding ABAQUS / Standard for the eigenmode buckling analysis.
For this thesis, 70 analyses were performed which would have resulted in a total time of 305 days just to complete all of the ABAQUS analyses.
The mesh size could not be reduced because of excessive element distortion leading to errors in the models. One way to speedup an analysis is to use symmetry which results in a speedup factor of 2. Using a mass scaling factor of 225 each analysis reduced to 15.7 hours, resulting in a speedup factor (reduction in analysis time) of 6.6.

Before using mass scaling, a suitable mass scaling factor had to be found to ensure that the amount of mass scaling used was within acceptable limits, as a too large mass scaling factor can lead to errors in a model.
The ABAQUS / Explicit User's Manual recommends that for the application of mass scaling to be valid, the accumulated kinetic energy should be a maximum of 5 to 10 percent of the of accumulated internal energy.

5.2.1 INVESTIGATION OF MASS SCALING EFFECTS

Figure 5.4 shows a graph of accumulated kinetic energy and accumulated internal energy versus displacement for the full crushing displacement of 0.2 m and using a mass scaling factor of 225. From the Figure 5.5 it can be observed that the maximum accumulated kinetic energy occurs in the region between 0 m and 0.02 m and this is the region where the accumulated internal energy is lowest, as shown in Figure 5.4. Therefore this is the region where the maximum ratio of accumulated kinetic energy to accumulated internal energy occurs.

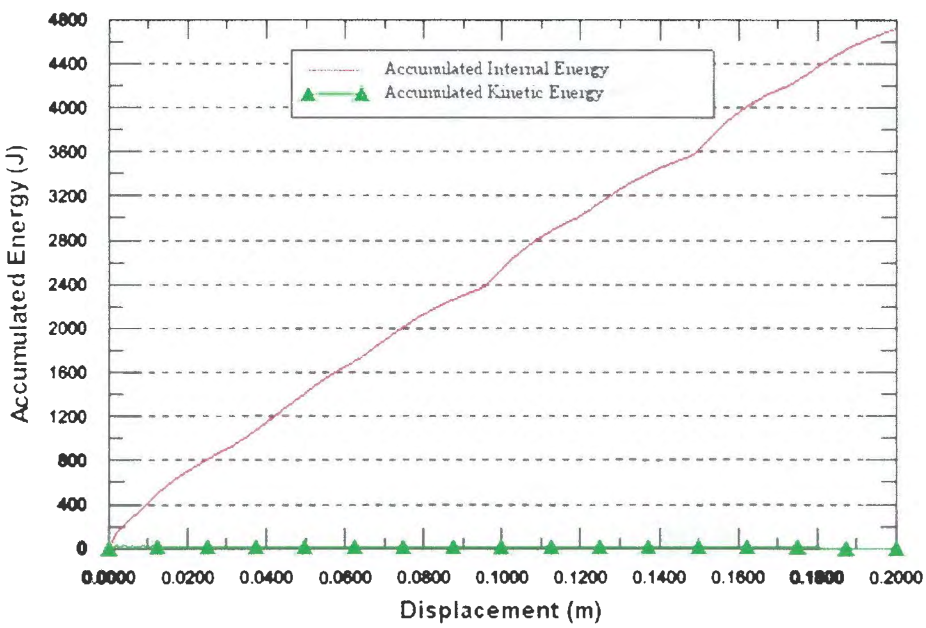

Figure 5.4: Graph of accumulated kinetic energy and accumulated internal energy versus displacement of a square tube for the full crushing displacement of 0.2 m.

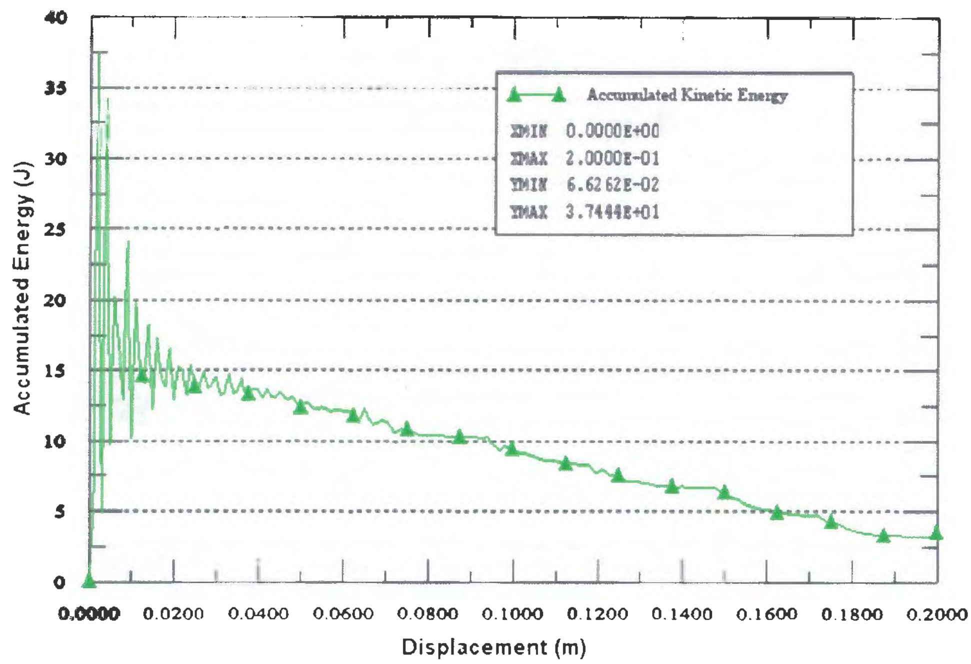

Figure 5.5: Graph of the same accumulated kinetic energy in Figure 5.4 plotted to a more appropriate scale for clarity.

Since 0 m to 0.02 m is the region where the maximum ratio of accumulated kinetic energy to accumulated internal energy occurs it was therefore decided to investigate the maximum ratios of accumulated kinetic energy to accumulated internal energy within this region for various mass scaling factors using no mass scaling factor, a mass scaling factor of 10 and a mass scaling factor of 225. Figures 5.6 to 5.8, respectively, were used to investigate these maximum ratios and have been plotted with the maximum ratios occurring at the displacement shown on the right side of the graphs, to indicate the displacement where the maximum ratios occur and to show clearly the values of both the accumulated kinetic and accumulated internal energies.

Figure 5.6 shows a graph of accumulated kinetic energy and accumulated internal energy versus displacement without using mass scaling. The maximum ratio of accumulated kinetic energy to accumulated internal energy occurs at a displacement of 0.001 m. At this point the accumulated kinetic energy is 0.22 J and the accumulated internal energy is 41.82 J. The maximum ratio of accumulated kinetic energy to accumulated internal energy is 0.52 percent.

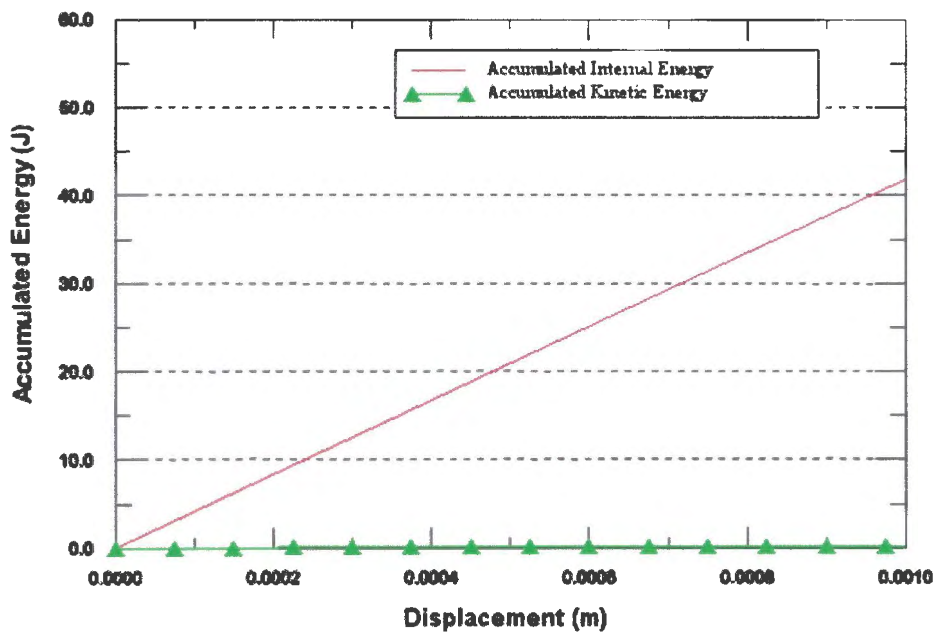

Figure 5.6: Graph of the maximum ratio of accumulated kinetic energy to accumulated internal energy occurs at a displacement of 0.001 m: Without mass scaling.

Figure 5.7 shows a graph of accumulated kinetic energy and accumulated internal energy versus displacement using a mass scaling factor of 10. The maximum ratio of accumulated kinetic energy to accumulated internal energy occurs at a displacement of 0.001 m. At this point the accumulated kinetic energy is 0.95 J and the accumulated internal energy is 51.30 J. The maximum ratio of accumulated kinetic energy to accumulated internal energy is 1.86 percent.

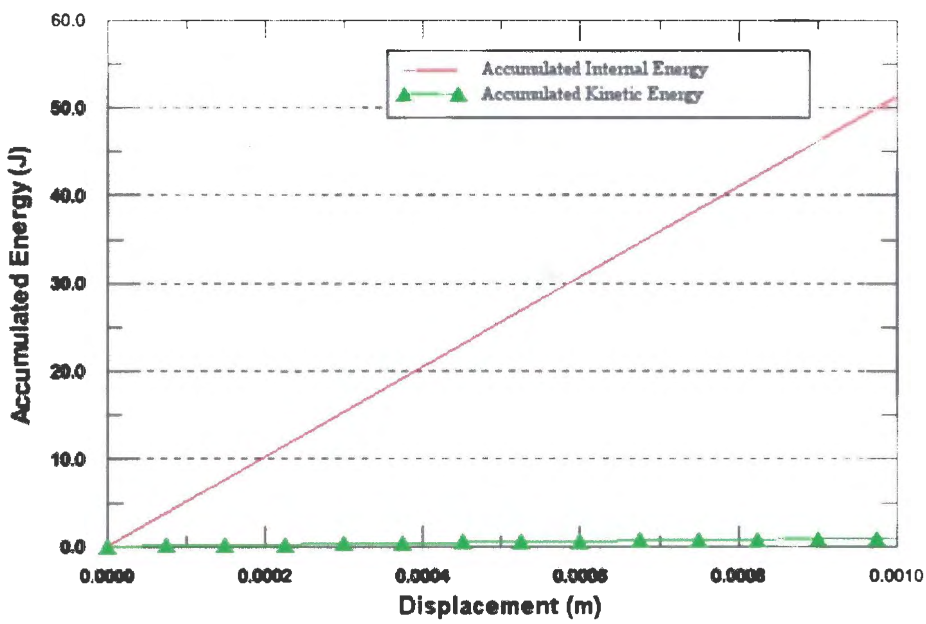

Figure 5.7: Graph of the maximum ratio of accumulated kinetic energy to accumulated internal energy occurs at a displacement of 0.001 m. Mass scaling factor = 10.

Figure 5.8 shows a graph of accumulated kinetic energy and accumulated internal energy versus displacement using a mass scaling factor of 225. The maximum ratio of accumulated kinetic energy to accumulated internal energy occurs at a displacement of 0.002 m. At this point the accumulated kinetic energy is 37.40 J and the accumulated internal energy is 144.20 J. The maximum ratio of accumulated kinetic energy to accumulated internal energy is 25.94 percent.

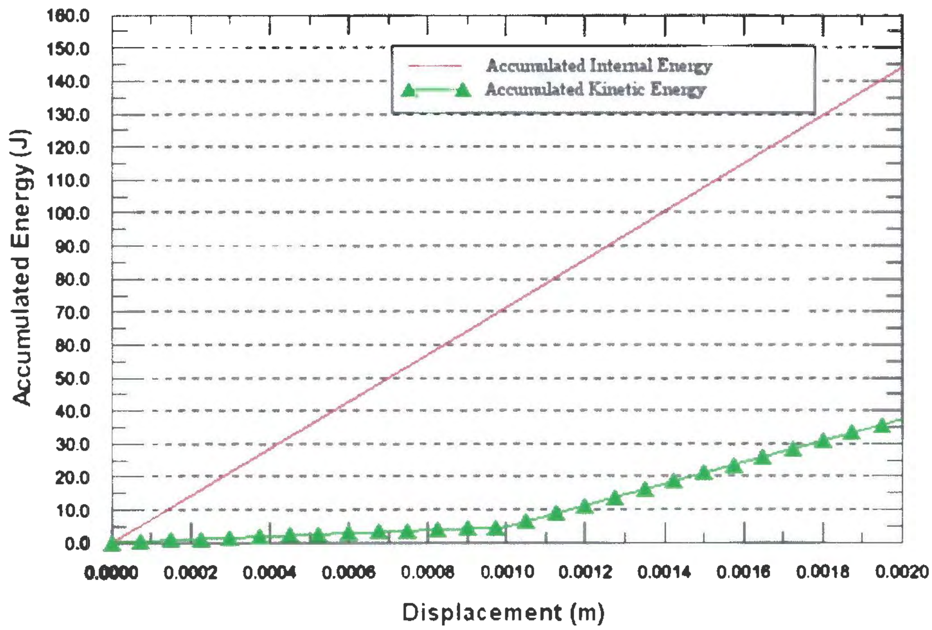

Figure 5.8: Graph of the maximum ratio of accumulated kinetic energy to accumulated internal energy occurs at a displacement of 0.002 m. Mass scaling factor = 225.

Figure 5.9 shows a reaction force versus displacement graph without using mass scaling. The maximum reaction force without using mass scaling is 79.1 KN.

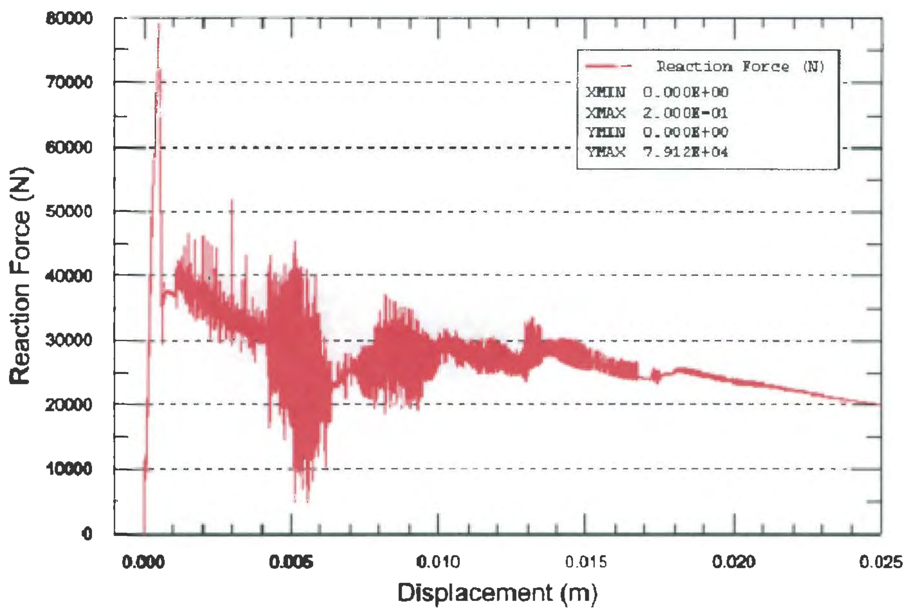

Figure 5.9: Reaction force versus displacement graph without using mass scaling.

Figure 5.10 shows a reaction force versus displacement graph using a mass scaling factor of 10. The maximum reaction force without using mass scaling is 101.5 KN. The analysis was terminated at a displacement of 0.005 m as the maximum peak reaction force occurs at approximately 0.001 m and its maximum value therefore had been determined.

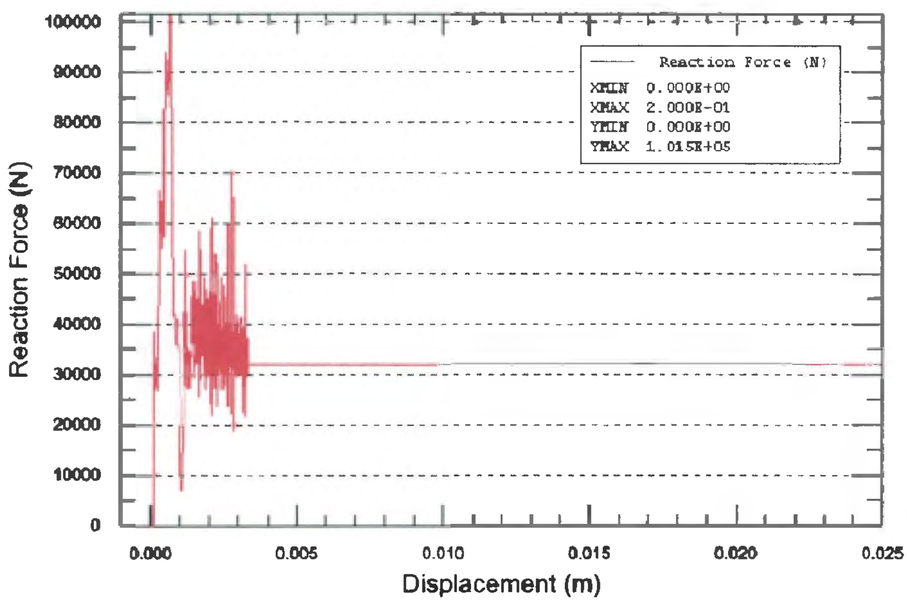

Figure 5.10: Reaction force versus displacement graph using a mass scaling factor of 10.

Figure 5.11 shows a reaction force versus displacement graph using a mass scaling factor of 225. The maximum reaction force without using mass scaling is 125.2 KN.

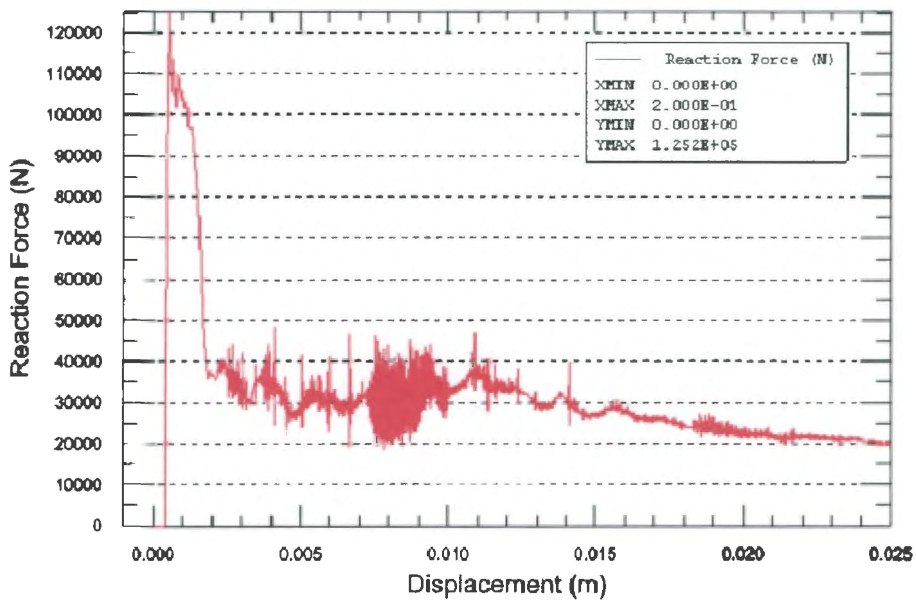

Figure 5.11: Reaction force versus displacement graph using a mass scaling factor of 225.

Figure 5.12 shows a reaction force versus displacement graph using a mass scaling factor of 450. The maximum reaction force without using mass scaling is 121.3 KN. From the graph it can be seen that the peak reaction force when using a mass scaling factor of 450 remains approximately the same as when using a mass scaling factor of 225.

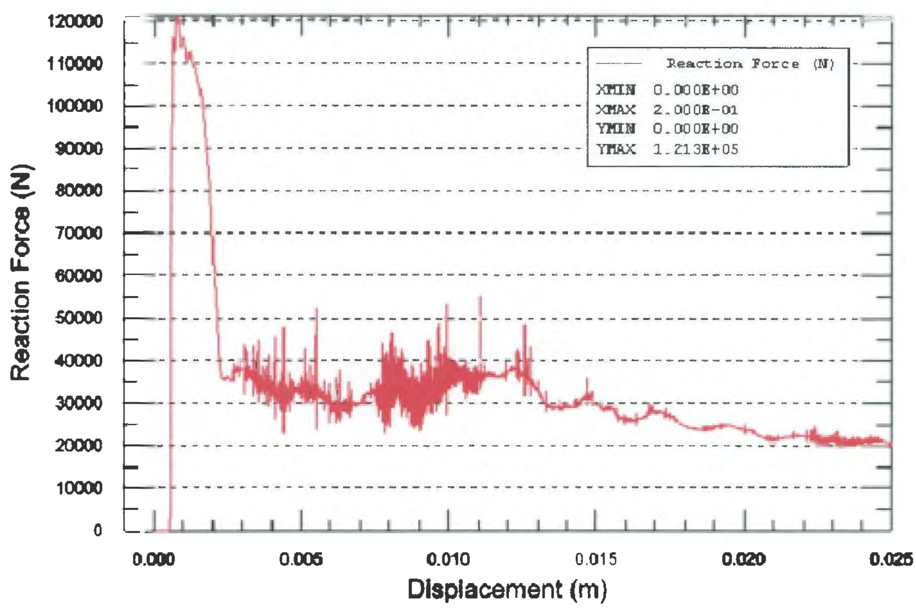

Figure 5.12: Reaction force versus displacement graph using a mass scaling factor of 450.

When using mass scaling factors of 10 and 225, the maximum ratios of accumulated kinetic energy to accumulated internal energy are 1.86 and 25.94 percent respectively. When using a mass scaling of 10, the maximum ratio of accumulated kinetic energy to accumulated internal energy falls within the acceptable limits of 5 to 10 percent specified in the ABAQUS / Explicit manual. However it can be clearly observed by the first peak reaction forces in Figure 5.9, that the respective first peak reaction force of 101.5 kN is greater than the first peak reaction force of 79.1 kN as shown in Figure 5.8 when no mass scaling is used. Therefore this shows that the maximum accumulated kinetic energy to accumulated internal energy ratio specified in the ABAQUS / Explicit manual may be invalid to produce reliable results.

The reason for the increase in the first peak reaction force can mainly be attributed to "noise" or scatter within this region. Figure 5.13 shows a reaction force versus displacement graph without using a mass scaling factor. The reaction forces for the second, third and fourth peaks are 33716 N, 38389 N and 39256 N respectively.

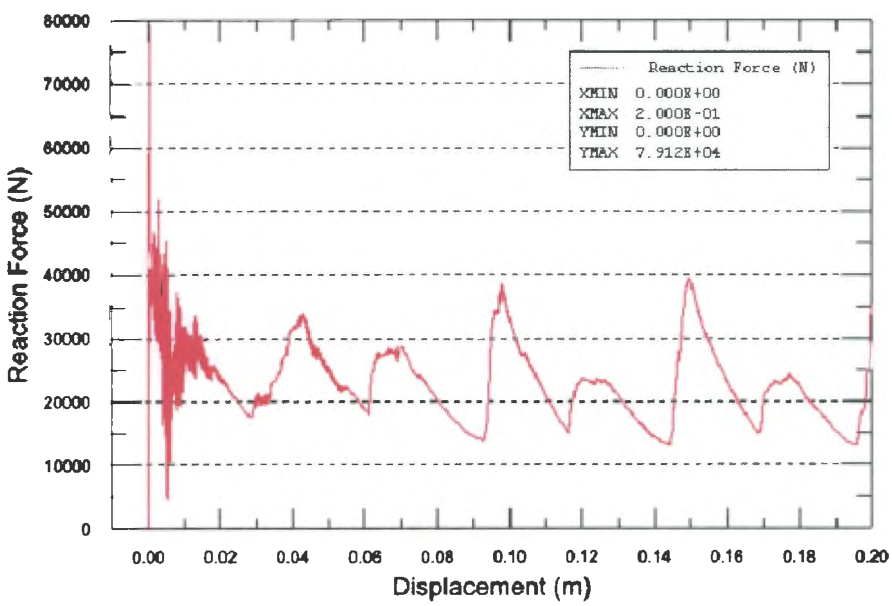

Figure 5.13: Reaction force versus displacement graph without using a mass scaling factor. (Full displacement = 0.2m).

Figure 5.14 shows a reaction force versus displacement graph without using a mass scaling factor. The reaction forces for the second, third and fourth peaks are 31196 N, 43534 N and 40790 N respectively.

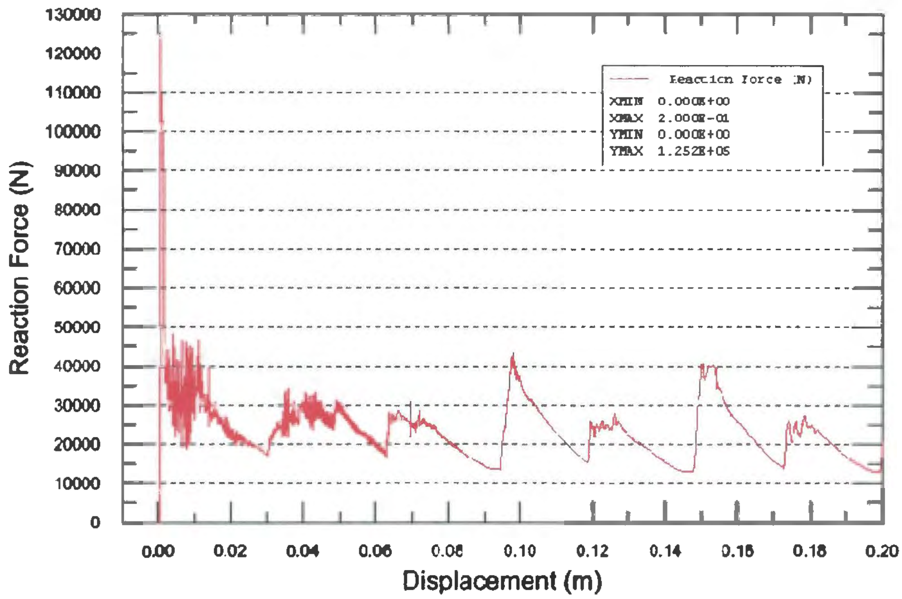

Figure 5.14: Reaction force versus displacement graph using a mass scaling factor of 225 (Full displacement = 0.2m).

From the Reaction force versus displacement graph in Figure 5.13 and Figure 5.14 it can be observed that the second, third and fourth peaks remain approximately the same as when using mass scaling and without using mass scaling.

5.2.2 DISCUSSION OF MASS SCALING EFFECTS

Due to the fact that mass scaling produces large errors in the model in the displacement region of 0 m to 0.025 m, as shown previously, all mass scaling in all future models was removed within this region of the model. It was therefore necessary to use two steps in the model. The first step used was without using mass scaling and the second step used was with using mass scaling. The first step without using mass scaling was in the displacement region of 0 m to 0.025 and the second step was in the displacement region 0.025 m to 0.2 m. The analysis time of each model then took a total time of 15.7 hours to complete. A mass scaling factor of 225 was then used in the second step of all future models as it was felt that an analysis time of 15.7 hours was acceptable, as well as it produced sufficiently reliable results. The use of mass scaling resulted in a speedup factor (or reduction in analysis time) of 6.6. and since no mass scaling was used in the first step of all of the tube models, it was therefore not possible to achieve the maximum desired speedup factor of 15, which would have been achieved if a mass scaling factor of 225 had been used throughout each tube model.

5.3 EIGENMODES OF VARIOUS TUBES

Section 5.3 shows the first 10 eigenmodes modes and their associated eigenvalues of square, hexagonal, circular and triangular shaped thin-walled tubes from the numerical analyses using ABAQUS.

5.3.1 SQUARE TUBE EIGENMODES

5.3.1.1 1ST EIGENMODE (associated eigenvalue = 233.02)

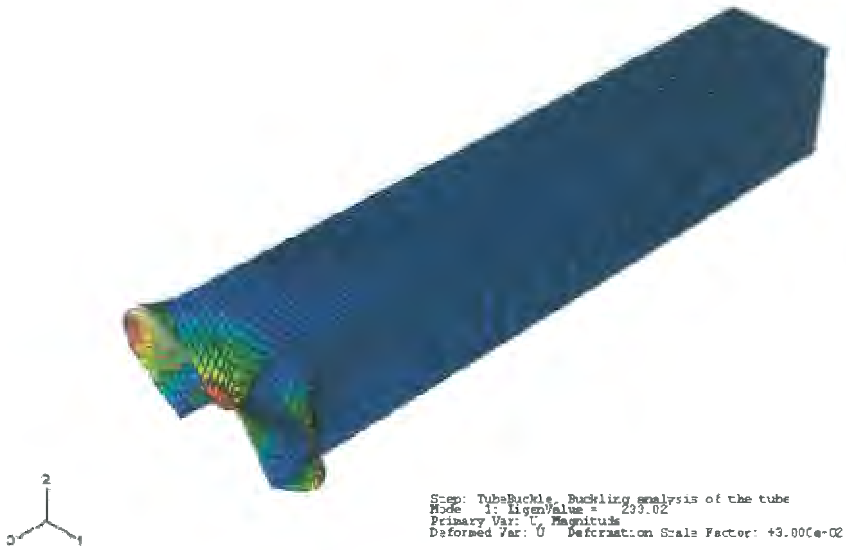

Figure 5.15 (a): 1st eigenmode

5.3.1.2 2ND EIEGENMODE (associated eigenvalue = 309.21)

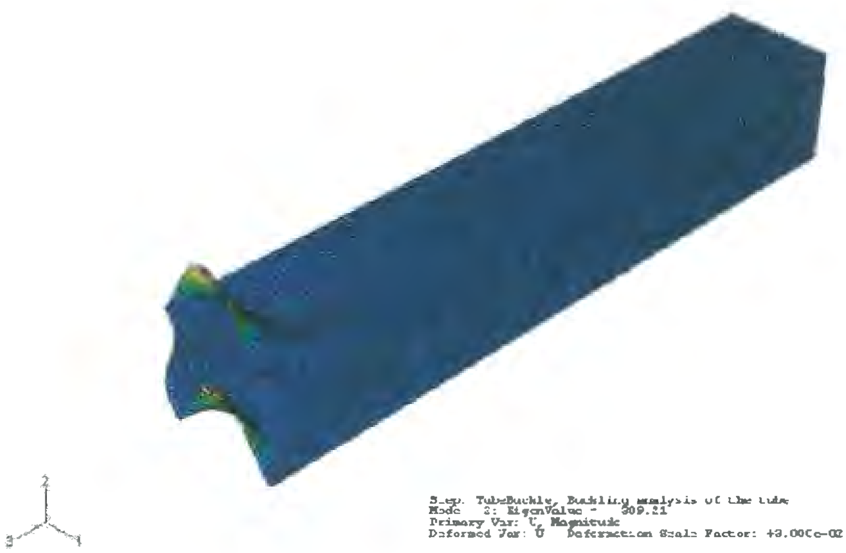

Figure 5.15 (b): 2nd eigenmode

5.3.1.3 3RD EIGENMODE (associated eigenvalue = 309.21)

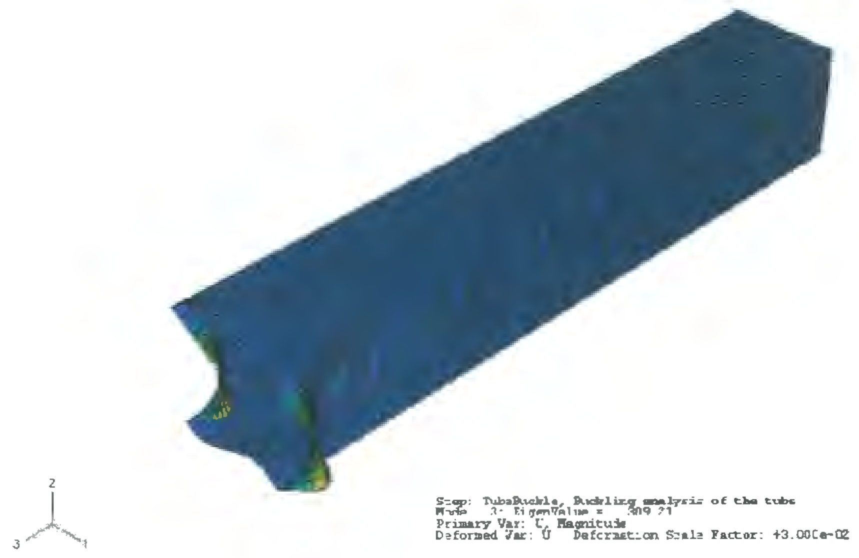

Figure 5.15 (c): 3rd eigenmode

5.3.1.4 4TH EIGENMODE (associated eigenvalue = 392.12)

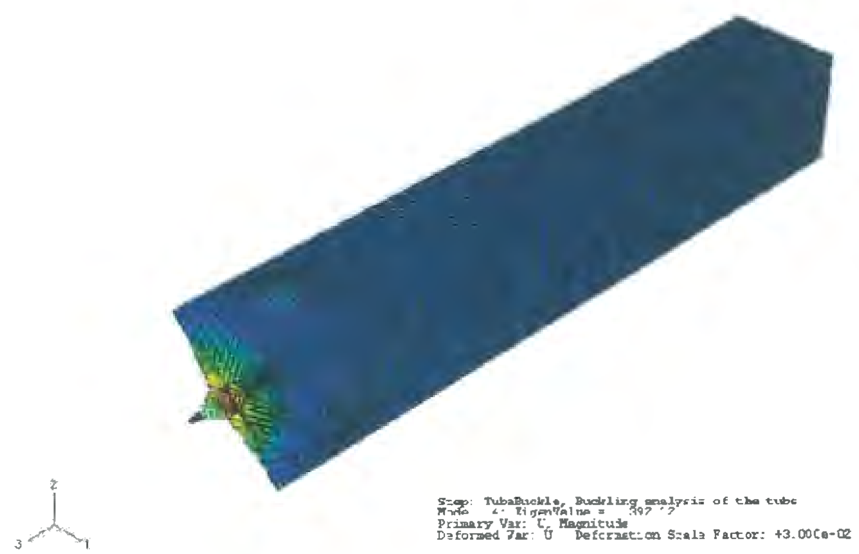

Figure 5.15 (d): 4th eigenmode

5.3.1.5 5TH EIGENMODE (associated eigenvalue = 420.93)

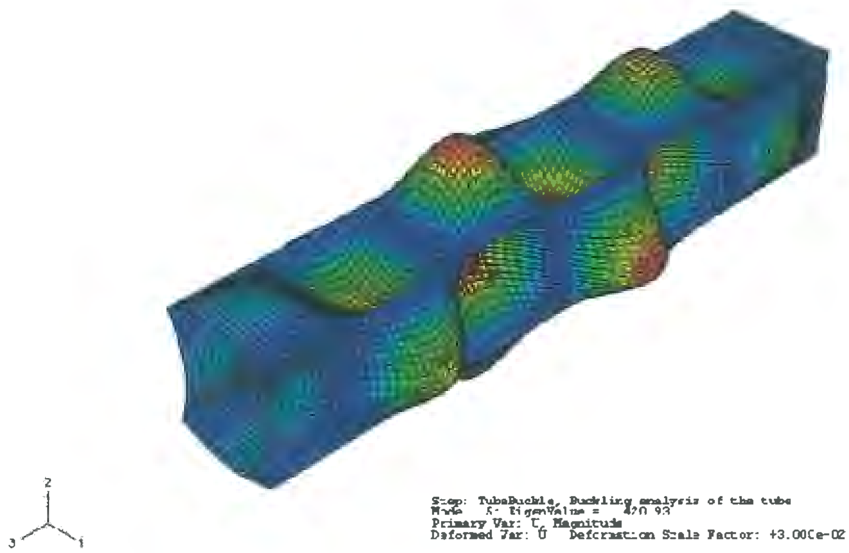

Figure 5.15 (e): 5th eigenmode

5.3.1.6 6TH EIGENMODE (associated eigenvalue = 424.53)

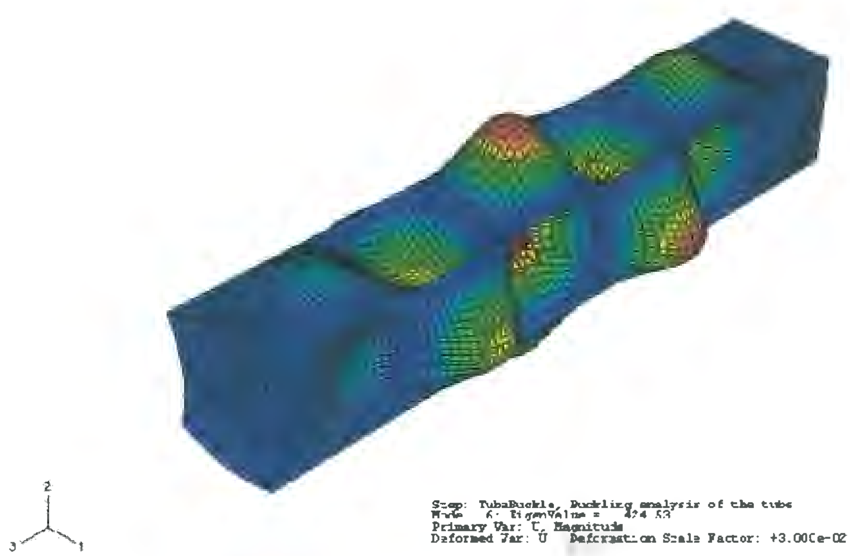

Figure 5.15 (f): 6th eigenmode

5.3.1.7 7TH EIGENMODE (associated eigenvalue = 452.99)

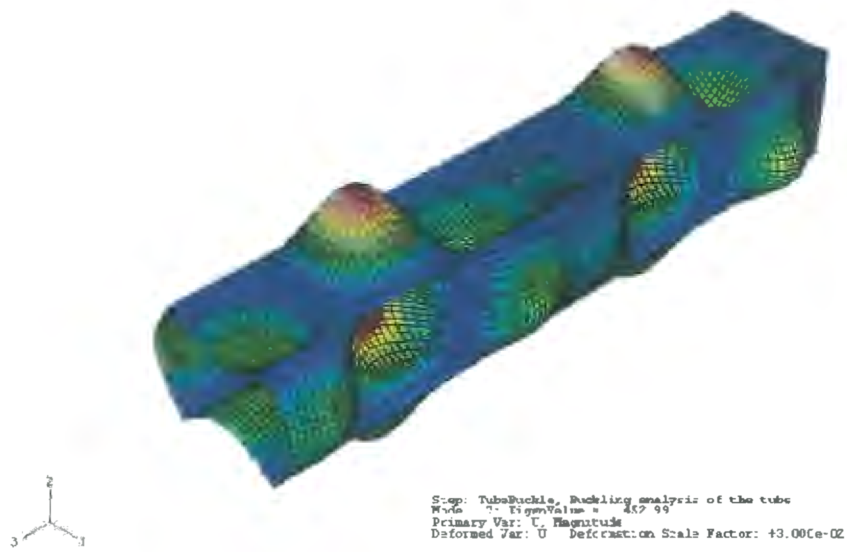

Figure 5.15 (g): 7th eigenmode

5.3.1.8 8TH EIGENMODE (associated eigenvalue = 460.24)

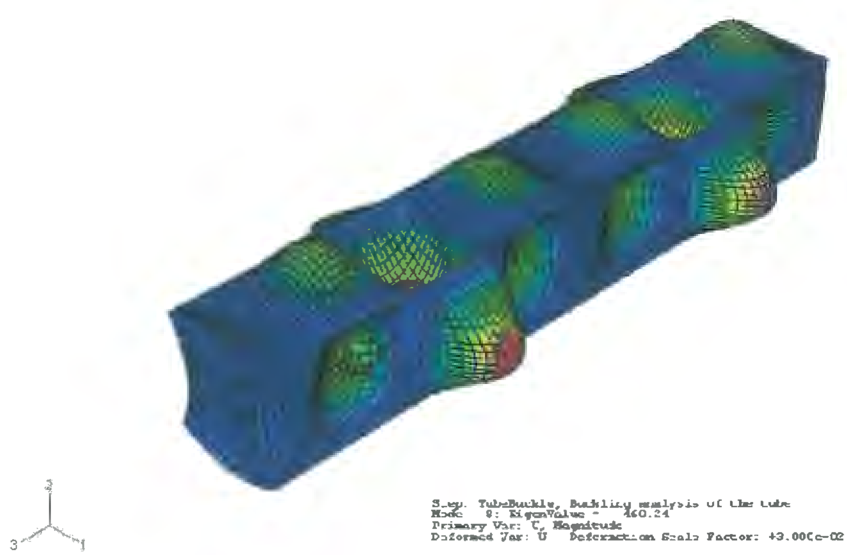

Figure 5.15 (h): 8th eigenmode

5.3.1.9 9^{TH} **EIGENMODE** (associated eigenvalue = 506.39)

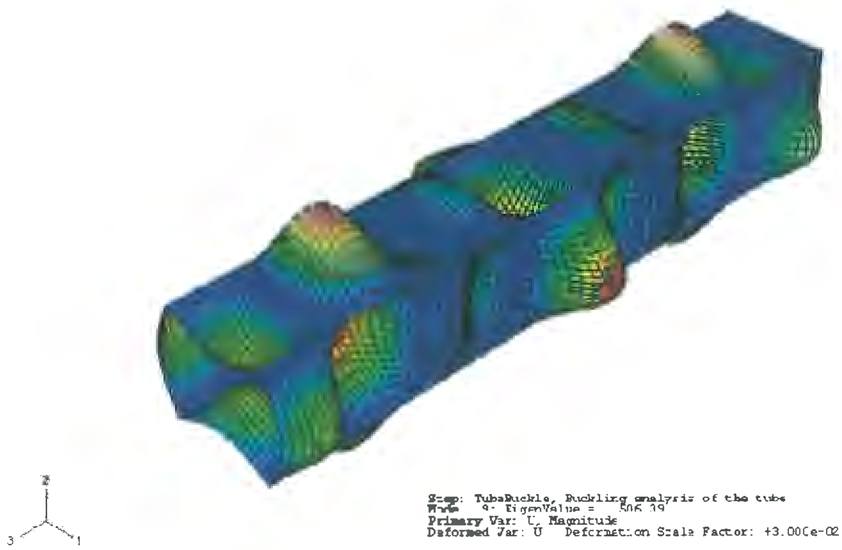

Figure 5.15 (i): 9th eigenmode

5.3.1.10 10^{TH} **EIGENMODE** (associated eigenvalue = 527.18)

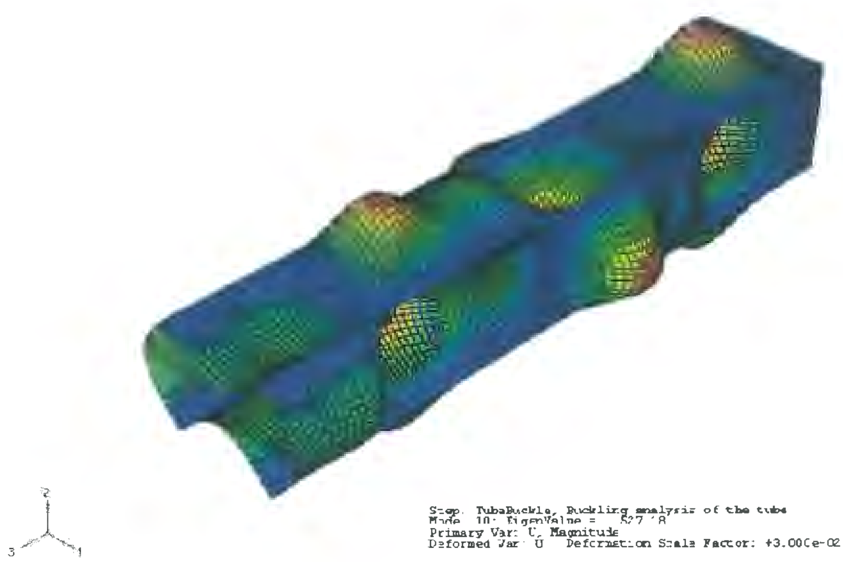

Figure 5.15 (j): 10th eigenmode

5.3.2 HEXAGONAL TUBE EIGENMODES

5.3.2.1 1st EIGENMODE (associated eigenvalue = 526.60)

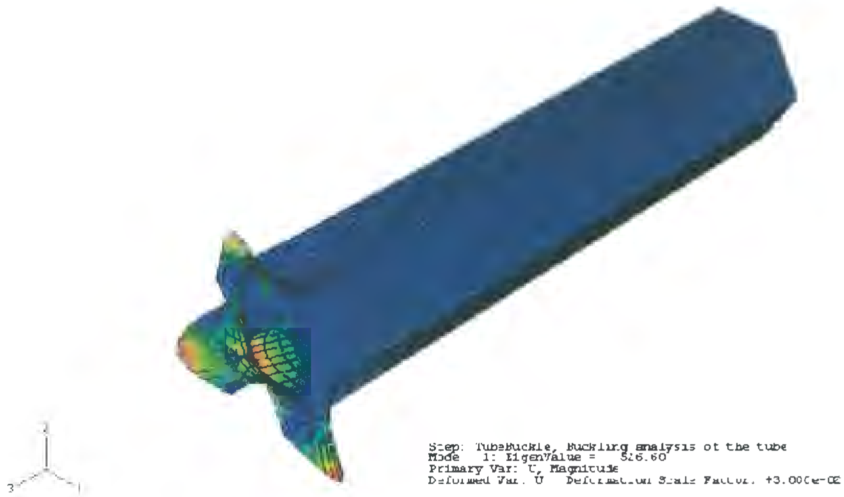

Figure 5.16 (a): 1st eigenmode

5.3.2.2 2ND EIGENMODE (associated eigenvalue = 606.21)

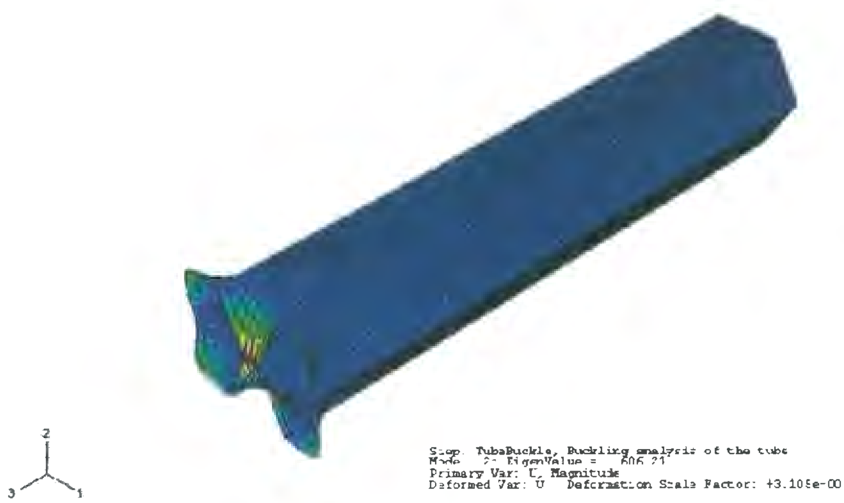

Figure 5.16 (b): 2nd eigenmode

<u>5.3.2.3</u> <u>3RD EIGENMODE</u> (associated eigenvalue = 606.57)

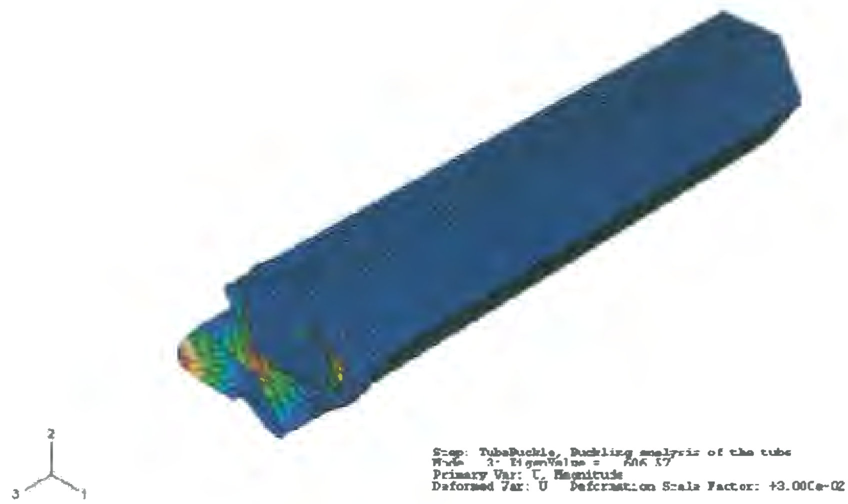

Figure 5.16 (c): 3rd eigenmode

<u>5.3.2.4</u> <u>4TH EIGENMODE</u> (associated eigenvalue = 768.93)

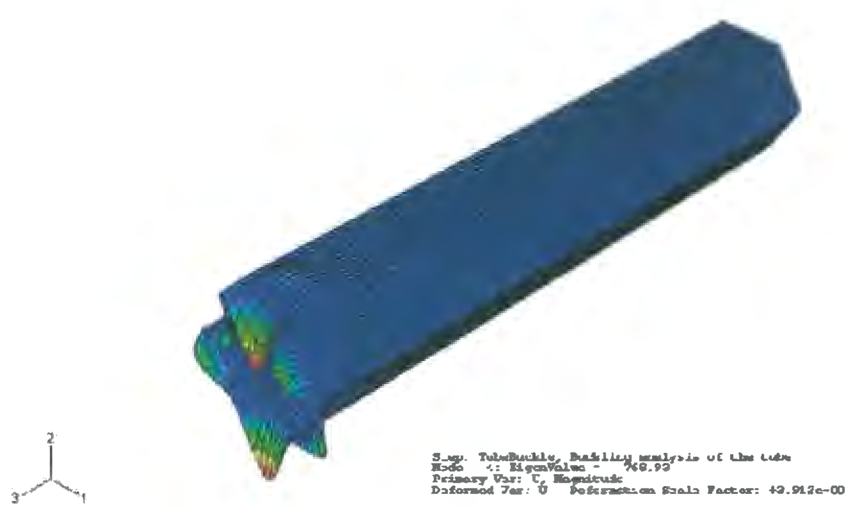

Figure 5.16 (d): 4th eigenmode

5.3.2.5 **5^{TH} EIGENMODE** (associated eigenvalue = 769.37)

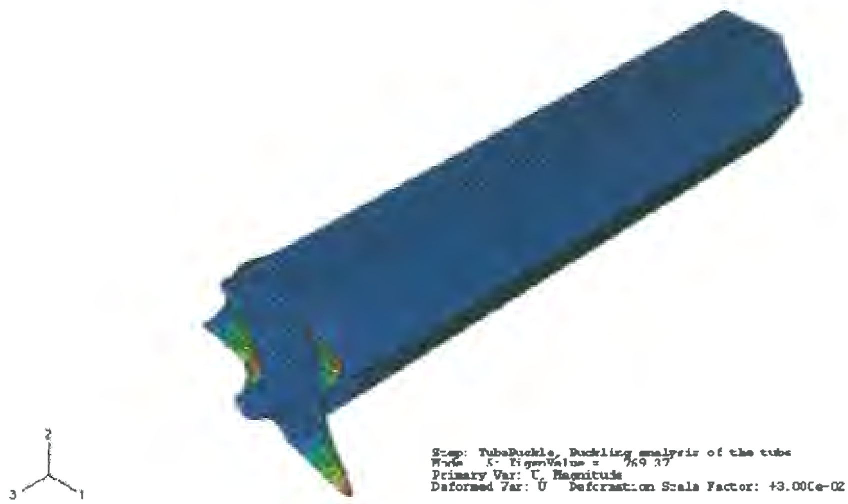

Figure 5.16 (e): 5th eigenmode

5.3.2.6 **6^{TH} EIGENMODE** (associated eigenvalue = 856.21)

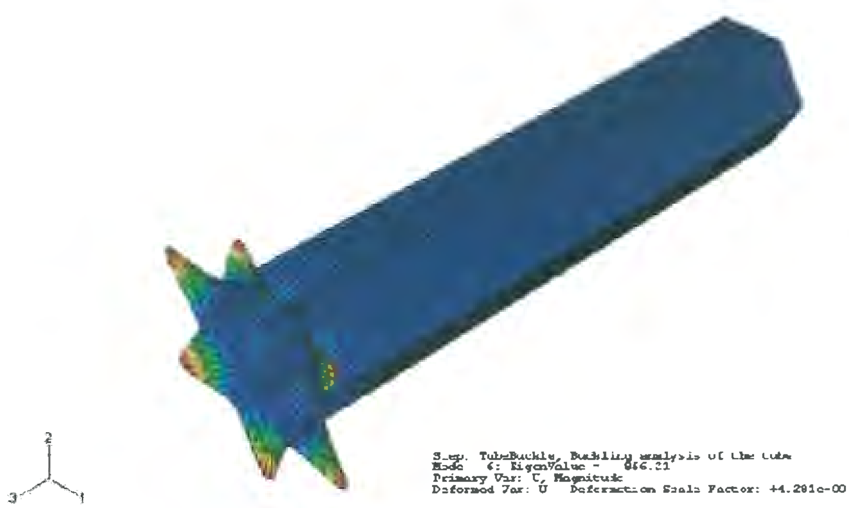

Figure 5.16 (f) 6th eigenmode

5.3.2.7 7TH EIGENMODE (associated eigenvalue = 941.77)

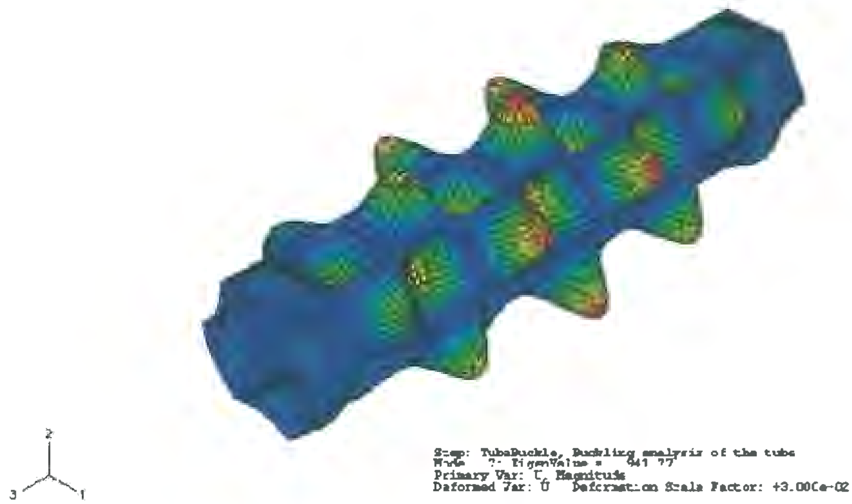

Figure 5.16 (g): 7th eigenmode

5.3.2.8 8TH EIGENMODE (associated eigenvalue = 944.28)

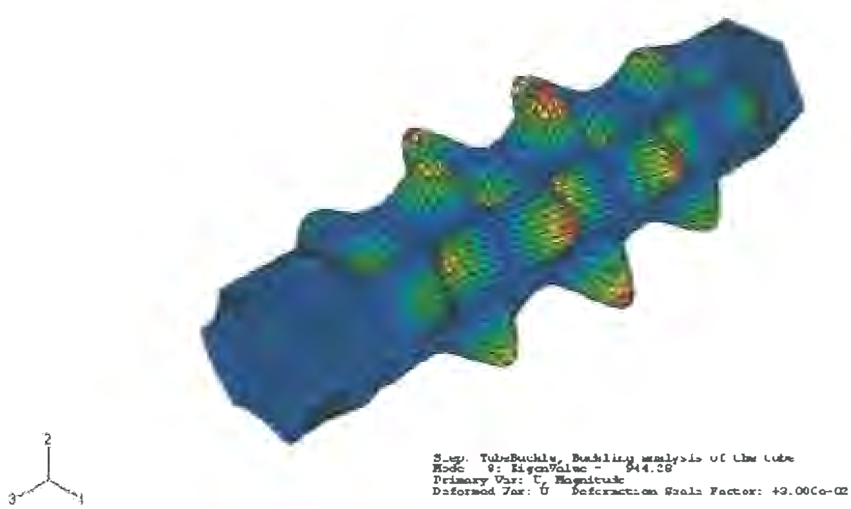

Figure 5.16 (h): 8th eigenmode

]

5.3.2.9 **9^{TH} EIGENMODE** (associated eigenvalue = 974.40)

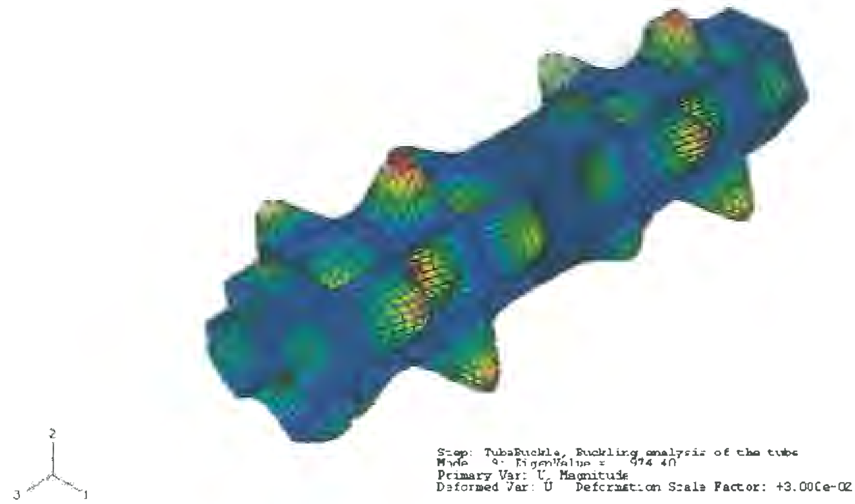

Figure 5.16 (i): 9th eigenmode

5.3.2.10 **10^{TH} EIGENMODE** (associated eigenvalue = 981.51)

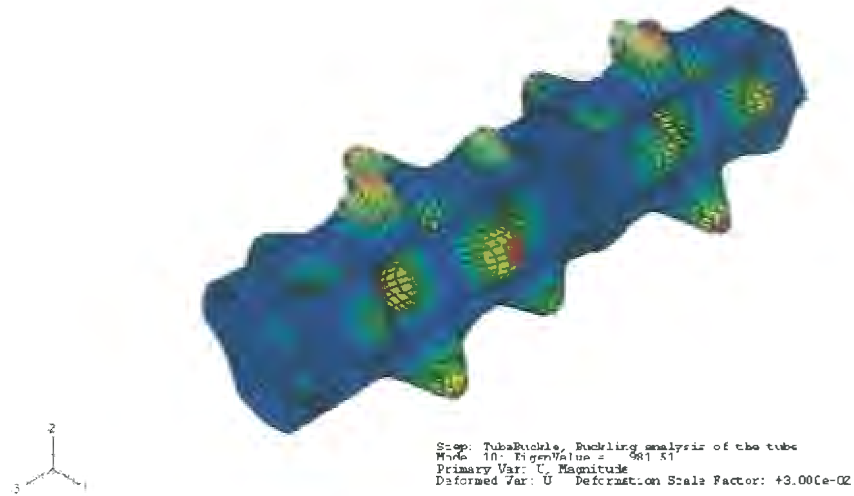

Figure 5.16 (j): 10th eigenmode

5.3.3 CIRCULAR TUBE EIGENMODES

5.3.3.1 1st EIGENMODE (associated eigenvalue = 2233.7)

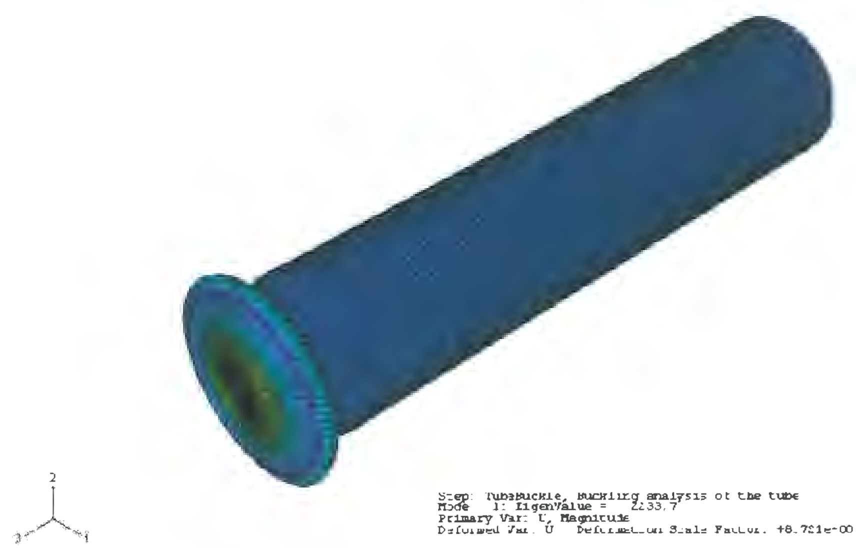

Figure 5.17 (a): 1st eigenmode

5.3.3.2 2ND EIGENMODE (associated eigenvalue = 2244.0)

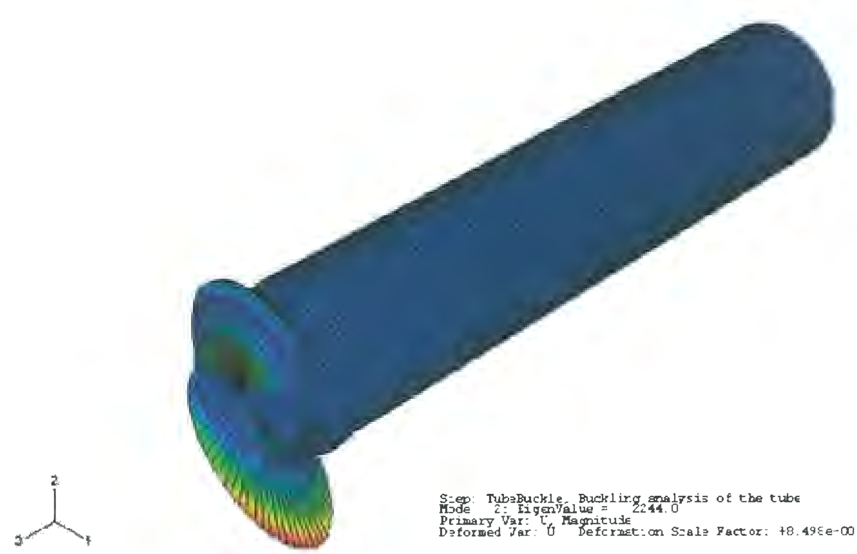

Figure 5.17 (b): 2nd eigenmode

5.3.3.3 <u>3RD EIGENMODE</u> associated eigenvalue = 2244.1)

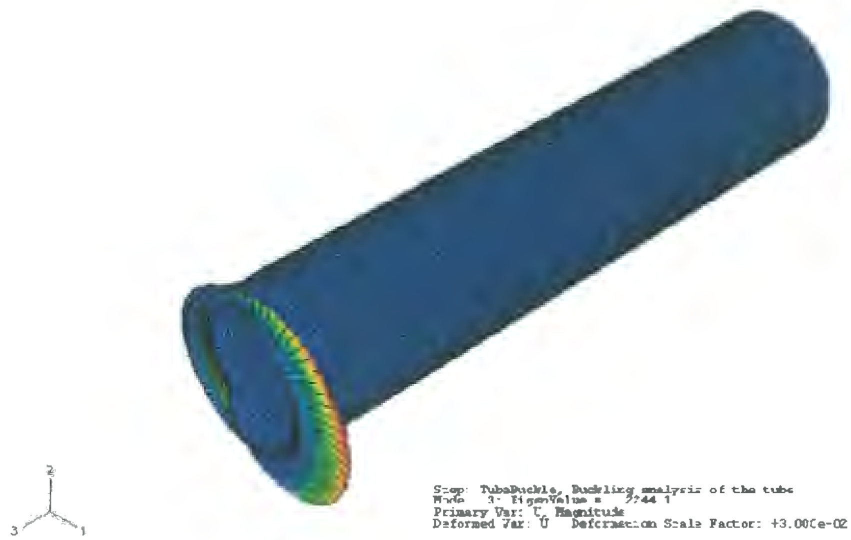

Figure 5.17 (c): 3rd eigenmode

5.3.3.4 <u>4TH EIGENMODE</u> associated eigenvalue = 2258.4)

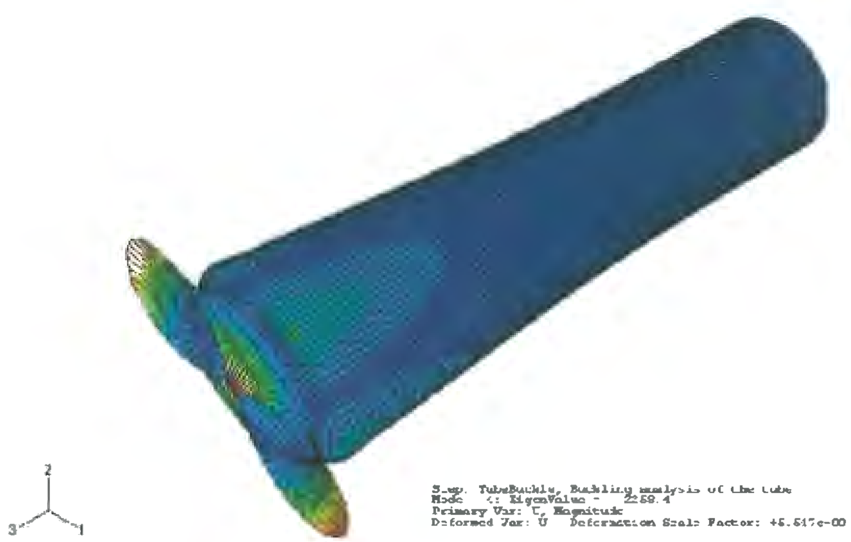

Figure 5.17 (d): 4th eigenmode

5.3.3.5 <u>5^TH EIGENMODE</u> associated eigenvalue = 2258.5)

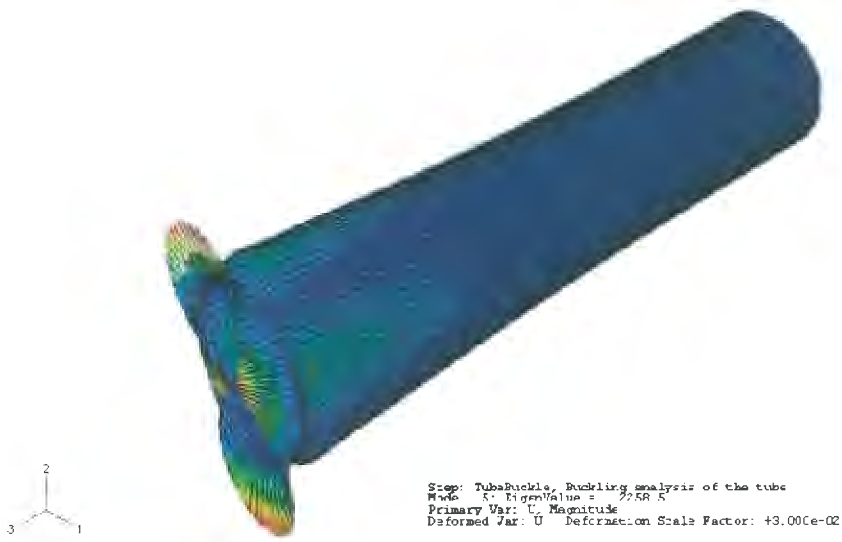

Figure 5.17 (e): 5th eigenmode

5.3.3.6 <u>6^TH EIGENMODE</u> (associated eigenvalue = 2277.2)

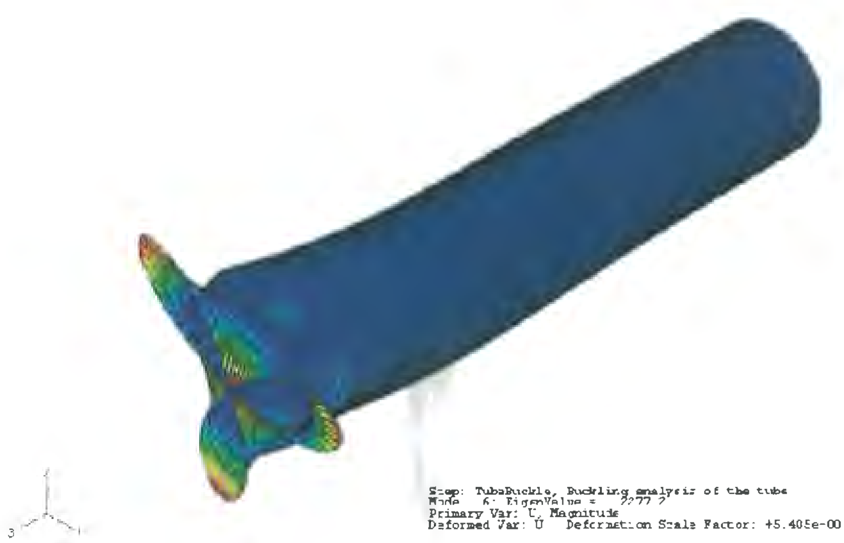

Figure 5.17 (f): 6th eigenmode

5.3.3.7 7[TH] EIGENMODE (associated eigenvalue = 2277.6)

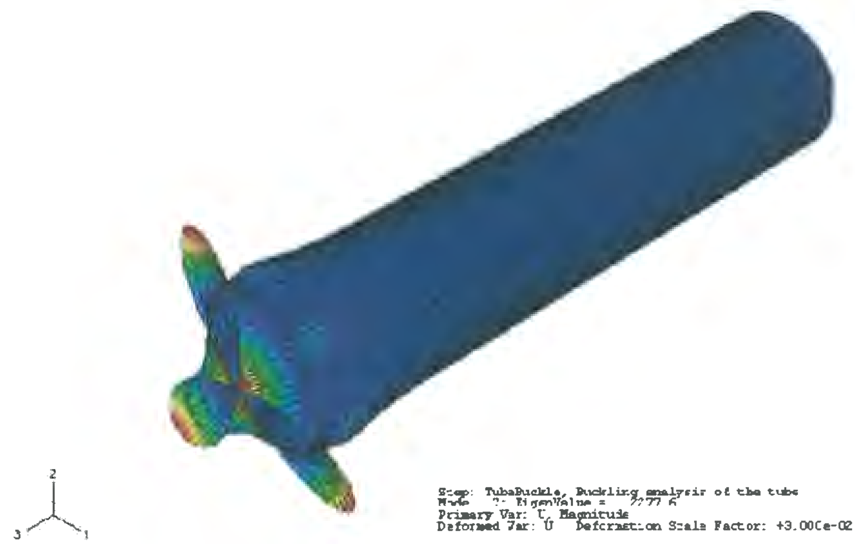

Figure 5.17 (g): 7th eigenmode

5.3.3.8 8[TH] EIGENMODE (associated eigenvalue = 2324.6)

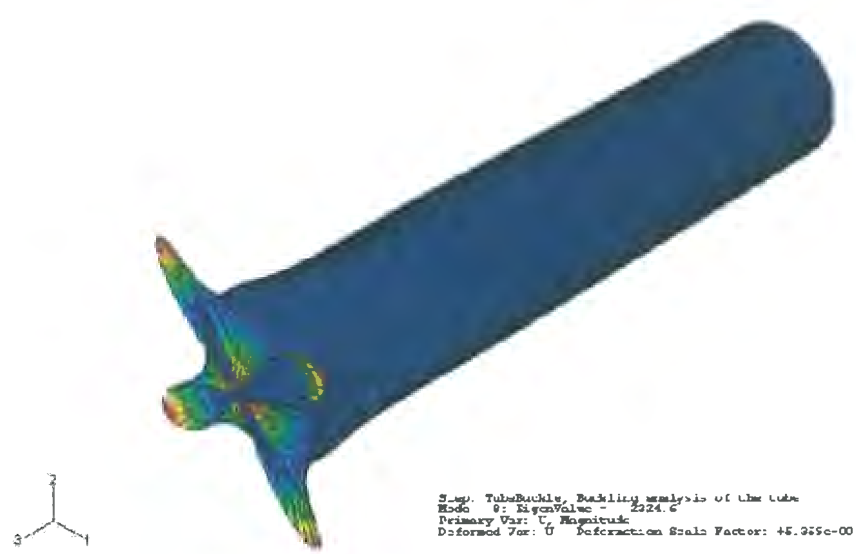

Figure 5.17 (h): 8th eigenmode

5.3.3.9 <u>9TH EIGENMODE</u> (associated eigenvalue = 2324.9)

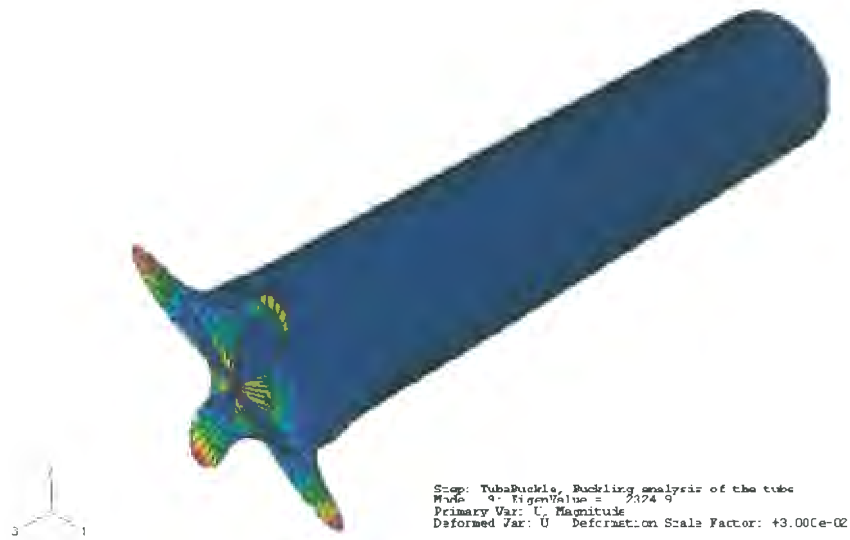

Figure 5.17 (i): 9th eigenmode

5.3.3.10 <u>10TH EIGENMODE</u> (associated eigenvalue = 2498.6)

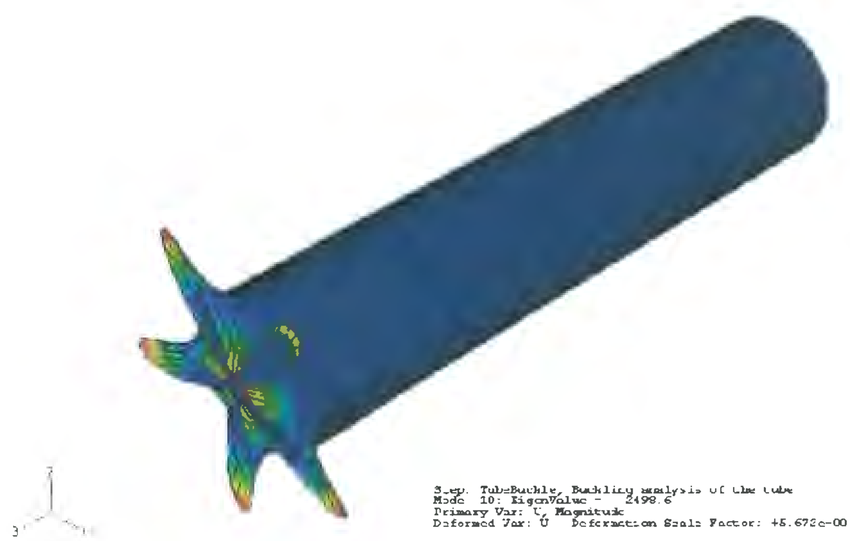

Figure 5.17 (j): 10th eigenmode

5.3.4 TRIANGULAR TUBE EIGENMODES

5.3.4.1 1TH EIGENMODE (associated eigenvalue = 153.07)

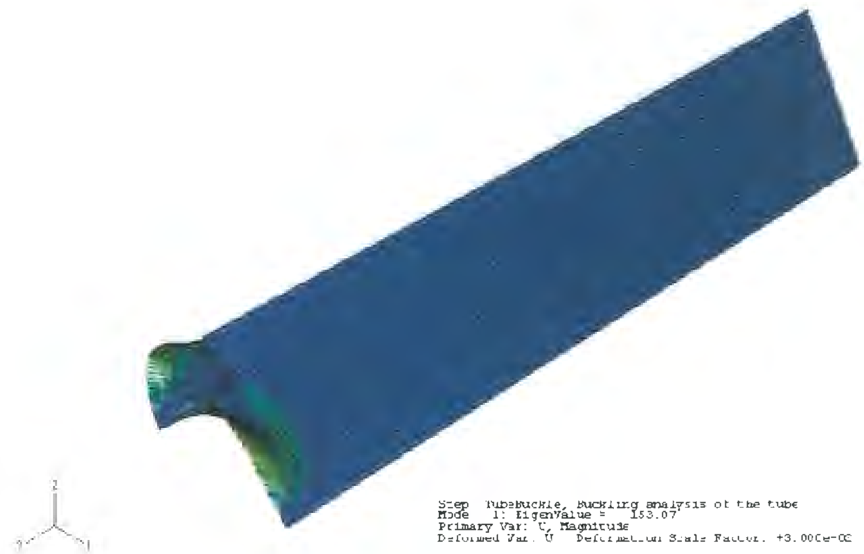

Figure 5.18 (a): 1st eigenmode

5.3.4.2 2ND EIGENMODE (associated eigenvalue = 153.07)

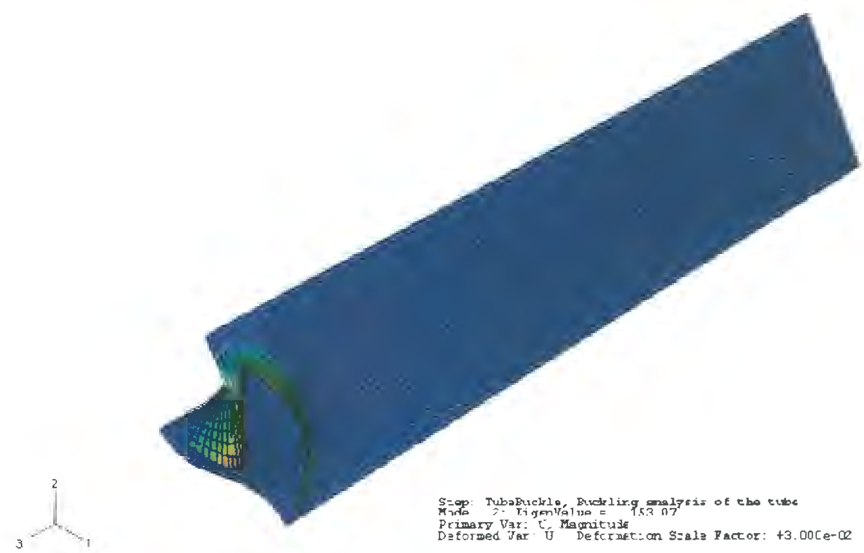

Figure 5.18 (b): 2nd eigenmode

5.3.4.3 3^{RD} EIGENMODE (associated eigenvalue = 222.55)

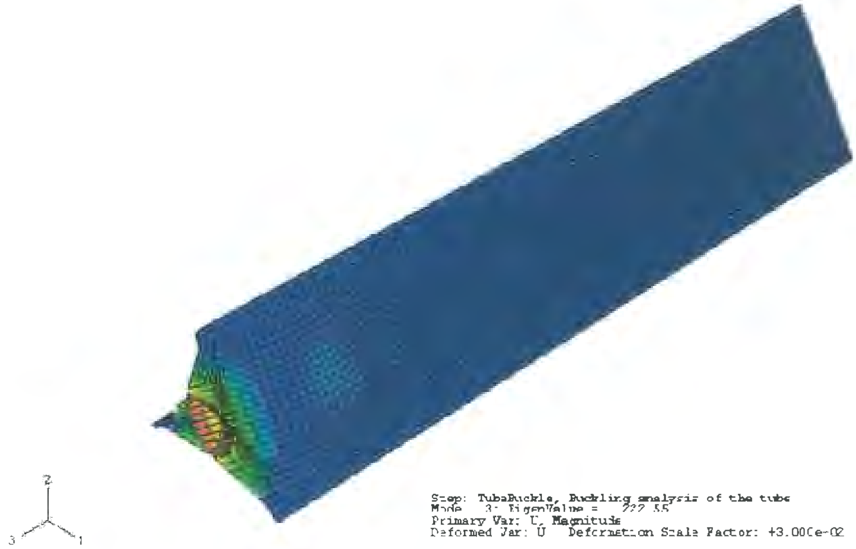

Figure 5.18 (c): 3rd eigenmode

5.3.4.4 4^{TH} EIGENMODE (associated eigenvalue = 281.49)

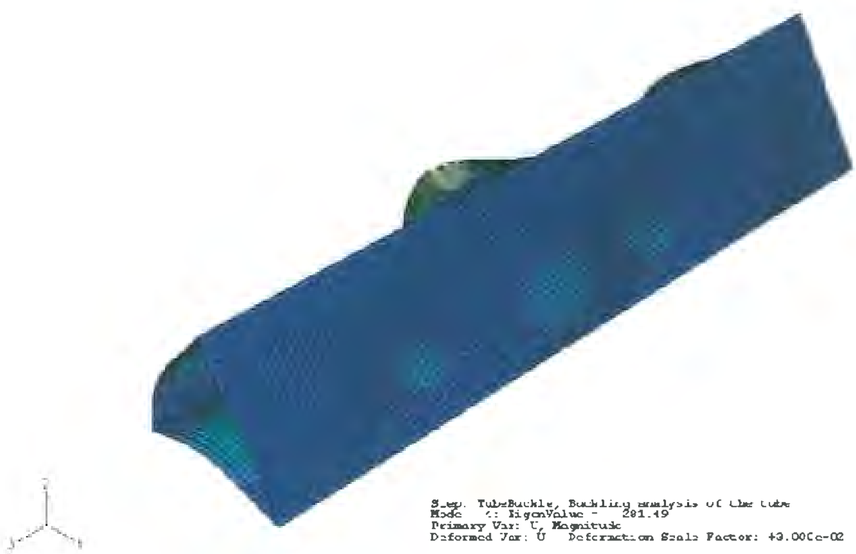

Figure 5.18 (d): 4th eigenmode

5.3.4.5 __5TH EIGENMODE__ (associated eigenvalue = 281.49)

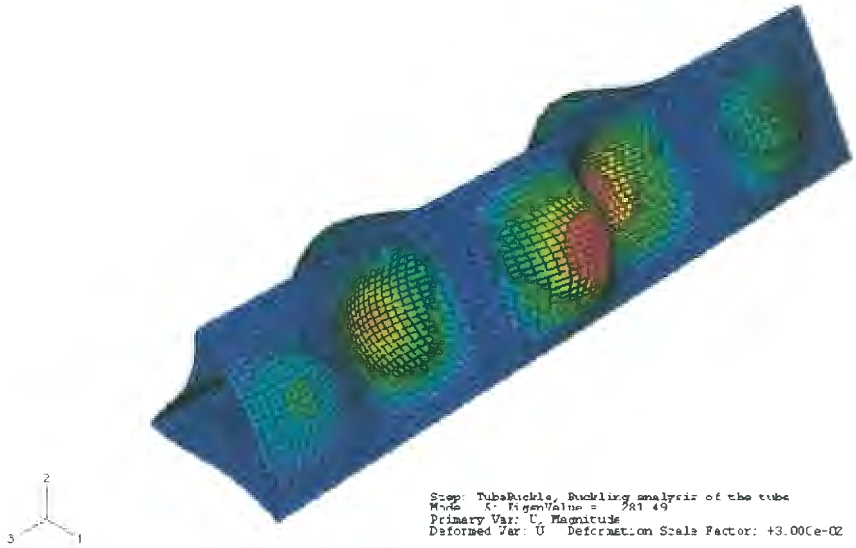

Figure 5.18 (e): 5th eigenmode

5.3.4.6 __6TH EIGENMODE__ (associated eigenvalue = 285.12)

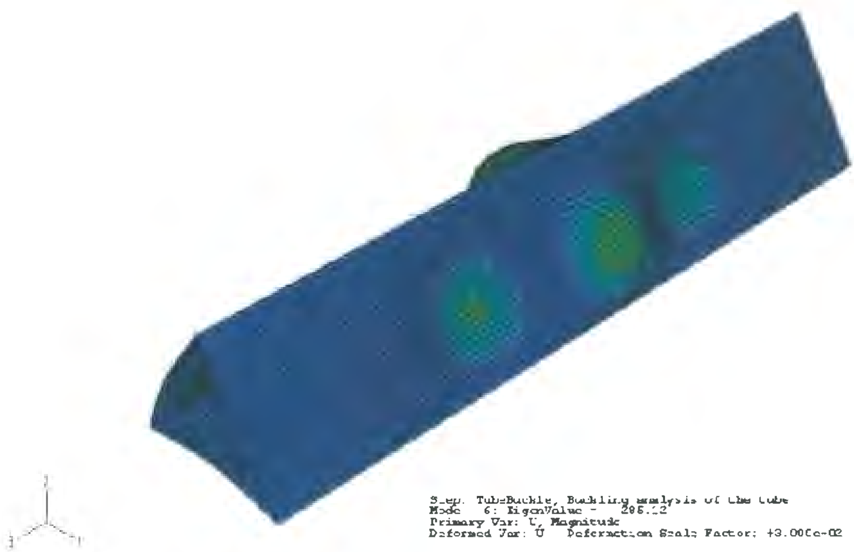

Figure 5.18 (f): 6th eigenmode

5.3.4.7 7^{TH} EIGENMODE (associated eigenvalue = 285.12)

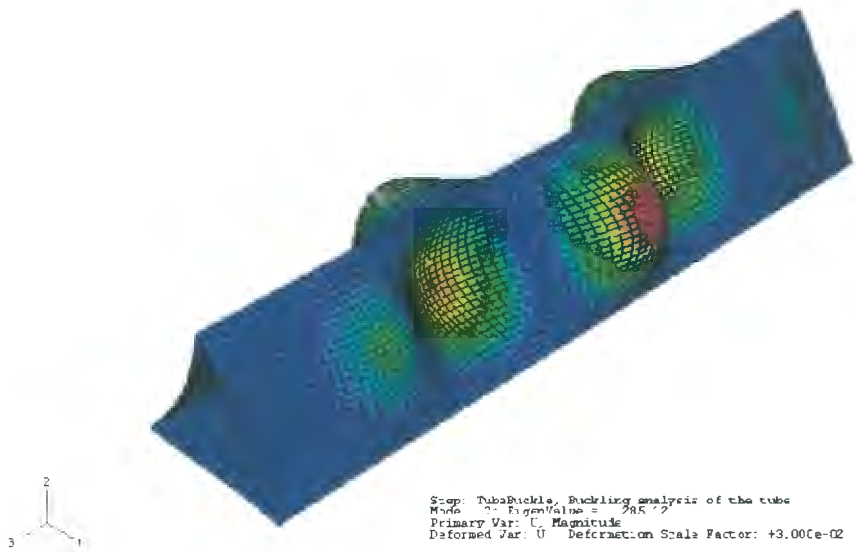

Figure 5.18 (g): 7th eigenmode

5.3.4.8 8^{TH} EIGENMODE (associated eigenvalue = 314.47)

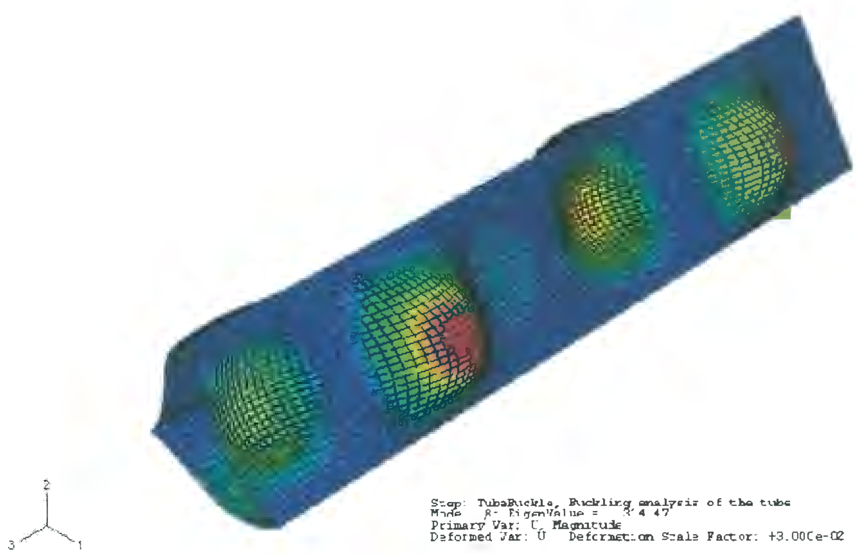

Figure 5.18 (h): 8th eigenmode

5.3.4.9 **<u>9TH EIGENMODE</u>** (associated eigenvalue = 314.47)

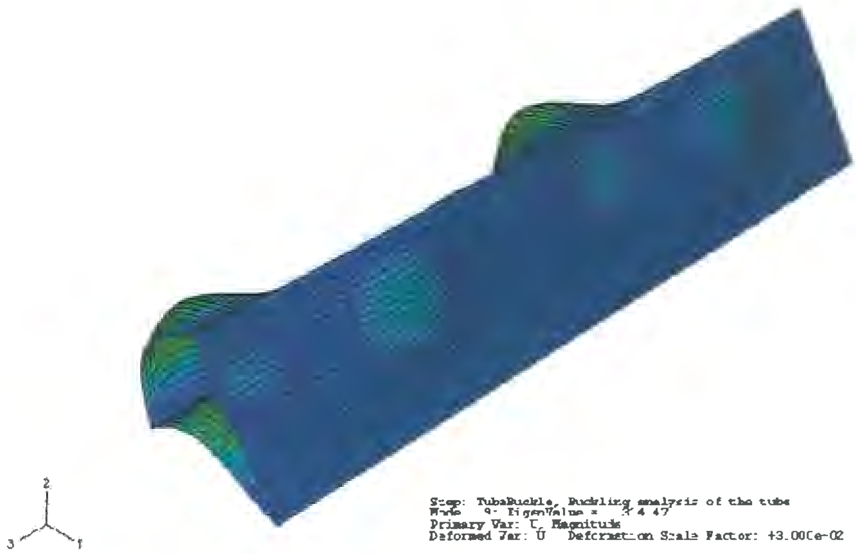

Figure 5.18 (i): 9th eigenmode

5.3.4.10 **<u>10TH EIGENMODE</u>** (associated eigenvalue = 319.24)

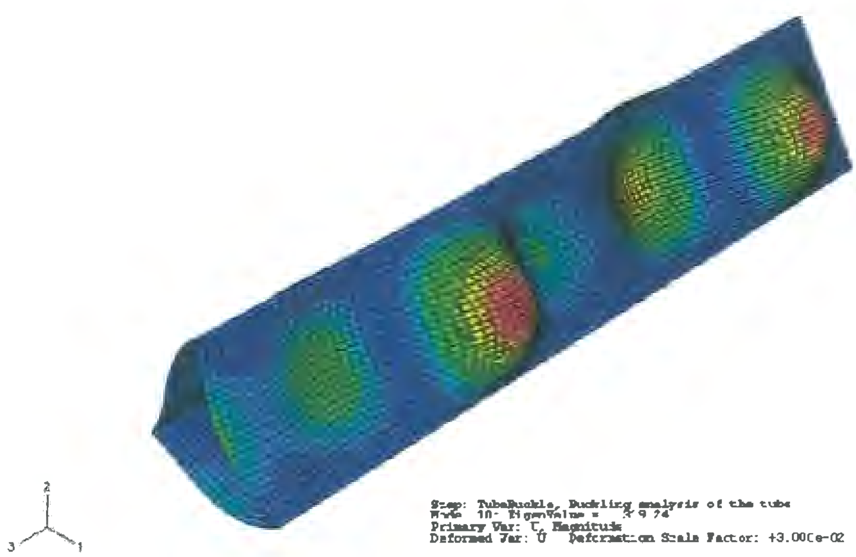

Figure 5.18 (j): 10th eigenmode

5.4 EFFECTS OF INITIAL EIGENMODE IMPERFECTION FACTORS (PERTURBING) SUBJECT TO DIFFERENT LOADING CONDITIONS

The purpose of this section is to investigate the significance that the introduction of imperfection factors (or perturbing) has on tubes when they are crushed subject to various loading conditions, and specifically the effect of two different velocity loading conditions. The imperfection factors introduced were not arbitrary imperfection shapes, as used by Nannucci [42], but precise ones predetermined by calculating the shape and magnitudes of these imperfections from an eigenmode buckling analysis for each tube beforehand. In order for the comparison to have maximum effect, a frictionless end boundary condition, i.e. between the bottom end of the tube and the bottom plate, was used.

5.4.1 SPECIFIC MASS AND INITIAL VELOCITY LOADING

5.4.1.1 WITHOUT THE INTRODUCTION OF INITIAL IMPERFECTION FACTORS

Figure 5.19 shows the final deformed square tube mesh of an analysis that includes no initial imperfection factors, subject to a specific mass and initial velocity loading. The initial velocity was 8.94 m.s^{-1} and the mass was 250 kg. The unperturbed mesh deforms into sharp folds. The profile is clearly not physically correct. The type of folding which occurs is non uniform and almost random-like folding. All four sides of the tube fold alternatively outwards and then inwards, or vice-versa, in a progressive manner. This is different to the folding mechanism which actually occurs and which is predicted by Jones [47] for a square tube of these dimensions and thickness.

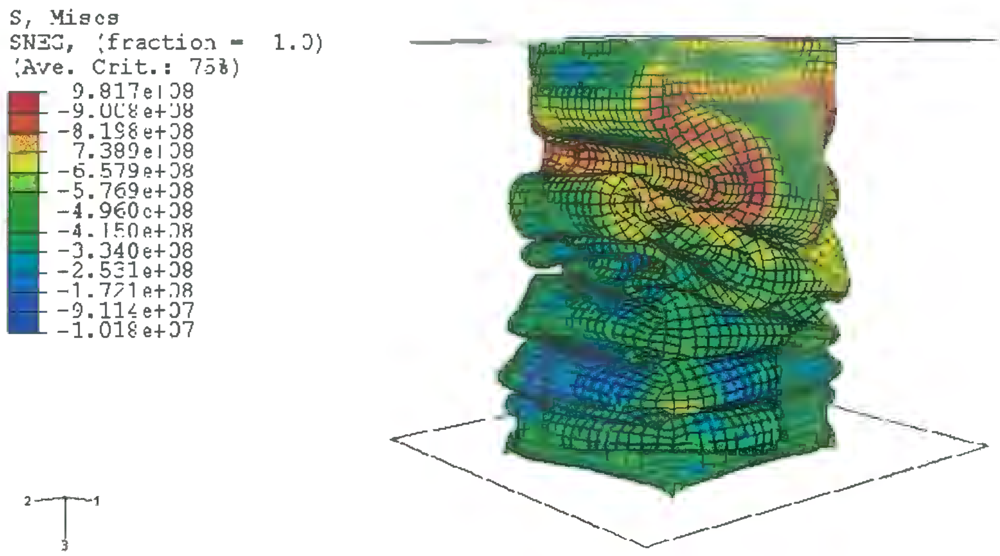

Figure 5.19 (a): Side view of a square tube crushed without the introduction of imperfection factors, subject to a specific mass (250 kg) and initial velocity (8.94 m.s^{-1}) loading.

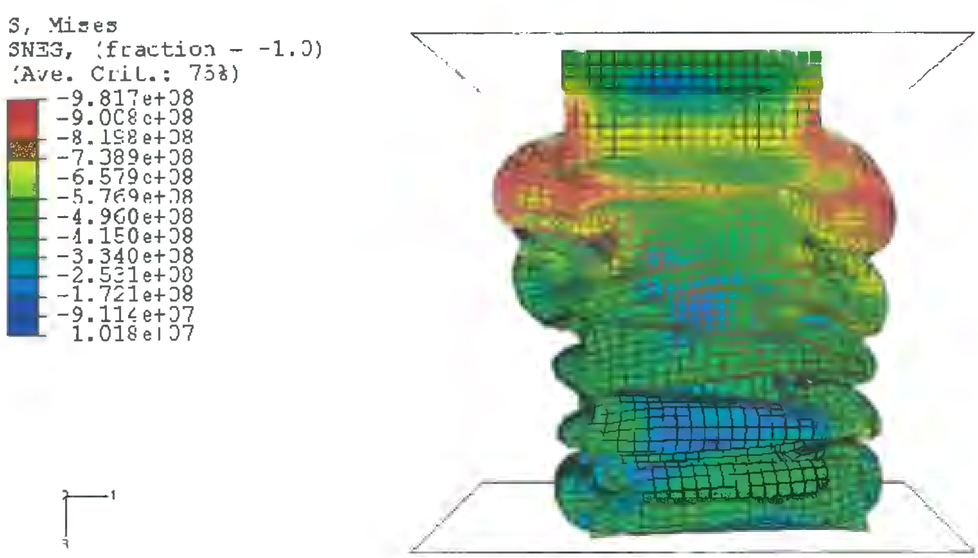

Figure 5.19 (b) Front view of a square tube crushed without the introduction of imperfection factors, subject to a specific mass (250 kg) and initial velocity (8.94 m.s^{-1}) loading.

5.4.1.2 WITH THE INTRODUCTION OF INITIAL IMPERFECTION FACTORS

Figure 5.20 shows a square tube crushed with the introduction of multiple imperfection factors, subject to a specific mass (250 kg) and initial velocity loading (8.94 $m.s^{-1}$). In contrast to the tube crushed without imperfection factors (Figure 5.19) which deforms into sharp folds, the tube crushed with introduced initial imperfection factors (Figure 5.20) folds into a smoothly buckled profile with regular folds. Even the small imperfection factors introduced into the mesh are enough to make the post buckling behaviour proceed smoothly.

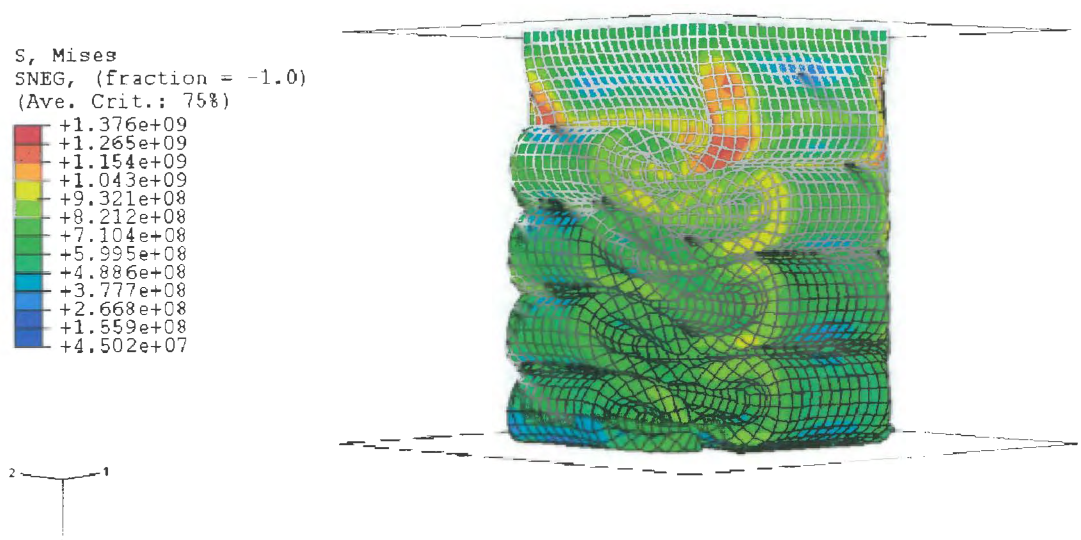

Figure 5.20 (a): Side view of a square tube crushed with the introduction of imperfection factors, subject to a specific mass (250 kg) and initial velocity (8.94 $m.s^{-1}$) loading.

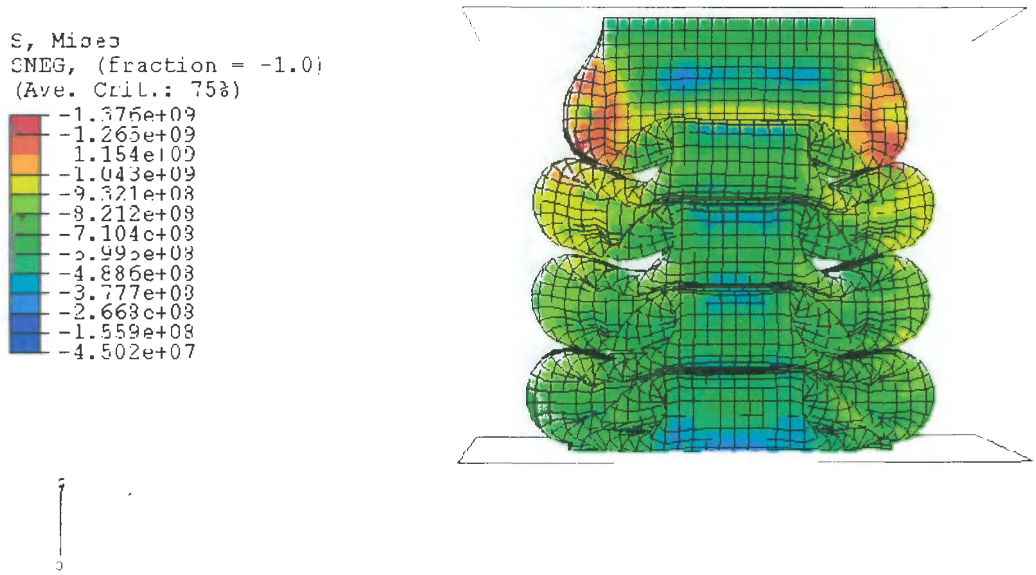

Figure 5.20 (b): Front view of a square tube crushed with the introduction of imperfection factors, subject to a specific mass (250 kg) and initial velocity (8.94 m.s^{-1}) loading.

5.4.2 CONSTANT VELOCITY LOADING

5.4.2.1 WITHOUT THE INTRODUCTION OF INITIAL IMPERFECTION FACTORS

Figure 5.21 shows a square tube crushed without the introduction of imperfection factors, subject to a constant velocity loading of 0.5 m.s^{-1}.

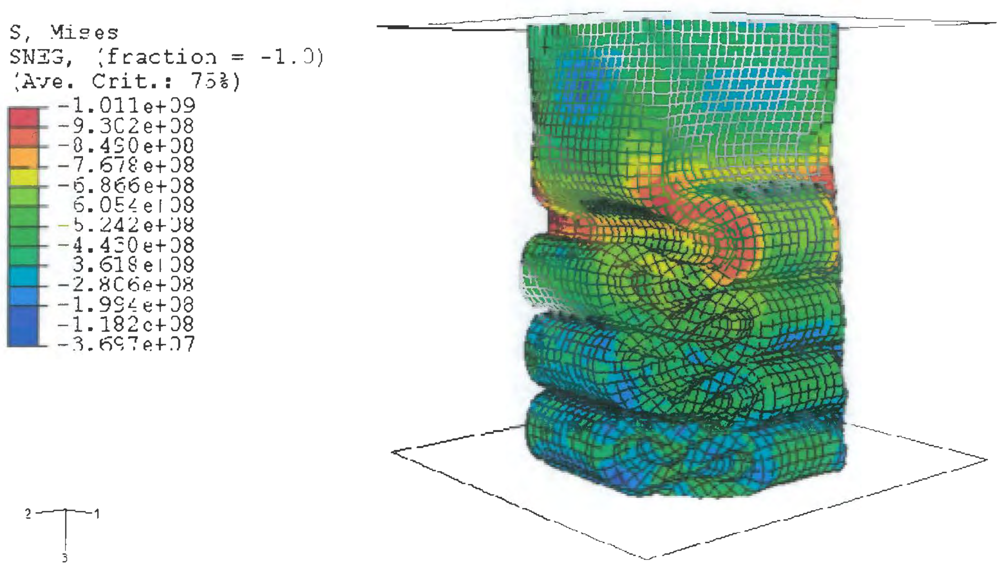

Figure 5.21 (a): Side view of a square tube crushed without the introduction of imperfection factors, subject to a constant velocity (0.5 m.s^{-1}) loading.

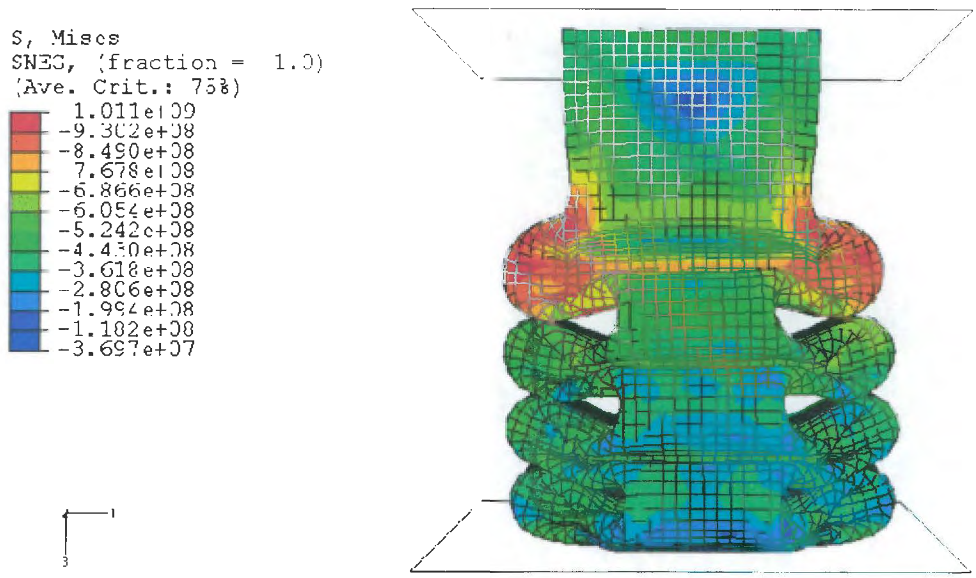

Figure 5.21 (b): Front view of a square tube crushed without the introduction of imperfection factors, subject to a constant velocity (0.5 m.s^{-1}) loading.

A comparison of Figure 5.19 and Figure 5.21 clearly indicates that the final deformed profile when using a specific mass and initial velocity loading is much more non uniform and incorrect, than when using a constant velocity loading. Therefore subjecting the tube model to a specific mass and initial velocity loading, without the introduction of imperfection factors, results in much greater errors mainly due to the resultant completely incorrect final deformed profile.

5.4.2.2 WITH THE INTRODUCTION OF INITIAL IMPERFECTION FACTORS

Figure 5.22 shows a square tube crushed with the introduction of imperfection factors, subject to a constant velocity loading. The folding mechanism remains virtually the same when subject to a constant velocity loading with or without the introduction of initial imperfection factors.

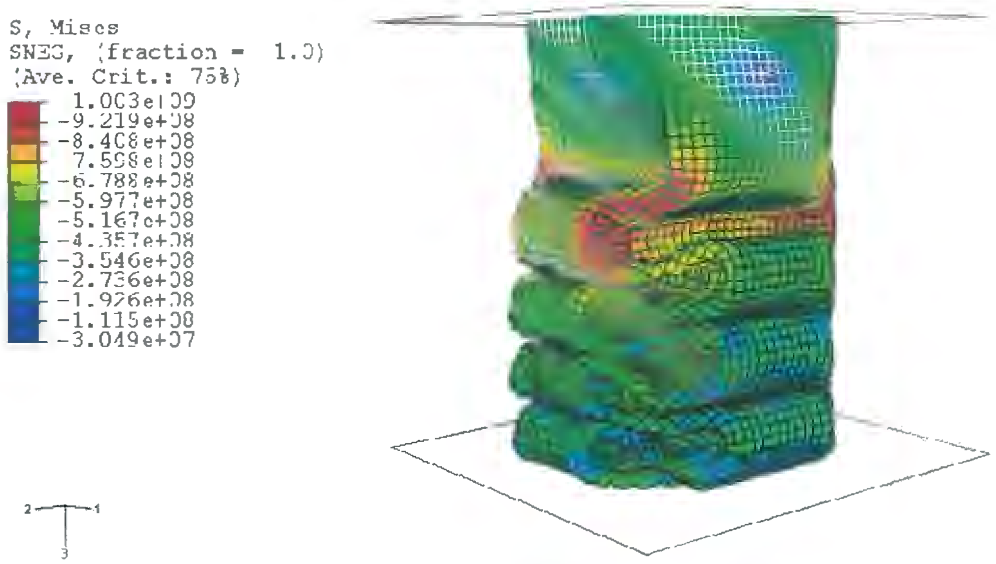

Figure 5.22 (a): Side view of a square tube crushed with the introduction of imperfection factors, subject to a constant velocity (0.5 m.s^{-1}) loading.

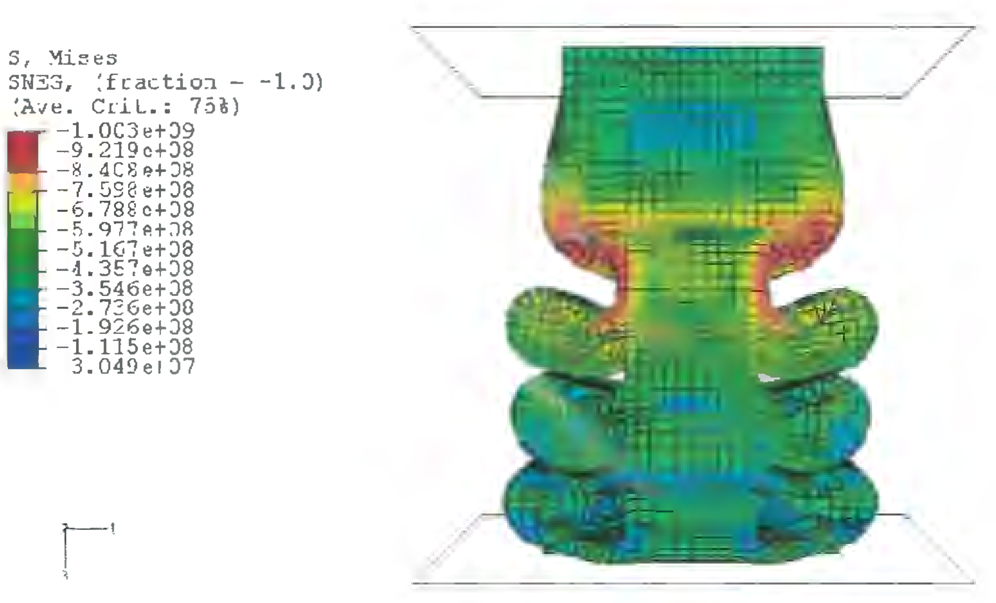

Figure 5.22 (b): Front view of a square tube crushed with the introduction of imperfection factors, subject to a constant velocity (0.5 m.s^{-1}) loading.

5.4.3 SUMMARY OF THE EFFECTS OF INITIAL EIGENMODE IMPERFECTION FACTORS UNDER VARIOUS LOADING CONDITIONS

When the initial imperfection factors (or perturbing) is not introduced into the model or when it is not done sufficiently accurate enough i.e. the introduced imperfection factors are either too large or too small, this results in three main types of errors:

i) Non uniform, random-like crushing, especially in the case of a specific mass and initial velocity loading.

ii) Over or under estimation of the peak reaction forces.

iii) Incorrect folding mechanism of the tube with regards to the sides of the tube folding inward or outward.

The above errors can occur when failing to use initial imperfection factors when required or else using initial imperfection factors incorrectly. It is therefore imperative that the modeller has a very good understanding of when and how to apply initial imperfection factors when modelling tubes.

5.5 DETAILED EFFECTS OF INITIAL EIGENMODE IMPERFECTION FACTORS UNDER DIFFERENT END BOUNDARY CONDITIONS SUBJECT TO A SPECIFIC MASS AND INITIAL VELOCITY LOADING

Since it was shown in Section 5.4 that a tube model without the introduction of imperfection factors subject to a specific mass and initial velocity loading condition, results in the greatest errors, it was decided to investigate and compare the tube models which were subjected to a specific mass and initial velocity in more detail, by investigating and comparing how they behave under different end boundary conditions. This section shows the detailed effects of eigenmode imperfection factors and lack thereof, under different end boundary conditions subject to a specific mass and initial velocity. The initial velocity was 8.94 $m.s^{-1}$ and the mass was 250 kg. Two types of end boundary conditions were used, namely

i) A frictionless end boundary condition.
ii) A fixed (encastred) end boundary condition.

The initial profiles of each of the square tubes are shown for comparison, with and without the introduction of imperfection factors, when they begin to deform. The final deformed profiles of the square tubes are also shown for comparison, with and without the introduction of imperfection factors, to illustrate the important role the introduction and use of proper imperfections has when modelling thin-walled tubes, particularly when these tubes are subjected to a specific mass and initial velocity.

5.5.1 USING A FRICTIONLESS END BOUNDARY CONDITION

5.5.1.1 USING NO INITIAL IMPERFECTION FACTORS FOR THE TUBE

Figure 5.23 shows the initial deformed profile of a square tube crushed without the introduction of imperfection factors, subject to a specific mass and initial velocity loading, using a frictionless end boundary condition. The tube does not fold progressively from the very bottom end as expected. All four sides start by folding inward and then outward as opposed to the actual correct folding method, as predicted theoretically or as under ideal experimental conditions.

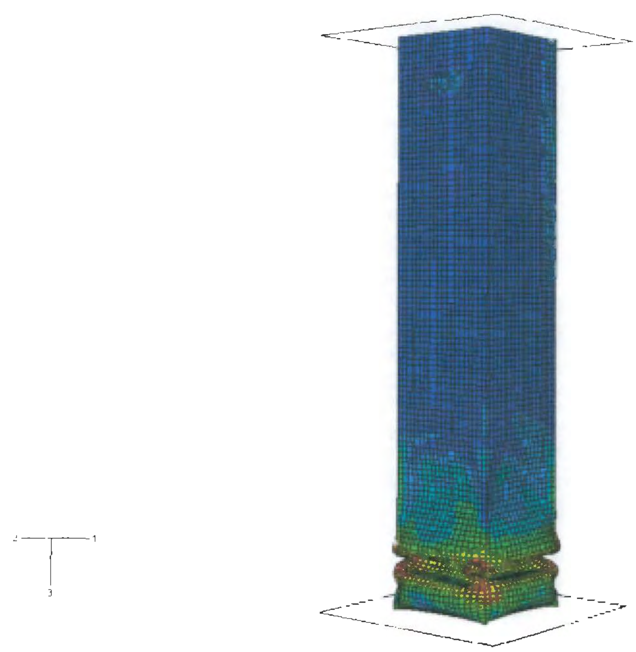

Figure 5.23: Initial deformed profile of a square tube crushed without the introduction of imperfection factors, subject to a specific mass and initial velocity loading, using a frictionless end boundary condition.

Figure 5.24 shows the final deformed square tube analysis using no eigenmode imperfection factors, subject to a specific mass and initial velocity loading. As shown in Section 5.4.1.1, the tube folds in a progressive but non uniform, random-like manner and a very incorrect deformed profile results. As a result of the incorrect deformed profile, associated large errors occur, such as incorrect reaction forces over the crushing distance as well as incorrect stresses and strains.

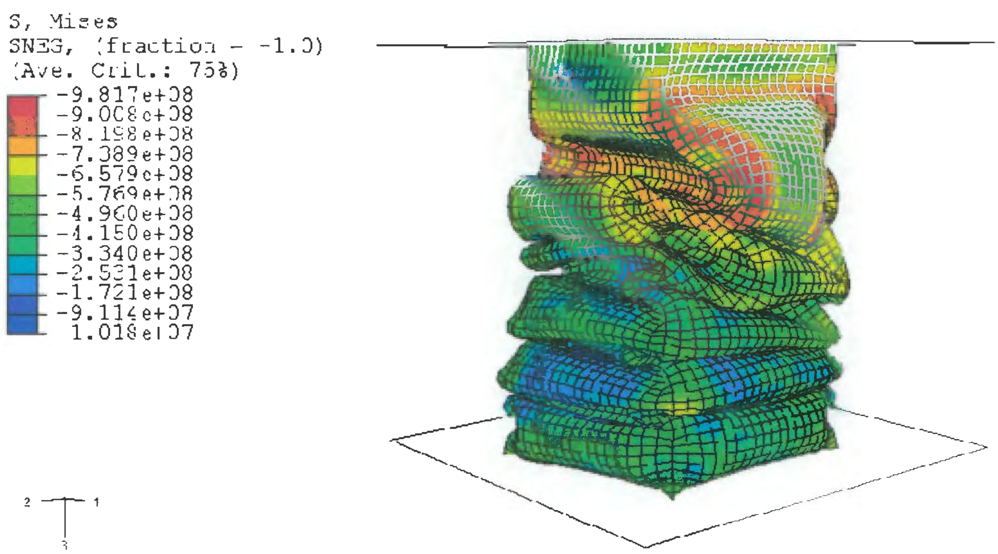

Figure 5.24 (a): Side view of a square tube crushed without the introduction of imperfection factors, subject to a specific mass and initial velocity loading, using a frictionless end boundary condition.

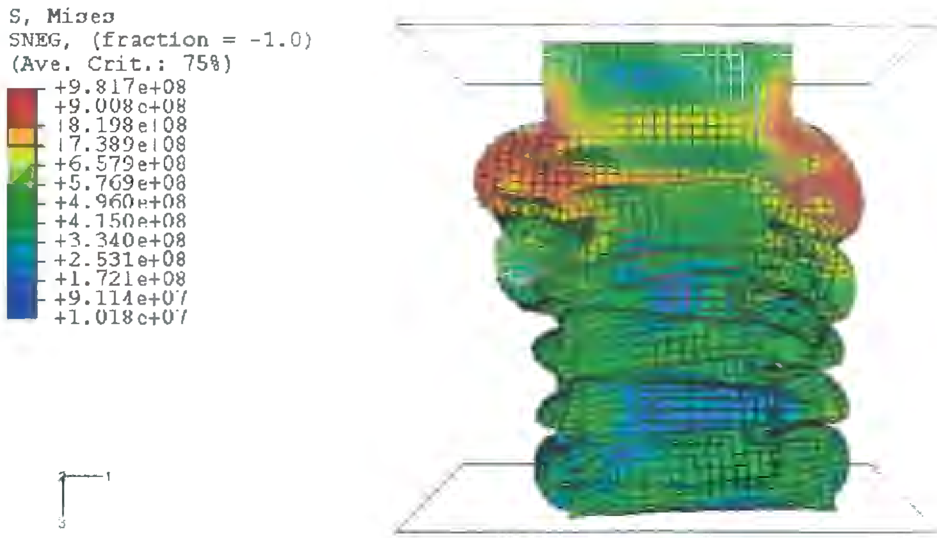

Figure 5.24 (b): Front view of a square tube crushed without the introduction of imperfection factors, subject to a specific mass initial velocity loading, using a frictionless end boundary condition.

5.5.1.2 USING MULTIPLE EIGENMODES AS INITIAL IMPERFECTION FACTORS FOR THE TUBE

Figure 5.25 shows an initial deformed profile of a square tube crushed using multiple eigenmode imperfection factors. Folding occurs progressively from the bottom end.

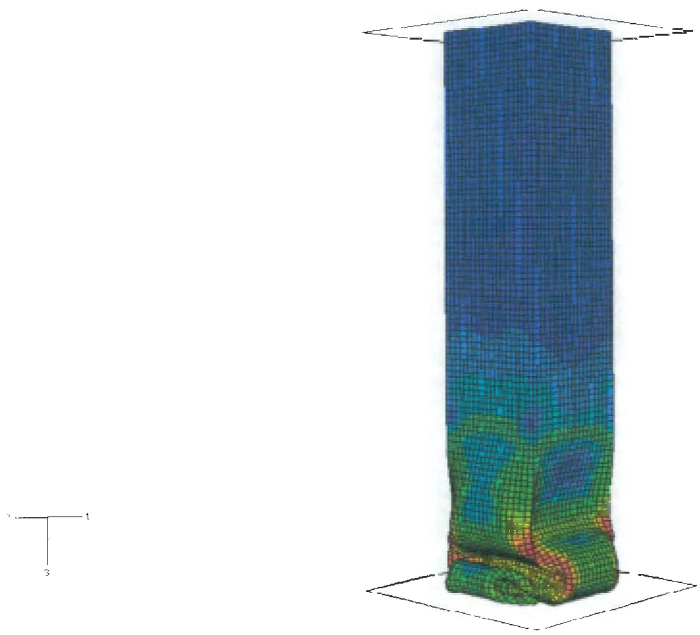

Figure 5.25: Initial deformed profile of a square tube crushed using multiple eigenmode imperfection factors, subject to a specific mass and initial velocity loading, using a frictionless end boundary condition.

Figure 5.26 shows the final deformed square tube analysis using multiple eigenmode imperfection factors. The correct type of uniform progressive folding occurs as predicted theoretically or as under ideal experimental conditions, thus illustrating the important significance of the introduction of imperfection factors in a tube model.

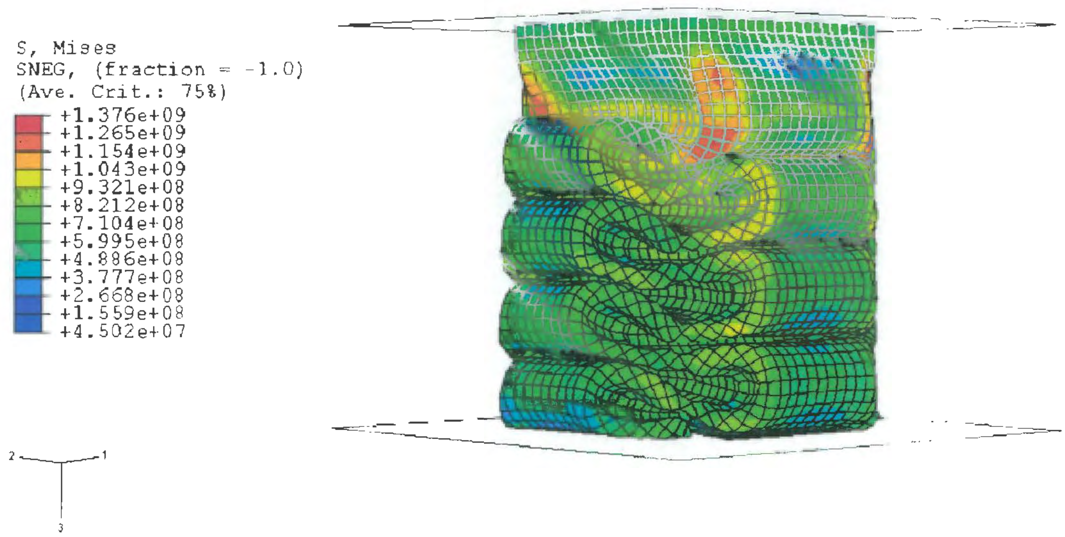

Figure 5.26 (a): Side view of a square tube crushed using multiple eigenmode imperfection factors, subject to a specific mass and initial velocity loading, using a frictionless end boundary condition.

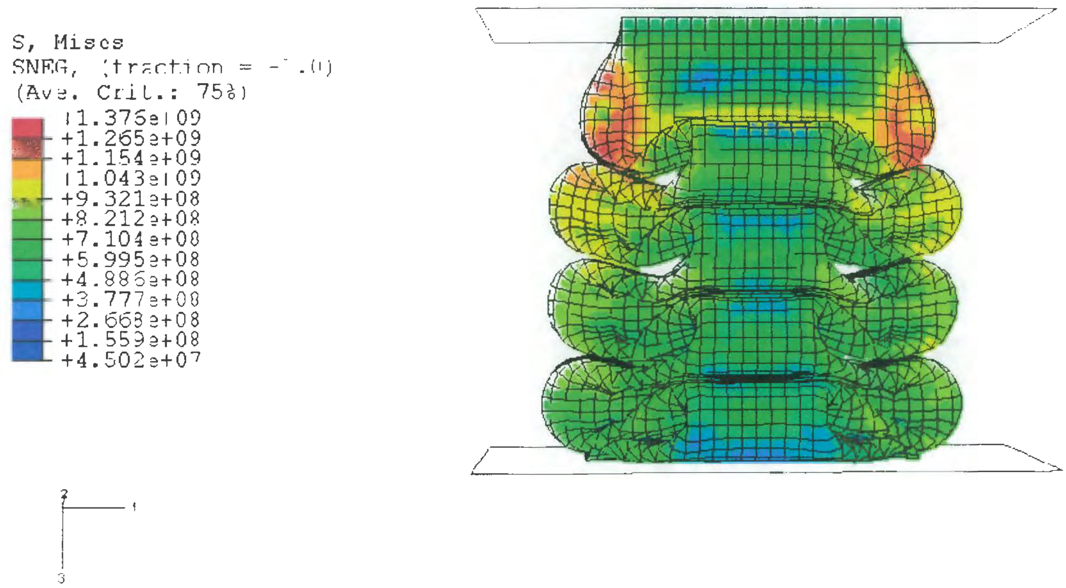

Figure 5.26 (b): Front view of a square tube crushed using multiple eigenmode imperfection factors, subject to a specific mass and initial velocity loading, using a frictionless end boundary condition.

5.5.2 USING A FIXED (ENCASTRED) END BOUNDARY CONDITION

5.5.2.1 USING NO INITIAL IMPERFECTION FACTORS FOR THE TUBE

Figure 5.27 shows the initial deformed profile of a square tube crushed without the introduction of imperfection factors. Folding begins to occur at $^{1}/_{3}$ and $^{2}/_{3}$ of its length from the bottom end of the tube in a semi-progressive, non uniform or random-like manner.

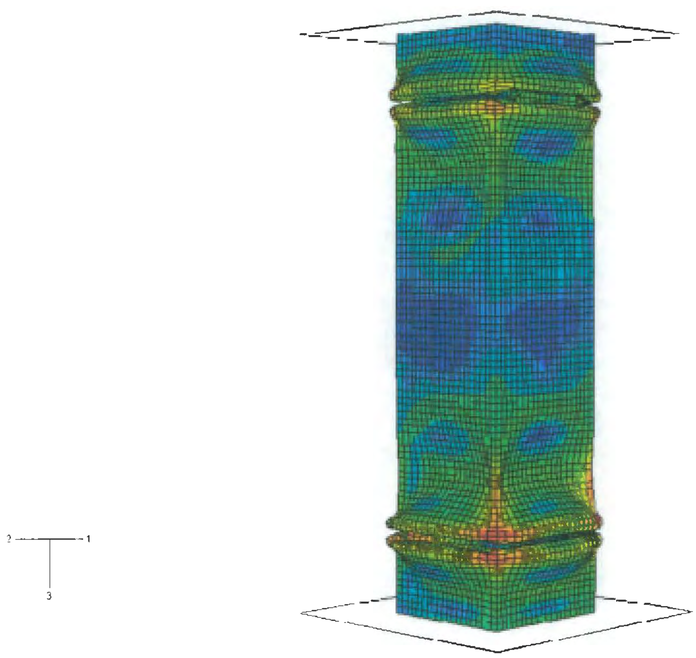

Figure 5.27: Initial deformed profile of a square tube crushed without the introduction of imperfection factors, subject to a specific mass and initial velocity loading, using a fixed (encastred) boundary condition.

Figure 5.28 shows the final deformed square tube mesh of an analysis using no eigenmode imperfection factors, subject to a specific mass and initial velocity loading. The tube folds in a progressive but non uniform, random-like manner which results in a very incorrect deformed profile. As a result of the incorrect deformed profile, associated large errors occur, such as incorrect reaction forces over the crushing distance as well as incorrect stresses and strains.

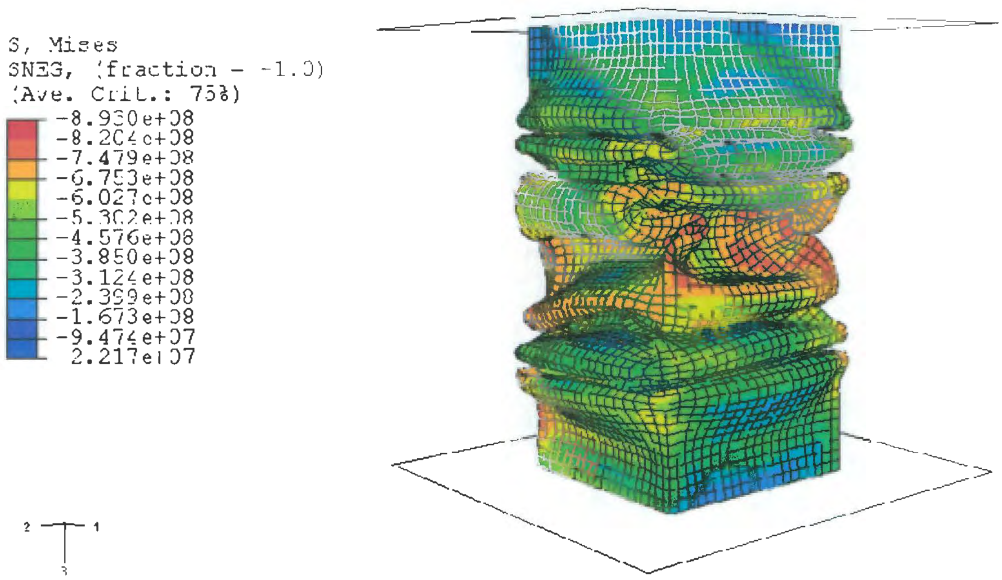

Figure 5.28 (a): Side view of a square tube crushed without the introduction of imperfection factors, subject to a specific mass and initial velocity loading, using a fixed (encastred) boundary condition.

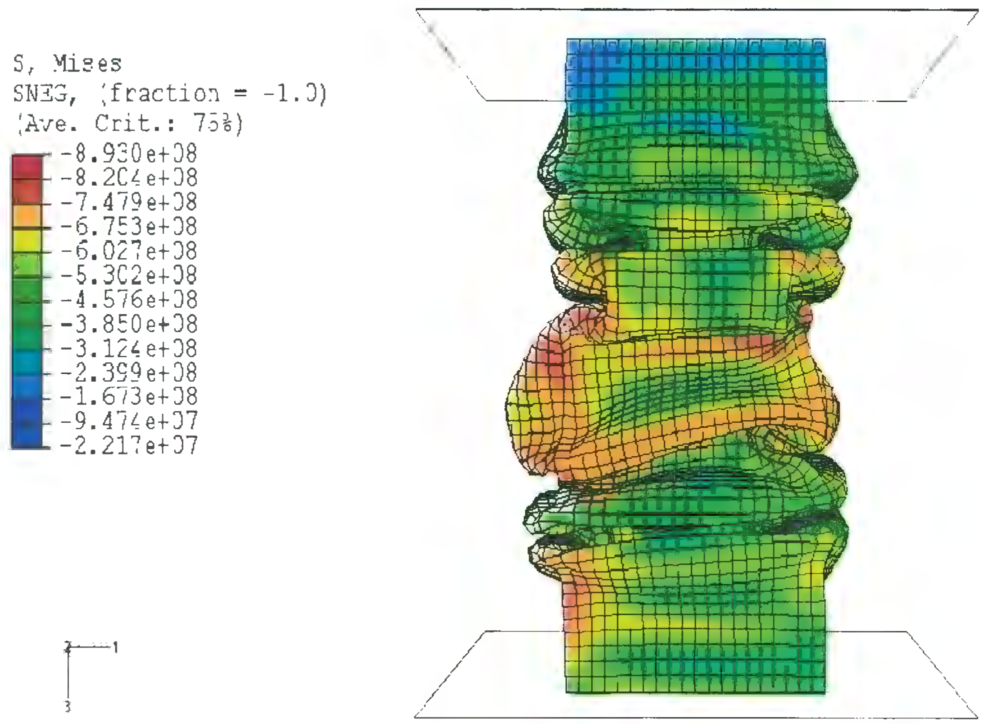

Figure 5.28 (b): Front view of a square tube crushed without the introduction of imperfection factors, subject to a specific mass and initial velocity loading, using a fixed (encastred) boundary condition.

5.5.2.2 USING MULTIPLE EIGENMODES AS INITIAL IMPERFECTION FACTORS FOR THE TUBE

Figure 5.29 shows that folding occurs progressively near to the top end of the tube and not from the bottom end as may have been expected. This is due to the influence that the fixed end boundary condition on the bottom of the tube has on the first eigenmode. The major part of the first eigenmode displacement occurs near the top end of the tube and thus has a direct influence on the progressive folding which therefore also begins near the top end of the tube.

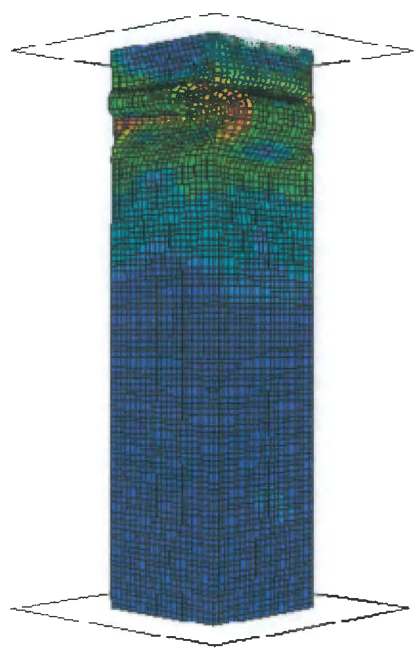

Figure 5.29: Initial deformed profile of a square tube crushed using multiple eigenmode imperfection factors, subject to a specific mass and initial velocity loading, using a fixed (encastred) boundary condition.

Figure 5.30, shows the final deformed square tube mesh of an analysis using multiple eigenmode imperfection factors. The correct type of uniform progressive folding occurs as predicted theoretically or as under ideal experimental conditions, thus illustrating the important significance of the introduction of imperfection factors in a tube model.

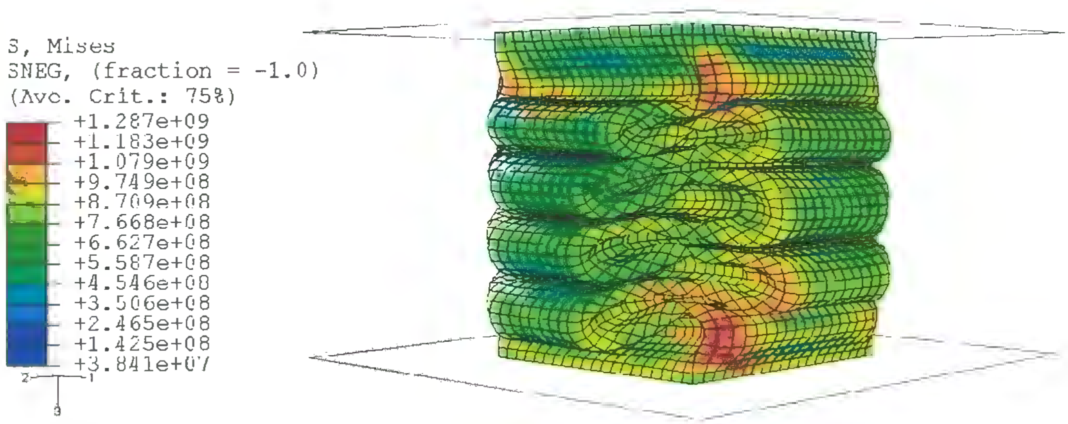

Figure 5.30 (a): Side view of a square tube crushed using multiple eigenmode imperfection factors, subject to a specific mass and initial velocity loading, using a fixed (encastred) boundary condition.

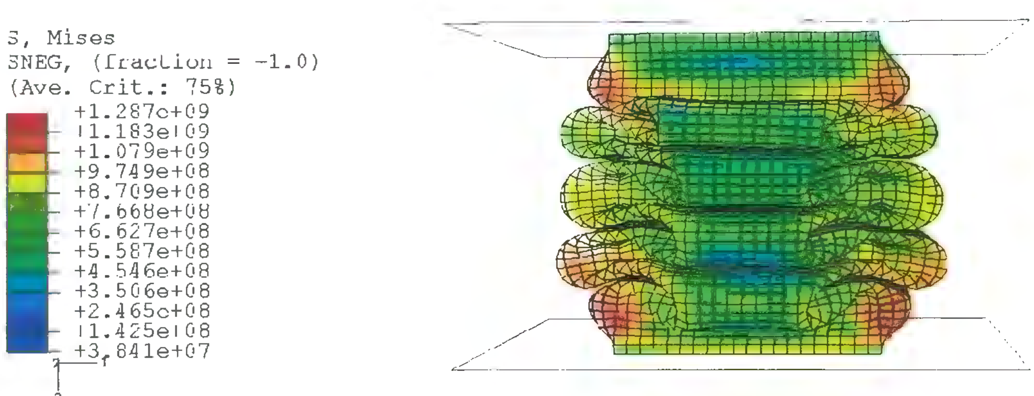

Figure 5.30 (b): Front view of a square tube crushed using multiple eigenmode imperfection factors, subject to a specific mass and initial velocity loading, using a fixed (encastred) boundary condition.

5.5.3 DISCUSSION OF THE INTRODUCTION OF INITIAL IMPERFECTION FACTORS

Sections 5.5.1 and 5.5.2 illustrate the important significance of the introduction of imperfection factors in a tube model. These two sections also illustrate the significant effect that the end boundary condition has on the tube, particularly when it begins to buckle, as well as on the final deformed profile.

5.6 DETAILED EFFECTS OF INITIAL EIGENMODE IMPERFECTION FACTORS UNDER A FRICTIONLESS END BOUNDARY CONDITION SUBJECT TO A CONSTANT VELOCITY LOADING

Section 5.6 shows the detailed effects of square tubes crushed under a frictionless end boundary condition using their associated individual eigenmodes as imperfection factors, using multiple eigenmodes as imperfection factors and using no imperfection factors, subject to a constant velocity loading of 0.5 $m.s^{-1}$.

The deformed profiles of square tubes as well as tables of the values of the peak reaction forces are shown. The final Reaction Forces versus Displacement graphs of these crushed square tubes can be seen in Appendix A.

The first Peak Reaction Force is always larger than the subsequent Peak Reaction Forces since the formation of the first buckling lobe requires a much greater force than for the formation of the subsequent buckling lobes once the progressive buckling has begun. The tube models using multiple eigenmodes as imperfection factors are the most accurate since when a long thin-walled tube undergoes progressive buckling all of the eigenmodes will be present, although to a lesser degree, starting from the first eigenmode which dominates, as discussed earlier in Section 4.6.

5.6.1 USING THE 1ST EIGENMODE AS AN IMPERFECTION FACTOR FOR THE TUBE

Figure 5.31 shows the final deformed profile of the square tube when using the 1st eigenmode as an imperfection factor. The profile is as predicted theoretically or as under ideal experimental conditions. This is as expected as the 1st eigenmode dominates all of the other eigenmodes. The deformed profile of this model using the 1st eigenmode is also almost identical to the deformed profile of the model using multiple eigenmodes as imperfection factors, in which the 1st eigenmode is allowed to dominate.

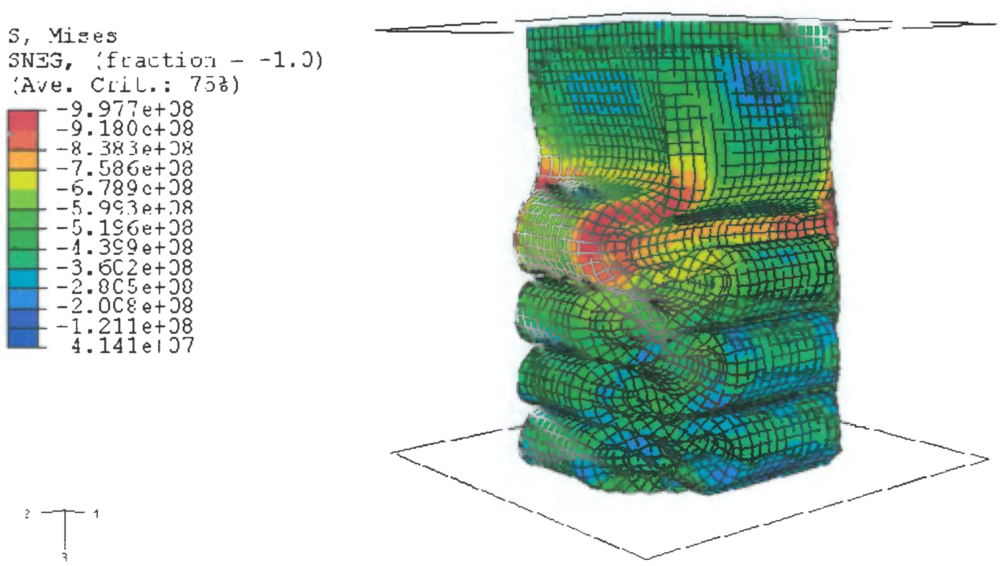

Figure 5.31: Final deformed profile of a square tube crushed against a frictionless end plate using the 1st eigenmode as an imperfection factor, subject to a constant velocity loading.

Table 5.1 shows the magnitudes of the peak reaction forces as well as the mean reaction force of a square tube crushed against a frictionless end plate using the 1st eigenmode as an imperfection factor. Note that in all cases the mean force is the overall mean reaction force and not the mean of the peak reaction forces.

Table 5.1: Peak Reaction forces of a square tube crushed against a frictionless end plate using the 1st eigenmode as an imperfection factor.

Peak Reaction Force No.	Reaction Force (N)
1	78115
2	48278
3	39210
4	52438
5	33502
6	60132
7	37836
Overall mean force	29362

5.6.2 USING THE 2ND EIGENMODE AS AN IMPERFECTION FACTOR FOR THE TUBE

Figure 5.32 shows the final deformed profile of the square tube when using the 2nd eigenmode as an imperfection factor. The final deformed profile shows that the tube begins to twist.

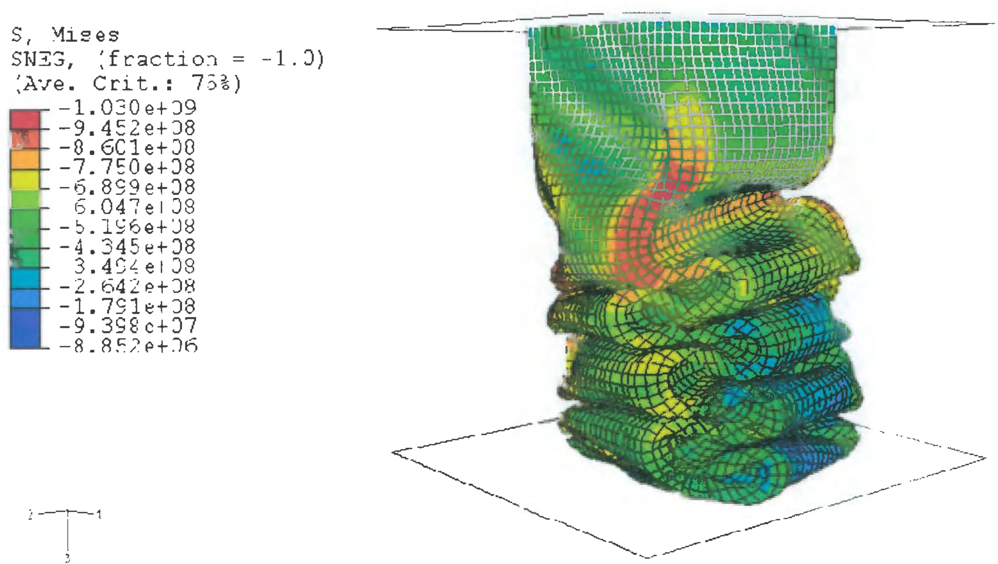

Figure 5.32: Final deformed profile of a square tube crushed against a frictionless end plate using the 2nd eigenmode as an imperfection factor, subject to a constant velocity loading.

Table 5.2 shows the magnitudes of the peak reaction forces as well as the mean reaction force of a square tube crushed against a frictionless end plate using the 2nd eigenmode as an imperfection factor.

Table 5.2: Peak Reaction forces of a square tube crushed against a frictionless end plate using the 2nd eigenmode as an imperfection factor.

Peak Reaction Force No.	Reaction Force (N)
1	91262
2	36079
3	44574
4	48176
5	53244
6	51725
7	59069
8	60653
Overall mean force	32312

5.6.3 USING THE 3RD EIGENMODE AS AN IMPERFECTION FACTOR FOR THE TUBE

Figure 5.33 shows the final deformed profile of the square tube when using the 3rd eigenmode as an imperfection factor. The final deformed profile shows that the tube begins to twist. further to approximately 45 degrees.

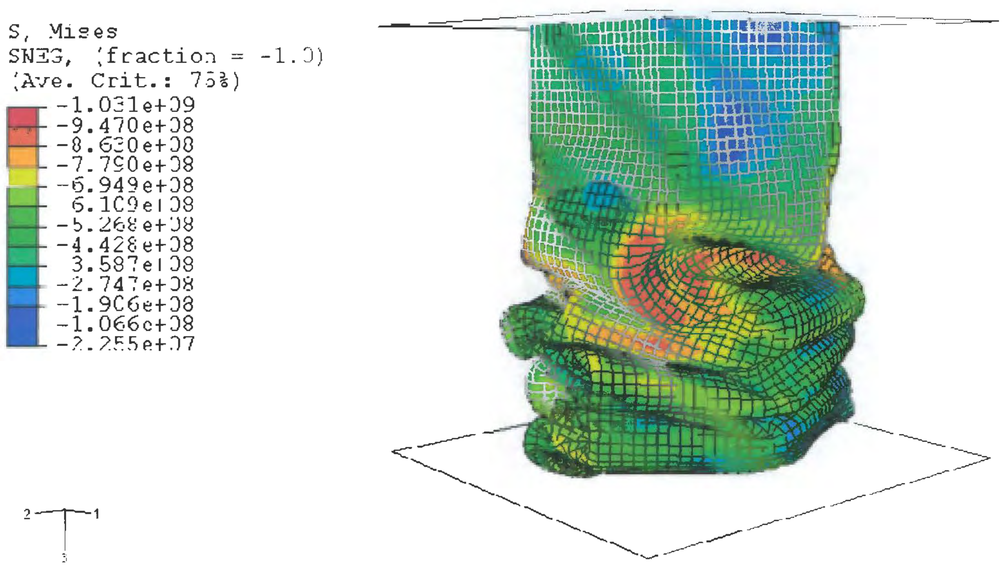

Figure 5.33: Final deformed profile of a square tube crushed against a frictionless end plate using the 3rd eigenmode as an imperfection factor, subject to a constant velocity loading.

Table 5.3 shows the magnitudes of the peak reaction forces as well as the mean reaction force of a square tube crushed against a frictionless end plate using the 3rd eigenmode as an imperfection factor.

Table 5.3: Peak Reaction forces of a square tube crushed against a frictionless end plate using the 3rd eigenmode as an imperfection factor.

Peak Reaction Force No.	Reaction Force (N)
1	91262
2	34800
3	45731
4	43819
5	43288
6	42229
7	40450
8	40053
Overall mean force	31508

5.6.4 USING THE 4^{TH} EIGENMODE AS AN IMPERFECTION FACTOR FOR THE TUBE

Figure 5.34 shows the final deformed profile of the square tube when using the 4^{th} eigenmode as an imperfection factor. The final deformed profile shows that the tube has twisted slightly but also moved horizontally on the bottom plate. The first two folds at the bottom of the tube have sides which abnormally fold outward. This can be attributed to the imperfection introduced by the 4^{th} eigenmode in which the bottom end of the tube is folded inward on all four sides, resulting in initial outward folds.

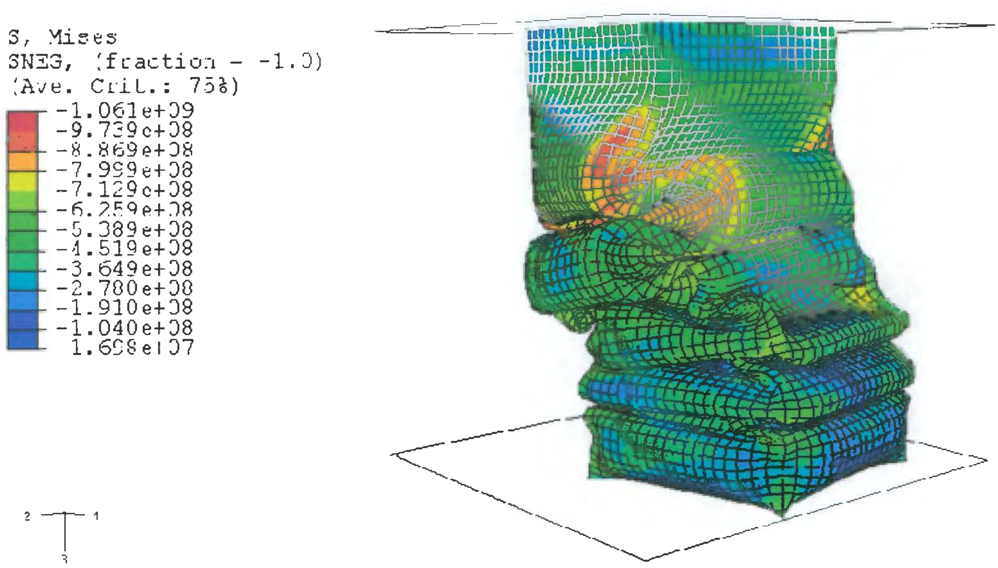

Figure 5.34: Final deformed profile of a square tube crushed against a frictionless end plate using the 4^{th} eigenmode as an imperfection factor, subject to a constant velocity loading.

Table 5.4 shows the magnitudes of the peak reaction forces as well as the mean reaction force of a square tube crushed against a frictionless end plate using the 4th eigenmode as an imperfection factor.

Table 5.4: Peak Reaction forces of a square tube crushed against a frictionless end plate using the 4th eigenmode as an imperfection factor.

Peak Reaction Force No.	Reaction Force (N)
1	93242
2	81027
3	73101
4	40823
5	39357
6	44241
7	45150
Overall mean force	38375

5.6.5 USING THE 5TH EIGENMODE AS AN IMPERFECTION FACTOR FOR THE TUBE

Figure 5.35 shows the final deformed profile of the square tube when using the 5th eigenmode as an imperfection factor. The final deformed profile shows that the tube deforms very similar to the tube model using multiple eigenmodes as imperfections factors. The difference though with this model is that the first two peak reaction forces are a lot higher, particularly the first peak reaction force, which is 14959 N greater in magnitude.

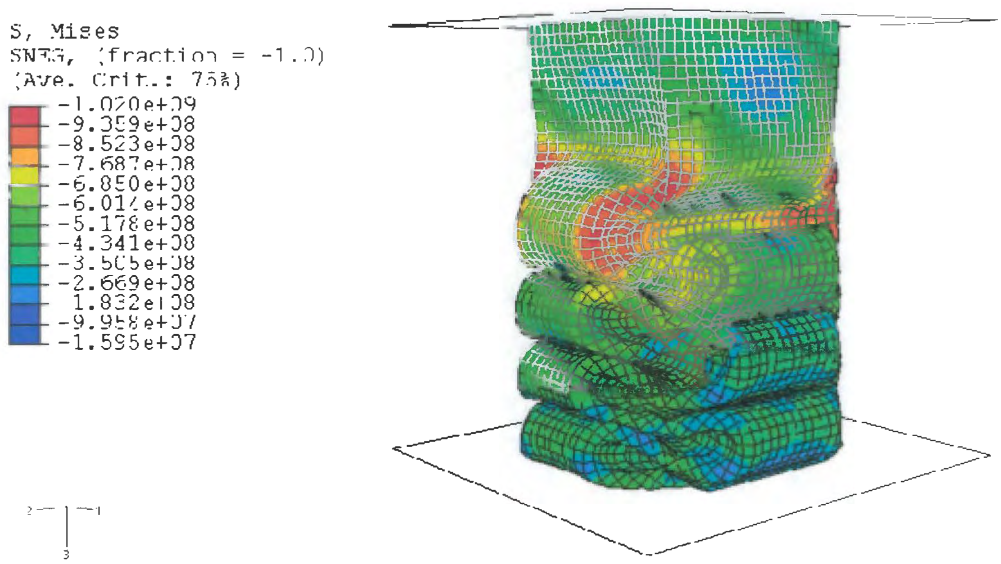

Figure 5.35: Final deformed profile of a square tube crushed against a frictionless end plate using the 5th eigenmode as an imperfection factor, subject to a constant velocity loading.

Table 5.5 shows the magnitudes of the peak reaction forces as well as the mean reaction force of a square tube crushed against a frictionless end plate using the 5th eigenmode as an imperfection factor.

Table 5.5: Peak Reaction forces of a square tube crushed against a frictionless end plate using the 5th eigenmode as an imperfection factor.

Peak Reaction Force No.	Reaction Force (N)
1	93093
2	61851
3	37481
4	52395
5	37452
6	49032
7	35820
Overall mean force	29379

5.6.6 USING THE 6TH EIGENMODE AS AN IMPERFECTION FACTOR FOR THE TUBE

Figure 5.36 shows the final deformed profile of the square tube when using the 6th eigenmode as an imperfection factor. The final deformed profile shows that the tube deforms with only three folds on the left side as opposed to the models using the 1st , 5th and multiple eigenmodes.

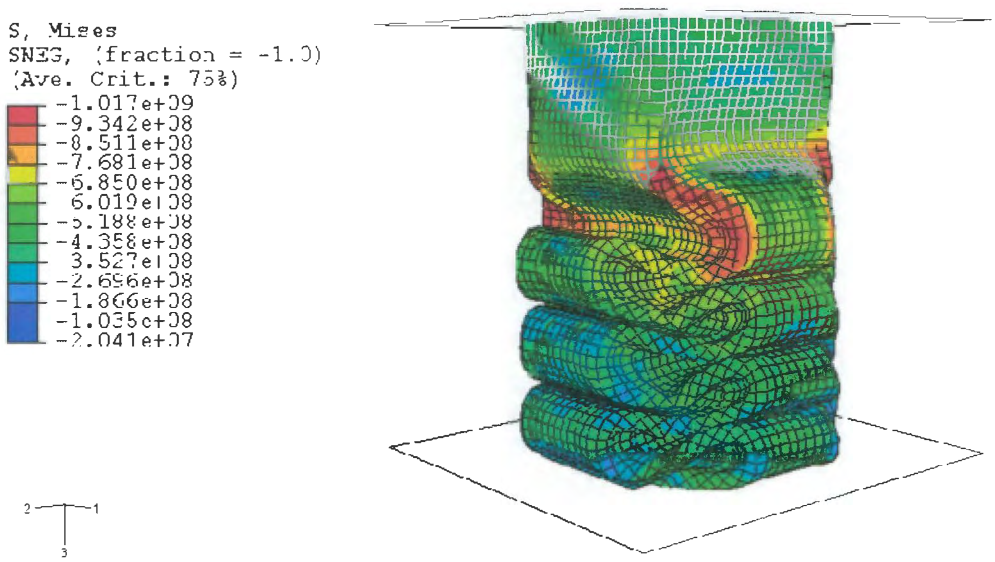

Figure 5.36: Final deformed profile of a square tube crushed against a frictionless end plate using the 6th eigenmode as an imperfection factor, subject to a constant velocity loading.

Table 5.6 shows the magnitudes of the peak reaction forces as well as the mean reaction force of a square tube crushed against a frictionless end plate using the 6^{th} eigenmode as an imperfection factor.

Table 5.6: Peak Reaction forces of a square tube crushed against a frictionless end plate using the 6^{th} eigenmode as an imperfection factor.

Peak Reaction Force No.	Reaction Force (N)
1	93530
2	47761
3	38635
4	52522
5	38052
6	51145
7	37733
Overall mean force	29532

5.6.7 USING THE 7TH EIGENMODE AS AN IMPERFECTION FACTOR FOR THE TUBE

Figure 5.37 shows the final deformed profile of the square tube when using the 7th eigenmode as an imperfection factor. The final deformed profile shows that the tube deforms almost identical to the previous tube model using the 6th eigenmode. The reaction forces vary slightly though between these two models.

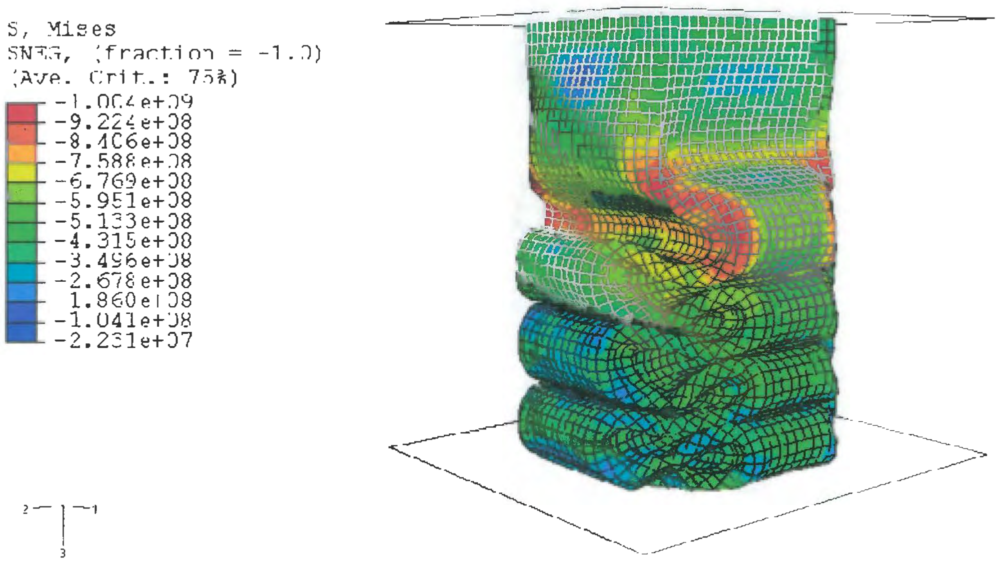

Figure 5.37: Final deformed profile of a square tube crushed against a frictionless end plate using the 8th eigenmode as an imperfection factor, subject to a constant velocity loading.

Table 5.7 shows the magnitudes of the peak reaction forces as well as the mean reaction force of a square tube crushed against a frictionless end plate using the 7th eigenmode as an imperfection factor.

Table 5.7: Peak Reaction forces of a square tube crushed against a frictionless end plate using the 7th eigenmode as an imperfection factor.

Peak Reaction Force No.	Reaction Force (N)
1	93555
2	45889
3	37564
4	51659
5	34358
6	51739
7	41474
Overall mean force	29541

5.6.8 USING THE 8TH EIGENMODE AS AN IMPERFECTION FACTOR FOR THE TUBE

Figure 5.38 shows the final deformed profile of the square tube when using the 8th eigenmode as an imperfection factor. The final deformed profile shows that the tube deforms slightly more than the previous two models using the 6th and 7th eigenmodes. The reaction forces also vary slightly compared with the previous two models.

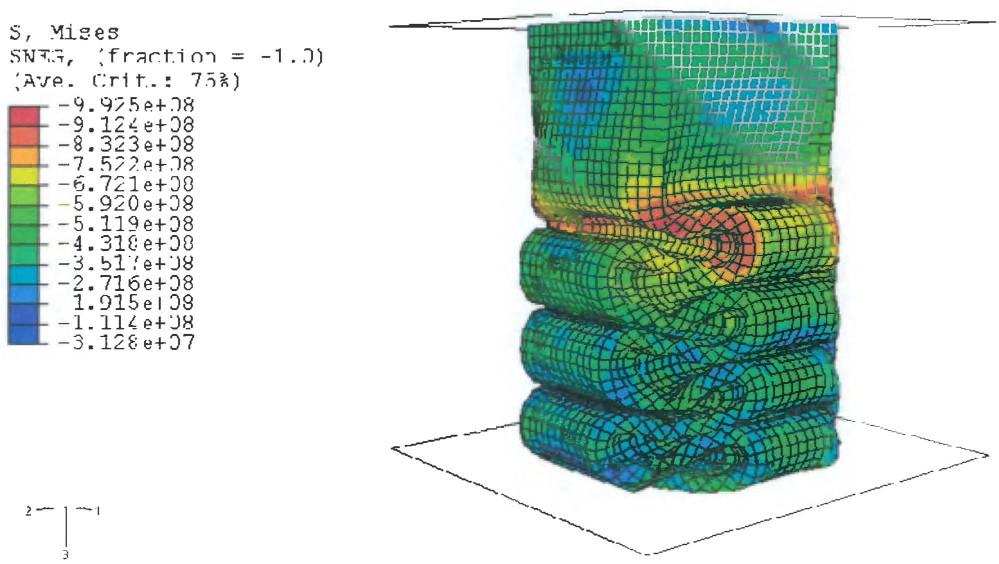

Figure 5.38: Final deformed profile of a square tube crushed against a frictionless end plate using the 8th eigenmode as an imperfection factor, subject to a constant velocity loading.

Table 5.8 shows the magnitudes of the peak reaction forces as well as the mean reaction force of a square tube crushed against a frictionless end plate using the 8th eigenmode as an imperfection factor.

Table 5.8: Peak Reaction forces of a square tube crushed against a frictionless end plate using the 8th eigenmode as an imperfection factor.

Peak Reaction Force No.	Reaction Force (N)
1	93516
2	47908
3	39682
4	48038
5	33648
6	51613
7	32981
Overall mean force	29303

5.6.9 USING THE 9TH EIGENMODE AS AN IMPERFECTION FACTOR FOR THE TUBE

Figure 5.39 shows the final deformed profile of the square tube when using the 9th eigenmode as an imperfection factor. The final deformed profile shows that the tube deforms almost identical to the previous tube model using the 8th eigenmode. The reaction forces vary slightly though between these two models.

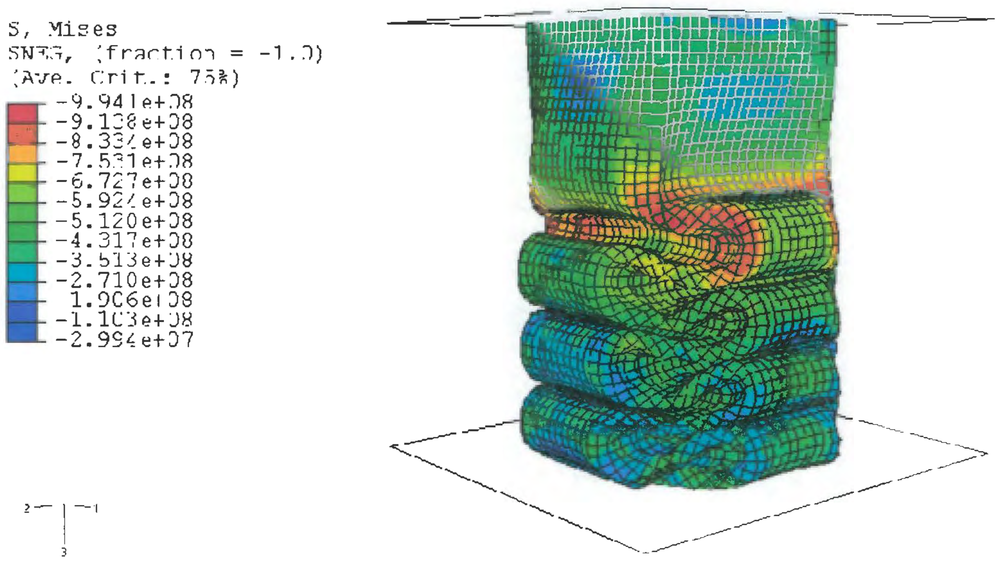

Figure 5.39: Final deformed profile of a square tube crushed against a frictionless end plate using the 9th eigenmode as an imperfection factor, subject to a constant velocity loading.

Table 5.9 shows the magnitudes of the peak reaction forces as well as the mean reaction force of a square tube crushed against a frictionless end plate using the 9th eigenmode as an imperfection factor.

Table 5.9: Peak Reaction forces of a square tube crushed against a frictionless end plate using the 9th eigenmode as an imperfection factor.

Peak Reaction Force No.	Reaction Force (N)
1	93704
2	46086
3	41849
4	48099
5	34193
6	49654
7	36671
Overall mean force	29606

5.6.10 USING THE 10TH EIGENMODE AS AN IMPERFECTION FACTOR FOR THE TUBE

Figure 5.40 shows the final deformed profile of the square tube when using the 10th eigenmode as an imperfection factor. The final deformed profile shows that the tube deforms almost identical to the tube models using the 1th, 5th and multiple eigenmodes. The reaction forces vary slightly though between all of these models.

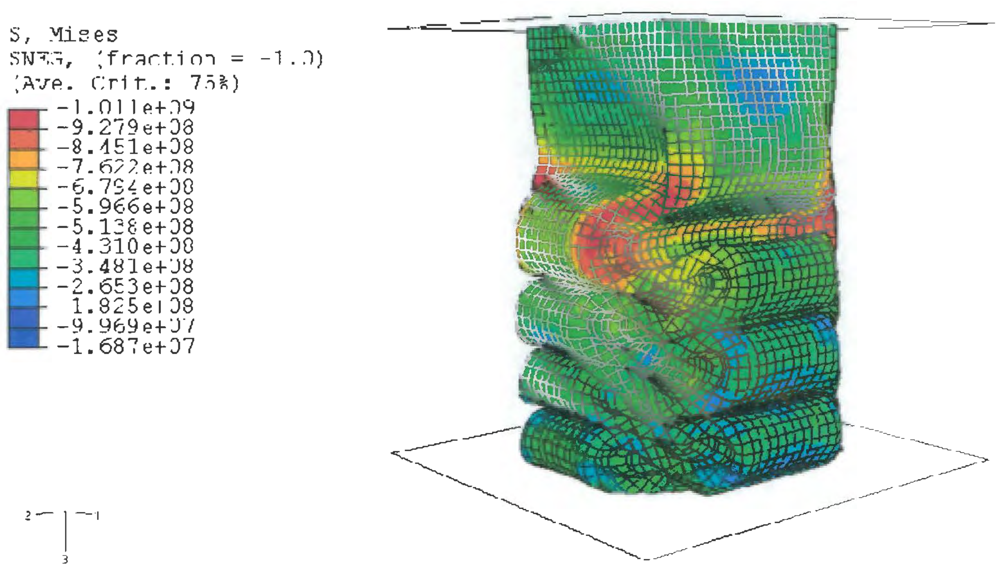

Figure 5.40: Final deformed profile of a square tube crushed against a frictionless end plate using the 10th eigenmode as an imperfection factor, subject to a constant velocity loading.

Table 5.10 shows the magnitudes of the peak reaction forces as well as the mean reaction force of a square tube crushed against a frictionless end plate using the 10th eigenmode as an imperfection factor.

Table 5.10: Peak Reaction forces of a square tube crushed against a frictionless end plate using the 10th eigenmode as an imperfection factor.

Peak Reaction Force No.	Reaction Force (N)
1	93762
2	47722
3	38718
4	48641
5	33707
6	50341
7	39767
Overall mean force	29536

5.6.11 USING MULTIPLE EIGENMODES AS IMPERFECTION FACTORS FOR THE TUBE

Figure 5.41 shows the final deformed profile of the square tube when using multiple eigenmodes as imperfection factors. This tube model uses a combination of eigenmodes scaled downwards in magnitude from the 1st eigenmode because it is the dominant eigenmode.

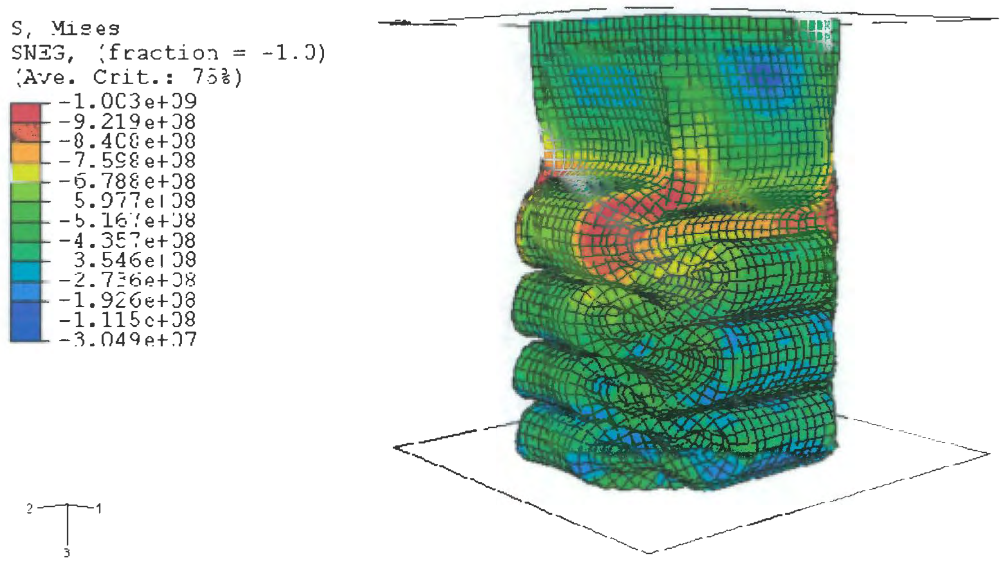

Figure 5.41: Final deformed profile of a square tube crushed against a frictionless end plate using multiple eigenmodes as imperfection factors, subject to a constant velocity loading.

Table 5.11 shows the magnitudes of the peak reaction forces as well as the mean reaction force of a square tube crushed against a frictionless end plate using multiple eigenvalues as imperfection factors.

Table 5.11: Peak Reaction forces of a square tube crushed against a frictionless end plate using multiple eigenvalues as imperfection factors.

Peak Reaction Force No.	Reaction Force (N)
1	78134
2	56017
3	38747
4	50642
5	32593
6	56293
7	39919
Overall mean force	29438

5.6.12 USING NO IMPERFECTION FACTORS FOR THE TUBE

Figure 5.42 shows the final deformed profile of the square tube when using the no imperfection factors. The final deformed profile shows that the tube deforms almost identical to the tube model using the 6th , 7th and 9th eigenmodes. The reaction forces vary though between these models. What is of significance in this model subject to a constant velocity loading, is that the deformed profile of this model tube is as predicated theoretically i.e. it deforms progressively with uniform folds. This is in contrast to the tube model subject to a specific mass and initial velocity loading which deforms non uniformly and incorrectly, as is predicted theoretically.

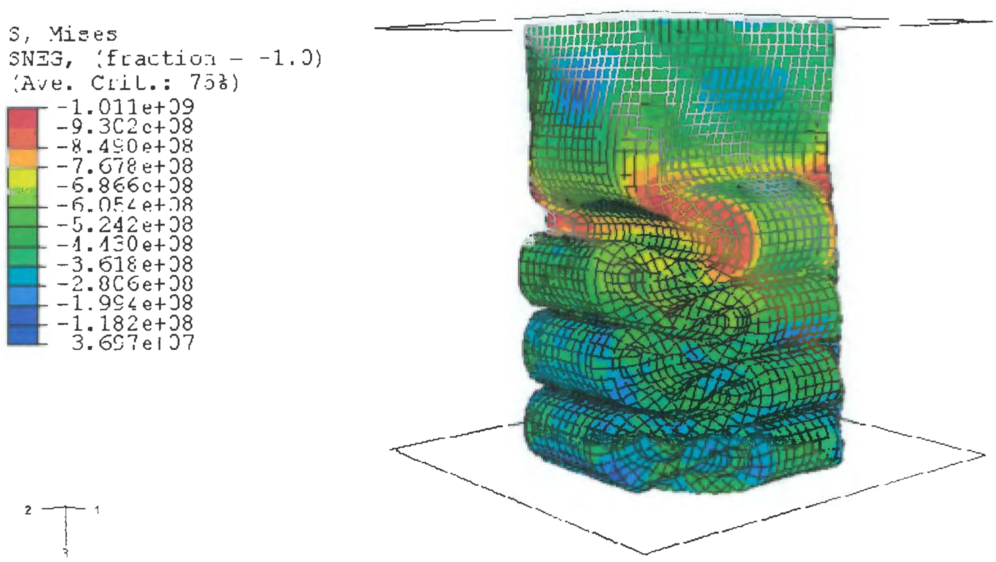

Figure 5.42: Final deformed profile of a square tube crushed against a frictionless end plate using no imperfection factors, subject to a constant velocity loading.

Table 5.12 shows the magnitudes of the peak reaction forces as well as the mean reaction force of a square tube crushed against a frictionless end plate using no imperfection factors.

Table 5.12: Peak Reaction forces of a square tube crushed against a frictionless end plate using no imperfection factors.

Peak Reaction Force No.	Reaction Force (N)
1	96008
2	45166
3	38892
4	52827
5	34368
6	49494
7	36142
Overall mean force	29857

5.7 COMPARISON OF THE PEAK AND AVERAGE REACTION FORCES OF A SQUARE TUBE USING A FRICTIONLESS END BOUNDARY CONDITION CRUSHED USING THE DIFFERENT EIGENMODES AS INITIAL IMPERFECTION FACTORS SUBJECT TO A CONSTANT VELOCITY LOADING

A graph of all of the previous Peak Reaction forces using each eigenmode separately, using multiple eigenmodes (a combination of all of each the individual eigenmodes) as imperfection factors to perturb the model as well as without using any imperfection factors, is plotted for comparison in Figure 5.43. The Peak Reaction Force graph using the 1st eigenmode as an imperfection factor has the most similar shape and magnitude as the Peak Reaction Force graph using multiple eigenmodes as imperfection factors. This result is as expected since the 1st eigenmode always dominates in a thin-walled tube when it buckles and it was therefore allowed to dominate in the tube model using multiple eigenmodes as imperfection factors.

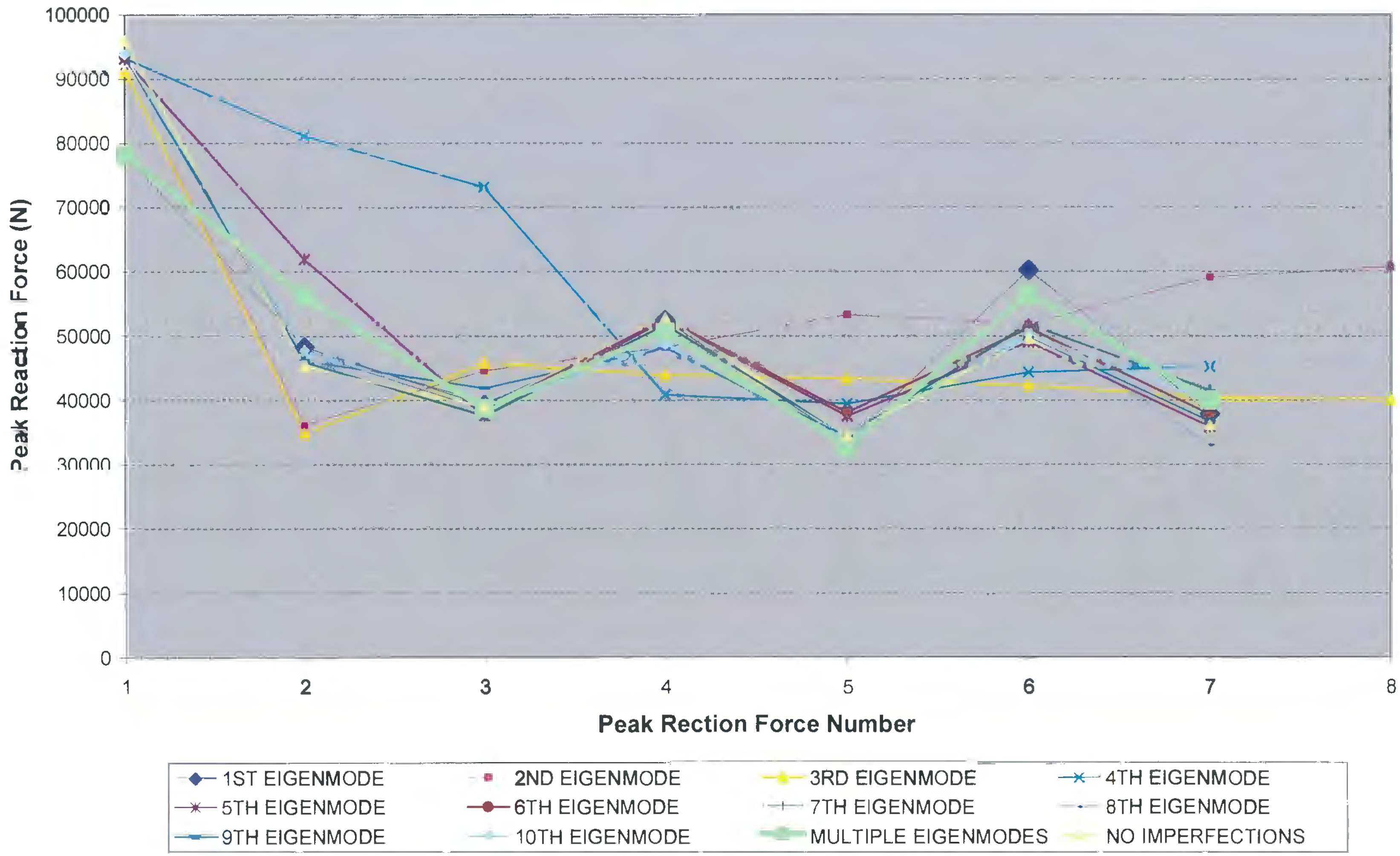

Figure 5.43: Comparison graph of the peak reaction forces of a square tube crushed against a frictionless end plate using different eigenmodes as an imperfection factors, subject to a constant velocity loading of 0.5 m.s^{-1}.

Figure 5.44 shows a comparison of the overall mean peak reaction forces using the different eigenmodes as initial imperfection factors, subject to a constant velocity loading of 0.5 m.s^{-1}.

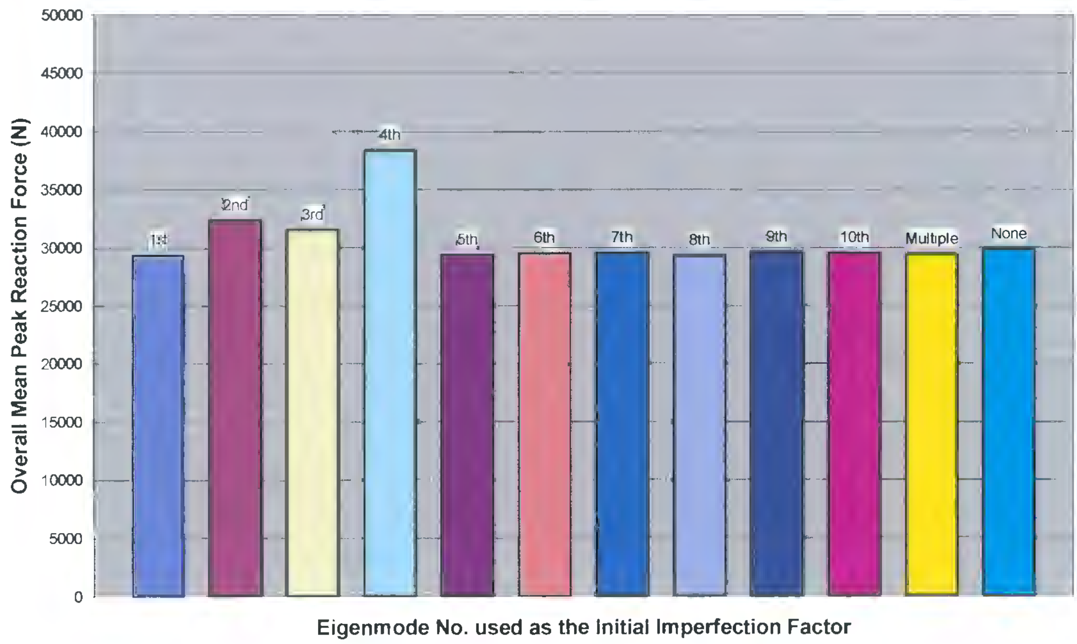

Figure 5.44: Overall mean peak reaction forces graph using the different eigenmodes as initial imperfection factors, subject to a constant velocity loading of 0.5 m.s^{-1}.

6. CONCLUSIONS

From reviewing the literature review, all the aspects of the numerical models used in this study, and most importantly, the results of this study, many conclusions can be drawn. These conclusions are presented here.

6.1 TIME SAMPLING

A very small time sampling interval of less than 1 microsecond is required in ABAQUS in order that the true initial peak reaction force be detected and recorded correctly. A time sampling interval greater than 1 microsecond usually results in large errors with a much smaller reaction force being recorded due to the fact that the peak reaction force occurs over an extremely short time duration.

6.2 MASS SCALING

1. The use of mass scaling enables an analysis to be performed economically without artificially increasing the loading rate in order to reduce analysis time of the model.

2. The use of mass scaling and the use of symmetry are the only two options for reducing the solution time of models involving a rate-dependent material or rate-dependent damping, such as dashpots.

3. The use of Mass Scaling is a very efficient method to reduce the amount of time it takes to undertake an analysis of a tube model in ABAQUS. While the use of symmetry can reduce the time of an analysis by a factor of 2, the use of Mass Scaling can reduce the time of an analysis by a much higher factor, such as by 15 as used in this thesis, without any significant loss of degree of

accuracy. This clearly has significant benefits, particular for the analysis of tube models, due to the much greater reduction in analysis time. Mass Scaling also has the added advantage that the graphical output, such as the deformed profile and associated stresses, etc., can be viewed for the whole model. This is not the case with symmetry where the graphical output can only be viewed for only half or sometimes a quarter of the model.

4. The principle of mass scaling is that by artificially increasing the material density, p, by a factor of f^2, this decreases the wave speed by a factor of f and increases the stable time increment by a factor of f. When the global stability limit is increased, fewer increments are required to perform the same analysis, which is the goal of mass scaling, i.e. to reduce the analysis time.

5. The speedup factor in time, due to the use of mass scaling, is equal to the square root of the mass scaling factor used.

6. Before using mass scaling, a suitable mass scaling factor has to be found to ensure that the amount of mass scaling used is within acceptable limits, as a too large mass scaling factor can lead to errors in a model. The ABAQUS / Explicit User's Manual recommends that for the application of mass scaling to be valid, the accumulated kinetic energy should be a maximum of 5 to 10 percent of the accumulated internal energy. However it has been shown by way of example from the models in this thesis that the maximum kinetic energy to accumulated internal energy ratio specified in the ABAQUS / Explicit manual may be invalid to produce reliable results. Other tests therefore need to be carried out by the modeller such as by comparing the results of a model using mass scaling to the results of a model without using mass scaling. In the models for this thesis, mass scaling could not and therefore was not used within a certain time region of the model. In certain circumstances and in other models yet to be studied, the use of mass scaling may not be permitted at all in order to produce reliable and acceptable results.

6.3 EIGENMODES AND ASSOCIATED EIGENVALUES OF VARIOUS TUBES

1. The first 10 eigenmodes and their associated eigenvalues were calculated for various thin-walled polygonal shaped tubes. When a load is applied to a long thin-walled tube all of its eigenmodes will be present, with the 1st eigenmode being the dominant eigenmode and with the 2nd, 3rd, etc. eigenmodes also being present but becoming progressively less and less dominant. This is because the first eigenvalue is significantly lower than the second, so the first eigenmode will dominate. This is typical for a long thin-walled square tube as opposed to a structure such as a thin-walled circular shaped tube which will have several low eigenvalues that are nearly the same.

2. Once the first eigenvalue of a tube is known, the initial buckling load of a tube can be determined very eloquently, simply by multiplying the first eigenvalue by the applied load used in the eigenmode analysis.

3. In the eigenmode buckling analysis it doesn't matter what initial applied load is used because the calculated initial buckling load will remain the same.

6.4 IMPERFECTION FACTORS

1. The introduction and use of imperfection factors from an eigenmode buckling analysis gives the exact modal shape of the tube and thus the collapse mode of the tube and hence greater accuracy in modelling than introducing arbitrary imperfection factors, particularly where no experimental tests have been performed to undertake a sensitivity analysis.

2. When imperfection factors are not used or applied correctly i.e. by using incorrectly shaped imperfection factors that are either too large or too small in magnitude, this results in four main types of errors:

i. Non uniform, random-like deformed profiles, especially in the case of a specific mass and initial velocity loading.

ii. Over or under estimation of peak reaction and other reaction forces and incorrect associated stresses and strains.

iii. Incorrect prediction of the collapse mode and deformed profile of the tube i.e. the folding mechanism of the tube with regards to the sides of the tube folding inward or outward.

iv. Incorrect prediction of where folding begins to occur along the length of the tube.

3. The eigenmodes have a practical use in the sense that a tube that is to be utilized as a shock absorber can be given and manufactured to the same profile as its natural eigenmodes. This will reduce the initial peak reaction force (the ultimate buckling force) to a similar size as the 2^{nd} and 3^{rd}, etc peak reaction forces and is the best method of introducing imperfections for the purpose of reducing the initial peak reaction force to the same magnitude as the subsequent peak reaction forces. This can also be achieved without affecting the mean force or the subsequent peak reaction forces. Ideally one would want to obtain a reaction force versus displacement graph as in Figure 6.1 where the initial peak reaction force has been greatly reduced to a size similar in magnitude to the subsequent peak reaction forces. One would want to utilise this typically for the energy absorption of an impact, in order to absorb the energy uniformly over the impact time period, in order to minimise shock and injury to passengers of vehicles, etc.

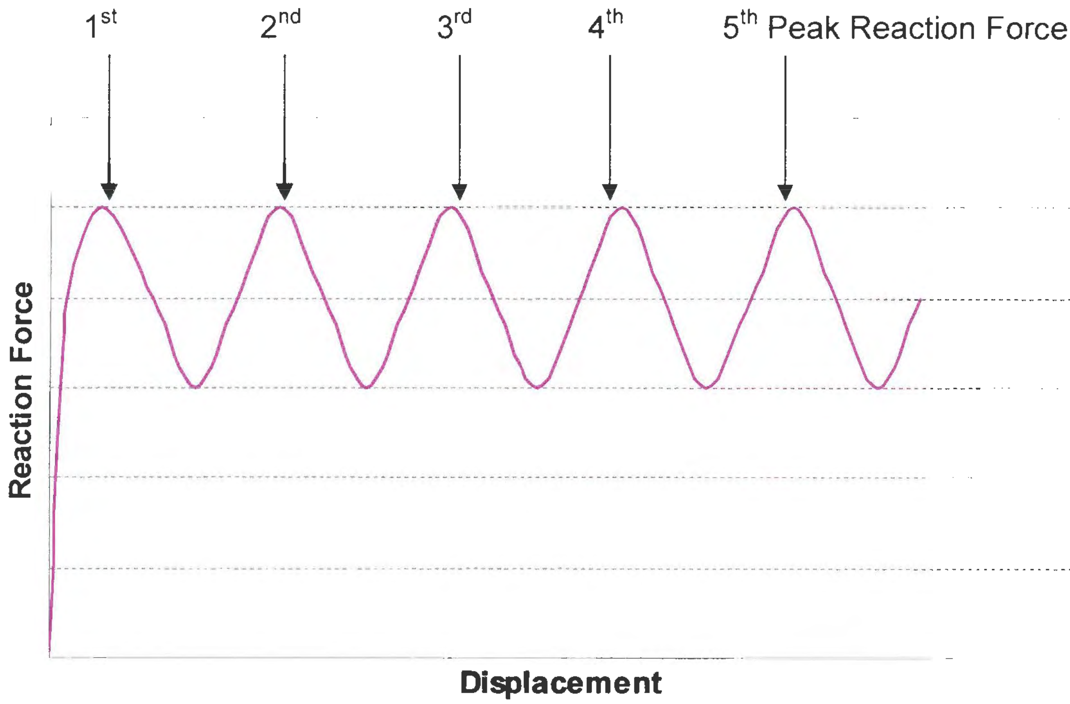

Figure 6.1: Ideal Reaction Force versus Displacement graph where the 1st peak reaction force has been greatly reduced in order to absorb the energy uniformly over the impact time period.

4. Equations to predict the collapse mode of square tubes have been formulated by Jones [47], but according to the literature and as far as the author is aware, no theoretical equations have been formulated to predict the collapse modes for other polygonal shaped tubes such as for hexangular, circular and triangular, etc tubes. The advantage of using a numerical method such as ABAQUS, as was undertaken in this thesis, is to determine the eigenmodes in order so that they may be applied to predict the collapse mode of any polygonal shaped tube.

5. Errors can occur either when failing to use initial imperfection factors when required or else using them incorrectly. It is therefore imperative that the modeller has a very good understanding of when and how to apply initial imperfection factors when modelling tubes.

6.5 THE EFFECTS OF INITIAL IMPERFECTION FACTORS UNDER DIFFERENT LOADING CONDITIONS

When a tube model undergoes crushing the deformed profile of a tube is much more non uniform and random-like and incorrect when using a specific mass and initial velocity loading, than when using a constant velocity loading. Considerable care needs to be taken by the modeller when modelling tubes under an initial velocity and mass loading by introducing sufficiently accurate initial imperfection factors into the model and of the correct magnitude.

6.6 THE EFFECTS OF EIGENMODE IMPERFECTION FACTORS SUBJECT TO VARIOUS END BOUNDARY CONDITIONS UNDER A SPECIFIC MASS AND INITIAL VELOCITY LOADING

When a tube model is crushed numerically under a specific mass and initial velocity loading without using any imperfection factors, it results in an incorrect, non uniform, random-like deformed profile, irrespective of the end boundary condition imposed upon the crushed tube. When a tube is subject to a frictionless end boundary condition and when no imperfection factors are introduced, folding begins from the bottom in a progressive non-uniform manner, however when imperfection factors are introduced folding also begins from the bottom but in a progressive uniform manner. When a tube is subject to a fixed (encastred) end boundary condition and when no imperfections are introduced, folding begins at $^1/_3$ and $^2/_3$ of its length from the bottom end in a semi-progressive, non uniform manner, however when imperfection factors are introduced folding begins at the top end of the tube in a progressive uniform manner. End boundary conditions therefore have a significant effect on the deformed profile of the crushed tube, particularly when it begins to buckle, as well as on the final deformed profile.

6.7 THE EFFECTS OF EIGENMODE IMPERFECTION FACTORS SUBJECT TO VARIOUS END BOUNDARY CONDITIONS UNDER A CONSTANT VELOCITY LOADING

When a tube model is crushed numerically subject to a frictionless end boundary condition under a constant velocity loading, it results in the following:

1. When no imperfection factors are introduced, the tube model still buckles progressively with a uniform deformed profile. This is opposed to the tube model which deformed non uniformly when subject to an initial mass and velocity loading.

2. Although it results in a correct deformed profile when no imperfection factors are used the resultant reaction forces, stress and strains vary compared to the models in which imperfection factors are used.

3. When the 2^{nd}, 3^{rd} and 4^{th} eigenmodes are used as imperfection factors to perturb the respective tube models, this results in the tube twisting horizontally and in some cases horizontal displacement occurs on the end plate.

4. The tube model using the 1^{st} eigenmode as an imperfection factor has similar reaction forces to the tube model using multiple eigenmodes as imperfection factors. This result was as expected since the 1^{st} eigenmode always dominates in a thin-walled tube when it buckles and it was therefore allowed to dominate in the tube model using multiple eigenmodes as imperfection factors.

6.8 CONCLUDING REMARKS

1. It has been stated by Karagiozova [30] that a tube under an axial load deforms depending on the shockwave and inertia of the hammer and the tube dimensions. It has been shown in this thesis that the way in which an analysis of a tube model deforms is also dependant on the type of loading, the end boundary conditions and very importantly on the type of imperfections introduced into the model.

2. The most accurate method to model a tube in a finite element package such as ABAQUS, is to firstly calculate and use the eigenmodes as initial imperfection factors to perturb the model for the analysis. Failing to use imperfection factors can produce very unreliable results, while the introduction and use of arbitrary imperfection factors can also produce unreliable results.

3. The four major potential problems which can arise when imperfection factors are not used or applied correctly have been highlighted by and discussed earlier in this thesis.

4. The ABAQUS / Explicit User's Manual recommends that for the application of mass scaling to be valid, the accumulated kinetic energy should be a maximum of 5 to 10 percent of the accumulated internal energy. However it has been shown in this thesis that the maximum kinetic energy to accumulated internal energy ratio specified in the ABAQUS / Explicit manual may be invalid to produce reliable results and that the maximum value may have to be less than the 5 percent value specified in certain models, such as the ones shown in this thesis.

5. It has been demonstrated in this thesis that the use of mass scaling can greatly reduce the time it takes to perform a numerical tube analysis and should therefore always be made use of where ever possible in a model. More importantly, it has demonstrated that mass scaling cannot always be used throughout in certain models and when it is used, the correct amount of mass

scaling needs to be applied in order to produce reliable results. It has been demonstrated in this thesis how to determine the correct amount of mass scaling to be applied.

6. Equations to predict the collapse mode of square tubes have been formulated by Jones [47], but according to the literature and as far as the author is aware, no theoretical equations have been formulated to predict the collapse modes for other polygonal shaped tubes. An algorithm has been provided in this thesis, by means of a numerical method using ABAQUS, to predict the collapse modes of other polygonal shaped tubes such as for hexagonal, circular and triangular, etc. shaped tubes. The ability to predict the collapse modes of any polygonal shaped tube therefore makes it a very useful algorithm indeed.

7. It is hoped that this thesis has illustrated some of the complexities involved in the modelling of thin-walled tubes and will therefore serve to facilitate the modelling of thin-walled tubes with an even greater degree of accuracy and reliability in the future.

7. RECOMMENDATIONS

1. A sensitivity study should be performed to investigate the effect of different initial applied loads in ABAQUS / Standard, have on the magnitude on the corresponding eigenvalues, although this will not affect the magnitude of the initial buckling load of a tube, nor the subsequent peak reaction forces.

2. Experimental and numerical research should be undertaken to investigate if hexagonal, triangular or a circular shaped tubes, having the same perimeter as a square shaped tube, reduce or increase the initial peak buckling load.

3. The use of tapered tubes with the narrow end being at the point of impact should be investigated as an alternative method to reduce the initial buckling load of a tube.

4. The effect of utilizing mass scaling at much higher loading rates should be carried out to investigate how mass scaling will be influenced at these high velocities. A critical high velocity loading rate could be determined if the influence of high loading rates is severe.

5. Sensitivity studies should be performed by increasing and decreasing the magnitudes of the scaling factors of the eigenmodes in order to achieve a near perfect tube model.

6. Further research should be carried out on the crushing of tubes having the same profiles as their eigenmodes as a method of reducing the initial buckling load of the tube i.e. reducing to peak load to the same size as the subsequent peaks, in order to absorb the energy uniformly over the impact time period, in order to minimise shock and injury to passengers of vehicles, etc.

7. Further research should be undertaken on tubes subject to higher load velocities when inertia effects become more important and dominant. At these high velocities the influence of the eigenmodes can also be studied.

8. More detailed studies should be performed on the effects of using different boundary conditions at the end of a tube. Aspects such as the resultant eigenmodes, the reaction forces and the manner in which the tube begins to buckle and its resultant folding profile can be studied.

9. An attempt should be made to formulate numerical equations for other polygonal shaped tubes as was done by Jones [47] for square tubes. When crushing a tube experimentally it does not always crush as predicted in theory because of random defects. Crushing a tube experimentally may sometimes produce a different collapse mode than if there were no defects. The fact that a numerical model using ABAQUS has been developed in this thesis, to predict the collapse mode for polygonal shaped tubes, means that they can now be accurately determined. Once the collapse mode for the different polygonal shaped tubes has been established, the search for a theoretical formulation and equations can commence more easily. Further mathematical research should therefore be undertaken to formulate equations to predict the collapse mode for other polygonal shaped tubes with this knowledge in hand once it has been established.

10. Since the basis of numerical eigenmode analysis has been set out in this thesis, it is recommended that future eigenmode analyses studies of thin plates and the application thereof be undertaken by the BISRU group headed by professor Nurick.

8. REFERENCES:

1. Mamalis A G and Johnson W, "The quasi-static crumpling of thin-walled circular cylinders and frustra under axial compression", *International Journal of Mechanical Sciences*, Volume 25, 1983, Issues 9-10, pages 713-732

2. Mamalis A G, Johnson W and Viegelahn G L, "The crumpling of steel thin-walled tubes and frustra under axial compression at elevated strain rates: Some experimental results", *International Journal of Mechanical Sciences*, Volume 26, Issues 11-12, 1984, pages 537-546

3. Ren W, Mingbao H, Zhuping H and Quingchun Y, "An experimental study of the dynamic axial plastic buckling of cylindrical shells", *International Journal of Impact Engineering*, Volume 1, Issue 3, 1983, pages 249-256

4. Thornton P H, "The crush behaviour of glass fibre reinforced plastic sections", *Composites, Science and Technology*, Volume 27, Issue 3, 1986, pages 199-223

5. Thornton P H and Jeryan R A, "Crash energy management in composite automotive structures" *International Journal of Impact Engineering*, Volume 7, Issue 2, 1988, pages 167-180

6. Hull D, "A unified approach to progressive crushing of fibre-reinforced composite tubes", *Composites, Science and Technology*, Volume 40, Issue 4, 1991, pages 377-421

7. Hamada H, Coppola J C and Hull D, "Effect of surface treatment on crushing behaviour of glass cloth/epoxy composite tubes" *Composites*, Volume 23, Issue 2, 1992, pages 93-99

8. Hamada H, Coppola J C, Hull D, Maekawa Z and Sato H, "Comparison of energy absorption of carbon/epoxy and carbon/PEEK composite tubes", *Composites*, Volume 23, Issue 4, 1992, pages 245-252

9. Marshall N S, "Active control of passive safety in passenger motor vehicles", *Masters Thesis*, University of Cape Town, 1995

10. Marshall N S and Nurick G N, "The effect of induced imperfections on the formation of the first lobe of symmetric progressive buckling of thin-walled square tubes", *Structures Under Shock and Impact*, 1996

11. Knebel K and Schweizerhof K, "Buckling of cylindrical shells containing granular solids", *Thin-Walled Structures*, Volume 23, Issues 1-4, 1995, pages 295-312

12. Grzebieta R H, "Research into failure mechanisms of some thin-walled round tubes", *Plasticity and Impact Mechanics*, 1997, pages 309-324

13. Karbhari V M and Haller J E, "Rate and architecture effects on progressive crush of braided tubes", *Composite Structures*, Volume 43, 1998, pages 93-108

14. Lancaster E R, Calladine C R and Palmer S C, "Paradoxical buckling behaviour of a thin cylindrical shell under axial compression" *International Journal of Mechanical Sciences*, Volume 42, 2000, pages 843-865

15. Seitzberger M, Rammerstorfer F G, Gradinger H P, Degischer H P, Blaimschein M and Watch C, "Experimental studies on the quasi-static axial crushing of steel columns filled with aluminium foam", *International Journal of Solids and Structures*, Volume 37, Issue 30, 2000, pages 4125-4147

16. Guillow S R, Lu G and Grzebieta R H, "Quasi-static axial compression of thin-walled circular aluminium tubes" *International Journal of Mechanical Sciences*, Volume 43, 2001, pages 2103-2123

17. Gupta N K, Sekon G S and Gupta P K, "A study of fold formation in axisymmetric axial collapse of round tubes", *International Journal of Impact Engineering*, Volume 27, 2002, pages 87-117

18. Pugsley A and Macaulay M, "The large scale crumpling of thin cylindrical columns", *Quarterly Journal of Mechanics and Applied Mathematics*, Volume 13, 1960, pages 1-9

19. Alexander J M, "An approximate analysis of the collapse of thin cylindrical columns", *Quarterly Journal of Mechanics and Applied Mathematics*, Volume 13, 1960, pages 10-15

20. Shaw M C, "Designs for safety: the mechanical fuse", *Mechanical Engineering*, ASME, Volume 94, 1972, pages 23-29

21. Ho D, "Buckling load of non-linear systems with multiple eigenvalues", *International Journal of Solids and Structures*, Volume 10, Issue 11, 1974, pages 1315-1330

22. Wierbicki T and Bhat S U, "A moving hinge solution for axisymmetric crushing of tubes", *International Journal of Mechanical Sciences*, Volume 28, No 3, 1986, pages 135-151

23. Grzebieta H, "An alternative method for determining the behaviour of round stocky tubes subjected to an axial crush load", *Thin-Walled Structures*, Volume 9, Issues 1-4, 1990, pages 61-89

24. Benson J and Hallquist J, "A single surface contact algorithm for the post-buckling analysis of shell structures", *Computer methods in*

applied mechanics and engineering, Volume 78, Issue 2, 1990, pages 141-163

25. Hunt G W and E Neto, "Localized buckling in long axially loaded cylindrical shells", *Journal of the Mechanics and Physics of Solids*, Volume 39, Issue 7, 1991, pages 881-894

26. Wierzbicki T, Bhat S U, Abromwicz W and Brodkin D, "Alexander Revisited – A two folding elements model of progressive crushing of tubes", *International Journal of Solids and Structures*, Volume 29, Issue 24, 1992, pages 3269-3288

27. Showkati H and Ansorian P, "Influence of primary boundary conditions on the buckling of shallow cylindrical shells", *Journal of Construction*, Steel Res. ,Volume 36, Issue 1,1996, pages 53-75

28. Gupta N K and Velmurugan R, "Axi-symmetric axial collapse of round tubes", *Plasticity and Impact Mechanics*, 1997, pages 309-324

29. Abramowicz W and Jones N, "Transition from initial global bending to progressive buckling of tubes loaded statically and dynamically", *International Journal of Impact Engineering*, Volume 19, Issues 5-6, 1997, pages 415-437

30. Karagiozova D and Jones N, "Dynamic elastic-plastic buckling of circular cylindrical shells under axial impact" *International Journal of Solids and Structures*, Volume 37, 2000, pages 2005-2034

31. Karagiozova D and Jones N, "Influence of stress waves on the dynamic progressive and dynamic plastic buckling of cylindrical shells", *International Journal of Solids and Structures*, Volume 38, 2001, pages 6723-6749

32. Remseth S N, Holthe K, Bergan P G and Holand I, "Tube collapse analysis using finite elements", *Computers and Structures*, Volume 8, Issues 3-4, 1978, pages 383-390

33. Miyazaki N, Hagihara S and Munakata T, "Bifurcation creep buckling analysis of circular cylindrical shells under axial compression", *International Journal of Pressure Vessels and Piping*, Volume 52, Issue 1, 1992, pages 1-10

34. Sasaki, Takeshi, Kurokawa and Tomoaki, "Axisymmetric collapse of a circular tube due to impact and its parametric study for a shock absorber", *Transactions of the Japanese Society of Mechanical Engineers*, Volume 63, Issue 616, 1997, pages 2610-2617

35. Otubushin A, "A detailed validation of a validation of a non-linear finite element code using dynamic axial crushing of a square tube", *International Journal of Impact Engineering*, Volume 21,Issues 5, 1998, pages 349-368

36. Choong K K and Ramm E, "Simulation of the buckling process of shells by using the finite element", *Thin-Walled Structures*, Volume 31, 1998, pages 39-72

37. Bathe, Walczak, Guillermin, Bouzinov and Chen, "Advances in crush analysis", *Computers and Structures*, Issue 72, 1999, pages 31-47

38. Bardi F C, Yun H D and Kyriakides S, "On the axisymmetric progressive crushing of circular tubes under axial compression", *International Journal of Solids and Structures*, Volume 40, 2003, pages 3137-3155

39. Webb D C, Webster J and Kormi K, "Finite element simulation of energy absorption under axial static compressive and impact loading", *International Journal of Crashworthiness*, Volume 6, Issue 3, 2001

40. Karagiozova D, Alves M and Jones N, "Inertia effects in axisymmetrically deformed cylindrical shells under axial impact", *International Journal of Impact Engineering*, Volume 24, 1998, pages 1083-1115

41. Nannucci P R, "Model of dynamic buckling of thin-walled cylindrical and square tubes as a vehicle energy absorber device using finite element analysis", *B.Sc. Thesis*, Department of Mechanical Engineering, University of Cape Town, 1996

42. Nannucci P R, Marshall N S and Nurick G N, "A computational investigation of the progressive buckling of square tubes with geometric imperfections", Proceedings of the 3rd Asia-Pacific Conference on Shock and Impact Loads on Structures, Singapore, 24-26 November, 1999

43. Karagiozova D and Jones N, "Dynamic effects on buckling and energy absorption of cylindrical shells under axial impact", *Thin-Walled Structures*, Volume 39, 2001, pages 583-610

44. Wang B and Lu G, "Mushrooming of circular tubes under dynamic axial loading", *Thin-Walled Structures*, Volume 40, 2002, pages 167-182

45. Andrews K R F, England G L and Ghani E, "Classification of the axial collapse of cylindrical tubes under quasi-static loading", *International Journal of Mechanical Sciences*, 25, 1983, pages 687-698

46. Korneck H, "An investigation into the response of square box columns to axial loading", *Undergraduate thesis*, University of Cape Town, 1992

47. Jones N, *Structural Impact*, Cambridge University Press, Cambridge, 1989, pages 385-431

48. Abromowicz W and Jones N, “Dynamic axial crushing of square tubes”, *International Journal of Impact Engineering*, 2 ,1984, pages 179-208

49. Abromowicz W and Jones N, “Dynamic axial crushing of circular tubes”, *International Journal of Impact Engineering*, 2 , 1984, pages 263 -281

50. Wierzbicki T and Abromowicz W, “On the crushing mechanics of thin-walled structures”, *Journal of Applied Mechanics*, 50, 1983, pages 727-734

51. Wierzbicki T and Abromowicz W, “Dynamic progressive buckling of circular square tubes”, *International Journal of Impact Engineering*, 50, 1983, pages 243-270

52. Abromowicz W, “The effective crushing distance in axially compressed thin-walled metal columns”, *International Journal of Impact Engineering*, 1, 1983, pages 309-318

53. Abromowicz W and Jones N, “Static and dynamic axial crushing of circular and square tubes”, *Metal forming and Impact Mechanics*, (Edited by S R Reid), Pergamon Press, Oxford, 1985, pages 225-247

54. Langseth M, Berstad T, Hopperstad O S and Clausen A H, “Energy absorption in axially loaded square thin-walled aluminium extrusions”, *Structures Under Shock and Impact III*, Proceedings of the Third International Conference held in Madrid, Spain, 1st-3rd June, Computational Mechanics Publications, Southampton, 1994, pages 401-410

9. BIBLIOGRAPHY

1. Fagan M J, *Finite Element Analysis – Theory and Practice*, Longman Group UK Limited, 1999

2. Jones N, *Structural Impact,* Cambridge University Press, Cambridge, 1989, chapters 2,9,10

3. Spyrakos C C, Raftoyiannis J, *Linear and Nonlinear Finite Element Analysis In Engineering Practice*, Distributed by Algor Publishing, Pittsburg, PA, 1997, chapter 9

4. *ABAQUS CAE Users Manual*, Version 6.3, Hibbitt, Karlson & Sorensen, Incorporated, USA, 2002

5. *ABAQUS Explicit Users Manual*, Version 6.3, Hibbitt, Karlson & Sorensen, Incorporated, USA, 2002, Volume 1

6. *ABAQUS Explicit Users Manual*, Version 6.3, Hibbitt, Karlson & Sorensen, Incorporated, USA, 2002, Volume 2

7. *ABAQUS Explicit Example Problems Manual*, Version 6.3, Hibbitt, Karlson & Sorensen, Incorporated, USA, 2002

10. APPENDICES

APPENDIX A:

THE EFFECTS OF EIGENMODE IMPERFECTION FACTORS USING A FRICTIONLESS END BOUNDARY CONDITION SUBJECT TO A CONSTANT VELOCITY LOADING

The Reactions Forces versus Displacement graphs of these crushed square tubes are shown.

A1: REACTION FORCE VS DISPLACEMENT GRAPH OF A SQUARE TUBE CRUSHED AGAINST A FRICTIONLESS END PLATE USING THE 1ST EIGENMODE AS AN IMPERFECTION FACTOR.

A2: REACTION FORCE VS DISPLACEMENT GRAPH OF A SQUARE TUBE CRUSHED AGAINST A FRICTIONLESS END PLATE USING THE 2ND EIGENMODE AS AN IMPERFECTION FACTOR.

A3: REACTION FORCE VS DISPLACEMENT GRAPH OF A SQUARE TUBE CRUSHED AGAINST A FRICTIONLESS END PLATE USING THE 3RD EIGENMODE AS AN IMPERFECTION FACTOR.

A4: REACTION FORCE VS DISPLACEMENT GRAPH OF A SQUARE TUBE CRUSHED AGAINST A FRICTIONLESS END PLATE USING THE 4TH EIGENMODE AS AN IMPERFECTION FACTOR.

FIGURE A5: REACTION FORCE VS DISPLACEMENT GRAPH OF A SQUARE TUBE CRUSHED AGAINST A FRICTIONLESS END PLATE USING THE 5TH EIGENMODE AS AN IMPERFECTION FACTOR.

FIGURE A6: REACTION FORCE VS DISPLACEMENT GRAPH OF A SQUARE TUBE CRUSHED AGAINST A FRICTIONLESS END PLATE USING THE 6^{TH} EIGENMODE AS AN IMPERFECTION FACTOR.

FIGURE A7: REACTION FORCE VS DISPLACEMENT GRAPH OF A SQUARE TUBE CRUSHED AGAINST A FRICTIONLESS END PLATE USING THE 7^{TH} EIGENMODE AS AN IMPERFECTION FACTOR.

FIGURE A8: REACTION FORCE VS DISPLACEMENT GRAPH OF A SQUARE TUBE CRUSHED AGAINST A FRICTIONLESS END PLATE USING THE 8^{TH} EIGENMODE AS AN IMPERFECTION FACTOR.

FIGURE A9: REACTION FORCE VS DISPLACEMENT GRAPH OF A SQUARE TUBE CRUSHED AGAINST A FRICTIONLESS END PLATE USING THE 9^{TH} EIGENMODE AS AN IMPERFECTION FACTOR.

FIGURE A10: REACTION FORCE VS DISPLACEMENT GRAPH OF A SQUARE TUBE CRUSHED AGAINST A FRICTIONLESS END PLATE USING THE 10^{TH} EIGENMODE AS AN IMPERFECTION FACTOR.

FIGURE A11: REACTION FORCE VS DISPLACEMENT GRAPH OF A SQUARE TUBE CRUSHED AGAINST A FRICTIONLESS END PLATE USING MULTIPLE EIGENVALUES AS IMPERFECTION FACTORS.

FIGURE A12: REACTION FORCE VS DISPLACEMENT GRAPH OF A SQUARE TUBE CRUSHED AGAINST A FRICTIONLESS END PLATE USING NO IMPERFECTION FACTORS.

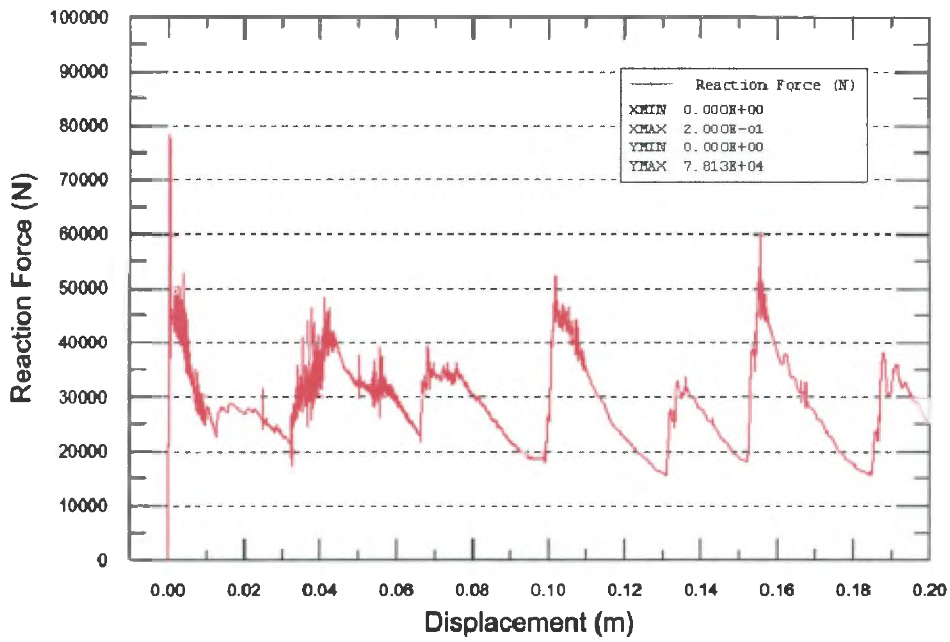

Figure A1: Reaction force vs displacement graph of a square tube crushed against a frictionless end plate using the 1st eigenmode as an imperfection factor.

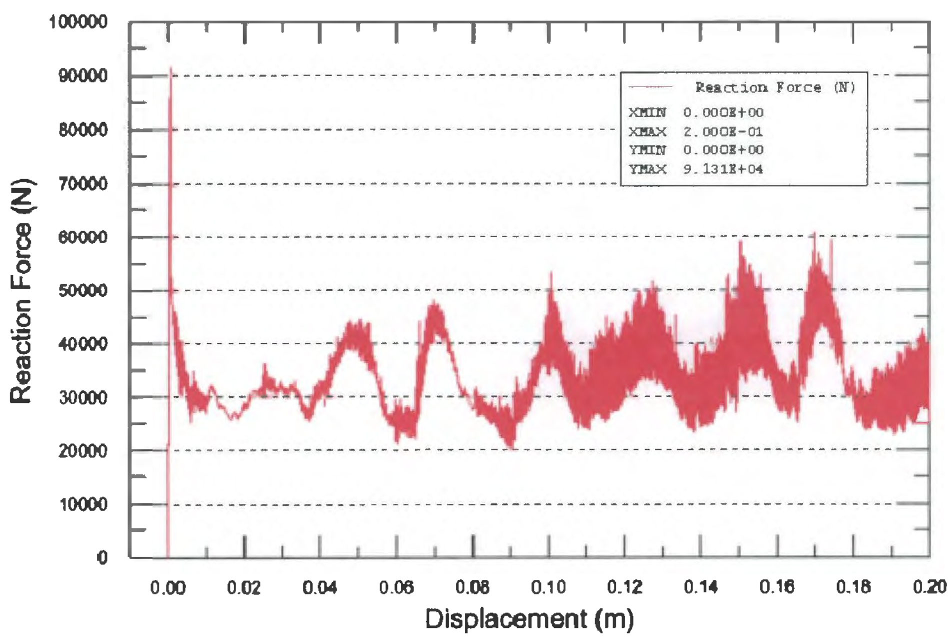

Figure A2: Reaction force vs displacement graph of a square tube crushed against a frictionless end plate using the 2nd eigenmode as an imperfection factor.

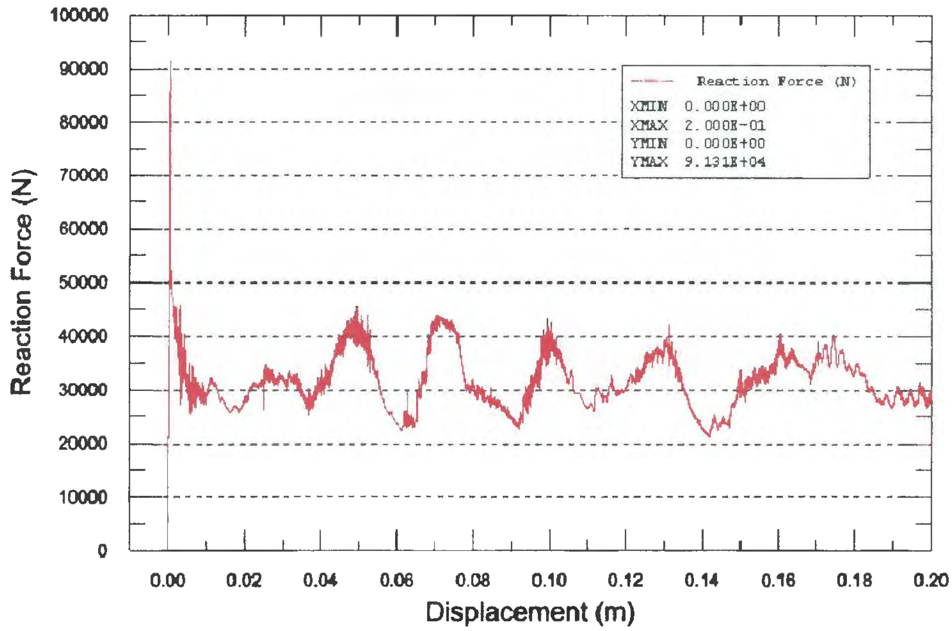

Figure A3: Reaction force vs displacement graph of a square tube crushed against a frictionless end plate using the 3rd eigenmode as an imperfection factor.

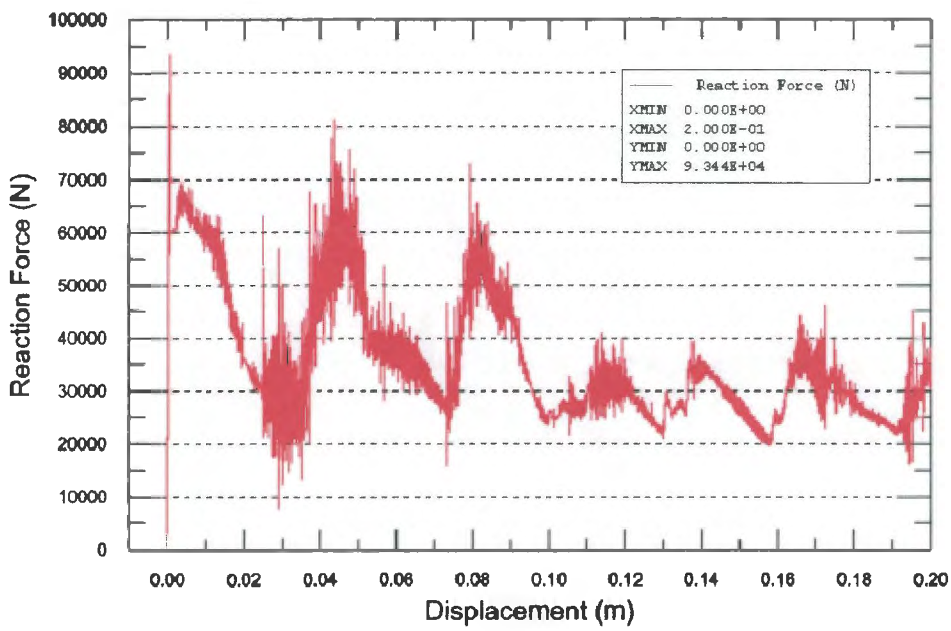

Figure A4: Reaction force vs displacement graph of a square tube crushed against a frictionless end plate using the 4th eigenmode as an imperfection factor.

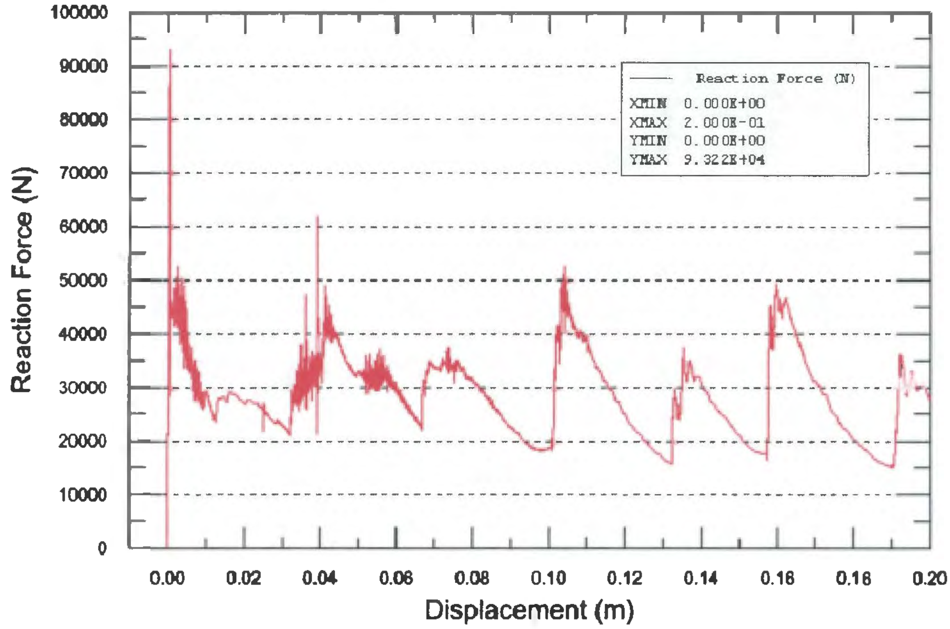

Figure A5: Reaction force vs displacement graph of a square tube crushed against a frictionless end plate using the 5th eigenmode as an imperfection factor.

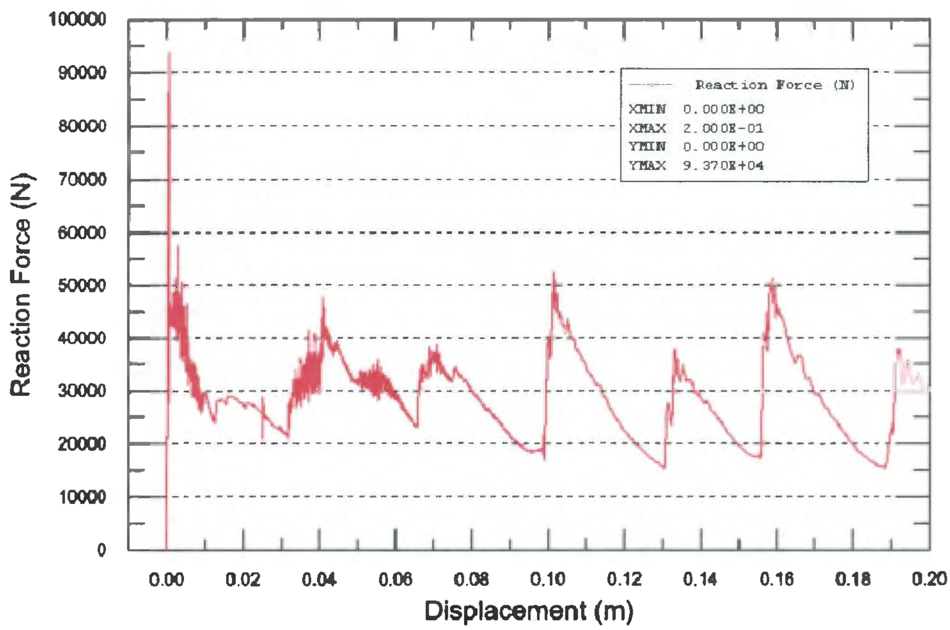

Figure A6: Reaction force vs displacement graph of a square tube crushed against a frictionless end plate using the 6th eigenmode as an imperfection factor.

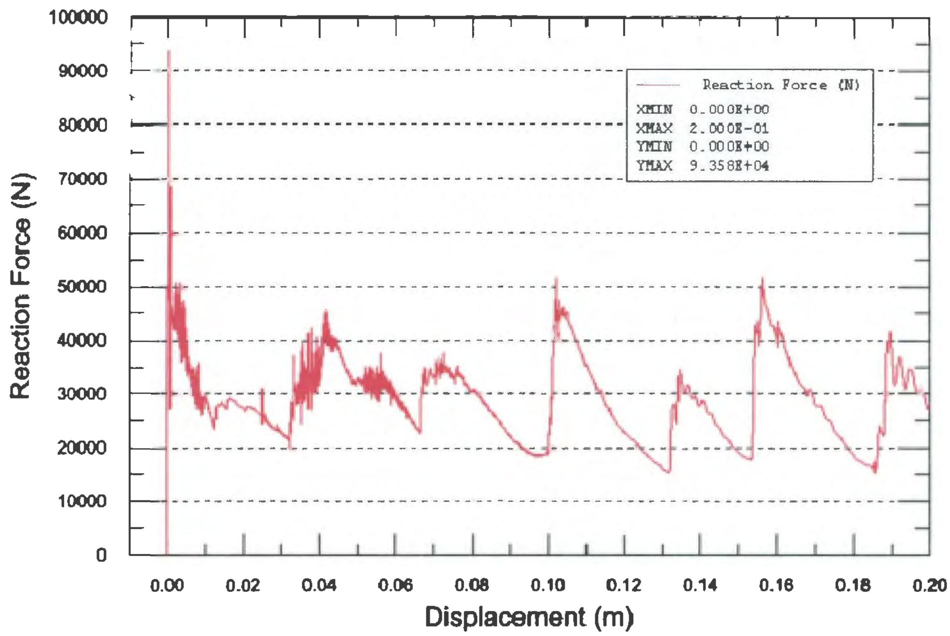

Figure A7: Reaction force vs displacement graph of a square tube crushed against a frictionless end plate using the 7th eigenmode as an imperfection factor.

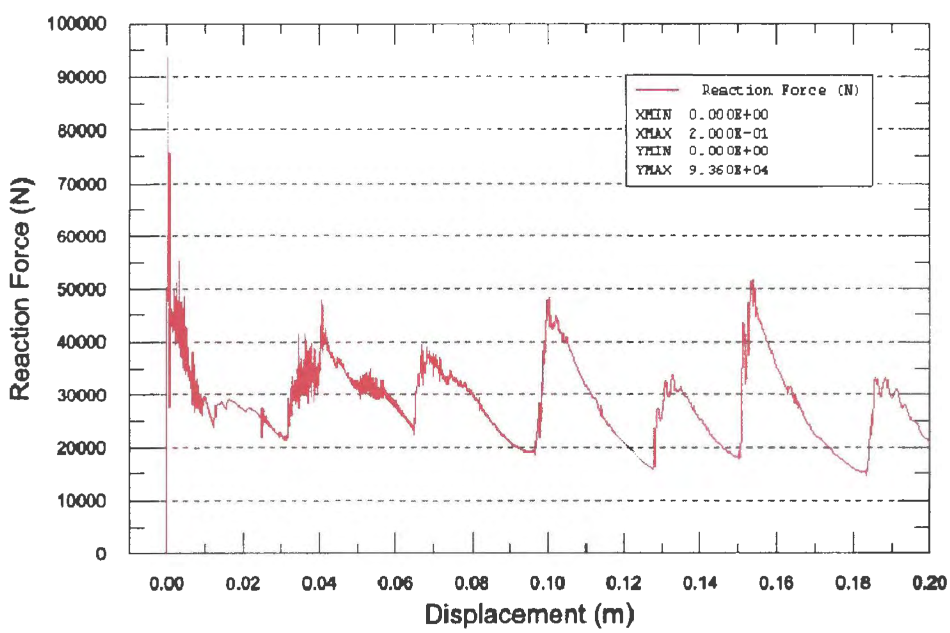

Figure A8: Reaction force vs displacement graph of a square tube crushed against a frictionless end plate using the 8th eigenmode as an imperfection factor.

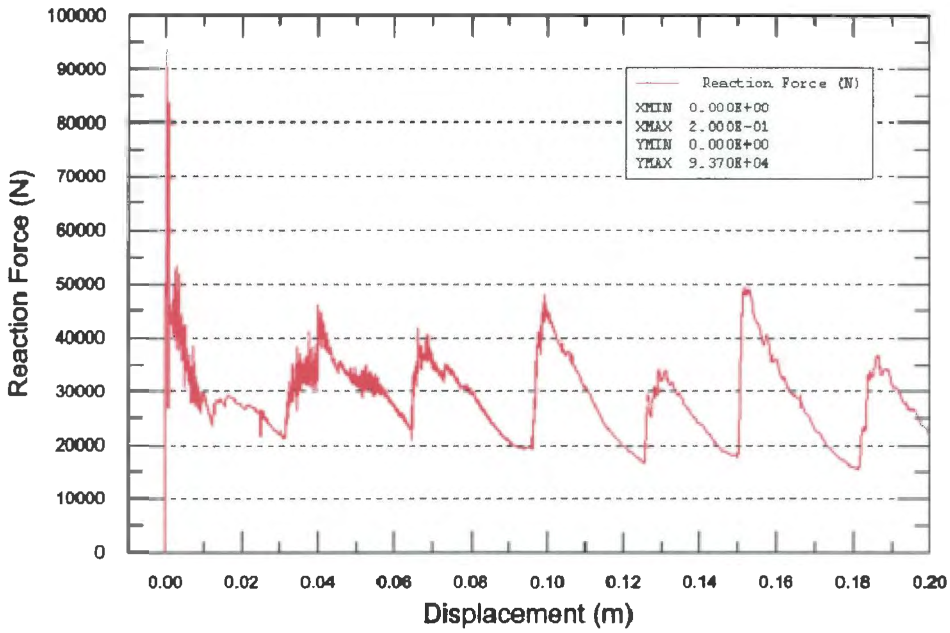

Figure A9: Reaction force vs displacement graph of a square tube crushed against a frictionless end plate using the 9th eigenmode as an imperfection factor.

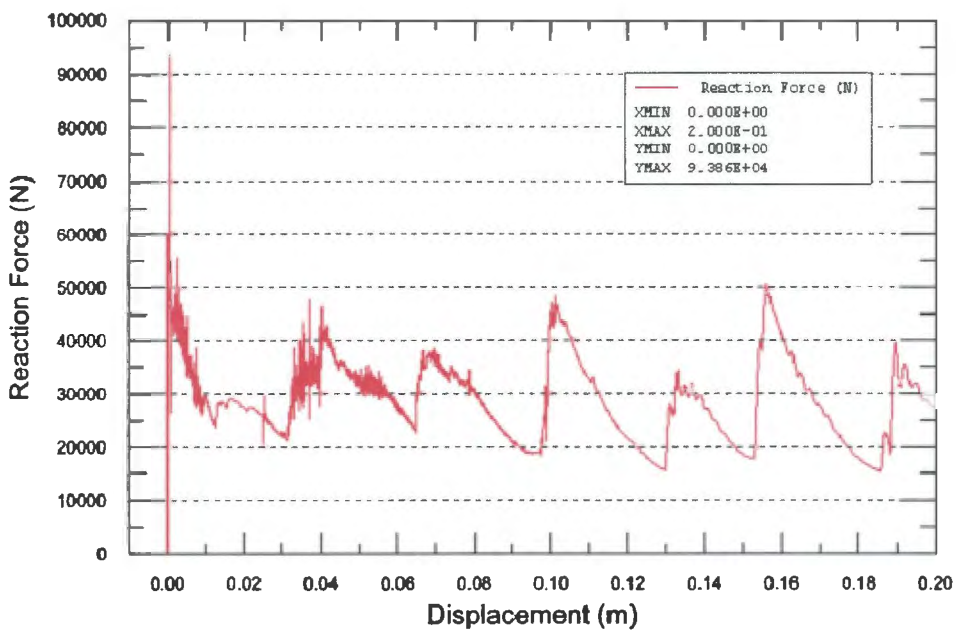

Figure A10: Reaction force vs displacement graph of a square tube crushed against a frictionless end plate using the 10th eigenmode as an imperfection factor.

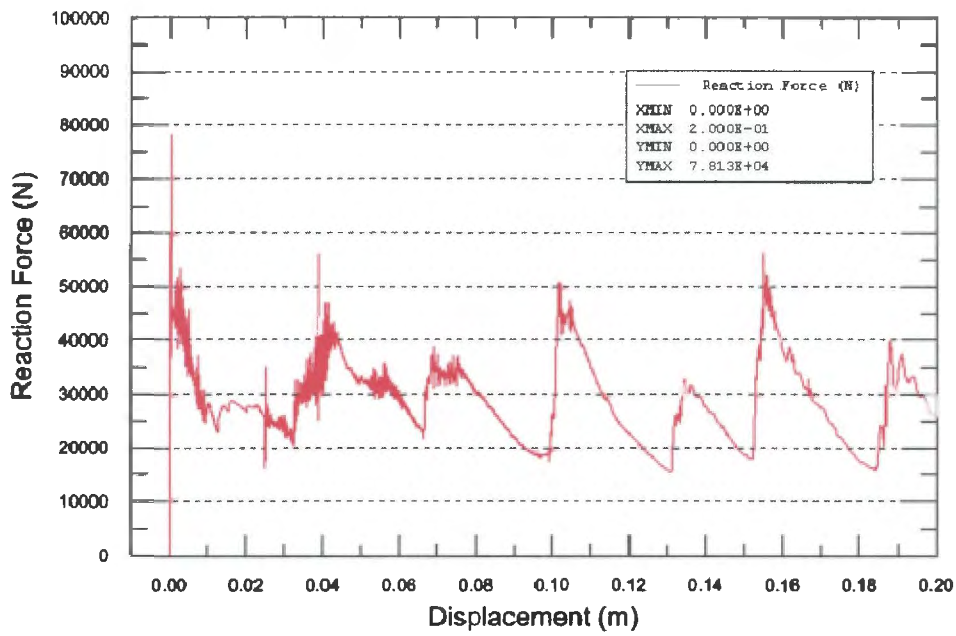

Figure A11: Reaction force vs displacement graph of a square tube crushed against a frictionless end plate using multiple eigenvalues as imperfection factors.

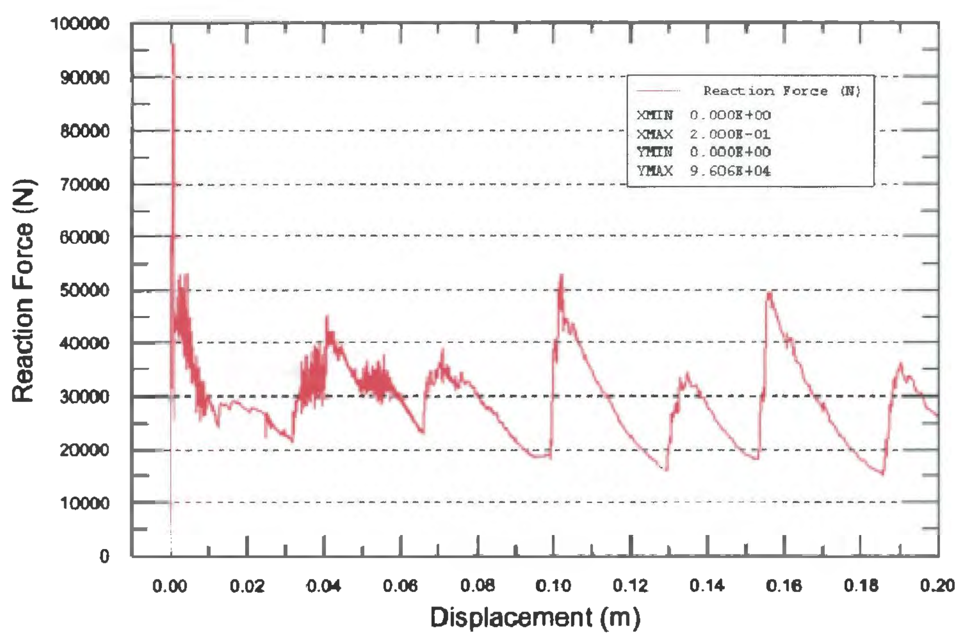

Figure A12: Reaction force vs displacement graph of a square tube crushed against a frictionless end plate using no imperfection factors.

APPENDIX B:

ABAQUS LISTING FOR A BUCKLING ANALYSIS OF A SQUARE TUBE TO DETERMINE THE EIGENMODES AND EIGENVALUES

NOTE: Because the input decks were generated by the pre-processor, ABAQUS CAE, each node and element is defined in the input deck instead of being generated by the suitable keywords when the input deck is created manually. Because of this the input decks are excessively long, so the majority of the node and element definitions have been omitted from the example input deck below.

```
*Heading
 Tube crush -- buckling analysis
** Job name: Square_tube_buckle Model name: Buckle
*Preprint, echo=NO, model=NO, history=NO, contact=NO
**
** PARTS
**
*Part, name=Plate
*End Part
*Part, name=Tube
*End Part
**
** ASSEMBLY
**
*Assembly, name=Assembly
**
*Instance, name=Tube-1, part=Tube
*Node
      1,       -0.025,        0.025,         0.3
      2,        0.025,        0.025,         0.3
      3,        0.025,        0.025,          0.
      4,       -0.025,        0.025,          0.
      5,        0.025,       -0.025,         0.3
      6,        0.025,       -0.025,          0.
      7,       -0.025,       -0.025,         0.3
      8,       -0.025,       -0.025,          0.
      9,      -0.0225,        0.025,         0.3
     10,        -0.02,        0.025,         0.3
```

```
9590, 9670, 9671,  627,  628
9591, 9671, 9672,  626,  627
9592, 9672, 9673,  625,  626
9593, 9673, 9674,  624,  625
9594, 9674, 9675,  623,  624
9595, 9675, 9676,  622,  623
9596, 9676, 9677,  621,  622
9597, 9677, 9678,  620,  621
9598, 9678, 9679,  619,  620
9599, 9679, 9680,  618,  619
9600, 9680,  166,    4,  618
** Region: (TubeSection:Picked)
*Elset, elset=_PickedSet3, internal, generate
    1,  9600,     1
** Section: TubeSection
*Shell Section, elset=_PickedSet3, material=Steel
0.0012, 3
*End Instance
**
*Instance, name=Plate-1, part=Plate
          0.,           0.,          0.3
*Node
      1,        -0.05,        -0.05,           0.
      2,         0.05,        -0.05,           0.
      3,        -0.05,         0.05,           0.
      4,         0.05,         0.05,           0.
*Element, type=R3D4
1, 1, 2, 4, 3
** Region: (MassSection:Picked)
*Element, type=MASS, elset=_PickedSet5_MASS_
2, 5
*Mass, elset=_PickedSet5_MASS_
250.,
*Node
      5,           0.,           0.,           0.
*Nset, nset=Plate-1-RefPt_, internal
5,
*Elset, elset=Plate-1
 1,
*End Instance
**
*Instance, name=Plate-2, part=Plate
*Node
      1,        -0.05,        -0.05,           0.
      2,         0.05,        -0.05,           0.
      3,        -0.05,         0.05,           0.
      4,         0.05,         0.05,           0.
*Element, type=R3D4
1, 1, 2, 4, 3
** Region: (MassSection:Picked)
*Element, type=MASS, elset=_PickedSet5_MASS_
2, 5
*Mass, elset=_PickedSet5_MASS_
250.,
*Node
      5,           0.,           0.,           0.
*Nset, nset=Plate-2-RefPt_, internal
5,
*Elset, elset=Plate-2
 1,
*End Instance
```

```
*Nset, nset=Top, instance=Tube-1
   1,   2,   5,   7,   9,  10,  11,  12,  13,  14,  15,  16,  17,
18,  19,  20
  21,  22,  23,  24,  25,  26,  27, 285, 286, 287, 288, 289, 290,
291, 292, 293
 294, 295, 296, 297, 298, 299, 300, 301, 302, 303, 442, 443, 444,
445, 446, 447
 448, 449, 450, 451, 452, 453, 454, 455, 456, 457, 458, 459, 460,
599, 600, 601
 602, 603, 604, 605, 606, 607, 608, 609, 610, 611, 612, 613, 614,
615, 616, 617
*Elset, elset=Top, instance=Tube-1
    1,    2,    3,    4,    5,    6,    7,    8,    9,   10,   11,
12,   13,   14,   15,   16
   17,   18,   19,   20, 2401, 2402, 2403, 2404, 2405, 2406, 2407,
2408, 2409, 2410, 2411, 2412
 2413, 2414, 2415, 2416, 2417, 2418, 2419, 2420, 4801, 4802, 4803,
4804, 4805, 4806, 4807, 4808
 4809, 4810, 4811, 4812, 4813, 4814, 4815, 4816, 4817, 4818, 4819,
4820, 7201, 7202, 7203, 7204
 7205, 7206, 7207, 7208, 7209, 7210, 7211, 7212, 7213, 7214, 7215,
7216, 7217, 7218, 7219, 7220
*Nset, nset=Bot, instance=Tube-1
   3,   4,   6,   8, 147, 148, 149, 150, 151, 152, 153, 154, 155,
156, 157, 158
 159, 160, 161, 162, 163, 164, 165, 423, 424, 425, 426, 427, 428,
429, 430, 431
 432, 433, 434, 435, 436, 437, 438, 439, 440, 441, 580, 581, 582,
583, 584, 585
 586, 587, 588, 589, 590, 591, 592, 593, 594, 595, 596, 597, 598,
618, 619, 620
 621, 622, 623, 624, 625, 626, 627, 628, 629, 630, 631, 632, 633,
634, 635, 636
*Elset, elset=Bot, instance=Tube-1
 2381, 2382, 2383, 2384, 2385, 2386, 2387, 2388, 2389, 2390, 2391,
2392, 2393, 2394, 2395, 2396
 2397, 2398, 2399, 2400, 4781, 4782, 4783, 4784, 4785, 4786, 4787,
4788, 4789, 4790, 4791, 4792
 4793, 4794, 4795, 4796, 4797, 4798, 4799, 4800, 7181, 7182, 7183,
7184, 7185, 7186, 7187, 7188
 7189, 7190, 7191, 7192, 7193, 7194, 7195, 7196, 7197, 7198, 7199,
7200, 9581, 9582, 9583, 9584
 9585, 9586, 9587, 9588, 9589, 9590, 9591, 9592, 9593, 9594, 9595,
9596, 9597, 9598, 9599, 9600
*Nset, nset=RigidRefTop, instance=Plate-1
 5,
*Nset, nset=RigidRefBot, instance=Plate-2
 5,
*Nset, nset=All, instance=Tube-1, generate
    1,  9680,     1
*Elset, elset=All, instance=Tube-1, generate
    1,  9600,     1
*Nset, nset=_PickedSet39, internal, instance=Plate-2
 5,
*Nset, nset=_PickedSet42, internal, instance=Plate-2
 5,
*Elset, elset=_TopSurf_SNEG, internal, instance=Plate-1
 1,
*Surface, type=ELEMENT, name=TopSurf
_TopSurf_SNEG, SNEG
*Elset, elset=_BotSurf_SPOS, internal, instance=Plate-2
```

```
 1,
*Surface, type=ELEMENT, name=BotSurf
_BotSurf_SPOS, SPOS
*Surface, type=NODE, name=Top_CNS_, internal
Top, 1.
*Surface, type=NODE, name=Bot_CNS_, internal
Bot, 1.
*Rigid Body, ref node=Plate-1.Plate-1-RefPt_, elset=Plate-1.Plate-1
*Rigid Body, ref node=Plate-2.Plate-2-RefPt_, elset=Plate-2.Plate-2
** Constraint: BotSurf-Tube
*Tie, name=BotSurf-Tube, adjust=yes, position tolerance=0.01
Bot_CNS_, BotSurf
*End Assembly
**
** MATERIALS
**
*Material, name=Steel
*Density
7850.,
*Elastic
  2.07e+11,  0.3,   0.
 1.953e+11,  0.3, 200.
  1.72e+11,  0.3, 600.
  1.46e+11,  0.3, 700.
 1.249e+11,  0.3, 800.
 1.094e+11,  0.3, 900.
 1.001e+11,  0.3,1000.
   9.7e+10,  0.3,1100.
*Plastic
 2.59e+08,        0.,       0.
 2.74e+08, 0.007185,       0.
 3.25e+08, 0.025556,       0.
 3.85e+08, 0.051413,       0.
 4.48e+08, 0.091745,       0.
 4.75e+08, 0.115659,       0.
 5.06e+08, 0.150734,       0.
 5.23e+08, 0.174145,       0.
 5.41e+08, 0.204152,       0.
 5.51e+08, 0.226766,       0.
 5.58e+08, 0.247764,       0.
 5.48e+08, 0.280197,       0.
 2.59e+08,        0.,     200.
 2.74e+08, 0.007185,     200.
 3.25e+08, 0.025556,     200.
 3.85e+08, 0.051413,     200.
 4.48e+08, 0.091745,     200.
 4.75e+08, 0.115659,     200.
 5.06e+08, 0.150734,     200.
 5.23e+08, 0.174145,     200.
 5.41e+08, 0.204152,     200.
 5.51e+08, 0.226766,     200.
 5.58e+08, 0.247764,     200.
 5.48e+08, 0.280197,     200.
 3.44e+07,        0.,     700.
 3.64e+07, 0.007185,     700.
 4.32e+07, 0.025556,     700.
 5.12e+07, 0.051413,     700.
 5.96e+07, 0.091745,     700.
 6.32e+07, 0.115659,     700.
 6.73e+07, 0.150734,     700.
 6.96e+07, 0.174145,     700.
```

```
 7.19e+07, 0.204152,     700.
 7.33e+07, 0.226766,     700.
 7.42e+07, 0.247764,     700.
 7.29e+07, 0.280197,     700.
  4.3e+06,        0.,   1000.
 4.54e+06, 0.007185,    1000.
  5.4e+06, 0.025556,    1000.
 6.39e+06, 0.051413,    1000.
 7.44e+06, 0.091745,    1000.
 7.89e+06, 0.115659,    1000.
  8.4e+06, 0.150734,    1000.
 8.68e+06, 0.174145,    1000.
 8.98e+06, 0.204152,    1000.
 9.15e+06, 0.226766,    1000.
 9.26e+06, 0.247764,    1000.
  9.1e+06, 0.280197,    1000.
*Rate Dependent
 40.4,5.
**
** INTERACTION PROPERTIES
**
*Surface Interaction, name=NoFric
1.,
*Friction
0.,
**
** BOUNDARY CONDITIONS
**
** Name: FixBot Type: Displacement/Rotation
*Boundary
_PickedSet42, 1, 1
_PickedSet42, 2, 2
_PickedSet42, 4, 4
_PickedSet42, 5, 5
_PickedSet42, 6, 6
** Name: FixTop Type: Displacement/Rotation
*Boundary
RigidRefTop, 1, 1
RigidRefTop, 2, 2
RigidRefTop, 3, 3
RigidRefTop, 4, 4
RigidRefTop, 5, 5
RigidRefTop, 6, 6
**
** INTERACTIONS
**
** Interaction: TopSurf-Tube
*Contact Pair, interaction=NoFric, adjust=0.01
Top_CNS_, TopSurf
** ----------------------------------------------------------------
**
** STEP: TubeBuckle
**
*Step, name=TubeBuckle, perturbation
Buckling analysis of the tube
*Buckle
10, , 18, 50
**
** BOUNDARY CONDITIONS
**
** Name: FixBot Type: Displacement/Rotation
```

```
*Boundary, op=NEW, load case=1
_PickedSet42, 1, 1
_PickedSet42, 2, 2
_PickedSet42, 4, 4
_PickedSet42, 5, 5
_PickedSet42, 6, 6
*Boundary, op=NEW, load case=2
_PickedSet42, 1, 1
_PickedSet42, 2, 2
_PickedSet42, 4, 4
_PickedSet42, 5, 5
_PickedSet42, 6, 6
** Name: FixTop Type: Displacement/Rotation
*Boundary, op=NEW, load case=1
RigidRefTop, 1, 1
RigidRefTop, 2, 2
RigidRefTop, 3, 3
RigidRefTop, 4, 4
RigidRefTop, 5, 5
RigidRefTop, 6, 6
*Boundary, op=NEW, load case=2
RigidRefTop, 1, 1
RigidRefTop, 2, 2
RigidRefTop, 3, 3
RigidRefTop, 4, 4
RigidRefTop, 5, 5
RigidRefTop, 6, 6
**
** LOADS
**
** Name: Load-1   Type: Concentrated force
*Cload
_PickedSet39, 3, 250.
**
** OUTPUT REQUESTS
**
*Restart, write, frequency=1
**
** FIELD OUTPUT: F-Output-1
**
*Output, field, variable=PRESELECT
*El Print, freq=999999
*Node Print, freq=999999
*node file
U,
*End Step
```

APPENDIX C:

ABAQUS LISTING FOR A CRUSHING ANALYSIS OF A SQUARE TUBE USING ITS EIGENMODES AS IMPERFECTION FACTORS TO PERTURB THE MODEL

NOTE: Because the input decks were generated by the pre-processor, ABAQUS CAE, each node and element is defined in the input deck instead of being generated by the suitable keywords when the input deck is created manually. Because of this the input decks are excessively long, so the majority of the node and element definitions have been omitted from the example input deck below.

```
*Heading
 Tube crush -- crushing analysis
** Job name: Square_tube_crush_mult_eigen Model name: Crush
*Preprint, echo=NO, model=NO, history=NO, contact=NO
**
** PARTS
**
*Part, name=Plate
*End Part
*Part, name=Tube
*End Part
**
** ASSEMBLY
**
*Assembly, name=Assembly
**
*Instance, name=Tube-1, part=Tube
*Node
      1,        -0.025,         0.025,           0.3
      2,         0.025,         0.025,           0.3
      3,         0.025,         0.025,            0.
      4,        -0.025,         0.025,            0.
      5,         0.025,        -0.025,           0.3
      6,         0.025,        -0.025,            0.
      7,        -0.025,        -0.025,           0.3
      8,        -0.025,        -0.025,            0.
```

```
      9,      -0.0225,        0.025,           0.3
     10,        -0.02,        0.025,           0.3

9591, 9671, 9672,  626,  627
9592, 9672, 9673,  625,  626
9593, 9673, 9674,  624,  625
9594, 9674, 9675,  623,  624
9595, 9675, 9676,  622,  623
9596, 9676, 9677,  621,  622
9597, 9677, 9678,  620,  621
9598, 9678, 9679,  619,  620
9599, 9679, 9680,  618,  619
9600, 9680,  166,    4,  618
** Region: (TubeSection:Picked)
*Elset, elset=_G2, internal, generate
    1,  9600,     1
** Section: TubeSection
*Shell Section, elset=_G2, material=Steel
0.0012, 3
*End Instance
**
*Instance, name=Plate-1, part=Plate
          0.,           0.,          0.3
*Node
      1,        -0.05,        -0.05,            0.
      2,         0.05,        -0.05,            0.
      3,        -0.05,         0.05,            0.
      4,         0.05,         0.05,            0.
*Element, type=R3D4
1, 1, 2, 4, 3
** Region: (MassSection:Picked)
*Element, type=MASS, elset=_PickedSet5_MASS_
2, 5
*Mass, elset=_PickedSet5_MASS_
1e-300,
*Node
      5,           0.,           0.,            0.
*Nset, nset=Plate-1-RefPt_, internal
5,
*Elset, elset=Plate-1
 1,
*End Instance
**
*Instance, name=Plate-2, part=Plate
*Node
      1,        -0.05,        -0.05,            0.
      2,         0.05,        -0.05,            0.
      3,        -0.05,         0.05,            0.
      4,         0.05,         0.05,            0.
*Element, type=R3D4
1, 1, 2, 4, 3
** Region: (MassSection:Picked)
*Element, type=MASS, elset=_PickedSet5_MASS_
2, 5
*Mass, elset=_PickedSet5_MASS_
1e-300,
*Node
      5,           0.,           0.,            0.
*Nset, nset=Plate-2-RefPt_, internal
5,
*Elset, elset=Plate-2
```

```
1,
*End Instance
*Nset, nset=Top, instance=Tube-1
   1,   2,   5,   7,   9,  10,  11,  12,  13,  14,  15,  16,  17,
18,  19,  20
  21,  22,  23,  24,  25,  26,  27, 285, 286, 287, 288, 289, 290,
291, 292, 293
 294, 295, 296, 297, 298, 299, 300, 301, 302, 303, 442, 443, 444,
445, 446, 447
 448, 449, 450, 451, 452, 453, 454, 455, 456, 457, 458, 459, 460,
599, 600, 601
 602, 603, 604, 605, 606, 607, 608, 609, 610, 611, 612, 613, 614,
615, 616, 617
*Elset, elset=Top, instance=Tube-1
    1,    2,    3,    4,    5,    6,    7,    8,    9,   10,   11,
12,   13,   14,   15,   16
   17,   18,   19,   20, 2401, 2402, 2403, 2404, 2405, 2406, 2407,
2408, 2409, 2410, 2411, 2412
 2413, 2414, 2415, 2416, 2417, 2418, 2419, 2420, 4801, 4802, 4803,
4804, 4805, 4806, 4807, 4808
 4809, 4810, 4811, 4812, 4813, 4814, 4815, 4816, 4817, 4818, 4819,
4820, 7201, 7202, 7203, 7204
 7205, 7206, 7207, 7208, 7209, 7210, 7211, 7212, 7213, 7214, 7215,
7216, 7217, 7218, 7219, 7220
*Nset, nset=Bot, instance=Tube-1
   3,   4,   6,   8, 147, 148, 149, 150, 151, 152, 153, 154, 155,
156, 157, 158
 159, 160, 161, 162, 163, 164, 165, 423, 424, 425, 426, 427, 428,
429, 430, 431
 432, 433, 434, 435, 436, 437, 438, 439, 440, 441, 580, 581, 582,
583, 584, 585
 586, 587, 588, 589, 590, 591, 592, 593, 594, 595, 596, 597, 598,
618, 619, 620
 621, 622, 623, 624, 625, 626, 627, 628, 629, 630, 631, 632, 633,
634, 635, 636
*Elset, elset=Bot, instance=Tube-1
 2381, 2382, 2383, 2384, 2385, 2386, 2387, 2388, 2389, 2390, 2391,
2392, 2393, 2394, 2395, 2396
 2397, 2398, 2399, 2400, 4781, 4782, 4783, 4784, 4785, 4786, 4787,
4788, 4789, 4790, 4791, 4792
 4793, 4794, 4795, 4796, 4797, 4798, 4799, 4800, 7181, 7182, 7183,
7184, 7185, 7186, 7187, 7188
 7189, 7190, 7191, 7192, 7193, 7194, 7195, 7196, 7197, 7198, 7199,
7200, 9581, 9582, 9583, 9584
 9585, 9586, 9587, 9588, 9589, 9590, 9591, 9592, 9593, 9594, 9595,
9596, 9597, 9598, 9599, 9600
*Nset, nset=RigidRefTop, instance=Plate-1
 5,
*Nset, nset=RigidRefBot, instance=Plate-2
 5,
*Nset, nset=All, instance=Tube-1, generate
    1,  9680,     1
*Elset, elset=All, instance=Tube-1, generate
    1,  9600,     1
*Nset, nset=_PickedSet32, internal, instance=Plate-2
 5,
*Nset, nset=_PickedSet34, internal, instance=Plate-2
 5,
*Nset, nset=_PickedSet36, internal, instance=Plate-2
 5,
*Nset, nset=_PickedSet37, internal, instance=Plate-2
```

```
 5,
*Nset, nset=_PickedSet48, internal, instance=Plate-2
 5,
*Elset, elset=_TopSurf_SNEG, internal, instance=Plate-1
 1,
*Surface, type=ELEMENT, name=TopSurf
_TopSurf_SNEG, SNEG
*Elset, elset=_BotSurf_SPOS, internal, instance=Plate-2
 1,
*Surface, type=ELEMENT, name=BotSurf
_BotSurf_SPOS, SPOS
*Elset, elset=_Tube_, internal, instance=Tube-1, generate
    1,  9600,     1
*Surface, type=ELEMENT, name=Tube
_Tube_,
*Surface, type=NODE, name=Bot_CNS_, internal
Bot, 1.
*Rigid Body, ref node=Plate-1.Plate-1-RefPt_, elset=Plate-1.Plate-1
*Rigid Body, ref node=Plate-2.Plate-2-RefPt_, elset=Plate-2.Plate-2
** Constraint: BotSurf-Tube
*Tie, name=BotSurf-Tube, adjust=yes, position tolerance=0.01
Bot_CNS_, BotSurf
*End Assembly
*Imperfection, file=Square_tube_buckle,
    step=1
1, 2.4e-5
2, 0.96e-5
3, 0.48e-5
4, 0.216e-5
5, 0.192e-5
6, 0.12e-5
7, 0.12e-5
8, 0.096e-5
9, 0.024e-5
10, 0.024e-5
**
** MATERIALS
**
*Material, name=Steel
*Density
7850.,
*Elastic
  2.07e+11,  0.3,   0.
 1.953e+11,  0.3, 200.
  1.72e+11,  0.3, 600.
  1.46e+11,  0.3, 700.
 1.249e+11,  0.3, 800.
 1.094e+11,  0.3, 900.
 1.001e+11,  0.3,1000.
   9.7e+10,  0.3,1100.
*Plastic
 2.59e+08,        0.,        0.
 2.74e+08, 0.007185,        0.
 3.25e+08, 0.025556,        0.
 3.85e+08, 0.051413,        0.
 4.48e+08, 0.091745,        0.
 4.75e+08, 0.115659,        0.
 5.06e+08, 0.150734,        0.
 5.23e+08, 0.174145,        0.
 5.41e+08, 0.204152,        0.
 5.51e+08, 0.226766,        0.
```

```
 5.58e+08, 0.247764,       0.
 5.48e+08, 0.280197,       0.
 2.59e+08,        0.,     200.
 2.74e+08, 0.007185,     200.
 3.25e+08, 0.025556,     200.
 3.85e+08, 0.051413,     200.
 4.48e+08, 0.091745,     200.
 4.75e+08, 0.115659,     200.
 5.06e+08, 0.150734,     200.
 5.23e+08, 0.174145,     200.
 5.41e+08, 0.204152,     200.
 5.51e+08, 0.226766,     200.
 5.58e+08, 0.247764,     200.
 5.48e+08, 0.280197,     200.
 3.44e+07,        0.,     700.
 3.64e+07, 0.007185,     700.
 4.32e+07, 0.025556,     700.
 5.12e+07, 0.051413,     700.
 5.96e+07, 0.091745,     700.
 6.32e+07, 0.115659,     700.
 6.73e+07, 0.150734,     700.
 6.96e+07, 0.174145,     700.
 7.19e+07, 0.204152,     700.
 7.33e+07, 0.226766,     700.
 7.42e+07, 0.247764,     700.
 7.29e+07, 0.280197,     700.
  4.3e+06,        0.,    1000.
 4.54e+06, 0.007185,    1000.
  5.4e+06, 0.025556,    1000.
 6.39e+06, 0.051413,    1000.
 7.44e+06, 0.091745,    1000.
 7.89e+06, 0.115659,    1000.
  8.4e+06, 0.150734,    1000.
 8.68e+06, 0.174145,    1000.
 8.98e+06, 0.204152,    1000.
 9.15e+06, 0.226766,    1000.
 9.26e+06, 0.247764,    1000.
  9.1e+06, 0.280197,    1000.
*Rate Dependent
 40.4,5.
**
** INTERACTION PROPERTIES
**
*Surface Interaction, name=Fric
*Friction
 0.3,
*Surface Interaction, name=NoFric
*Friction
0.,
**
** BOUNDARY CONDITIONS
**
** Name: FixTop Type: Displacement/Rotation
*Boundary
RigidRefTop, 1, 1
RigidRefTop, 2, 2
RigidRefTop, 3, 3
RigidRefTop, 4, 4
RigidRefTop, 5, 5
RigidRefTop, 6, 6
** Name: only z-direc Type: Displacement/Rotation
```

```
*Boundary
_PickedSet48, 1, 1
_PickedSet48, 2, 2
_PickedSet48, 4, 4
_PickedSet48, 5, 5
_PickedSet48, 6, 6
** Name: velocity BC Type: Velocity/Angular velocity
*Boundary, type=VELOCITY
_PickedSet32, 3, 3
** ----------------------------------------------------------------
**
** STEP: TubeCrush no MS
**
*Step, name="TubeCrush no MS"
Crushing of square tube with constant vel=0.5 m/s No Mass Scaling
*Dynamic, Explicit
, 0.05
*Bulk Viscosity
0.06, 1.2
**
** BOUNDARY CONDITIONS
**
** Name: FixTop Type: Displacement/Rotation
*Boundary, op=NEW
RigidRefTop, 1, 1
RigidRefTop, 2, 2
RigidRefTop, 3, 3
RigidRefTop, 4, 4
RigidRefTop, 5, 5
RigidRefTop, 6, 6
** Name: only z-direc Type: Displacement/Rotation
*Boundary, op=NEW
_PickedSet48, 1, 1
_PickedSet48, 2, 2
_PickedSet48, 4, 4
_PickedSet48, 5, 5
_PickedSet48, 6, 6
** Name: velocity BC Type: Velocity/Angular velocity
*Boundary, op=NEW, type=VELOCITY
_PickedSet32, 3, 3, 0.5
**
** INTERACTIONS
**
** Interaction: TopPlate-Tube
*Contact Pair, interaction=NoFric, mechanical constraint=KINEMATIC,
cpset=TopPlate-Tube
Tube, TopSurf
** Interaction: Tube-Self
*Contact Pair, interaction=Fric, mechanical constraint=KINEMATIC,
cpset=Tube-Self
Tube,
**
** OUTPUT REQUESTS
**
*Restart, write, number interval=1, time marks=NO
**
** FIELD OUTPUT: F-Output-1
**
*Output, field
*Node Output
A, RF, U, V
```

```
*Element Output
ENER, LE, PE, PEEQ, S
*Contact Output
CSTRESS,
**
** HISTORY OUTPUT: H-Output-All
**
*Output, history, variable=PRESELECT
**
** HISTORY OUTPUT: H-Output-RigidRefBot
**
*Output, history, time interval=1e-06
*Node Output, nset=RigidRefBot
RF1, RF2, RF3, RM1, RM2, RM3, U1, U2
U3, UR1, UR2, UR3, V1, V2, V3, VR1
VR2, VR3
**
** HISTORY OUTPUT: H-Output-RigidRefTop
**
*Node Output, nset=RigidRefTop
RF1, RF2, RF3, RM1, RM2, RM3, U1, U2
U3, UR1, UR2, UR3, V1, V2, V3, VR1
VR2, VR3
*End Step
** ----------------------------------------------------------------
**
** STEP: Tubecrush with MS=225
**
*Step, name="Tubecrush with MS=225"
Crushing of square Tube with const vel=0.5m\s Mass Scaling=225
*Dynamic, Explicit
, 0.35
*Bulk Viscosity
0.06, 1.2
** Mass Scaling: Semi-Automatic
**               Whole Model
*Fixed Mass Scaling, factor=225.
**
** OUTPUT REQUESTS
**
*Restart, write, number interval=1, time marks=NO
**
** FIELD OUTPUT: F-Output-1
**
*Output, field
*Node Output
A, RF, U, V
*Element Output
ENER, LE, PE, PEEQ, S
*Contact Output
CSTRESS,
**
** HISTORY OUTPUT: H-Output-All
**
*Output, history, variable=PRESELECT
**
** HISTORY OUTPUT: H-Output-RigidRefBot
**
*Output, history, time interval=1e-06
*Node Output, nset=RigidRefBot
RF1, RF2, RF3, RM1, RM2, RM3, U1, U2
```

```
U3, UR1, UR2, UR3, V1, V2, V3, VR1
VR2, VR3
**
** HISTORY OUTPUT: H-Output-RigidRefTop
**
*Node Output, nset=RigidRefTop
RF1, RF2, RF3, RM1, RM2, RM3, U1, U2
U3, UR1, UR2, UR3, V1, V2, V3, VR1
VR2, VR3
*End Step
```